Measurement of WZ production and searches for anomalous top quark decays and Higgs boson production using tri-lepton final states in $p\bar{p}$ collisions at $\sqrt{s} = 1.96$ TeV

by

Carrie L. McGivern

Submitted to the graduate degree program in Physics and the Graduate
Faculty of the University of Kansas in partial fulfillment of the
requirements for the degree of Doctor of Philosophy

Chairperson Graham Wilson, Ph.D.

Philip Baringer, Ph.D.

Alice Bean, Ph.D.

David Lerner, Ph.D.

Douglas McKay, Ph.D.

Date defended: April 9, 2012

The Dissertation Committee for Carrie L. McGivern certifies that this is
the approved version of the following dissertation:

Measurement of WZ production and searches for anomalous top
quark decays and Higgs boson production using tri-lepton final
states in $p\bar{p}$ collisions at $\sqrt{s} = 1.96$ TeV

Chairperson Graham Wilson, Ph.D.

Date approved: April 12, 2012

Abstract

We present the results of three analyses; a WZ production cross section measurement, a search for new physics in anomalous top quark decays, and the search for the standard model Higgs boson, all with final states of three or more leptons – either electrons or muons – plus an imbalance of transverse momentum using Tevatron proton and anti-proton collisions at a center–of–mass energy of $\sqrt{s} = 1.96$ TeV with the DØ detector at the Fermi National Accelerator Laboratory in Chicago, IL. The first analysis reports a measurement of the $WZ \to \ell'\nu\ell\bar{\ell}$ cross section. Using 4.1 fb^{-1} of integrated luminosity, we measure a cross section of $3.90^{+1.01}_{-0.85}(stat + syst) \pm 0.31(lumi)$ pb, which is found to be in good agreement with the standard model prediction. The second analysis is an extension of the first, in which we use the same dataset and look for the flavor changing neutral current decay of $t \to Zq$ in $p\bar{p} \to t\bar{t} \to WbZq \to \ \ell'\nu\ell\bar{\ell} +$jets decays. Here q is considered to be either a u or c quark, and both the q and b quarks decay hadronically. We find no evidence of flavor changing neutral current production and set upper limits on the branching ratio of $BR(t \to Zq) < 3.2\%$ observed, with an expected limit of $< 3.8\%$, at the 95% confidence level. Finally, we present a search for the standard model Higgs boson, using associated WH and ZH production, in the $ee\mu$ final state. Now using 9.7 fb^{-1}, the full dataset available at DØ, we observe no excess above the standard model background prediction and extract limits on the Higgs boson production cross section times branching ratio for a Higgs boson mass range of $m_H =$ 100 – 200 GeV/c^2, in intervals of 5 GeV/c^2.

Acknowledgements

First and foremost I would like to thank my husband, John Olney, for his unwavering support and encouragement and his many attempts at distraction when I got frustrated. A never-ending thanks to my parents, Denny and Joyce McGivern, and family for their constant love and support.

I am beyond grateful to my mentor and thesis advisor, Prof. Graham Wilson, for all his help and direction. He was gracious enough to take me in and make me feel like I was his only student. Also a special thanks to my supervisor at Fermilab, Dr. James Kraus, for his ever patient explanations. Jim has been my faithful collaborator on all analyses and an endless source of programming and analysis help.

I could not have gotten anywhere without my collaborators and friends at Fermilab. Dr. Konstantinos Petridis and Ruchika Nayyar have been a godsend on the VH analysis, answering endless questions regarding their framework. Prof. Christian Schwanenberger, Dr. Yvonne Peters, and Prof. Stefan Soldner–Rembold have helped immensely with the FCNC publication, while the WZ publication would not have occurred without Prof. Andrew Askew, Dr. Ketino Kaadze, and Prof. Yurii Maravin. A happy thanks to my CTT peeps, past and further past, for their operational support (especially at 4 am); Dr. Marc Buehler, Dr. George Ginther, Jose Andres Garcia Gonzalez, Dr. Stefan Grünendahl, Ivan Heredia–De La Cruz, Dr. William Lee, Ricardo Magaña–Villalba, and Jamieson Olsen.And I cannot forget my good friends at Fermilab; Dr. Zeynep Isvan, Dr. Mark Mathis, Michelle Prewitt, Dr. Mandy Rominsky, Louise Suter and her boytoy Joe. You guys will be missed most of all.

Many thanks to my friends at Kansas; Dr. Justace Clutter, Sriharsha Pothapragada, Jennifer Sibille, and Victoria Zhukova, for making my time there enjoyable. May we never lose touch. I would also thank my good friends at Iowa with whom I have stayed in contact with; Prof. Vincent Rodgers, Dr. Firdevs Duru, and Dr. Aaron Breneman. You guys are my very best friends (especially Firdevs!).

Thanks to all those who believed in and encouraged me.

It means more than words can say...

Contents

List of Tables

List of Figures

Outline

We start with a review of the standard model, followed by hadron collider phenomenology and the Higgs mechanism in Chapter 1. This is followed by a detailed description of the Tevatron accelerator and the multi-purpose DØ detector in Chapter 2, while Chapter 3 describes how the physical objects are reconstructed in the various subdetectors, along with the DØ standard particle identification definitions. Chapter 4 presents the analysis and results of the $WZ \rightarrow$ tri-lepton plus missing transverse energy cross section measurement. An extension of this analysis is presented in Chapter 5, where we search for the flavor changing neutral current decays of pair-produced top quarks via $t \rightarrow Zq$, where q is either a c or u quark, using tri-lepton events with additional jets. We finish with a search for the Higgs boson decay of $VH \rightarrow VWW^{*} \rightarrow$ tri-leptons plus missing transverse energy, where V is either the W or Z boson, that is discussed in Chapter 6. Finally, the conclusion is given in Chapter 7. The standard Monte Carlo reweighting, a brief description of the Common Samples Group skims used, and information on the multivariate anaylsis technique of boosted decision trees are described in the appendices.

1 Introduction

Not from the stars do I my judgment pluck;
And yet methinks I have astronomy,
But not to tell of good or evil luck,
Of plagues, of dearths, or seasons' quality;
Nor can I fortune to brief minutes tell,
Pointing to each his thunder, rain and wind,
Or say with princes if it shall go well,
By oft predict that I in heaven find:
But from thine eyes my knowledge I derive,
And, constant stars, in them I read such art
As truth and beauty shall together thrive,
If from thyself to store thou wouldst convert;
Or else of thee this I prognosticate:
Thy end is truth's and beauty's doom and date.
– William Shakespeare, Sonnet 14

The standard model (SM) of particle physics was predominantly developed in the 1960's and 70's. It is a description of how quantum electrodynamics (QED – the electromagnetic force), quantum chromodynamics (QCD – the strong force), and the weak force interact and govern particle decays via the SU(3) × SU(2)$_L$ × U(1)$_Y$ gauge field theory. It consists of quarks and leptons (known as fermions) that make up matter and gauge bosons which mediate, or carry, the fundamental forces mentioned above.

Quarks and leptons are spin-1/2 particles and consist of three generations (or families). As spin-1/2 particles they obey Fermi-Dirac statistics, meaning that more than one fermion cannot occupy the same quantum state. There are six leptons in all; electron (e), muon (μ), and tau (τ), each with their own corresponding neutrino (ν), and six quarks; up (u), down (d), charm (c), strange (s), top (t), and bottom (b). Additionally each quark carries a color charge; red (R), green (G), or blue (B). Furthermore, each particle has a corresponding anti-particle, denoted with an overhead bar $\bar{f}$, which is exactly the same except it has an opposite electric charge and inverted internal quantum numbers. Most matter consists of the first generation – electron, up quark, and down quark – since the heavier particles in the higher generations can quickly decay into lighter particles. Searches are ongoing for a possible fourth generation of fermions [1]. The spin and chirality of a particle define its “handedness”. For example, only left-handed fermions interact with weak-force particles and therefore form doublet fields, while right-handed fermions have singlet fields.

Due to color confinement, quarks cannot be found alone in nature. They are grouped either in baryons (three-quark particles, such as protons – uud) or mesons (quark-anti-quark pairs, such as positively charged pions – $u\bar{d}$). As a consequence of this grouping, all particles are color neutral or “colorless”, ie. $u_R u_G d_B$ or $u_R \bar{d}_{\bar{R}}$.

Gauge bosons are integer spin particles. The W and Z bosons are mediators of the weak force, photons (γ) carry the electromagnetic force, and gluons (g) carry the strong force. Like quarks, gluons also carry a color charge. The Higgs (H) boson which describes how particles are imparted with mass, discussed in more detail in Sec. 1.1, still has yet to be discovered but current cross section limit measurements are narrowing down its most likely mass value.

Figure 1-1 [2] summarizes the fundamental particles found in the SM, along with each particle’s mass, charge, and spin.

For the last 40 odd years, most of the SM’s theoretical predictions have been validated through experimental results. The SM has been confirmed by the existence and form of the neutral weak current [3], the existence and masses of the W and Z weak gauge bosons [4], and the existence of the charm quark [5], first observed contained in the J/ψ meson. It has also postulated the gluon boson [6] and the existence of the top quark [7] years before they were discovered.

Despite its successful predictions, the SM – with its exclusion of gravity – does not describe all of nature in one unified fundamental theory and needs extensions to match the experimental observations. For example, the SM states that neutrinos are massless, but there is evidence in the form of neutrino oscillations that indicated that they must contain some mass [8], albeit extremely small. The SM also does not explain the origins of dark energy or dark matter. One of the more prominent issues relates

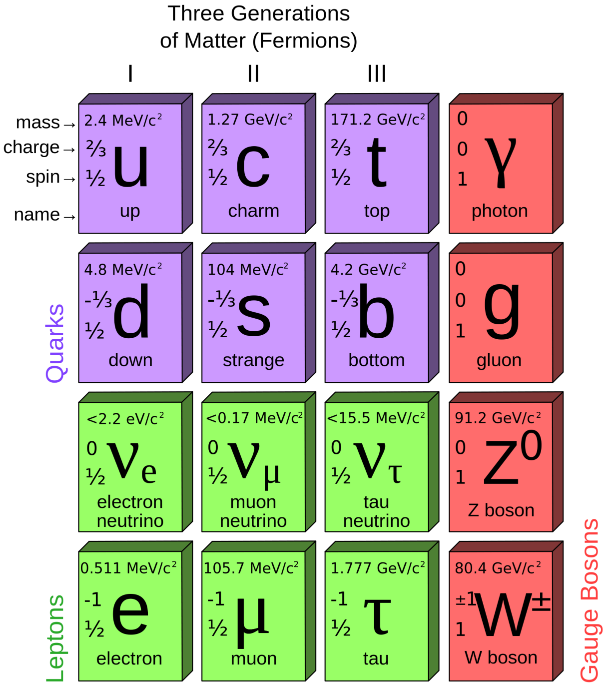

Figure 1-1: Standard model quark, lepton, and gauge boson summary [2].

to the Higgs Hierarchy Problem [9], in which the Higgs boson mass is significantly less than the Planck mass. We can explore theories beyond the SM (BSM) to account for these inconsistencies. One such theory with a number of possible models that offers a solution to most of these problems is supersymmetry (SUSY) [10].

1.1 Hadron Collider Phenomenology

Heavy diboson production (such as WZ) cross sections were first measured at the Tevatron [11, 12, 13]. Figure 1-2 summarizes the heavy gauge boson and diboson cross sections with theory predictions, in picobarn pb (where 1 barn $= 10^{-24}$ cm^2), along with when and where the observation was made [14]. As noted before, the Higgs boson is still the only piece of the SM puzzle yet to be discovered.

In general, the partial decay width, $\Gamma(X \rightarrow A + B)$, is a function of the invariant

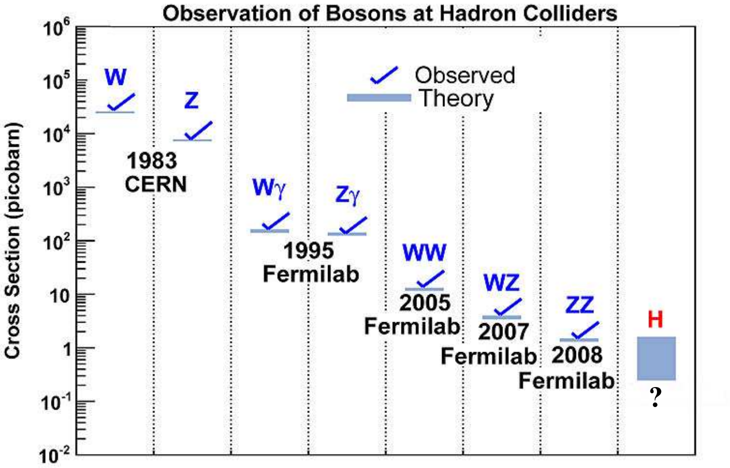

Figure 1-2: Heavy boson and diboson SM cross section values, including theoretical predictions [14].

amplitude squared, $|\mathcal{M}|^2$:

$$\Gamma(X \to A + B) = \frac{p_f}{32\pi^2 m_X^2} \int |\mathcal{M}|^2 \, d\Omega, \tag{1-1}$$

where p_f is the magnitude of the final particles' momentum ($|\mathbf{p_A}| = |\mathbf{p_B}| = p_f$), m_X is the mass of the decaying particle, and $d\Omega$ is the solid angle. The partial decay widths for the W and Z boson decaying leptonically are given by

$$\begin{aligned} \Gamma(W \to \ell\nu) &= \frac{g^2}{48\pi} M_W, \\ \Gamma(Z \to \ell\bar{\ell}) &= \frac{g^2}{48\pi \; cos^2\theta_W} (c_V^2 + c_A^2) M_Z, \end{aligned} \tag{1-2}$$

where g is the weak coupling constant, c_V and c_A are the vector and axial-vector couplings, respectively, θ_W is the Weinberg or weak mixing angle, and M_W and M_Z are the W and Z boson masses. The branching fraction, or ratio BR, values are then determined by dividing the partial decay widths by the total decay width, Γ_{tot} – the sum of all possible decays.

The focus of this thesis is tri-lepton final states, we look for the purely leptonic decays of the W and Z bosons, where $W \rightarrow \ell\nu$ and $Z \rightarrow \ell\bar{\ell}$, with ℓ being either an electron or muon. Taus are included in the signal acceptance, but are only considered after they decay into electrons or muons. Highly energetic multi-lepton final states have long been considered as golden channels in high energy physics. They provide clean, low background signatures that are sensitive to the physics being studied. Looking at the branching fractions of the W and Z bosons in Fig. 1-3 it is obvious that the probability of a leptonic decay is relatively small, as compared to hadronic decays. This BR value

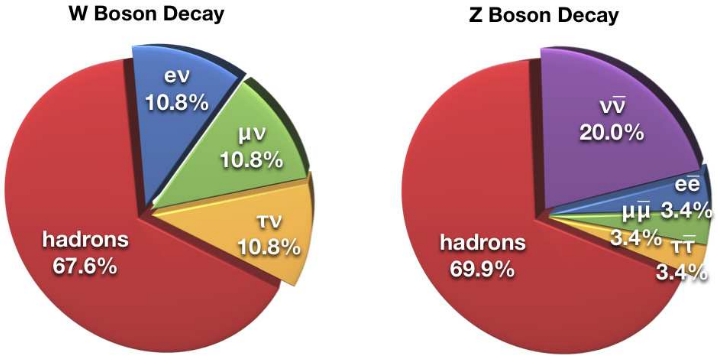

Figure 1-3: (a) W and (b) Z boson decay channels and their corresponding branching fractions in percentage.

becomes even smaller the more leptons that are included, for example $BR(W \rightarrow \ell\nu) \sim (3\times 10\%) \sim 30\%$, the factor of three comes from the three possible leptons being allowed, while $BR(WW \rightarrow \ell\nu\ell\nu) \sim (3 \times 10\%)^2 \sim 9\%$. This number becomes even smaller with the addition of a third lepton. Despite the low signal acceptance, multi-lepton signatures are incredibly clean with respect to the background contribution. The cross section for jet production is at least an order of magnitude greater than that for W and Z boson production. Even with the massive branching ratio for $WZ \rightarrow q\bar{q}q\bar{q}$ decays, where the quarks decay hadronically, an analysis would be dominated by multi-jet backgrounds and it would be very difficult to distinguish the signal from inelastic collisions and other jet background sources.

Feynman diagrams are a pictorial way to look at interactions. Time and space flow in given directions and one can visualize the initial state, the non-visible middle interaction, and then the final state particles that are produced. Figure 1-4 shows the three leading-order (LO) Feynman diagrams for WZ diboson production, where each intersection or vertex has an associated coupling parameter.

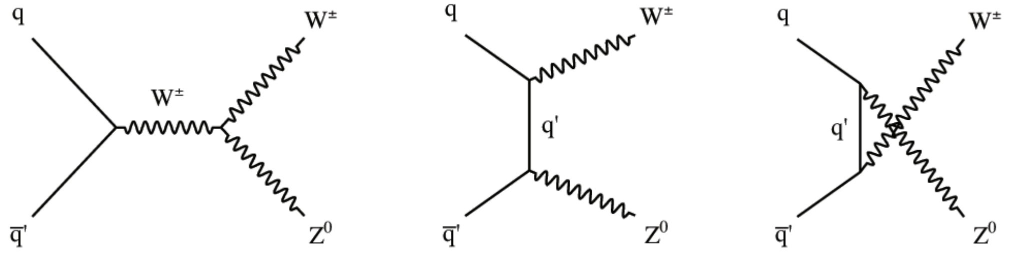

Figure 1-4: Leading-order Feynman diagrams for WZ diboson s-, t-, and u-channel production.

The diboson s-channel production diagrams are of particular interest due to the triple gauge-boson couplings (TGCs) [15, 16, 17] that occur between the $WW\gamma$ or WWZ vertices (depending on which diboson process is being studied). Deviations of these TGCs from their SM values would indicate new physics and could give some insight into the mechanism for the breaking of the $SU(2) \times U(1)$ electroweak gauge symmetry, discussed in Sec. 1.2.

SM diboson production is also a significant background to Higgs boson and BSM searches (such as SUSY models, flavor changing neutral currents, Z' searches, etc.) and therefore an important process to understand. Likewise, the associated production of the Higgs boson with the W boson leading to a tri-lepton signature, $WH \rightarrow WWW^{*}$ [a], where $W \rightarrow \ell\nu$, is important as it can shed light on the purely gauge coupling nature of the associated process and decay [18].

At the Tevatron, with a center–of–mass (cm) energy of $\sqrt{s} = 1.96$ TeV, the predominant SM neutral Higgs boson production comes from gluon fusion ($gg \rightarrow H$, shown in Fig. 1-5(a)), followed by vector boson fusion (VBF, $q\bar{q} \rightarrow q\bar{q}H$, Fig. 1-5(b)) and the associated production with a heavy boson ($q\bar{q} \rightarrow VH$, where $V = W$ or Z boson, Fig. 1-5(c)). The cross section, in femtobarn fb, as a function of the Higgs boson mass,

---

[a] The * indicates that one of the bosons could be a virtual particle, or not necessarily on-shell.

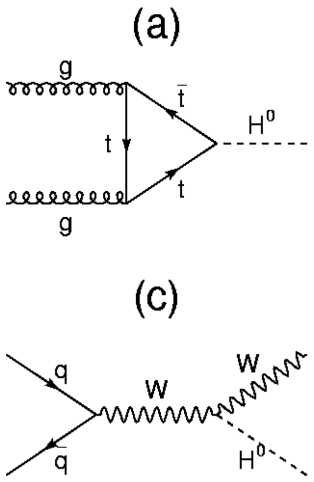

Figure 1-5: LO Feynman diagrams for Higgs boson production at hadron colliders; (a) gluon fusion, (b) vector boson fusion, and (c) associated production with a W boson (this type of diagram can also give ZH production by replacing the W boson with a Z boson) [19].

m_H, can be seen in Fig. 1-6(a) [20].

Similiarly at the Large Hadron Collider (LHC) at CERN (the European Organization for Nuclear Research), currently running at a cm energy of $\sqrt{s} = 7$ TeV, the same production processes are relevant but in a different ordering due to the lack of anti-quarks and with much higher cross section values. Here gluon fusion and VBF are predominant over associated production, as shown in Fig. 1-6(b).

Another important component of the Higgs boson search is the branching ratios of the final state channels, shown in Fig. 1-7 [21] as a function of the Higgs boson mass. For low Higgs boson masses, where $m_H < 135$ GeV/c^2 [b], the $H \to b\bar{b}$ decay branching ratio dominates. For masses greater than 135 GeV, the $b\bar{b}$ decay drops off steeply and the decay of $H \to WW^*$ takes over.

Since the Higgs boson couples strongly to the top quark and W boson masses, current electroweak precision measurements have indirectly constrained the SM Higgs boson mass to be $m_H < 161$ GeV [22]. The first direct limits set on the Higgs boson

---

[b] We use the standard convention of $c = \hbar = 1$. Unless otherwise stated, units of GeV are used for energy, momentum, and mass.

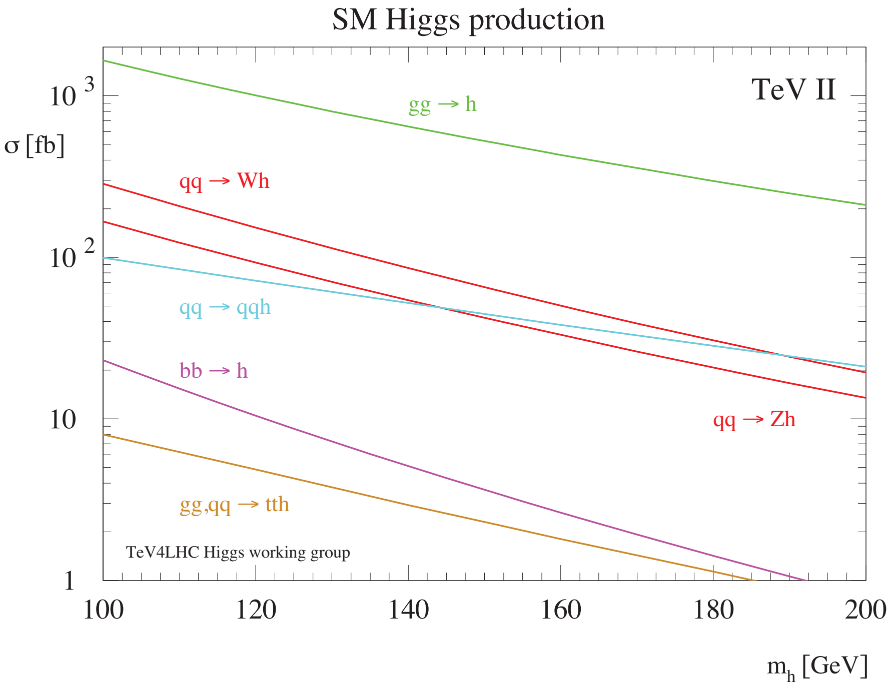

(a)

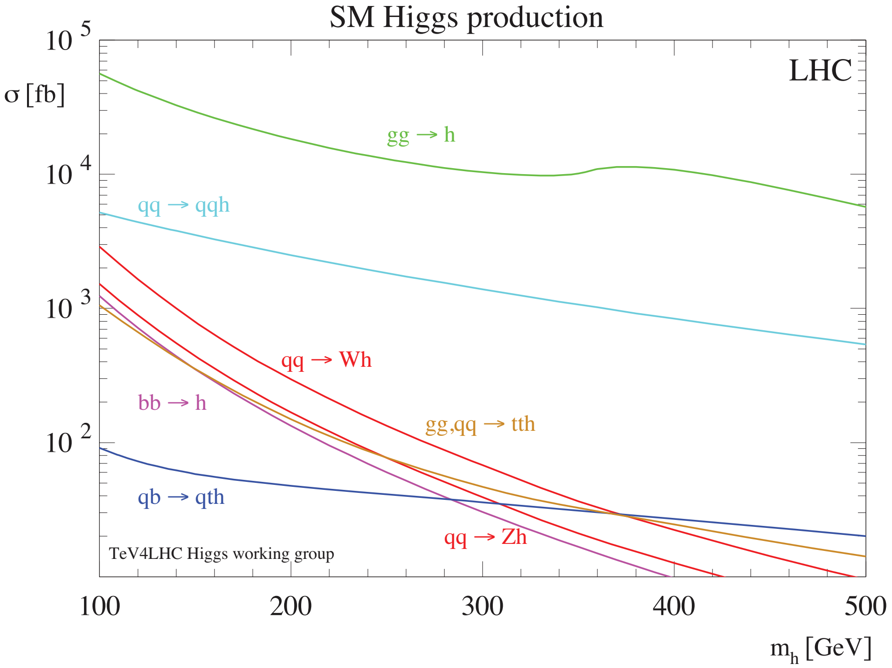

(b)

Figure 1-6: SM Higgs boson cross section versus mass for the (a) Tevatron RunII at a cm energy of $\sqrt{s} = 1.96$ TeV and (b) LHC at a cm energy of $\sqrt{s} = 14$ TeV [20].

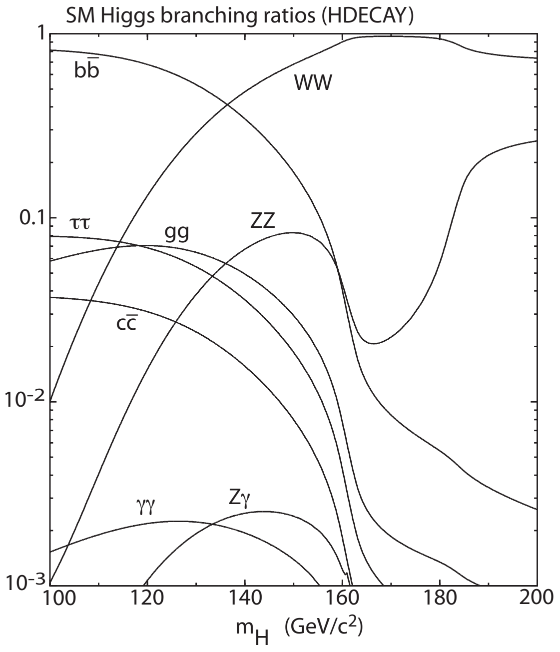

Figure 1-7: SM Higgs boson decay branching ratios versus mass [21].

mass range come from the Large Electron Positron (LEP) collider at CERN from data taken between 1981 – 2000. They were able to exclude a Higgs boson mass below 114.4 GeV at the 95% confidence level (C.L.) [23]. More recently, in 2011, the Tevatron further narrowed down this exclusion region by excluding masses in the range of 100 – 109 GeV and 156 – 177 GeV [24]. From there, the CERN experiments have significantly reduced the mass range in which the Higgs boson can be found. In early December 2011 both of the two main experiments at the LHC; A Toroidal LHC ApparatuS (ATLAS) and the Compact Muon Solenoid (CMS), announced their exciting results [25]. The ATLAS Collaboration was able to exclude the mass ranges 112.9 – 115.5 GeV, 131 – 238 GeV, and 251 – 466 GeV at the 95% C.L. [26]. They did observe an excess of events around $m_H \sim 126$ GeV with a local significance of 3.5 standard deviations (sigma), but more data is needed to declare a discovery. Likewise, the CMS Collaboration has excluded the mass range of 127 – 600 GeV at 95% C.L. and 128 – 525 GeV at 99% C.L. [27]. They also see an excess at $m_H \sim 125$ GeV. It is exciting that both collaborations see a slight excess, which may or may not be statistically significant, in the low mass region.

Figure 1-8 shows the most current observed and expected 95% C.L. upper limits as ratios of cross section to the SM cross section, as functions of the Higgs boson mass, in intervals of 5 GeV for the Tevatron combined result [28]. As more integrated luminosity is added and the individual analyses that go into the combination become more sensitive and efficient, the Tevatron combined limits are able to exclude a wider, higher mass region, now from 147 – 179 GeV. The exciting news is that the Tevatron also sees an excess at low Higgs boson mass of $\sim 2\sigma$, in the broad range of 115 – 135 GeV, in agreement with the LHC experiments. Chapter 6.3.4 describes how cross section limits are derived in more detail.

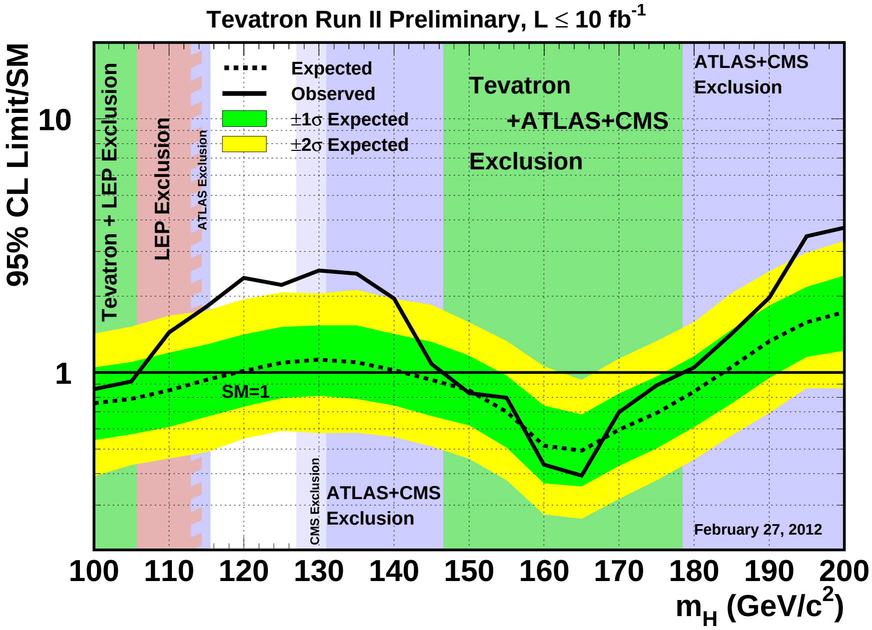

Figure 1-8: Shown are the most current observed and expected 95% C.L. upper limits on the ratios to the SM Higgs boson cross section, as functions of the mass, in intervals of 5 GeV for the Tevatron combined result [28]. The bands indicate the $\pm 1\sigma$ (68%) and $\pm 2\sigma$ (95%) probability regions where the limits can fluctuate, in the absence of signal. The Tevatron exclusion limits are shown in green, while the LEP (pink) and LHC's CMS and ATLAS (purple) exclusion regions are also visible.

A more extensive, but slightly out of date, history of the Higgs boson searches can be found in the Particle Data Group (PDG) article 'Higgs Bosons: Theory and Searches (2010)' [29].

1.2 Standard Model Formalism

Electroweak diboson production is mediated by the non-Abelian $SU(2)_L \times U(1)_Y$ gauge invariant Lagrangian, $\mathcal{L}_{EW}$. It includes the sum of four terms (defined explicitly in Eq. 1-3); $\mathcal{L}_{gauge}$ describes the gauge boson field's ($W^{\pm}$, Z^0, γ) kinetic energies and self-interactions, $\mathcal{L}_{fermion}$ describes the fermion's kinetic energies and interactions with the gauge bosons, $\mathcal{L}_{\phi}$ is the Higgs scalar (ϕ) term describing the gauge boson masses and couplings, and finally $\mathcal{L}_{Yukawa}$ describes the fermion's mass and couplings to this Higgs scalar field [30]. Putting it all together, the electroweak standard model is described by [30]

$$\begin{aligned} \mathcal{L}_{EW} &= \mathcal{L}_{gauge} + \mathcal{L}_{fermion} + \mathcal{L}_{\phi} + \mathcal{L}_{Yukawa}, \\ \mathcal{L}_{EW} &= \left[-\frac{1}{4}\overrightarrow{W}_{\mu\nu} \cdot \overrightarrow{W}^{\mu\nu} - \frac{1}{4} B_{\mu\nu} B^{\mu\nu} \right] + \left[\bar{L}\gamma^{\mu} D_{\mu} L + \bar{R}\gamma^{\mu} D'_{\mu} R \right] \\ &+ \left[(D_{\mu}\phi)^{\dagger}(D^{\mu}\phi) - V(\phi^{\dagger}\phi) \right] + \left[- \left(G_1 \bar{L}\phi R + G_2 \bar{L}\phi_c R + h.c. \right) \right], \end{aligned} \tag{1-3}$$

where the following are defined as:

$$\overrightarrow{W}_{\mu\nu} = \partial_{\mu}\overrightarrow{W}_{\nu} - \partial_{\nu}\overrightarrow{W}_{\mu} - g\overrightarrow{W}_{\mu} \times \overrightarrow{W}_{\nu}, \tag{1-4}$$

$$B_{\mu\nu} = \partial_{\mu}B_{\nu} - \partial_{\nu}B_{\mu}, \tag{1-5}$$

$$D_{\mu} = i\partial_{\mu} - g\frac{\overrightarrow{\tau}}{2} \cdot \overrightarrow{W}_{\mu} - g'\frac{Y}{2}B_{\mu}, \tag{1-6}$$

$$D'_{\mu} = i\partial_{\mu} - g'\frac{Y}{2}B_{\mu}, \tag{1-7}$$

$$\phi = \frac{1}{\sqrt{2}} \begin{bmatrix} \phi_1 + i\phi_2 \\ \phi_3 + i\phi_4 \end{bmatrix} = \begin{bmatrix} \phi^{+} \\ \phi^{0} \end{bmatrix}, \tag{1-8}$$

$$\phi_c = i\tau_2\phi^{\dagger}, \tag{1-9}$$

$$L = \begin{bmatrix} \nu_f \\ f \end{bmatrix}_L \text{(fermions) and } L_j = \begin{bmatrix} u_j \\ d_j \end{bmatrix}_L \text{(quark family j)}, \tag{1-10}$$

$$R = f_R \text{ (fermions) and } R_u = u_{jR}, R_d = d_{jR} \text{ (quark family j)}. \tag{1-11}$$

Y is the weak hypercharge charge, $\frac{\vec{\tau}}{2}$ are the 2×2 Pauli matrices, g and g' are the gauge couplings to the $\mathrm{SU}(2)_L$ and $\mathrm{U}(1)_Y$ fields, respectively, defined by $e = g\sin\theta_W = g'\cos\theta_W$, and ϕ is the complex Higgs scalar doublet, with ϕ_c the complex conjugate doublet. The L represents a left-handed fermion doublet field, while R is the right-handed singlet field, and G_i are the corresponding Yukawa coupling parameters.

In order to give the gauge bosons mass (and likewise the fermions), the gauge invariance of the $\mathrm{SU}(2)_L \times \mathrm{U}(1)_Y$ symmetry must be spontaneously broken. To this end, we start with the Higgs potential $\mathrm{V}(\phi^\dagger\phi)$ and, due to $\mathrm{SU}(2)_L \times \mathrm{U}(1)_Y$ invariance and renormalizability, assume it has the form

$$V(\phi^\dagger\phi) = \mu^2\phi^\dagger\phi + \lambda(\phi^\dagger\phi)^2, \tag{1-12}$$

where μ^2 has to be less than zero for spontaneous symmetry breaking to occur and vacuum stability requires that λ be greater than zero. Figure 1-9 shows an illustration of the resulting Higgs potential. An interesting feature is that the true minimum energy of the field is not at $z = 0$ but at points along a circle where $|z| = \phi$.

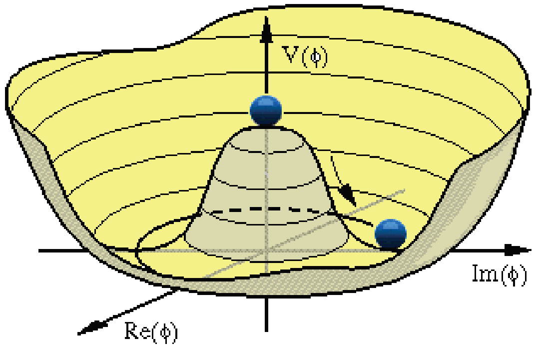

Figure 1-9: Diagram of the Higgs “sombrero hat” potential.

Starting with Eq. 1-12, we calculate the ground state or vacuum expectation value (vev or v), which represents the configuration of the field at minimum energy, by finding the minimum of V($\phi^\dagger\phi$) with respect to $\phi^\dagger\phi$. In doing so, we find

$$\left\langle \phi^\dagger \phi \right\rangle = -\frac{\mu^2}{2\lambda} = v^2. \tag{1-13}$$

We arbitrarily set ϕ_3 in Eq. 1-8 equal to $\pm v$, since ϕ_3 is uncharged and real, and set the rest of the components in ϕ to zero. By choosing $+v$ the symmetry is now broken because the ground state does not have the same symmetry properties any more which are present for the Higgs potential, we can write the vacuum expectation value as

$$\langle \phi \rangle = \frac{1}{\sqrt{2}} \begin{bmatrix} 0 \\ v \end{bmatrix}. \tag{1-14}$$

We plug $\langle\phi\rangle$ into $\mathcal{L}_\phi$, expand the matrices, square with the complex conjugate, and then look for second-order terms in v, which will correspond to the mass terms. We can read off the charged W boson's mass immediately. To calculate the neutral Z and photon boson masses, we introduce the neutral gauge bosons as

$$Z_\mu = \frac{gW_\mu^3 - g'B_\mu}{\sqrt{g^2 + g'^2}} \qquad A_\mu = \frac{g'W_\mu^3 + gB_\mu}{\sqrt{g^2 + g'^2}} \tag{1-15}$$

and rewrite B$_\mu$ and W$_\mu^3$ in terms of Z_μ and A_μ and again pick off the v^2 terms. The SM gauge boson mass functions are calculated to be (including their experimental values [29]);

$$\begin{aligned} M_W &= \frac{vg}{2} = \frac{v\sin\theta_W}{2e} = 80.398 \pm 0.025 \text{ GeV}, \\ M_Z &= \frac{v}{2}\sqrt{g^2 + g'^2} = \frac{v}{2e} = 91.188 \pm 0.002 \text{ GeV}, \\ M_A &= 0 \text{ GeV}, \\ m_H &= \sqrt{2\lambda}v = \ ? \text{ GeV}. \end{aligned} \tag{1-16}$$

The gauge bosons self-interactions are calculated from the $\overrightarrow{W}_{\mu\nu} \cdot \overrightarrow{W}^{\mu\nu}$ term in $\mathcal{L}_{gauge}$

after spontaneous symmetry breaking has occurred and describes the three- and four-point couplings between the W, Z, and photon bosons. This term also includes the Higgs boson three- and four-point self-interaction terms, describing how the Higgs boson can couple to itself. The boson to fermion couplings are determined from $\mathcal{L}_{fermions}$ and the covariant derivative D_μ (Eq. 1-6). After multiplying $\overrightarrow{\tau} \cdot \overrightarrow{W}_\mu$ out, writing B_μ and W^3_μ in terms of the two neutral fields A_μ and Z_μ derived using Eqs. 1-15 and 1-16, and collecting like terms, the covariant derivative D_μ can be written in terms of the gauge boson fields as

$$D_\mu = \partial_\mu + ig\frac{1}{\sqrt{2}}(\tau^+ W^+_\mu + \tau^- W^-_\mu) + ieQA_\mu + \frac{ig'}{\cos\theta_W}\left(\frac{\tau^3}{2} - Q\sin^2\theta_W\right)Z_\mu. \quad (1\text{-}17)$$

After plugging Eq. 1-17 into $\mathcal{L}_{fermions}$ and expanding the fermion doublet and singlet fields, the coupling terms can be read off and the vertex factors, used in Feynman calculus to calculate a process's amplitude, determined.

1.3 Flavor Changing Neutral Current Production in Top Quark Decays

Flavor changing neutral currents (FCNC) allow for the transitions between quarks of different flavor ("flavor changing") but same electric charge ("neutral current"), such as $b \to s$ or $t \to u$. FCNC decays are important as sensitive indicators of BSM physics, as they are highly suppressed in the SM. Since the top quark is extremely massive, it decays rapidly via $t \to Wb$ with an almost 100% probability. Therefore, the top quark does not have time for hadron formation and hence can not form top-flavored meson states [31].

For the FCNC $t \to Vq$ decay, where $V = \gamma$ or Z boson, an additional term is added to the SM Lagrangian stated in Eq. 1-3;

$$\mathcal{L}_{\text{FCNC}} = e\frac{i\sigma_{\mu\nu}q^{\nu}}{m_t + m_q}\bar{t}(\kappa_{\gamma} - i\tilde{\kappa}_{\gamma}\gamma_5)qA^{\mu} \\ +\tfrac{g}{2\cos\theta_W}\bar{t}\left[\gamma_{\mu}(v_Z - a_Z\gamma_5) + \tfrac{i\sigma_{\mu\nu}q^{\nu}}{m_t+m_q}(\kappa_Z - i\tilde{\kappa}_Z\gamma_5)\right]qZ^{\mu} + h.c., \tag{1-18}$$

where t, q, A^{μ}, and Z^{μ} are the quantum fields for the top quark, up/charm quark, photon, and Z boson, respectively, q^{ν} is the momentum of the boson, m_t (m_q) is the top (up/charm) quark mass, and κ_{γ}, $\tilde{\kappa}_{\gamma}$, κ_Z, $\tilde{\kappa}_Z$, v_Z, and a_Z are the gauge boson coupling parameters [31].

We focus on the decay of a top quark into a Z boson and either a u or c quark, $t \rightarrow Zq$. Figure 1-10(a) shows the SM-violating LO Feynman diagram we are searching for, while Fig. 1-10(b) shows an example of a higher-order diagram where a radiative loop makes the decay more likely, also known as the more famous “penguin” diagram.

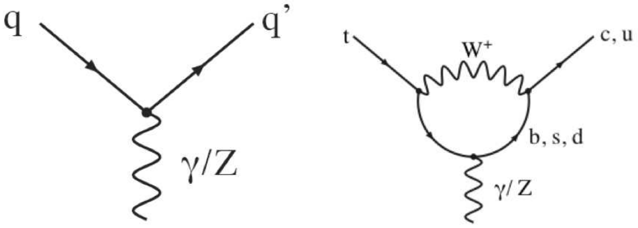

Figure 1-10: Feynman diagrams for FCNC $t \rightarrow Zq$ decay. (a) The SM-violating LO diagram and (b) an example of a possible higher-order radiative correction loop diagram [32].

2 The Tevatron and DØ Detector

2.1 The Tevatron

The Tevatron was commissioned in October of 1985, taking the laboratory from a fixed target accelerator to a colliding one. It was the highest energy operating proton-anti-proton ($p\bar{p}$) collider in the world and up until recently the highest energy accelerator in the world. With a diameter of roughly two kilometers, the Tevatron complex is located in Batavia, IL and had two experimental large-scale detectors, Collider Detector at Fermilab (CDF) and DØ.

The Tevatron systems that create the proton/anti-proton beams necessary for collisions consist of many parts, shown in Fig. 2-1 [33]; the Proton Source (made up of the Pre-accelerator, Linac, and Booster systems), Main Injector, the Anti-Proton Source (Target, Debuncher, and Accumulator), Recycler, and finally the Tevatron [34].

The Pre-accelerator, or "Preacc", begins the journey. Neutral hydrogen atoms are converted into negatively charged ions by adding an electron to the atom. The H^- ions are then injected into a Cockcroft-Walton generator, which is an electrically charged

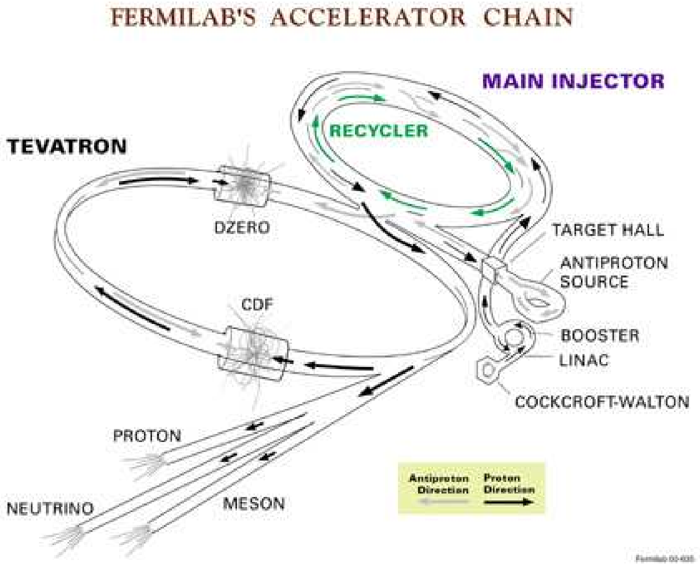

Figure 2-1: Tevatron accelerator components [33].

dome set to have a potential difference of -750 kV, causing the ions to accelerate up to an energy of 750 keV. An electron volt, eV, is a unit of energy and is the amount of energy gained by an electron accelerated across a one Volt potential, with 1 eV = 1.602×10^{-19} J. From the Preacc, the negatively charged hydrogen ions are transported to the Linear Accelerator ("Linac") via a transfer line called the 750 keV line. Here the ions are accelerated further to an energy of 400 MeV using low-energy drift tubes and high-energy side-coupled cavities. The Booster synchrotron accelerator then strips the negatively charged ions of their electrons, producing the proton beam and accelerates the protons to 8 GeV.

Once the proton beam has been established, it is transferred to the Main Injector (MI), a synchrotron accelerator a little over two miles in diameter. From here, the beam can either be accelerated up to an energy of 150 GeV if it is bound for the Tevatron, or if it will be used for anti-proton production, up to an energy of 120 GeV.

The anti-proton beam is created when the 120 GeV protons from the MI strike a nickel alloy target, producing a spray of secondary particles. Magnets, defining specific charge and momentum, are used to collect the generated 8 GeV anti-protons and send them to the Debuncher. The Debuncher, the first of two synchrotrons that make up the Anti-Proton Source ("Pbar Source"), is then used to collect the high-momentum spread anti-protons and keep them at a constant energy of 8 GeV. From here the anti-protons move to the Accumulator, a storage ring which keeps the beam cool and stable.

The Recycler is located along the MI tunnel ceiling and is used as an anti-proton storage ring. It is mainly used to further store the anti-proton beam and cool it to a constant kinetic energy and transverse energy of 8 GeV, once it leaves the Pbar Accumulator.

The Tevatron accepts protons and anti-protons from the MI, accelerating them from $\sim$150 GeV to their final energy of 980 GeV each. Superconducting magnets are used to control and focus the beams, allowing for collisions at two points along the ring; the CDF and DØ collision points. Protons are circulated clockwise, while anti-protons

Table 2-1: RunI and RunII beam statistics.

Periods	Years	$\sqrt{s}$ (TeV)	Bunches	Freq. of Crossings (ns)	Peak Luminosity ($\mathrm{cm}^{-2}\ \mathrm{s}^{-1}$)
RunI	1992 – 1996	1.8	6	3500	$1 - 2\times10^{31}$
RunII	2001 – 2011	1.96	36	396	$3 - 4\times10^{32}$

counter-clockwise.

Table 2-1 summarizes the Tevatron's beam statistics which govern the proton and anti-proton beams that collide at DØ [35].

On a historical note, the Tevatron ended operations on September 30, 2011 after 28 years of successful running. It delivered (recorded) a total integrated luminosity of 11.9 (10.7) fb^{-1} to DØ during Run II. After the standard DØ data quality [36] criteria are applied, the final dataset size available is 9.7 fb^{-1}. Table 2-2 summarizes the total integrated luminosity collected in each of the RunII data epochs, along with the length of time it took to record each dataset. Data was recorded during the first year of RunII collisions from March 2001 to April 2002, but due to ongoing calibrations and its small integrated luminosity size, it is not commonly used (likewise with RunI data).

Table 2-2: Total integrated luminosity and time period (starting in 2002) for the DØ RunII epochs. The data epochs are defined by major Tevatron shutdowns and upgrades to the detector components.

Data Epochs	RunIIa	RunIIb1	RunIIb2	RunIIb3	RunIIb4
Luminosity (fb^{-1})	1078	1222	3056	1942	2438
Time Period	4/02 – 2/06	6/06 – 8/07	10/07 – 6/09	9/09 – 7/10	9/10 – 9/11

2.2 The DØ RunII Detector

In March of 2001 the Tevatron started the RunII phase of beam collisions, after successfully completing RunI from 1992 to 1996. During the extended shutdown from 1996 to 2001, the DØ detector itself acquired additional upgrades which, among many, consisted of brand new silicon microstrip and central fiber trackers, the addition of a solenoid magnet between the central fiber tracker and the calorimeters, preshower detectors between the solenoid magnet and calorimeters, and an almost complete overhaul of the muon system. All these changes, along with detector trigger upgrades, prepared the DØ detector for instantaneous luminosities beyond the goal of $\mathcal{L} = 10^{32}$ cm^{-2} s^{-1}.

There are three main parts to the DØ detector, shown in Fig. 2-2; the central tracking detectors, the sampling uranium/liquid-argon calorimeter, and the muon system [35].

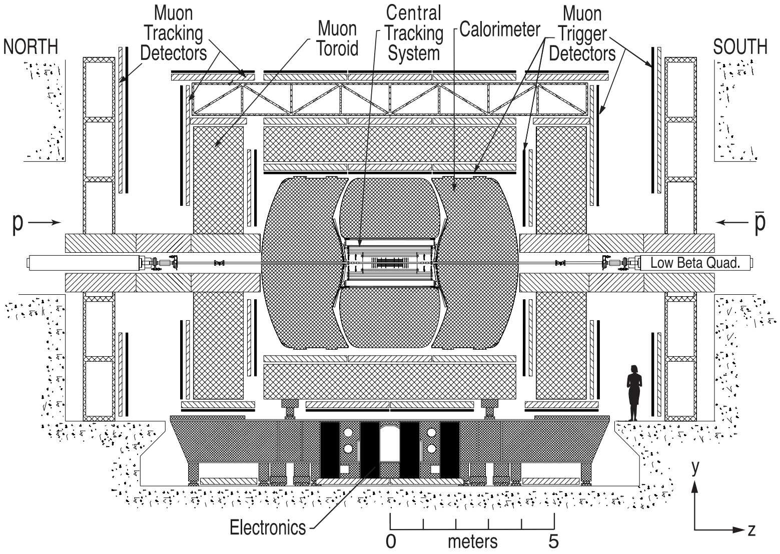

Figure 2-2: DØ detector schematic, excluding the forward proton detector.

Figure 2-3 shows which particles are expected in which subdetector. Charged particles will be seen in the tracking detectors, while further upstream photons and electrons will deposit their energy into the electromagnetic calorimeter. Neutrons, protons, pions, and kaons will shower later and deposit their energy into the hadronic calorimeters. Muons will leave minimal energy in the calorimeter but be reconstucted in the muon system.

In the DØ reference frame, we define the center of the detector as the origin, with the $+z$-axis pointing in the direction of the proton beam (as shown in the corner of Fig. 2-2), the $+x$-axis points out from the center of the Tevatron ring, and the $+y$-axis points up. We take advantage of the detector's cylinderical symmetry and define a radial transverse distance as $r = \sqrt{x^2 + y^2}$, a polar angle θ with respect to the beampipe, and an azimuthal angle ϕ with respect to the x-axis. A useful quantity to determine the

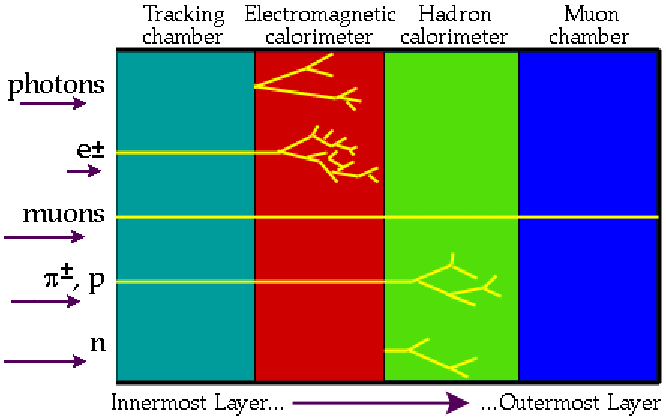

Figure 2-3: Diagram of particle interactions in specific parts of the detector.

location of a particle is the pseudorapidity

$$\eta = -\ln\left(\tan\frac{\theta}{2}\right), \tag{2-1}$$

where $\eta = 0$ when perpendicular to the z-axis. In the relativistic limit where $E >> m$, η is a good approximation for the rapidity of the particle

$$y = \frac{1}{2}\ln\left(\frac{E+p_z}{E-p_z}\right). \tag{2-2}$$

We use the term "detector η" (η_{det}) when measuring with respect to the detector's origin or "physics η" (η) when with respect to an event's primary interaction vertex location, which may not be located at the origin. We define a $\Delta\mathcal{R}$ as the opening angle in η and ϕ such that $\Delta\mathcal{R}=\sqrt{(\Delta\eta)^2+(\Delta\phi)^2}$. Since we can not accurately measure the momentum of a particle in the z-direction for all events, we define a transverse momentum such that $p_T = \sqrt{p_x^2+p_y^2}$, and similarily with the transverse energy of a particle, $E_T = \sqrt{E_x^2+E_y^2}$.

2.2.1 Central Tracking Detectors

The silicon microstrip tracker (SMT), the central fiber tracker (CFT), and the central/forward preshower detectors (CPS and FPS, respectively) comprise the central

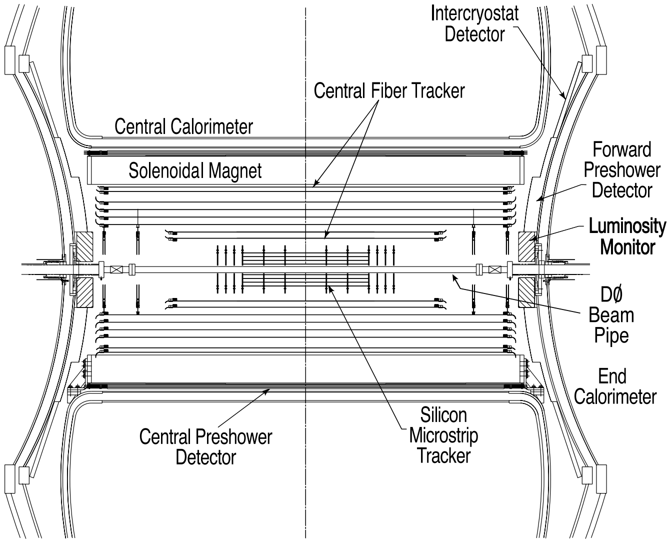

Figure 2-4: The new RunII central tracking system.

tracking system, shown in more detail in Fig. 2-4.

At the heart of the tracking system is the SMT, Fig. 2-5. It consists of six silicon barrel sections, twelve F-Disks, and four far-forward H-Disks, providing roughly a total of 793k read-out channels. The barrels are used to track particles primarily in $r - \phi$, while the disks look both in the $r - z$ and $r - \phi$ directions. Between RunIIa and RunIIb, in 2006, an inner barrel called Layer 0 was installed just outside of the radius of the beampipe to improve the tracking resolution, resulting in the removal of two H-Disks. The SMT is used to measure a charged particle's momentum and vertex location, and provides coverage in detector pseudorapidity up to $|\eta_{det}| < 3$, which almost completely covers both the calorimeter and muon detector ranges.

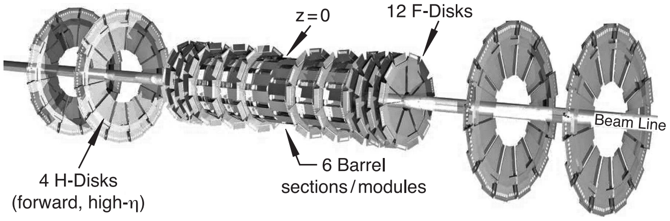

Figure 2-5: Silicon microstrip tracker.

Outside the SMT is the CFT. It consists of eight concentric cylinders with scintillating fibers in axial doublet layers (parallel with the beampipe) and alternating stereo doublet layers (the layers alternate between ±3° in ϕ with respect to the axial layers). The axial layers are used in the fast Level 1 triggering (and in conjunction with the axial layers of the SMT at Level 2), while the stereo layers add z information for three-dimensional track reconstruction. The roughly 77k fibers are coupled to visible light photon counters (VLPC) via clear fiber waveguides. The VLPCs digitize the track information for both on- and off-line analysis. The CFT covers $|\eta_{det}| < 1.6$.

Enclosing the SMT and CFT is a 2 Telsa superconducting solenoidal magnet. This was installed during the RunII upgrades to improve tracking and momentum resolution.

The CPS is located just beyond the solenoid magnet in front of the central calorimeter and covers $|\eta_{det}| < 1.2$, while the FPS sits in front of the end cap calorimeters and covers $1.4 < |\eta_{det}| < 2.5$, both shown in Fig. 2-4. The preshower detectors are used to measure the energy losses in the upstream material due to the mass of the solenoid magnet and to aid in electron and photon identification and triggering.

2.2.2 Electromagnetic and Hadronic Calorimeters

The primarily sampling uranium/liquid-argon calorimeter detectors, shown in Fig. 2-6(a), consist of an inner electromagnetic (EM) calorimeter closest to the beampipe which measures particle energies resulting from electromagnetic interactions (i.e. electrons and photons), followed by the fine and coarse hadronic calorimeters (FH and CH, respectively) that measure the energy deposited by showering hadrons (such as pions, kaons, and neutrons).

The central calorimeter (CC) covers a pseudorapidity range of $|\eta_{det}| < 1.1$, while the North and South end cap calorimeters (EC) extend the coverage to $|\eta_{det}| \approx 4$. The calorimeter is divided up into "cells", or basic units of energy measurement, shown in Fig. 2-6(b). The position of each cell is given by its center location, $\eta \times \phi$ in the CC and $\theta \times \phi$ in the EC, with respect to the detector's origin. A tower is a group of cells and

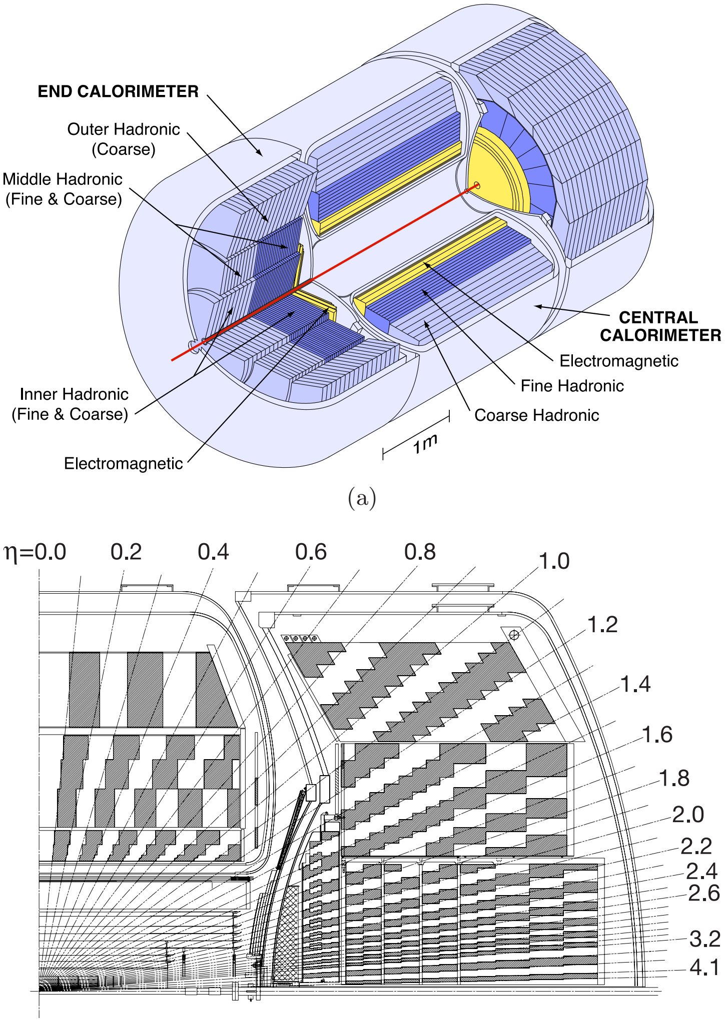

(a)

(b)

Figure 2-6: (a) The uranium/liquid-argon electromagnetic, fine hadronic, and coarse hadronic calorimeter detectors. (b) Schematic view showing the transverse and longitudinal cell segmentation pattern. The dark blocks indicate groups of cells clumped together for signal readout. Pseudorapidity intervals are also shown.

is typically $\eta \times \phi = 0.1 \times 0.1$ in size. The calorimeters measure the energy deposited during an event and are used to help calculate the event's imbalance of transverse energy ($\not\!\!E_T$ or MET). Depending on the type of particle, as it traverses the electromagnetic, fine hadronic, and coarse hadronic sections of the detector it will interact with absorber plates and create a shower of secondary particles. The EM sections use thin, nearly pure, depleted uranium plates. The fine hadronic sections use an uranium-niobium (2%) alloy and the coarse hadronic modules contain thick plates of copper (in the CC) or stainless steel (in the EC). The resulting shower then ionizes the liquid-argon atoms and creates a current in the gas, which is due to the potential difference applied between the plates. The hardware configuration is shown in Fig. 2-7.

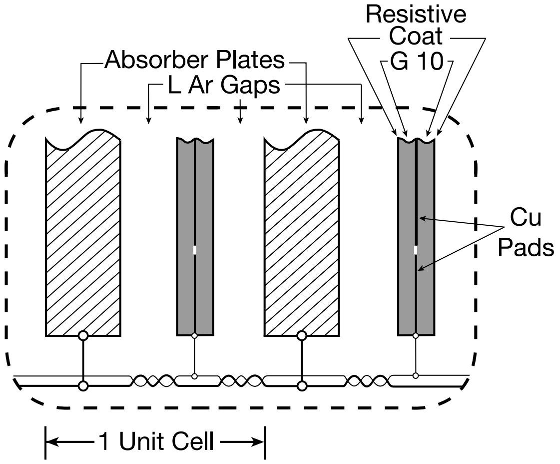

Figure 2-7: Uranium/liquid-argon plates configuration.

Electronic amplifiers are used to measure the resulting current signal and calculate the energy deposited. When a particle showers, the depth that the shower traverses the calorimeter depends on the nature of how that particle interacts with the calorimeter's material. This information is used to differentiate various particles and measure their transverse energies. For example, electrons produce showers earlier in the detector compared to other particles such as pions and kaons. An electron traveling through the EM calorimeter will lose energy through bremsstrahlung and/or $e\bar{e}$ pair production. The depth of the electron shower in a particular material is characterized by the radiation length, X_0, which is the mean distance an electron will travel before losing $1 - e^{-1}$ (or 63%) of its energy to bremsstrahlung [29]. The EM layers have a total thickness of approximately $20.5X_0$ near $\eta_{det} = 0$, so that most of the electron's energy will be deposited before reaching the hadronic layers. Similarly, the depth of hadronic showers is determined by the nuclear interaction length, λ_I. For a given material λ_I is usually much longer than X_0, such that the total thickness of the EM layers at DØ is only $0.76\lambda_I$ in the central calorimeter and $0.97\lambda_I$ in the end cap calorimeters [37].

The intercryostat detector (ICD), shown in Fig. 2-4, provides coverage in the range of $1.1 < |\eta_{det}| < 1.4$, where there is incomplete coverage due to the calorimeter cryostats.

2.2.3 Muon Detectors

The muon system is comprised of the central and forward muon detectors. The central muon detector uses proportional wire drift tubes (PDTs) covering a pseudorapidity range of $|\eta_{det}| < 1.0$ to detect and measure the muons produced in the interaction region. The forward muon system, installed between RunI and RunII, use mini-wire drift tubes (MDTs) and covers $1 < |\eta_{det}| < 2$. Both central and forward regions have scintillation detectors.

There are three wire drift chamber layers, shown in Fig. 2-8(a); the inner-most A-layer and the outer B- and C-layers, which lie beyond a 1.8 Tesla toroidal magnetic field. The polarity of the solenoidal and toroidal magnets can be reversed to study particle charge asymmetries and help cancel out detector systematics. The wire drift chambers are used for triggering and precise coordinate measurements. The trigger scintillation counters, Fig. 2-8(b), also used in muon triggering, provide a fast timing signal that allows a muon detected in a PDT ("local" muon) to be matched to the appropriate bunch crossing. The cosmic cap and cosmic bottom scintillator counters, also shown in Fig. 2-8(b), are used to reduce the cosmic ray background.

2.2.4 Data Aquisition

At the end of operational running, the DØ Experiment had recorded ~ 11 fb^{-1} of integrated luminosity to tape. To accomplish this, the data acquisition system (DAQ) relies on three levels of triggering. Level 1 triggering consists of fast hardware triggers that reduce the incoming 1.7 MHz of data to < 1.8 kHz at peak rate. The next level searches for more specific particle signatures in the detector subsystems using both

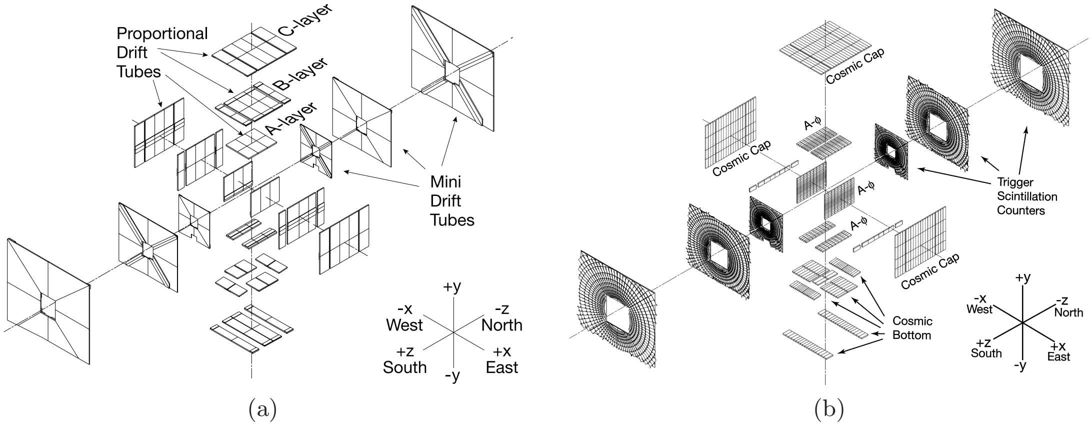

(a) (b)

Figure 2-8: Expanded view of (a) the muon wire drift chambers and (b) the muon scintillation detectors.

hardware and programmable firmware. This Level 2 trigger then further reduces the rate to $<$ 900 Hz at peak. The final trigger level (Level 3) uses more complex software algorithms to reconstruct a particle's trajectory and momentum and makes more sophisticated cuts based on that information, reducing the rate to $<$ 200 Hz at peak rate. When an event passes all three levels, it is then written to tape for analysis, typically with a raw data event size of $\sim$ 250 kB. Trigger suites are created to maximize the physics events collected, while rejecting as many of the less interesting underlying events as possible [38]. They include triggers at all three DAQ levels to allow specific objects to be reconstructed. There are trigger suites to trigger on electrons, di-electrons, muons, di-muons, taus, multi-jets, and B-physics events. At the highest luminosities, only the most interesting events are passed and most likely heavily prescaled, to save on the available bandwidth. As the luminosity decreases over the course of collisions, the prescales are relaxed and more triggers are used to collect events.

Each subdetector is responsible for keeping track of their detector's performance. If there is any downtime which could effect the quality of the data collected, those runs are marked as bad by the Data Quality group [36]. These bad runs are then removed from the dataset available to the physics analyzers but are still available to experts to diagnose problems.

2.2.5 Luminosity System

Luminosity monitors (LM), shown in Fig. 2-4 and in more detail in Fig. 2-9, are positioned in the far-forward regions, or at high pseudorapidities, on the end cap calorimeters to measure the Tevatron's instantaneous luminosity and the beam halo rates. The detector consists of two arrays of 24 plastic scintillation counters with photomultiplier tube (PMT) readouts positioned at $z = \pm 140$ cm. The LM covers a pseudorapidity range of $2.7 < |\eta_{det}| < 4.4$.

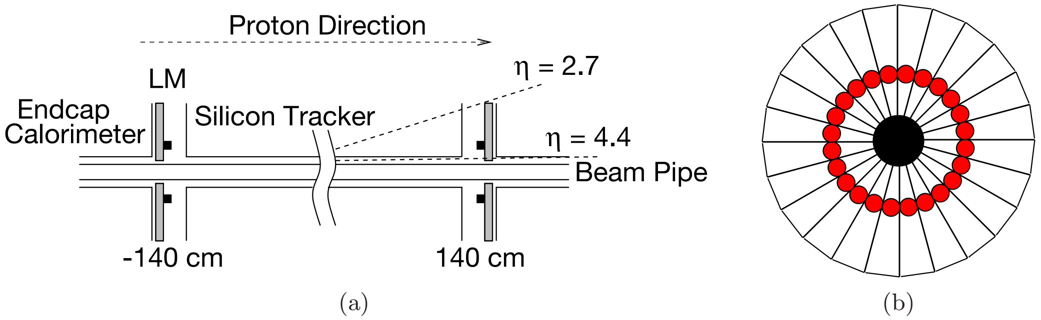

Figure 2-9: Location of the luminosity monitors, (a) $r-z$ view and (b) $r-\phi$ view, where the solid dots represent the location of the photomultiplier tubes.

The instantaneous luminosity is determined by measuring the rate of empty bunch crossings, since the LMs can at most determine only if one interaction has occurred. Poisson statistics give the relation between the number of empty event crossings and the luminosity. Coincidences in both North and South sides are used to reduce the noise and uncertainty in the measurement. Given the probability of an empty crossing, $P(0)$, the luminosity can be determined for each bunch individually using

$$P(0) = e^{-\sigma_{eff}\mathcal{L}/\nu} \times \left[2e^{(-\sigma_{SS}/2\nu)\mathcal{L}} - e^{-\sigma_{SS}\mathcal{L}/\nu}\right], \tag{2-3}$$

where σ_{eff}, known as the luminosity constant, is the effective inelastic cross section seen by the LMs, σ_{SS} is the single-sided (SS) cross section, or the cross section for only one LM side to fire, and ν is the bunch crossing frequency, ~ 47 kHz [39]. The expression in brackets represents the correction factor for two SS events faking a doublesided coincidence. Both CDF and DØ use an inelastic cross section of $\sigma_{in} = 60.7 \pm 2.4$ mb [40]. The luminosity constant is taken to be $48.3 \pm 1.9 \pm 0.6$ mb, while σ_{SS} is measured to be 10.8 mb with backgrounds, for RunIIb [39].

Since it takes time to replenish the intensity of the anti-proton beam, the beams only collide for $\sim 12 - 15$ hours at a time, called "stores", until the luminosity is too low for interactions containing interesting physics to occur. At DØ, stores are split into "runs" which depend on the instantaneous luminosity. A typical run is two hours long. Figure 2-10 shows the instantaneous luminosity profile of a typical store recorded by DØ, along with the total trigger rates of each Level as a function of time. As it can be observed, as time goes on, the instantaneous luminosity decreases since protons and anti-protons are lost as the beams circulate and collide/interact. The run is changed so that new prescales are used, increasing the DAQ rates as the luminosity drops. The average instantaneous luminosity is stored in one minute blocks called LBNs. If there are issues with any part of the detector, these blocks can be marked as bad and not used in physics analyses. A common systematic uncertainty used in all analyses is the luminosity uncertainty and is taken to be 6.1% [41].

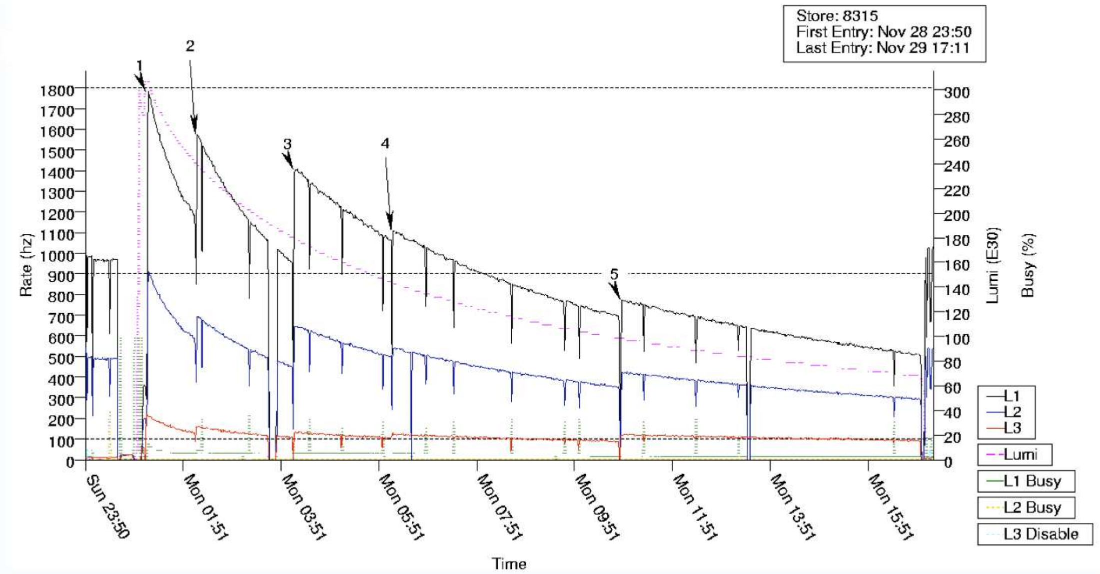

Figure 2-10: Typical instantaneous luminosity profile of a store, along with the total trigger rates as a function of time.

2.3 Level 1 Central Track Trigger

The Level 1 central track trigger (L1CTT or CTT) receives discriminator hits from the CFT and CPS. The axial layers, sketched in Fig. 2-11, consist of eight doublet layers (A – H) or sixteen singlet layers. Figure 2-12 shows the singlet numbering for both the CFT scintillating fibers and the CPS axial strips for a 4.5° sector slice. The different colors represent the three low-voltage differential signaling (LVDS) links that supply the data for one sector.

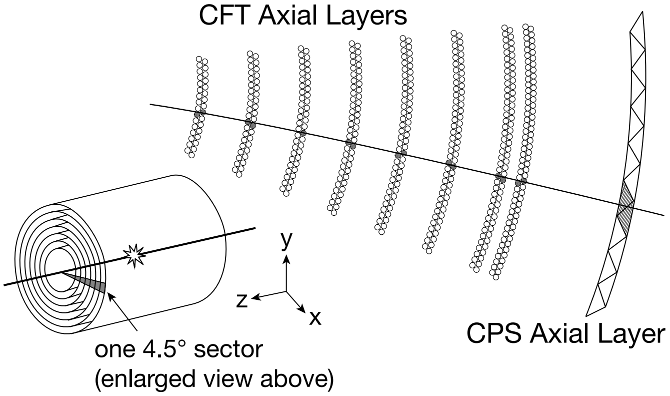

Figure 2-11: Sketch of the CFT and CPS axial layers. A hypothetical track is shown traveling through both trackers, striking either one or both singlet layers in each doublet layer. (Note: the separation of the CFT and CPS is not to scale).

Every 45° increment in azimuth defines an octant, with octant 0 starting at $\phi = 0°$. Each octant is then split into ten 4.5° sectors, which are further divided into four azimuthal divisions, for a total of eight octants, 80 sectors, and 320 azimuthal divisions. For each event the number of fibers, or singlets, hit – those that caused the CFT discriminator to fire – in each division are recorded in the raw data, which is accessible both on- and off-line.

Object tracks are reconstructed from fiber hits when a pre-defined set of track equations have been satisfied [42]. The track equations are grouped into four track p_T bins; "LOW" with 1.5 GeV $< p_T <$ 3 GeV, "MEDIUM" with 3 GeV $< p_T <$ 5 GeV, "HIGH" with 5 GeV $< p_T <$ 10 GeV, and "MAX" with $p_T >$ 10 GeV. Once reconstructed, a

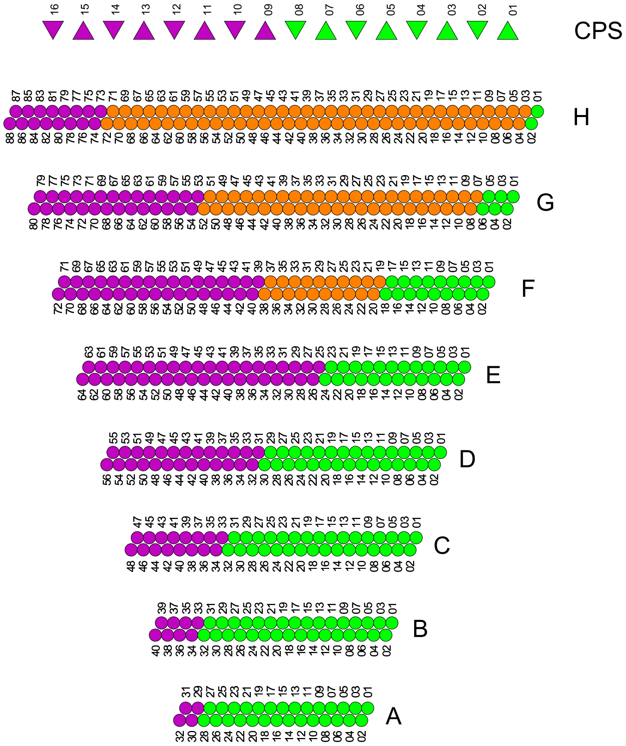

Figure 2-12: A schematic of a single 4.5° CFT and CPS sector, including the numbering of the 480 CFT singlet fibers in the 8 doublet layers and the 16 CPS axial strips. The different colors represent the three LVDS links that supply the data for one sector.

trigger with specific conditions is compared to the track. If it passes a trigger at Level 1, the event is kept in the data stream and sent to Level 2 for further analysis.

A common AND/OR logic term used at Level 1 in a number of triggers is TTK(1,10). This term requires that at least one track be reconstructed with a $p_T > 10$ GeV. Figure 2-13 shows the rate, in Hz, as a function of instantaneous luminosity in linear and logarithmic scales [43].

At Level 1, the TTK(1,10) term is ANDed to a muon trigger to create the MUHI trigger suite. The muon trigger requires that at least one local muon, with $p_T > 13$ GeV, in a wide region ($|\eta_{det}| < 1.6$) satisfies specific scintillator and wire requirements and is matched to a TTK(1,10) track. Due to the large rates associated with these triggers, the

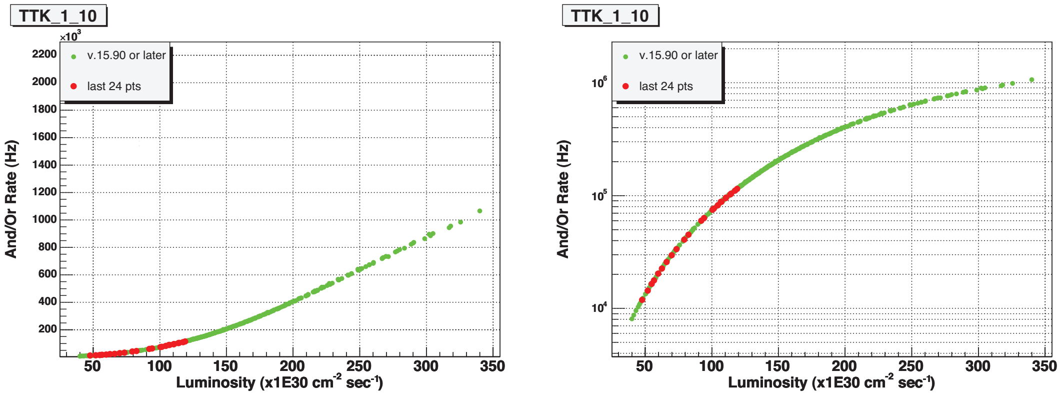

(a) (b)

Figure 2-13: AND/OR logic term TTK(1,10) rate versus instantaneous luminosity; (a) linear scale and (b) logarithmic scale of rates.

MUHI triggers are almost all turned off at luminosities greater than 220×10^{30} cm^{-2} s^{-1}. In order to run these triggers at higher luminosity we introduce occupancy track global veto terms, discussed in more detail in Section 2.3.1.

The CTT track list information is sent to Level 1 CalTrk (to match tracks to electrons, jets, or taus) or to Level 1 Muon (to match tracks to muons) to trigger on these objects, shown in Fig. 2-14 [38]. This is then sent to the Trigger Framework and a trigger decision is made. The event is either kept and sent to Level 2 or it is dumped.

2.3.1 Occupancy Track Global Veto Trigger Terms

The rate due to physics processes is linear with instantaneous luminosity, but the rates from fake triggering increase non-linearly with luminosity, driving up the rates that can be handled by the DAQ system, as is evident in Fig. 2-15. This forces the triggers to be prescaled at high luminosities or completely turned off. Track global veto (TGV) terms have been introduced to copies of the trigger terms that allow previously heavily prescaled triggers to run at almost all luminosities.

The TGV terms trigger on the singlet occupancy of the eight octants. A naming scheme has been devised such that TGV(i,j) refers to a trigger condition with threshold

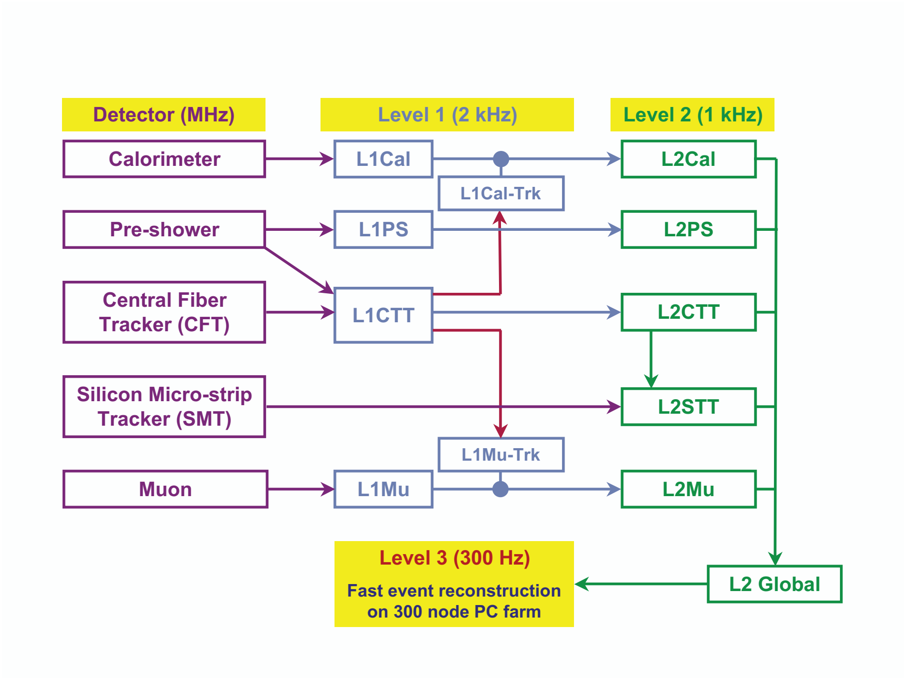

Figure 2-14: Schematic of the Level 1 and Level 2 logic chain.

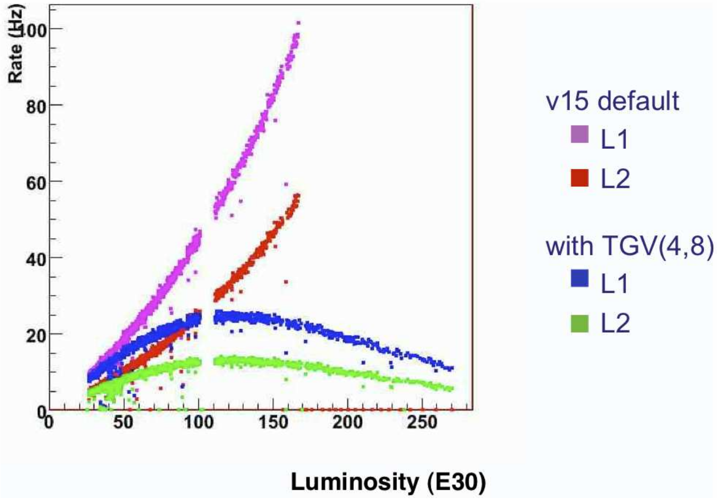

Figure 2-15: An example of Level 1 and Level 2 rates versus instantaneous luminosity for a muon trigger with and without the TGV term ANDed on.

i (ranging from 0 to 13) on the truncated octant sum j (ranging from 1 to 8). The chosen threshold values are listed in Table 2-3. $j = 1$ refers to the least occupied octant of the eight, $j = 2$ refers to the sum of the two least occupied octants, and so on until $j = 8$, which is the sum of all eight octants. The individual threshold values i are determined as follows; first an offset, which accounts for the background noise of the singlets spontaneously firing, is defined as $240 \times j$ for each truncated octant sum j. The threshold step size is chosen to be 86 singlets per octant (eg. $86 \times 4 = 344$), corresponding to $\sim 1.8\%$ of the singlets firing out of the total possible number of singlets in each truncated octant sum. This corresponds to one additional interaction in the event. The total number of singlets in each truncated octant sum is $4800 \times j$. If the number of singlets hit in an event is less than or equal to the threshold i of a specific truncated octant sum then the event is passed, likewise if the singlet occupancy is greater than the threshold then the event is rejected. It should be noted that these TGV(i,j) terms were easily encoded into the central track trigger term (CTTT) board.

Table 2-3: TGV term threshold values. j represents the truncated octant sums, eg. $j = 3$ is the sum of the three lowest occupied octants. % Hit refers to the percentage of fibers hit for that TGV threshold i term with respect to the total number of singlets available in that truncated sum.

Term	$j = 1$	2	3	4	5	6	7	8	% Hit
TGV(0,j)	240	480	720	960	1200	1440	1680	1920	$\sim$ 5.0
TGV(1,j)	326	652	978	1304	1630	1956	2282	2608	$\sim$ 6.8
TGV(2,j)	412	824	1236	1648	2060	2472	2884	3296	$\sim$ 8.6
TGV(3,j)	498	996	1494	1992	2490	2988	3486	3984	$\sim$ 10.4
TGV(4,j)	584	1168	1752	2336	2920	3504	4088	4672	$\sim$ 12.2
TGV(5,j)	670	1340	2010	2680	3350	4020	4690	5360	$\sim$ 14.0
TGV(6,j)	756	1512	2268	3024	3780	4536	5292	6048	$\sim$ 15.8
TGV(7,j)	842	1684	2526	3368	4210	5052	5894	6736	$\sim$ 17.6
TGV(8,j)	928	1856	2784	3712	4640	5568	6496	7424	$\sim$ 19.4
TGV(9,j)	1014	2028	3042	4056	5070	6084	7098	8112	$\sim$ 21.2
TGV(10,j)	1100	2200	3300	4400	5500	6600	7700	8800	$\sim$ 23.0
TGV(11,j)	1186	2372	3558	4744	5930	7116	8302	9488	$\sim$ 24.8
TGV(12,j)	1272	2544	3816	5088	6360	7632	8904	10176	$\sim$ 26.6
TGV(13,j)	1358	2716	4074	5432	6790	8148	9506	10864	$\sim$ 28.4
Step Size	86	172	258	344	430	516	602	688	$\sim$ 1.792
Offset	240	480	720	960	1200	1440	1680	1920	
Total Singlet #	4800	9600	14400	19200	24000	28800	33600	38400	

When we logically AND these TGV terms to the TTK terms, we can run them at higher instantaneous luminosities, as seen in Fig. 2-15. Figure 2-16 shows the rate, in

Hz, versus instantaneous luminosity for term TGV(10,8) in the linear scale. This term represents a trigger that must have less than 8800 singlets fired when summed over all eight octants.

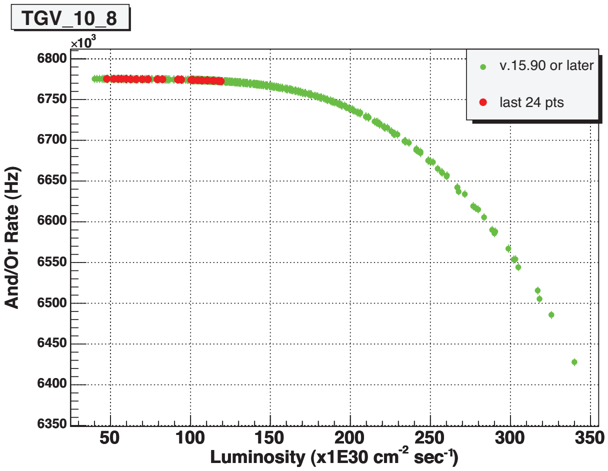

Figure 2-16: Linear plot of TGV(10,8) rates versus instantenous luminosity.

3 Object Reconstruction

To take advantage of the reconstruction efficiencies and uncertainities calculated by the Object ID groups we use the standard definitions of charged track, primary vertex, electron, ICR-electron, jet, missing transverse energy, and muon in the data analyses that follow. The object reconstruction description follows.

3.1 Charged Particle Track

The first step in object reconstruction is to identify tracks of charged particles produced in the tracking system (SMT and CFT, Section 2.2.1). DØ uses two such algorithms; the Histogramming Track Finder (HTF) [44] and the Alternative Algorithm (AA) [45]. The two methods are run independently to create track lists, which are then merged with the duplicate tracks removed.

3.1.1 Histogramming Track Finder Algorithm

A common method used in numerous high energy physics experiments for track reconstuction is the Kalman track fit algorithm [46]. Unfortunately, the downside to using this approach alone is that the number of mathematical operations grows very quickly with the number of hits, typically more than $10^4 - 10^6$. Additionally, without a distinct layer structure, such as in the SMT, the pattern recognition becomes very difficult and is sensitive to the single hit inefficiency [44]. To overcome these issues, we marry the Kalman track algorithm with the HTF method in the hopes of reducing the number of input hit calculations.

The position of a charged particle in a vacuum in a homogeneous magnetic field ($\mathbf{B}$) can be characterized by three parameters in the plane perpendicular to the $\mathbf{B}$-field's direction by (ρ,d_0,ϕ), where the curvature $\rho = q|\mathbf{B}|/p_T$ (q is the charge), d_0 is the impact parameter, or the distance of closest approach to (0,0), and ϕ is the azimuthal angle of the track at the point of closest approach to (0,0). For trajectories with small impact parameters, $d_0 \sim 0$, the (x,y) coordinate space position can be mapped to a point in parameter space (ρ,ϕ), or to a compact area if the coordinates are not precisely known.

A simple and common technique divides the parameter space into cells of $-\rho_0 < \rho < \rho_0$, $0 < \phi < 2\pi$, where $\rho_0 = qB/p_T^{min}$ and p_T^{min} is the minimal p_T of the tracks to be found, creating a 2D histogram. For every pair of hits the cell's content is incremented. Since all hits from the same track correspond to the same point in parameter space, a track with n hits will produce a peak of height $n(n-1)/2$, while hits from different tracks will produce a randomly distributed background [44]. Taken as is, this technique requires $\sim N_h^2$ operations, where N_h is the total number of hits in the event. This can be improved even more with a slight modification, known as the Hough transform. Note that each hit in (x,y) space corresponds to a line in parameter space, or when the errors are taken into account, to a band. All those lines intersect at one point, which corresponds to the (ρ,ϕ) parameters. The parameter space is again divided into cells, looping over ρ divisions, for each ρ the coverage in ϕ is calculated and then filled into the histogram. The number of operations needed now is reduced to $\sim N_h \times N_p$, where N_p is the number of ρ divisions. Once the cells with less than N_h^{min} hits are discarded, the track candidates are converted into "templates", a collection of hits organized into measuring planes plus a set of (approximately) known trajectory parameters [44]. Usually a template matches to a candidate for one track, but can have several hits associated with the same measuring plane, although at most only one associated plane is expected to survive the final filtering process.

At this point a 2D Kalman filter is applied, in which all three parameters (ρ,d_0,ϕ) are fitted and the effects due to the materials of the tracker are taken into account. The z coordinate space and η information can also be added to further reduce the number of fake templates. Ghost (two or more reconstructed tracks associated with the same charged particle) and fake (tracks not associated to any charged particles) tracks are reduced by requiring that no SMT tracks with less than two SMT hits are used and that tracks extrapolated from the SMT into the CFT have corresponding CFT hits and vice versa.

3.1.2 Alternative Algorithm Track Finder

The AA method begins by looking for an initial “track hypothesis” consisting of three SMT hits, with axial and stereo hits found in either the barrels or disks, searching from the inner-most layer outwards. By starting with the SMT, the number of combinatorics from axial and stereo hits are significantly reduced and the particle’s original parameters can be determined instead of lost to decays or material interactions. Unfortunately if hits are not found in the SMT after the first pass of the AA track finder a track cannot be reconstructed. Since each axial hit can have one or more associated stereo hits, each track hypothesis can also have one axial and numerous stereo projections. As a track hypothesis is being constructed it is constrained by the following conditions. Firstly, the track hypothesis can use any hits in the first six layers of the SMT barrels or in any of the F-disks. Secondly, the axial angle between a preceding hit and following hit must be less than a given value, typically less than 0.08 radians. Finally, the radius of the circle from the constructed track hypothesis must be greater than 30 cm, which corresponds to a particle with minimum p_T of 180 MeV, and its impact parameter with respect to the beam spot must be less than 2.5 cm. On top of these conditions, the track hypothesis must also have a $\chi^2 < 16$. These parameter limits can be changed to increase or decrease the acceptance of the tracking algorithm.

To build a track hypothesis, each potential track is extrapolated to the next layer of the SMT or CFT and an expectation window is calculated, this is a region where if there were to be a hit from the track it would fall within the surface area. The finder then looks for hits within this window and tries to match the hit with the already established track hypothesis. If the addition of the hit results in a χ^2 less than 16, the hit is associated with the track hypothesis. For every hit within the expectation window that satisfies the χ^2 condition, a new track hypothesis is created. Since each track hypothesis can have hundreds of stereo hits associated with a given axial hit, the AA finder removes these fake tracks by including the downstream detectors. Misses, or missed hits, are introduced when a hit is not found within the expectation window, defined separately for missed axial and stereo hits. Inside misses are misses between any two hits in the track hypothesis, while forward (backward) misses are misses for the forward (backward) track extrapolation. A track hypothesis is built in this manner until it reaches the end of the detector or three misses are found after the last associated hit.

Track hypotheses that satisfy the given conditions are added to a pool of tracks which are then filtered and ordered according to the number of associated hits reconstructed or a combination of hits with misses, if misses occur. Hypotheses with the largest amount of hits are placed at the top of the pool. A track hypothesis is declared an AATrack if the number of shared axial hits (between two potential AATracks) is less than a given percentage of the total number of axial hits. Fake tracks are reduced by extrapolating the track hypothesis to the primary vertex of the event. If the impact parameter of the hypothesis with respect to the primary vertex is small, an additional two hits are added to the hypothesis hit count and the pool is reordered to reflect these changes, so that tracks associated with the primary vertex are preferred, and the selection of AATracks is run again. Tracks with less than three SMT hits can be recovered after a second AA pass if CFT-only tracks are reconstructed in the same manner as described above, with additional conditions on the distance between the track hypothesis and primary vertex. Track hypotheses are then extrapolated back in to the SMT in attempts to pick up more hits. As in the HTF method, duplicate tracks are then removed from the track list.

3.2 Primary Vertex

The primary vertex (PV) (or any other vertex) of an event can be a powerful tool to reduce the background contribution, for example, by removing objects created in additional interactions (so called “minimum-bias” events). The window of collision locations extends from a width of about $\sigma_r = 40\ \mu$m in the radial direction and $\sigma_z =$ 28 cm along the z-axis.

Both of the two methods used to reconstruct tracks, discussed in Secs. 3.1.1 and 3.1.2, are used to determine the position of the primary vertex. By working backwards from the reconstructed tracks, the most likely vertex can be determined. These vertices are added to a vertex list for both methods and duplicate vertices are removed.

3.3 Electron

Electromagnetic clusters due to electrons need to be separable from other shower sources; such as neutral pions that overlap with a charged track, photons that convert to an e^+e^- pair, charged pions that start to shower early due to the solenoid, and fluctuations in hadronic jet shower shapes [47]. To reconstruct electrons, a Simple Cone algorithm [48] is used to form an initial shower cluster from energy deposited in the calorimeter, centered on a tower with at least $p_T > 0.5$ GeV. A list of towers is made, with the highest-p_T tower designated as the seed tower. A $\eta \times \phi$ circle is drawn around the seed tower and the total overall energy in the towers in a $\Delta\mathcal{R}$ cone of less than 0.4 is determined. Similarly, the energy from the towers in the EM calorimeter alone, within a $\Delta\mathcal{R} < 0.2$, is calculated. The initial cluster is accepted if at least 90% of the energy deposited is found in the EM layers (E_{EM}) versus the entire calorimeter (E_{tot}) within this 0.2 cone,

$$f_{EM} = \frac{E_{EM}(\Delta\mathcal{R} < 0.2)}{E_{tot}(\Delta\mathcal{R} < 0.2)} > 0.9, \tag{3-1}$$

and the energy of the cluster is $E_T > 1.5$ GeV [49]. The cluster is also required to be isolated, such that

$$f_{iso} = \frac{E_{tot}(\Delta\mathcal{R} < 0.4) - E_{EM}(\Delta\mathcal{R} < 0.2)}{E_{EM}(\Delta\mathcal{R} < 0.2)} < 0.2. \tag{3-2}$$

By requiring $f_{iso} < 0.2$, it further ensures that most of the energy deposited in the calorimeter is found in the EM layers, rejecting more hadronic showers which tend to have wider transverse shower shapes and penetrate deeper into the calorimeter.

For each shower cluster, the algorithm looks for a central preshower cluster to match with the CC cluster (the highest energy cluster within a cone of $\eta \times \phi = 0.1 \times 0.1$) or a forward preshower cluster to match with the EC cluster (within a cone of $\theta \times \phi = 0.1 \times 0.1$). If a match is found, the energy and position of the EM cluster is adjusted to include the preshower cluster information.

To help distinguish electrons from photons, since their shower develops in much the same way, the electron is matched to a track, or to all of the tracks within a window of $\eta \times \phi = 0.5 \times 0.5$, reconstructed in the central tracking system.

Due to an imperfect calorimeter, the energy of the cluster measured (E_{meas}) in the towers is lower than the true energy (E_{true}) of the electron. To account for this, an energy scale correction [50] is applied to the EM cluster

$$E_{meas} = \alpha E_{true} + \beta, \tag{3-3}$$

where α is the energy scale and β is the energy offset, determined for clusters in the CC and EC independently using a binned maximum likelihood method.

The following quantities are also used to help further define the purity of electrons in the calorimeter.

- **H–Matrix** : Characterizes the lateral and longitudinal shower shapes of the EM clusters and is used to discriminate between electromagnetic and hadronic showers. A 7×7 (8×8) covariance matrix, M, is built for each calorimeter tower in η_{det} in the CC (EC) region. Due to the symmetry of the calorimeter, the same matrix can be applied to towers at the same absolute value of η_{det}. The covariance matrix for clusters in the CC use the fractional energy deposited in each of the four EM calorimeter layers, the total shower energy, the z-position of the primary vertex, and σ_ϕ, the transverse shower width in ϕ. EM objects reconstructed in the EC use an additional variable which describes σ_z, the transverse shower width in z [51]. Using electrons from Monte Carlo (MC) simulation, the matrix elements are built using two of the variables, x_i and x_j;

$$M_{ij} = \frac{1}{N}\sum_{n=1}^{N}(x_i^n - \bar{x}_i)(x_j^n - \bar{x}_j), \tag{3-4}$$

summed over N reference electrons. The shape of the electromagnetic cluster is then compared to the reference using

$$\chi^2_{HMx} = \sum_{ij}^{7\ or\ 8}(x_i - \bar{x}_i)H_{ij}(x_j - \bar{x}_j), \tag{3-5}$$

where $H \equiv M^{-1}$. A genuine electron will have a shower shape with a low χ^2_{HMx} value.

- **Track Isolation** : Describes the track isolation of the EM cluster. This quantity is the sum of all track momenta, for tracks with a minimum $p_T > 0.5$ GeV, in a hollow cone of $0.05 < \Delta\mathcal{R} < 0.4$ around the EM cluster.

- **Spatial Track Match** : The $\chi^2_{spatial}$ probability is used to discriminate fake tracks that point towards an EM cluster and is defined as

$$\chi^2_{spatial} = \left(\frac{\Delta\phi}{\sigma(\phi)}\right)^2 + \left(\frac{\Delta z}{\sigma(z)}\right)^2, \tag{3-6}$$

  where $\Delta\phi$, Δz and $\sigma(\phi)$, $\sigma(z)$ are the separation and resolution in ϕ and z between the EM cluster position in the third layer of the EM calorimeter and the extrapolated track position.

- **Hits–on–Road** : The probability of an EM object being an electron or photon using track hit information from the SMT and CFT [52]. This variable is used to reduce the number of fakes coming from photons and neutral pions.

- **NNout** : An artificial neutral network (ANN) that uses at most seven variables to determine if an EM cluster is more electron-like than jet-like. The seven variables used include [53]: (i) fraction of EM cluster energy deposited in the first EM (EM1) layer, (ii) the number of EM1 cells in a cone of $\Delta\mathcal{R} < 0.2$, (iii) track isolation, (iv) the number of EM1 cells in an annulus cone of $0.2 < \Delta\mathcal{R} < 0.4$, (v) the number of tracks in a cone of $\Delta\mathcal{R} < 0.05$, (vi) χ^2_{HMx8}, and (vii) number of CPS clusters.

- $\mathbf{E_T/p_T}$: ratio of the measured transverse energy of the cluster to the measured p_T of the track. Typically, an electron will have $E_T/p_T \sim 1$.

- **Shower Width** : Describes the azimuthal and z-directions of the shower shape of an EM cluster at the third layer in the EM calorimeter and are given by [54]

$$\begin{aligned} SigPhi &< 7.3|\eta_{det}|^2 - 35.9|\eta_{det}| + 45.7, && (3\text{-}7) \\ SigZ &< 7.5|\eta_{det}|^2 - 36|\eta_{det}| + 44.8. && (3\text{-}8) \end{aligned}$$

- **Electron Likelihood** : The eight likelihood input variables include; f_{EM}, f_{iso}, H–Matrix, E_T/p_T, the number of tracks in a cone of $\Delta\mathcal{R} < 0.4$, track isolation, and distance of closest approach to the primary vertex [55]. The likelihood of an electron is then given by

$$\mathcal{L}(x) = \frac{\prod_{i=1}^{8} P_e(x_i)}{\prod_{i=1}^{8} P_e(x_i) + \prod_{i=1}^{8} P_{bkg}(x_i)}, \tag{3-9}$$

  where x_i is the ith variable and P_e (P_{bkg}) is the probability that the object is an electron (background). Electrons will have a likelihood close to one, while background will tend towards zero.

3.3.1 Intercryostat Region Electron

Intercryostat region (ICR) electrons fall within the gaps between the CC and EC calorimeters, corresponding to the region in pseudorapidity of $1.1 < |\eta_{det}| < 1.5$, where calorimeter coverage is minimial due to the cryostat structure. Since a good portion of the shower can be missed by the EM layers, an ICR electron is expected to have a narrow shower cone and a larger fraction of non-EM energy as compared to CC/EC electrons [56]. The ICR electron is first identified as a tau object, with $E_T > 10$ GeV, and matched to a central track, with $p_T > 20$ GeV, with at least one SMT hit and ten CFT hits. A neutral network is then used to separate ICR electrons from taus and hadronic jets.

3.3.2 Electron Identification Qualities

Table 3-1 defines the EM ID group's standard electron identification qualities for "Tight" CC and EC, "Point05" CC, and "Point1" EC electrons [54, 57] used in the presented analyses.

Table 3-1: Standard electron ID quality thresholds.

Variable	Tight CC	Tight EC	Point05 CC	Point1 EC
f_{iso} [<]	0.07	0.07	0.15	0.10
f_{EM} [>]	0.97	0.97	0.90	0.90
H–Matrix [<]	25	15	–	40
Track isolation (GeV) [<]	2.5	2	3.5	100
$\chi^2_{spatial}$ [>]	0	0	0	0
NNout [>]	0.6	0.4	0.3	0.05
LHood [>]	0.8	–	0.05	0.05
E_T/p_T[<]	4	–	8	–
p_T(GeV) [>]	15	15	–	–
SigPhi [<]	–	20	–	100
Hits–on–Road [>]	0.5	–	–	–

3.4 Hadronic Jet

An important function of the fine and coarse hadronic calorimeters is to separate out jets showers from hadronic decays from those of electron or photon clusters. Jets are reconstructed from energy deposits found within the CC and EC calorimeters using the RunII midpoint cone algorithm [58] with a given cone radius (usually with $\Delta\mathcal{R} < 0.7$). The algorithm is designed to be used at both DØ and CDF and is used to reconstruct parton jets (MC generated parton level jets), particle jets (MC generated stable particle jets, occuring after parton hadronization), and detector jets (jets reconstructed from calorimeter towers or cells in both data and MC simulations).

The "E-scheme" [59] uses four–momenta to combine several items (i) into a single item;

$$\mathbf{p}^J = (E^J, p^J) = \sum_i (E^i, p_x^i, p_y^i, p_z^i), \tag{3-10}$$

where J represents the calorimeter tower of interest. The usual kinematic variables are then calculated, such that the transverse momentum is $p_T^J = \sqrt{(p_x^J)^2 + (p_y^J)^2}$, the azimuthal angle is $\phi^J = \arctan\left(\frac{p_y^J}{p_x^J}\right)$, and the pseudorapidity $\eta_J = -\ln\left(\tan\frac{\theta^J}{2}\right)$.

A simple cone algorithm is used to build a list of items that become preclusters, which serves as the input into the RunII cone algorithm [59]. The algorithm loops over the calorimeter towers, ordered by decreasing p_T, and required to have $p_T^J > 0.5$ GeV. The leading-p_T object becomes a precluster seed, P, and is removed from the list. The algorithm then starts a second loop over the items, I, where if $\Delta\mathcal{R}(P,I) < 0.3$ and $p_T^I > 0.1$ MeV, it is combined with precluster P and also removed from the list. This looping continues until no item with $p_T^I > 0.5$ GeV is left. Those preclusters that satisfiy $p_T^P > 1$ GeV are sent as proto-jet candidate inputs to the next stage of reconstruction, while the ones that fail are removed from the list.

The RunII cone algorithm loops over the precluster P list, which has also been ordered by decreasing p_T, and determines the $\Delta\mathcal{R}$ between P and its closest proto-jet candidate. If $\Delta\mathcal{R} > \mathcal{R}_{cone}/2$ (where $\mathcal{R}_{cone}$ is either 0.7 or 0.5, depending on the Jet ID requirement, see Sec. 3.4.2) then the precluster becomes a seed for a proto-jet candidate, PC. The next step forms a cone of radius $\mathcal{R}_{cone}$ around the PC candidate. All items within this cone are combined to form a new proto-jet candidate, PC', which replaces PC. This process continues until one of the three following conditions is met;

- Proto-jet candidate has $p_T^{PC'} < 3$ GeV,
- Proto-jet candidate is stable, i.e. $\Delta\mathcal{R}(PC', PC) < 0.001$, or
- Fifty iterations have occurred.

The proto-jet candidate is discarded if $p_T^{PC'}$ is less than 3 GeV. After the last iteration, the proto-jet candidate is added to the list of proto-jets, as long as another duplicate proto-jet does not exist.

Soft radiation can cause the cone algorithm to join multi-proto-jet candidates together. To minimize this effect, another list of proto-jet candidates is made that is seeded by the midpoints between all of the precluster seeded proto-jets and added to the final list of proto-jets. The list of midpoints is kept, even if they are found near another proto-jet candidate and have duplicate entries.

The final step merges or splits the two proto-jet lists, preclusters and midpoints, making sure to avoid double counting. If two proto-jets share at least one item, the sum of the item's momenta which are shared with its highest-p_T neighbor is calculated. The two proto-jets are "merged" if the sum of the p_T is greater than 50% of the p_T of this neighbor and the neighbor is removed from the list. The two proto-jets are "split" if the sum is less than 50%. The list of proto-jets is then reordered by decreasing p_T and the process is continued until no proto-jet remains.

Proto-jets that pass the above merge/split step become the final jet candidates and are required to have $p_T > 8$ GeV and a detector pseudorapidity acceptance of $|\eta_{det}| < 3.4$.

3.4.1 Jet Energy Scale

The jet energy scale (JES) is a correction applied to jets that corrects the measured energy (E_{jet}^{meas}) to the jet's true energy (E_{jet}^{true}) by taking into account the energy of all the particles in the jet before interacting with the detector [37] and is given by

$$E_{jet}^{true} = \frac{E_{jet}^{meas} - E_0}{\mathcal{R}_{jet} \times \mathcal{S}_{jet}}. \tag{3-11}$$

E_0 is the energy offset resulting from such things as minimum-bias interactions, events from previous crossings, uranium decay, and electronics noise. $\mathcal{R}_{jet}$ is the energy response or the fraction of the energy that is actually measured. The showering correction, $\mathcal{S}_{jet}$, is due to the energy that is lost (gained) from particles inside (outside) the jet cone that have showers that extend outside (inside) the cone boundary.

3.4.2 Jet Identification Qualities

Jets are reconstructed using two possible cone radii. A "JCCA" jet requires that $\Delta\mathcal{R} < 0.7$, while a "JCCB" jet narrows that cone radius to $\Delta\mathcal{R} < 0.5$. "Good" jets are passed with the "goodjet" flag and have had EM objects removed, while "vertex confirmed" jets are good jets with at least two tracks, both with $p_T > 0.5$ GeV, matched to the primary vertex and within $\Delta\mathcal{R} < 0.5$ of a calorimeter jet.

3.5 Missing Transverse Energy

The missing transverse energy, $\not{E}_T$ or MET, of an event results from an energy imbalance in the transverse plane and is defined as the negative of the vector sum of all transverse momenta in the event;

$$\not{E}_T = -\sum_i (\mathbf{p_T})_i. \tag{3-12}$$

This imbalance can be caused by either a physical object, such as a neutrino or BSM object, or instrumentation sources. Such possible sources include calorimeter noise, poorly measured muon tracks, unclustered energy deposits, etc. [60].

The raw $\not{E}_T$ is measured in the calorimeter, using the electromagnetic and fine hadronic parts, but usually not the coarse hadronic part due to an increase in noise. Although, there are definitions available which can use any of the three. The missing energy then needs to be corrected for physical objects in the event, such as muons or hadronic jets with energy deposited in the coarse hadronic calorimeter, to get a true sense of a neutrino's energy. Recomputation works by subtracting the raw energy of the calorimeter objects and replacing it by the corrected object values, for example it is replaced with the JES corrected energy and includes the CH energy. Likewise, the $\not{E}_T$ is corrected for muons reconstructed in the event that pass certain selection criteria, being careful not to double count muons in jets.

A modified MET variable called ${\not{E}_T}^{special}$ is often used to help reduce the contribution from the Z/γ^* background. This variable assigns less significance to the missing energy in an event when the opening angle, $\Delta\phi$, between the $\not{E}_T$ and any other lepton or jet is small, as this may be a potential source of mismeasurement. The ${\not{E}_T}^{special}$ is defined as follows:

$$\begin{aligned} {\not{E}_T}^{special} &= \not{E}_T \text{ if } \Delta\phi(\not{E}_T, \text{nearest lepton/jet}) > \pi/2, \text{ or} \\ {\not{E}_T}^{special} &= \not{E}_T \times sin(\Delta\phi(\not{E}_T, \text{nearest lepton/jet})) \text{ otherwise.} \end{aligned} \tag{3-13}$$

The ${\not{E}_T}^{significance}$ is used to discriminate real MET from events with fake or mismeasured missing energy. It is a likelihood function, defined as

$$L = 2\log\left(\frac{\not{E}_T}{2\sigma}\right)^2, \tag{3-14}$$

where σ is the variance on the probability distribution of a unit vector in the direction of the measured MET [61]. It measures, in standard deviations, how different the projection of the MET in the direction of the measured MET is from zero.

3.6 Muon

Muons are reconstructed using information from the wire drift chambers and scintillation counters in the three layers of the muon detector. The muon is also matched to a track reconstructed in the central tracking system. Pattern recognition is used to combine the hits in the wire chamber and create a "segment" (or straight line) that fits the hits [62]. The found segment is then combined with scintillator hit information for the segment's timing information. Firstly, the "global" hit information is transformed into "local" hits, keeping the point of origin the same between both coordinate systems. A local muon is identified based on the information found in the muon detector, rather than the central tracker. Links are then made between the segment hits, requiring a minimum of two hits. As the algorithm progresses, further hits are added to the segment link, provided that they satisfy certain criteria, creating a "tree" of links. When all trees are determined, each is then fitted in the x- and y-direction, and the z-direction separately, where the lowest χ^2 fit describes the best segment. The segments are fitted to scintillator hits to determine the timing and, for the forward system, a better position. If possible, to better improve the angular resolution of the segment, the vertex information is used to update the position of the segment. Next local segments in the B and C layers are matched in the same region and same octant, to create a better fit. Finally, the local segments are filtered, given certain requirements, and then transformed back into the global coordinate system. To improve the local muon's momentum resolution, the muon can be matched to a track in the central tracking system. This is done by extrapolating the local muon track inward, modeling the minimum ionizing interaction with the calorimeter, and fitting to a central track.

Isolation requirements are designed to separate prompt muons from electroweak processes from secondary muons produced in heavy flavor quark decays. Track isolation and/or calorimetic energy deposition surrounding the muon can be used to reject these secondary muons. A variable referred to as "etTrkCone" is the scalar sum of the transverse momenta of all the tracks inside a cone of $\Delta\mathcal{R}(\text{track},\mu) < 0.5$ around the muon track with the exception of the muon track itself;

$$\mathcal{I}^{trk}_{\Delta\mathcal{R}<0.5} \equiv |\Sigma_{tracks\in\Delta\mathcal{R}<0.5}\ p_T| - |p^{\mu}_T|. \tag{3-15}$$

To avoid contribution of tracks from pile-up, an additional cut of Δz(track,μ) < 2 cm is also required. The other significant isolation variable is "etHalo". This is the scalar sum of the transverse energies of all calorimeter clusters inside a hollow cone $0.1 < \Delta\mathcal{R}$(cluster,μ) < 0.4 around the muon;

$$\mathcal{I}^{cal}_{0.1<\Delta\mathcal{R}<0.4} \equiv |\Sigma_{clusters\in 0.1<\Delta\mathcal{R}<0.5}\ E_T|. \tag{3-16}$$

To reduce noise and pile-up, only the EM and coarse hadronic calorimeters are used in this measurement.

A cosmic timing veto, along with distance of closest approach cuts, are included to reject muons from background cosmic rays.

3.6.1 Muon Identification Qualities

The standard muon definition requires three quantities [63]; muon ID quality, track quality, and muon isolation and are described in more detail below.

A muon ID quality candidate is categorized by two quantities; type and quality. The muon type depends on the parameter "nseg". Positive nseg values indicate that a local muon was matched to a track in the SMT or CFT, while negative values are for those local muons not matched to a central track. If a local muon consists of A-layer hits only, it is assigned |nseg| = 1, while |nseg| = 2 (3) muons have B- or C-layer (A- and B- or C-layer) hits. For nseg = +1, a muon is considered "Loose" quality if it has at least one scintillator hit and at least two A-layer wire hits, while a "Medium" muon also requires that it is located in the bottom part of the detector (in Octants 5 or 6 with $|\eta_{det}| < 1.6$) and that its probability to reach the BC-layer is less than 0.7, indicating that it is a low momentum muon. For nseg = +2, a muon is "Loose" if it has at least one BC-layer scintillator hit and at least two BC-layer wire hits, with "Medium" also requiring that the muon be reconstructed in the bottom part of the detector. For nseg = +3, a muon is "Medium" if it has at least two A-layer wire hits, at least one A-layer scintillator hit, at least two BC-layer wire hits, and at least one BC-layer scintillator hit (although this requirement is dropped for central muons). A "Loose" nseg = +3 muon meets the criteria above but allows for one requirement to fail, with the A-layer wire and scintillator requirements taken together as one and requiring that there is at least one scintillator hit.

The track quality of the track matched to the muon depends on the following track parameters; the number of hits in either the SMT or CFT, the χ^2 per degree of freedom of the central track fit, and the distance of closest approach with respect to the beamline (dca). A track is defined as "Loose" if $|dca| < 0.2$ cm when there are no SMT hits and $|dca| < 0.04$ cm for tracks with $n_{hit}^{SMT} > 0$ (in RunIIa, this cut was less than 0.02 cm). A "New Medium" track satisfies Loose requirements and the χ^2 per degree of freedom is less than 9.5 and there are at least two CFT hits.

An isolated muon is considered "NPLoose" if etTrkCone < 4 GeV and is "NPTight" if etHalo < 2.5 GeV and etTrkCone < 2.5 GeV. To help reject low-p_T secondary muons and increase the efficiency of high-p_T prompt muons, a scaled isolation working point is available. "TopScaledLoose" requires that etTrkCone/p_T < 0.2 and etHalo/p_T < 0.2.

4 WZ Cross Section Measurement

WZ boson pairs are produced in the SM via the LO Feynman diagrams shown in Fig. 4-1. The production of the WZ boson pairs through the three channels interfere and maintain unitarity at high energies. In the case of the t- and u-channels, the W and Z bosons are radiated from the initial state quarks, while the s-channel production occurs via a triple gauge coupling, which is a natural consequence of the non-Abelian nature of the SM.

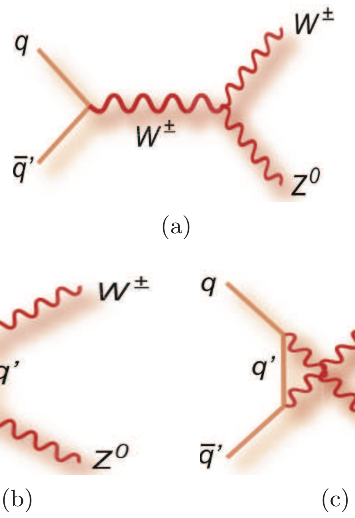

(b) (c)

Figure 4-1: Leading-order (a) s-, (b) t-, and (c) u-channel WZ production diagrams.

Figure 4-2 shows the s-channel LO Feynman diagram where the both W and Z boson decay leptonically. As discussed in Section 1.1, despite having low branching ratios

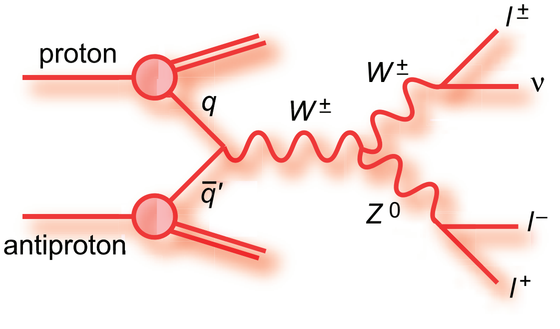

Figure 4-2: Tree-level s-channel WZ to tri-leptons plus missing transverse momentum production diagram.

($BR(Z \to \ell\bar{\ell}) \sim 3.4\%$ and $BR(W \to \ell\nu) \sim 10.8\%$) as compared to hadronic decays, the backgrounds in the tri-lepton final states are extremely minimal or clean. Numerous limits and measurements have been set on the WZ cross section by the Tevatron experiments. Table 4-1 summarizes these results.

Table 4-1: Summary of WZ cross section limits and measurements.

Experiment (Year)	Luminosity	Final state	Cross section (at 95% C.L.)
DØ (1990) [64]	90 pb^{-1}	$WZ \to e\nu e\bar{e}$, $\mu\nu e\bar{e}$	$\sigma_{WZ} < 47$ pb
CDF (2005) [65]	195 pb^{-1}	$ZZ \to \ell\bar{\ell}\nu\bar{\nu}$, $\ell\bar{\ell}\ell'\bar{\ell}'$, $WZ \to \ell'\nu\ell\bar{\ell}$	$\sigma_{WZ+ZZ} < 15.2$ pb
DØ (2005) [66]	0.3 fb^{-1}	$WZ \to \ell'\nu\ell\bar{\ell}$	$\sigma_{WZ} < 13.3$ pb, $\sigma_{WZ} = 4.5^{+3.8}_{-2.6}$ pb
CDF (2007) [12]	1.1 fb^{-1}	$WZ \to \ell'\nu\ell\bar{\ell}$	$\sigma_{WZ} = 5.0^{+1.8}_{-1.6}$ pb
DØ (2007) [67]	1.0 fb^{-1}	$WZ \to \ell'\nu\ell\bar{\ell}$	$\sigma_{WZ} = 2.7^{+1.7}_{-1.3}$ pb

The WZ analysis [68] discussed in this chapter supersedes DØ's 2007 1.0 fb^{-1} measurement. Not only is the integrated luminosity increased by a factor of four, but we allow for electrons to be reconstructed in the ICR region, increasing the electron acceptance. We also optimized the selection criteria of each channel individually to $s/\sqrt{s+b}$, where s is the expected WZ diboson signal and b is the total background, to improve the cross section measurement.

Section 4.1 describes the data and Monte Carlo (MC) samples used in this updated analysis, followed by the object identification criteria and event selection in Section 4.2. Section 4.3 describes the estimation of the data-driven backgrounds, while the results are given in Section 4.4.

4.1 Data and Monte Carlo Samples

Data used for this analysis was collected between April 20, 2002 and December 11, 2008, corresponding to ~ 4.1 fb^{-1} of integrated luminosity after the standard data quality [36] requirements have been applied. To take advantage of the work done by the Common Samples Group (CSG), we use the official skims discussed in Appendix B. 2MUhighpt skims (defined in Appendix B) are used to select the $X\nu\mu\bar{\mu}$ candidate events, where

$X = e$ or μ, and estimate the backgrounds from $V +$ jets processes (discussed more in Section 4.3). The QCD skims are used to measure the muon misidentification ratios. The skims used to select the di-electron final states are discussed in Section 2.1 of Ref. [68].

MC samples, produced by the CSG using the CTEQ6L1 parton distribution function (PDF) set [69], are used to estimate the WZ signal acceptance and the ZZ and $t\bar{t}$ backgrounds. The diboson samples (WZ and ZZ) are simulated using the PYTHIA generator [70], while the $t\bar{t}$ production uses the ALPGEN generator [71] interfaced to PYTHIA for appropriate hadronization and showering, at a top mass of $m_t = 172$ GeV. All MC samples are properly reweighted for the data luminosity profile and the beam-position distribution (both described in more detail in Appendix A), and normalized to the next-to-leading-order (NLO) cross sections of the samples. The MC samples used for RunIIa and RunIIb, along with the NLO cross section multiplied by branching fractions and the number of events before data quality (DQ) is applied, are listed in Table 4-2. To correctly simulate the luminosity of the dataset in the MC samples, "zero-bias" interactions – events from a random snapshot of a beam crossing – are overlaid on top of the MC simulations. Data quality requirements are then applied to the MC samples to account for any bad runs or bad LBNs at the time the zero-bias event was recorded.

Table 4-2: MC samples used in the analysis. The NLO cross section times branching fractions and the number of events before data quality cuts are applied are listed. *lp* represents light partons.

Process	$\sigma_{NLO} \times BR$ (pb)	Events before DQ RunIIa	Events before DQ RunIIb
$WZ \to 3\ell 3\nu, \ell = e, \mu, \tau$	0.1064	188412	363320
$ZZ \to$ inclusive	1.334	590647	540273
$t\bar{t} + Xlp \to 2\ell 2\nu 2b + Xlp, X = 0, 1, 2$	0.782	3180331	1483272

4.2 Object and Event Selection

This analysis uses electrons (both central and forward, along with allowing electrons reconstructed in the ICR), muons, and missing transverse energy, $\not\!\!E_T$. We take advantage of the reconstruction efficiencies and uncertainties calculated by the Object ID groups (discussed in Chapter 3) by using the standard electron, ICR-electron, muon, and $\not\!\!E_T$ definitions. Candidate events are selected in six distinct channels: $\mu\nu\mu\bar{\mu}$, $e\nu\mu\bar{\mu}$, $\mu\nu e\bar{e}$, $e\nu e\bar{e}$, and $\mu\nu e\bar{e}_{ICR}$ and $e\nu e\bar{e}_{ICR}$, where one leg of the Z boson is reconstructed in the ICR.

Events must have at least three energetic or high-p_T leptons, either electrons or muons, and a significant imbalance of transverse momentum. As mentioned in the Introduction, taus are included in the signal selection if they decay into electrons or muons. Events are further selected from the 2MUhighpt skims using the single muon logical OR triggers, which consists of several triggers which may be satisfied by a single muon. Only events with at least one primary vertex within ±60 cm in z of the detector origin are considered.

Along with the lepton ID efficiency, we need to estimate the overall event trigger efficiency of the three leptons. We use the official single electron [72] $p_T - \eta$ and single muon [73] $\eta - \phi$ trigger efficiency parametrizations, determined by the Object ID groups using data. We estimate the trigger efficiency for a given MC event using the following:

$$\epsilon_{trigger} = 1 - \prod_i (1 - \epsilon_i), \tag{4-1}$$

where $\epsilon_{trigger}$ is the event's total trigger efficiency and ϵ_i is the trigger efficiency for a given lepton. Due to multiple, high-p_T leptons in the event, the overall trigger efficiency is $\approx 98 \pm 2\%$ or greater for each final state.

To select the WZ candidate events, we first identify the leptons from the Z boson decay by selecting the same-flavor opposite-sign electric charge muon pairs. Out of the possible muon pairs, the pair with the invariant mass closest to the nominal Z boson mass ($m_Z = 91$ GeV) is selected. This assignment is checked in MC simulation and found to be 100% correct for $e\nu\mu\bar{\mu}$ events and 89% correct for $\mu\nu\mu\bar{\mu}$ events. A similar method is used for the $X\nu e\bar{e}$ and $X\nu e\bar{e}_{ICR}$ final states, and is discussed in detail in Ref. [68]. Due to the handling of detector efficiencies and systematics, ICR-electrons have a different energy scale compared to that of CC/EC electrons [56, 74]. As a consequence, a shifted nominal Z boson mass value of 84.9 GeV is used instead. Finally, out of the remaining leptons in the event, the lepton with the highest transverse momentum is selected as the W boson decay candidate.

The kinematic cuts and selection criteria are optimized according to $s/\sqrt{s+b}$ for each final state separately. The majority of the background comes from processes with a genuine Z boson plus an additional object that is misidentified as the W boson decay lepton. These processes are Z+jets, ZZ, and $Z\gamma$. A small background contribution from $W+$jets is also expected. An additional but small background is from $t\bar{t}$ production. The ZZ and $t\bar{t}$ backgrounds are estimated using MC simulations, while the V+jets ($V =$ W or Z boson) and $Z\gamma$ backgrounds are estimated using data-driven methods, described in Section 4.3.

4.2.1 $X\nu\mu\bar{\mu}$ Final States

We require the two muons from the Z boson decay to be minimally of "Medium, Loose, NPLoose" muon ID, track, and isolation quality, respectively. In the $\mu\nu\mu\bar{\mu}$ channel, the third muon from the W boson decay must be at least "Medium, Loose, NPTight". The electron in the $e\nu\mu\bar{\mu}$ final state must be of "Tight" quality in all regions of the calorimeter. The kinematic requirements common to both final states are as follows:

- p_T of the most energetic muon from the Z boson decay must be greater than 20 GeV,
- p_T of the two other leptons must be greater than 15 GeV,
- 65 GeV $< M_{\mu\mu} <$ 115 GeV for the two Z boson muons,

- The muons from the Z boson decay must have opposite electrical charges,
- $\Delta\mathcal{R} > 0.5$ between any two muons, and
- $\Delta z_{dca} < 3$ cm between any two leptons' tracks.

Further requirements on $\mu\nu\mu\bar{\mu}$ events include:

- $\not\!\!E_T > 20$ GeV,

while $e\nu\mu\bar{\mu}$ events require the additional following:

- $\not\!\!E_T > 25$ GeV, and
- $\Delta\mathcal{R} > 0.6$ between any two muons and the electron.

4.2.2 $X\nu e\bar{e}$ Final States, With and Without an ICR Electron

The selection criteria for the $X\nu e\bar{e}$ channels is similar to the $X\nu\mu\bar{\mu}$ channels and can be found in detail in Ref. [68].

4.2.3 Acceptance × Efficiency

The acceptance of a detector describes the fraction of events that would be seen if it is assumed to be a perfect detector, in which all objects are reconstructed correctly. The detector acceptance describes the number of events that should be found in the detector, while the kinematic acceptance describes the number of events that should pass given the kinematic selection criteria. The WZ MC sample, discussed in Sec. 4.1, is used to calculate the acceptance of the kinematic criteria; such as the p_T thresholds, pseudorapidity, $\Delta\mathcal{R}$, the mass window on the Z boson candidate, and the $\not\!\!E_T$ requirement. To determine the true kinematic acceptance ($\mathcal{A}$), and remove as much of the detector efficiency (ϵ) as possible, we select very loose quality muons ("Loose" quality and "Loose" track), which are selected with a greater than 95% efficiency. Table 4-3 summarizes the acceptances and uncertainties for all final states. A systematic uncertainty of 5% due to the PDF chosen is assigned.

Table 4-3: Acceptance ($\mathcal{A}$) for each final state with statistical, systematic, and total uncertainties. The efficiency (ϵ) of the selection criteria and Acceptance × efficiency ($\mathcal{A} \times \epsilon$) for each final state with total uncertainties.

Channel	$\mathcal{A}$	$\Delta\mathcal{A}$ (Stat.)	$\Delta\mathcal{A}$ (Syst.)	$\Delta\mathcal{A}$	ϵ	$\Delta\epsilon$	$\mathcal{A} \times \epsilon$	$\Delta(\mathcal{A} \times \epsilon)$
$e\nu e\bar{e}$	0.0246	0.0003	0.0012	0.0012	0.4146	0.0532	0.0102	0.0014
$\mu\nu e\bar{e}$	0.0278	0.0003	0.0014	0.0014	0.4136	0.0336	0.0115	0.0011
$e\nu\mu\bar{\mu}$	0.0274	0.0002	0.0014	0.0014	0.3905	0.0448	0.0107	0.0011
$\mu\nu\mu\bar{\mu}$	0.0305	0.0002	0.0015	0.0015	0.4382	0.0478	0.0134	0.0013
$e\nu e\bar{e}_{ICR}$	0.0077	0.0001	0.0004	0.0004	0.4286	0.9469	0.0033	0.0004
$\mu\nu e\bar{e}_{ICR}$	0.0083	0.0001	0.0004	0.0004	0.5060	0.0415	0.0042	0.0004

We use the Object ID groups' lepton efficiencies (ID, trigger) to estimate the efficiency of the event selection for events that pass the kinematic acceptance. The efficiency (ϵ) and the product of the acceptance and efficiency ($\mathcal{A} \times \epsilon$) for each final state is also given in Table 4-3.

To study the effect of lepton misassignment on the $\mathcal{A} \times \epsilon$ of the selection criteria, we look at the MC generator level truth information. Leptons in the $\mu\nu e\bar{e}$, $e\nu\mu\bar{\mu}$, and $\mu\nu e\bar{e}_{ICR}$ final states will be assigned to the correct W or Z boson 100% of the time. But for the same-flavor lepton topologies ($e\nu e\bar{e}$, $\mu\nu\mu\bar{\mu}$, and $e\nu e\bar{e}_{ICR}$), there is a chance that the leptons are not correctly assigned to the bosons. The $\mathcal{A} \times \epsilon$ is calculated for these channels and the difference (with respect to the values in Table 4-3) was found to be of the order of 1%.

The WZ system modeling is an additional source of systematic uncertainty that can affect $\mathcal{A} \times \epsilon$ [68]. We rely on WZ PYTHIA MC samples that generate the WZ process at LO with additional soft gluon radiation. However, a more proper description of the NLO WZ diboson production is given with the MCFM generator [75]. To estimate the effect due to the WZ production modeling in PYTHIA, the system p_T distribution from the WZ MC sample is reweighted to match the one from the MCFM sample while the normalization of the sample is preserved. Then, this sample is used to calculate a new $\mathcal{A} \times \epsilon$. The difference is found to vary from 2 – 3% up to 5% for the different channels. Thus, a conservative 5% systematic uncertainty is taken for all topologies.

4.3 Data-Driven Background Estimation

The methods used to estimate the $V+$jets and $Z\gamma$ backgrounds are discussed below.

4.3.1 Vector Boson + Jets Background

A significant source of background is from processes where a jet fakes one of the isolated leptons. This can be from a misidentified jet or the semi-leptonic decay of a heavy flavor jet from vector boson plus jet production. This $V+$jets background, where V is either a W or Z boson, is estimated in two steps. First we measure the ratio of the number of objects that pass the standard lepton identification requirements, designated as *true* leptons, to the number of leptons that pass non-isolated requirements, *false* leptons, $\epsilon_f = \frac{N^{\ell}_{true}}{N^{\ell}_{false}}$, using the multi-jet/QCD sample in data (described in Appendix B). The definitions are constructed so that there is no overlap between the *true* and *false* criteria, and that *false* leptons are more likely to be misidentified jets or leptons from semi-leptonic decays of heavy flavor jets. The misidentification ratios are determined as a function of η_{det}. As a consistency check, we also determine the ratios as a function of p_T and find that the $V+$jets background estimate using either the η_{det}- or p_T-dependent ratios agree well.

Secondly, we create a Z + non-isolated lepton normalization sample by selecting events with two *true* leptons, missing transverse momentum that satisfies the selection cut, and only one *false* lepton. We require that the two good leptons form the Z boson candidate. The η_{det} distribution of *false* leptons in the normalization sample is then multiplied by the measured misidentification ratios, $\epsilon_f(\eta_{det})$. The integral of this product distribution provides an estimate of the $V+$jets background.

To ensure an unbiased non-lepton triggered estimation of the misidentification ratios, events in the multi-jet sample are collected using the QCD skims provided by the CSG and must have a high-p_T jet, assumed to be the trigger object, satisfying the following selection criteria:

- be a "good" JCCB jet,
- $p_T > 15$ GeV, and
- $|\eta_{det}| < 1.1$.

To calculate the muon misidentification ratio, we require an event to have a non-isolated (*false*) muon and be spatially separated from the trigger jet by $\Delta\mathcal{R} > 1.57$ or $\pi/2$, as to avoid overlap. A *false* muon is defined as follows:

- "Loose" muon ID quality,
- "Loose" track quality,
- nseg > 0,
- etTrkCone > 5 GeV,
- $p_T > 15$ GeV, and
- $|\eta_{det}| < 2$.

To help remove the contribution from real $W \to \ell\nu$ events, we require that the missing energy in the event be less than 10 GeV. We studied all possible combinations of track and isolation quality for a "Medium" quality muon, which we define as the *true* muon. The misidentification ratios for the different definitions of *true* muons are shown in Figs. 4-3 – 4-4 for RunIIa and RunIIb, respectively.

Electron misidentification ratios are calculated in a similar fashion and can be found in more detail in Ref. [68].

Although $W \to \ell\nu$ contamination is highly suppressed by the $\not{E}_T < 10$ GeV requirement, we study the potential systematic uncertainty of the W boson contamination, which can lead to an overestimation in the ratios. We recalculate the misidentification ratios using $\not{E}_T < 20$ GeV. We find the new ratios to be similar to those obtained from the original $\not{E}_T$ threshold within statistical uncertainties. We then estimate the

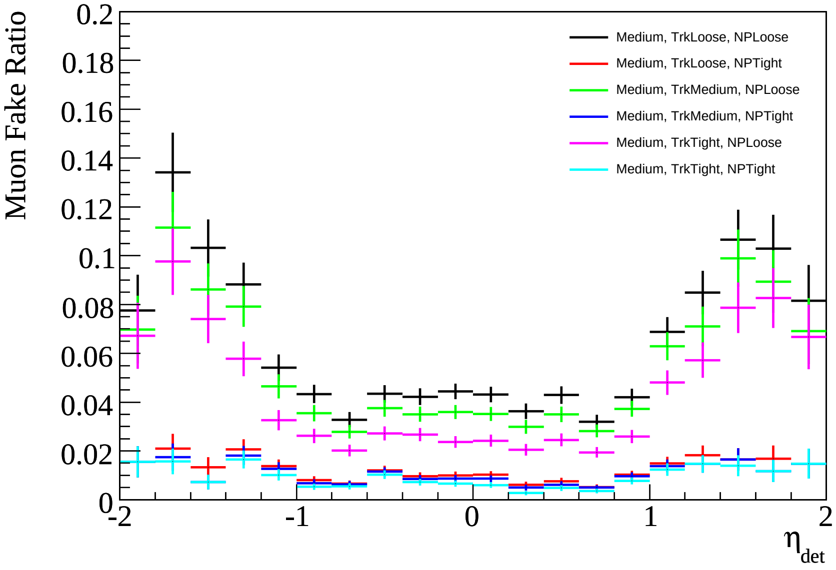

(a)

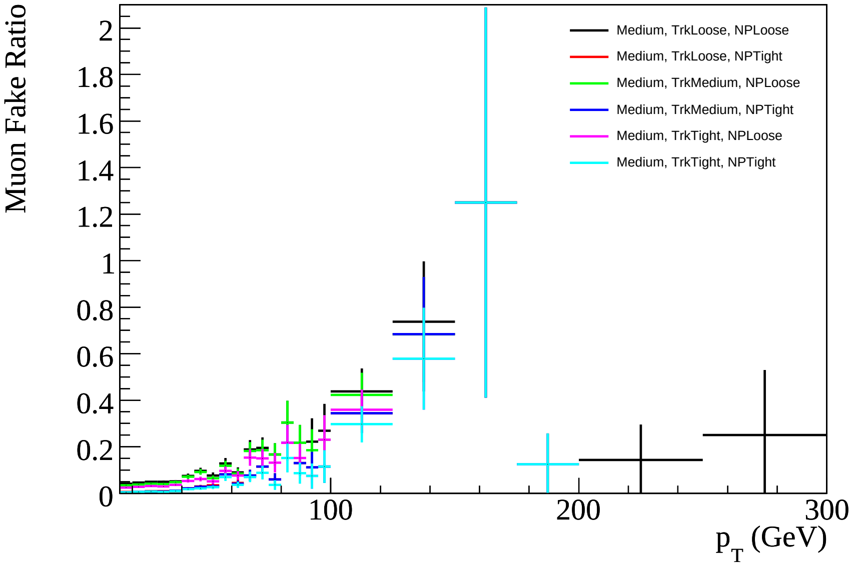

(b)

Figure 4-3: “Medium” quality muon misidentification ratios versus (a) η_{det} and (b) p_T for the different muon track and isolation requirements for the RunIIa dataset. This analysis used “Medium, TrkLoose, NPTight” muons.

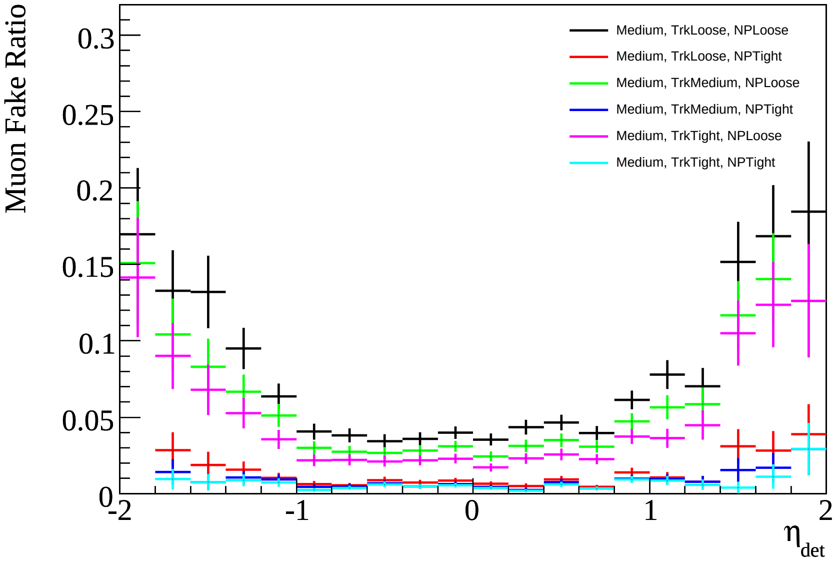

(a)

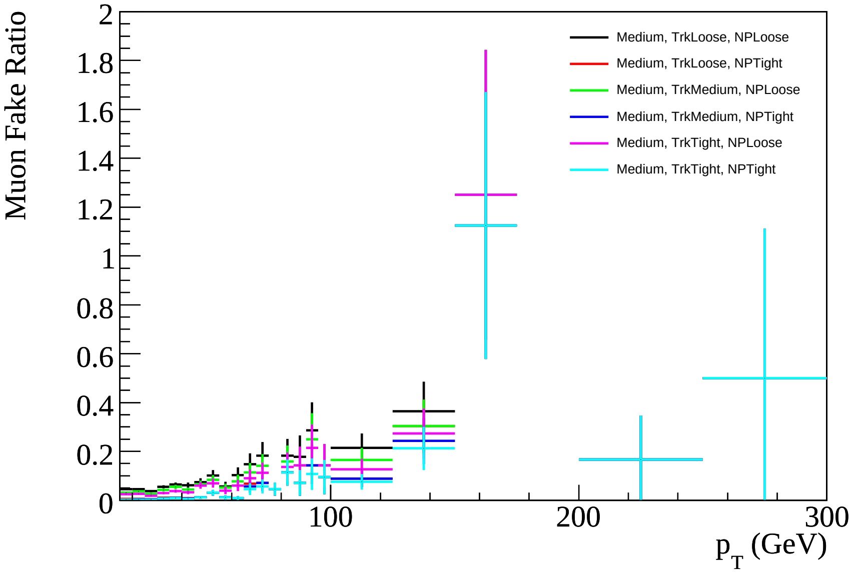

(b)

Figure 4-4: “Medium” quality muon misidentification ratios versus (a) η_{det} and (b) p_T for the different muon track and isolation requirements for the RunIIb dataset. This analysis used “Medium, TrkLoose, NPTight” muons.

$V+$jets background using the new ratios and the difference is assigned as a systematic uncertainty. Similarly, we also vary the $\Delta\mathcal{R}$ requirement by ±0.2 and find the difference is negligible between the original ratios and those obtained with new $\Delta\mathcal{R}$ thresholds. Lastly, the systematic uncertainty due to the statistics in the multi-jet sample, used to measure the misidentification ratios, is included in the uncertainty on the estimated $V+$jets background.

4.3.2 $Z\gamma$ Background

Final states containing $W \to e\nu$ decays can be mimicked by $Z\gamma$ production when a photon is either incorrectly matched to a charged track or it converts and one of the conversion particles is selected as the electron from the W boson decay. A more detailed description of this background estimation can be found in Ref. [68]. We start by verifying that we understand the material description of the detector by observing that the photon-to-electron misidentification rates, determined using data and MC simulation, agree within uncertainty for a controlled sample. We then use $Z\gamma$ PYTHIA MC simulation to determine the misidentification rates, as a function of p_T, in the CC and EC regions of the calorimeter separately. Next, these rates are fit to a first-order polynomial function, $f_{\gamma\to e}(p_T)$, for the selection criteria used to select the W boson electron [68].

To estimate the $Z\gamma$ background, we use the $Z\gamma$ NLO Baur generator [76] to determine the photon's p_T distribution in the CC and EC regions separately. The photon to electron misidentification rate $f_{\gamma\to e}(p_T)$ is then applied, in the corresponding calorimeter regions, using the following equation:

$$N_{Z\gamma} = \sigma_{\ell\bar{\ell}\gamma} \times \mathcal{L}_{data} \times (\mathcal{A} \times \epsilon_{fs}) \times f_{\gamma\to e}(p_T), \tag{4-2}$$

where the next-to-leading-order cross section $\sigma_{\ell\bar{\ell}\gamma}$ – which corresponds to the generator level cuts of $\{p_T^\gamma > 15$ GeV, $M(\ell\bar{\ell}) > 20$ GeV, and $\Delta\mathcal{R}(\ell_{1,2},\gamma) > 0.4\}$ – is 2.90 ± 0.2 pb, $\mathcal{L}_{data}$ is the total integrated luminosity of dataset used, and $\mathcal{A} \times \epsilon_{fs}$ is the acceptance times efficiency of the final state selection criteria measured for the $Z\gamma$ process [68]. Since the Baur generator is only a 4-vector particle generator, we use PMCS [77] to simulate the detector geometry and certified data-obtained muon and electron ID efficiencies, provided by the Object ID groups, to estimate the Z boson leptons' ID and trigger efficiencies.

The largest systematic uncertainty comes from the measured $\not\!\!E_T$ in the event. Since the $Z\gamma$ final state does not have real missing transverse energy, the efficiency of the $\not\!\!E_T$ requirement depends strongly on how well the simulation describes the $\not\!\!E_T$ resolution in the MC and also how well the simulation describes the composition of final state particles in the inclusive $Z\gamma$ production [68]. To estimate this uncertainty, we compare the efficiency of the $\not\!\!E_T$ cut in data to $Z\gamma$ PYTHIA MC simulation using the same selection criteria. The differences obtained in the $\not\!\!E_T$ distributions are then taken as a systematic uncertainty.

4.4 Results

4.4.1 Event Yields

We find 34 WZ candidate events, with an estimated 23.3 ± 1.5 signal and 6.0 ± 0.6 background events, where the uncertainties are statistical only. Observed candidate, signal, and background events for each of the six channels are summarized in Table 4-4.

The dimuon invariant mass (from the two muons that reconstruct the Z boson candidate) in data, with the expected signal and backgrounds overlaid, is shown in Fig. 4-5(a), while Fig. 4-5(b) shows the combination of all channels. We calculate the transverse mass from the W boson using

$$M_T^W = \sqrt{2p_T^\ell \not\!\!E_T(1 - cos(\phi^\ell - \phi^{\not\,E_T}))}, \tag{4-3}$$

where p_T^ℓ and ϕ^ℓ are the transverse momentum and azimuthal angle, respectively, of the W boson electron or muon and $\phi^{\not\,E_T}$ is the azimuthal angle of the missing transverse

Table 4-4: Number of observed candidate events, expected number of signal events, and expected number of background events for each topology with statistical and systematic uncertainties.

Source	$e\nu e\bar{e}$	$\mu\nu e\bar{e}$	$e\nu\mu\bar{\mu}$	$\mu\nu\mu\bar{\mu}$	$e\nu e\bar{e}_{ICR}$	$\mu\nu e\bar{e}_{ICR}$
ZZ	$0.29 \pm 0.04 \pm 0.05$	$0.99 \pm 0.07 \pm 0.17$	$0.40 \pm 0.04 \pm 0.06$	$1.26 \pm 0.07 \pm 0.22$	$0.10 \pm 0.02 \pm 0.02$	$0.49 \pm 0.05 \pm 0.08$
$V + \text{jets}$	$0.41 \pm 0.11 \pm 0.08$	$0.21 \pm 0.05 \pm 0.06$	$0.03 \pm 0.01 \pm 0.01$	$0.17 \pm 0.04 \pm 0.03$	$0.22 \pm 0.07 \pm 0.08$	$0.35 \pm 0.16 \pm 0.16$
$Z\gamma$	$0.18 \pm 0.01 \pm 0.07$	< 0.001	$0.66 \pm 0.02 \pm 0.34$	< 0.001	$0.10 \pm 0.01 \pm 0.03$	< 0.001
$t\bar{t}$	$0.03 \pm 0.01 \pm 0.01$	$0.02 \pm 0.01 \pm 0.003$	$0.04 \pm 0.01 \pm 0.01$	$0.03 \pm 0.01 \pm 0.01$	$0.001 \pm 0.001 \pm < 0.001$	$0.03 \pm 0.01 \pm 0.004$
Total background	$0.91 \pm 0.12 \pm 0.12$	$1.23 \pm 0.09 \pm 0.18$	$1.13 \pm 0.05 \pm 0.35$	$1.46 \pm 0.08 \pm 0.23$	$0.42 \pm 0.08 \pm 0.09$	$0.88 \pm 0.17 \pm 0.18$
WZ signal	$4.4 \pm 0.1 \pm 0.8$	$5.0 \pm 0.1 \pm 0.7$	$4.7 \pm 0.1 \pm 0.6$	$5.8 \pm 0.1 \pm 0.8$	$1.5 \pm 0.1 \pm 0.2$	$1.9 \pm 0.1 \pm 0.2$
Total expected	$5.3 \pm 0.2 \pm 0.8$	$6.2 \pm 0.1 \pm 0.7$	$4.7 \pm 0.1 \pm 0.7$	$7.3 \pm 0.1 \pm 0.8$	$1.9 \pm 0.1 \pm 0.2$	$2.8 \pm 0.2 \pm 0.3$
Observed	7	9	9	5	1	3

momentum. The transverse mass in data, with the expected signal and backgrounds overlaid, are shown in Fig. 4-6 for the $X\nu\mu\bar{\mu}$ channels and all channels combined.

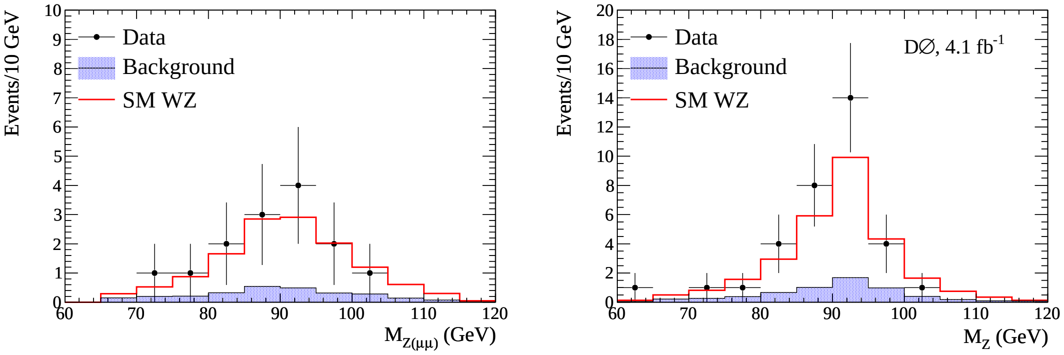

(a) (b)

Figure 4-5: Invariant mass of selected Z boson candidates in (a) $X\nu\mu\bar{\mu}$ channels and (b) of all channels combined. Candidate events from data (black) are shown, along with WZ signal (red histogram) and total background (blue histogram) overlaid.

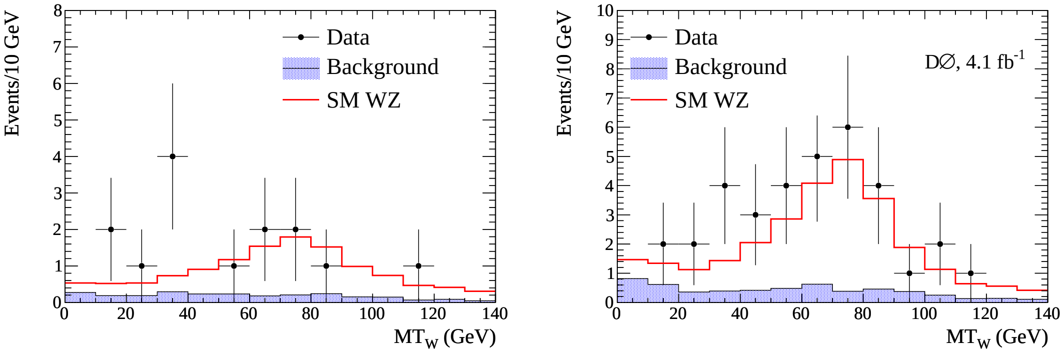

(a) (b)

Figure 4-6: Transverse mass of selected W candidates in (a) $X\nu\mu\bar{\mu}$ channels and (b) all channels combined. Candidate events from data (black) are shown, along with WZ signal (red histogram) and total background (blue histogram) overlaid.

4.4.2 Systematic Uncertainties

Several sources of uncertainty are considered in this analysis. One of the most prevalent is from the lepton ID efficiencies, or how well the detector can identify the particle objects. Determined by the Object ID groups, we assign an uncertainty of 5%, 4%, and 6% for each electron [78], muon [79], and ICR-electron [74], respectively. A systematic uncertainty of 5% is assigned due to the PDF choice and another 5% uncertainty due to the modeling of the WZ system. In addition, we assign a 5% and 10% uncertainty on the estimated $t\bar{t}$ [80, 81] and ZZ [82] backgrounds, respectively, due to the uncertainty in their theoretical cross sections. For the V + jets background, the major sources of systematic uncertainty come from the $\not\!\!E_T$ requirement and the statistics used in the measurement of the lepton misidentification ratios. Those effects are estimated separately for each final state (discussed in Sec. 4.3.1) and are found to be between 20 – 30%. The $\not\!\!E_T$ systematic uncertainty on the $Z\gamma$ background (refer to Sec. 4.3.2) is estimated to be 40%, 58%, and 30% for $e\nu e\bar{e}$, $e\nu\mu\bar{\mu}$, and $e\nu e\bar{e}_{ICR}$ channels, respectively. Finally, a systematic uncertainty due to the integrated luminosity is assigned at 6.1%.

A breakdown of the systematic errors is shown in Table 4-5 for each of the final state channels. Listed are the central values of each signal and background estimate and their calculated statistical uncertainty (stat), along with the PDF, lepton ID (LepID), and theoretical cross section uncertainties (XSec) from the MC samples. We include the systematic errors from data due to MET and the uncertainty on the misidentification ratio measurement's statistical sample size (MissID.Ratio). The uncertainty from luminosity is also included.

4.4.3 Cross Section Measurement

The individual final state cross sections of WZ production times $BR(WZ \to \ell'\nu\ell\bar{\ell})$ can be determined by the following formula

$$\sigma_{WZ} \times BR(WZ \to \ell'\nu\ell\bar{\ell}) = \frac{n_{obs} - n_{bkg}}{(\mathcal{A} \times \epsilon) \times \mathcal{L}}, \tag{4-4}$$

where n_{obs} (n_{bkg}) is the number of observed candidate (estimated background) events and $\mathcal{A}$, ϵ, and $\mathcal{L}$ are the acceptance, efficiency of the selection criteria, and the total

Table 4-5: Detailed breakdown of the sources of systematic uncertainty and their individual values.

Channel	Central ± Stat ± Syst
$WZ \pm (stat) \pm (PDF) \pm (LepID) \pm (Lumi)$	
$e\nu e\bar{e}$	$4.40 \pm 0.10 \pm 0.22 \pm 0.66 \pm 0.27$
$\mu\nu e\bar{e}$	$5.00 \pm 0.10 \pm 0.25 \pm 0.55 \pm 0.31$
$e\nu\mu\bar{\mu}$	$4.70 \pm 0.10 \pm 0.24 \pm 0.42 \pm 0.29$
$\mu\nu\mu\bar{\mu}$	$5.80 \pm 0.10 \pm 0.29 \pm 0.70 \pm 0.35$
$e\nu e\bar{e}_{ICR}$	$1.50 \pm 0.10 \pm 0.08 \pm 0.18 \pm 0.09$
$\mu\nu e\bar{e}_{ICR}$	$1.90 \pm 0.17 \pm 0.10 \pm 0.17 \pm 0.12$
$ZZ \pm (stat) \pm (PDF) \pm (LepID) \pm (XSec) \pm (Lumi)$	
$e\nu e\bar{e}$	$0.29 \pm 0.04 \pm 0.01 \pm 0.04 \pm 0.03 \pm 0.02$
$\mu\nu e\bar{e}$	$0.99 \pm 0.07 \pm 0.05 \pm 0.11 \pm 0.10 \pm 0.06$
$e\nu\mu\bar{\mu}$	$0.40 \pm 0.04 \pm 0.02 \pm 0.04 \pm 0.04 \pm 0.02$
$\mu\nu\mu\bar{\mu}$	$1.26 \pm 0.07 \pm 0.06 \pm 0.15 \pm 0.13 \pm 0.08$
$e\nu e\bar{e}_{ICR}$	$0.10 \pm 0.02 \pm 0.01 \pm 0.01 \pm 0.01 \pm 0.01$
$\mu\nu e\bar{e}_{ICR}$	$0.49 \pm 0.05 \pm 0.02 \pm 0.04 \pm 0.05 \pm 0.03$
$V + \text{jets} \pm (stat) \pm (MET) \pm (MissID.Ratio)$	
$e\nu e\bar{e}$	$0.41 \pm 0.11 \pm 0.07 \pm 0.03$
$\mu\nu e\bar{e}$	$0.21 \pm 0.05 \pm 0.05 \pm 0.03$
$e\nu\mu\bar{\mu}$	$0.03 \pm 0.01 \pm 0.01 \pm 0.01$
$\mu\nu\mu\bar{\mu}$	$0.17 \pm 0.04 \pm 0.03 \pm 0.01$
$e\nu e\bar{e}_{ICR}$	$0.22 \pm 0.07 \pm 0.03 \pm 0.07$
$\mu\nu e\bar{e}_{ICR}$	$0.35 \pm 0.16 \pm 0.01 \pm 0.16$
$Z\gamma \pm (stat) \pm (MET)$	
$e\nu e\bar{e}$	$0.18 \pm 0.01 \pm 0.07$
$e\nu\mu\bar{\mu}$	$0.66 \pm 0.02 \pm 0.34$
$e\nu e\bar{e}_{ICR}$	$0.10 \pm 0.01 \pm 0.03$
$t\bar{t} \pm (stat) \pm (PDF) \pm (LepID) \pm (XSec) \pm (Lumi)$	
$e\nu e\bar{e}$	$0.03 \pm 0.01 \pm 0.002 \pm 0.005 \pm 0.002 \pm 0.002$
$\mu\nu e\bar{e}$	$0.02 \pm 0.01 \pm 0.001 \pm 0.002 \pm 0.001 \pm 0.001$
$e\nu\mu\bar{\mu}$	$0.04 \pm 0.01 \pm 0.002 \pm 0.004 \pm 0.002 \pm 0.002$
$\mu\nu\mu\bar{\mu}$	$0.03 \pm 0.01 \pm 0.002 \pm 0.004 \pm 0.002 \pm 0.002$
$e\nu e\bar{e}_{ICR}$	$0.001 \pm 0.001 \pm < 0.001 \pm < 0.001 \pm < 0.001 \pm < 0.001$
$\mu\nu e\bar{e}_{ICR}$	$0.03 \pm 0.01 \pm 0.002 \pm 0.003 \pm 0.002 \pm 0.002$

integrated luminosity, respectively. However, n_{obs} in each final state is small enough that the usual approximation of Poisson statistics to Gaussian statistics does not apply. Therefore, to calculate the uncertainties on the individual cross sections we use a log-likelihood method with Poisson statistics, discussed in detail in Ref. [68]. The individual final state cross section values, with asymmetric Poisson uncertainties, are summarized in Table 4-6.

Table 4-6: WZ production cross section measurements with asymmetric statistical + systematic and luminosity uncertainties.

Channel	σ_{WZ} Cross Section (pb)
$e\nu e\bar{e}$	$4.45^{+2.43}_{-1.77}(stat + syst) \pm 0.34(lumi)$
$\mu\nu e\bar{e}$	$5.06^{+2.35}_{-1.81}(stat + syst) \pm 0.32(lumi)$
$e\nu\mu\bar{\mu}$	$5.48^{+2.48}_{-1.91}(stat + syst) \pm 0.36(lumi)$
$\mu\nu\mu\bar{\mu}$	$1.95^{+1.51}_{-1.08}(stat + syst) \pm 0.14(lumi)$
$e\nu e\bar{e}_{ICR}$	$1.31^{+3.20}_{-1.31}(stat + syst) \pm 0.09(lumi)$
$\mu\nu e\bar{e}_{ICR}$	$3.80^{+3.87}_{-2.55}(stat + syst) \pm 0.29(lumi)$

The measured value of the combined cross section is taken from the minimum of the negative log-likelihood, shown in Fig. 4-7. The uncertainty on this value is estimated by moving up 0.5 units in negative log-likelihood, corresponding to ±1 standard deviation with Gaussian errors, yielding an asymmetric error. The resulting combined cross section is $3.90^{+1.01}_{-0.85}(stat + syst) \pm 0.31(lumi)$ pb. We compare this to the NLO SM prediction of $3.68 \pm 0.22(scale) \pm 0.12(PDF)$ pb [83] and find it to be in excellent agreement, indicating the lack of evidence for any new physics.

Figure 4-8 shows a good example of a clean tri-lepton $\mu\nu\mu\bar{\mu}$ candidate event. The XY view gives a good overview of the tracking system and the energy deposited in the calorimetry. The individual fiber hits can be seen, along with all possible reconstructed tracks, giving an appreciation of the track finding algorithms. The lego view shows the energy deposited in the calorimeter as a function of η and ϕ, also noted are the triggers that fired in this event. In both event displays, the muons shown have overlaid the p_T of tracks as determined from the central tracker. The muons are shown in green and the missing transverse energy in yellow.

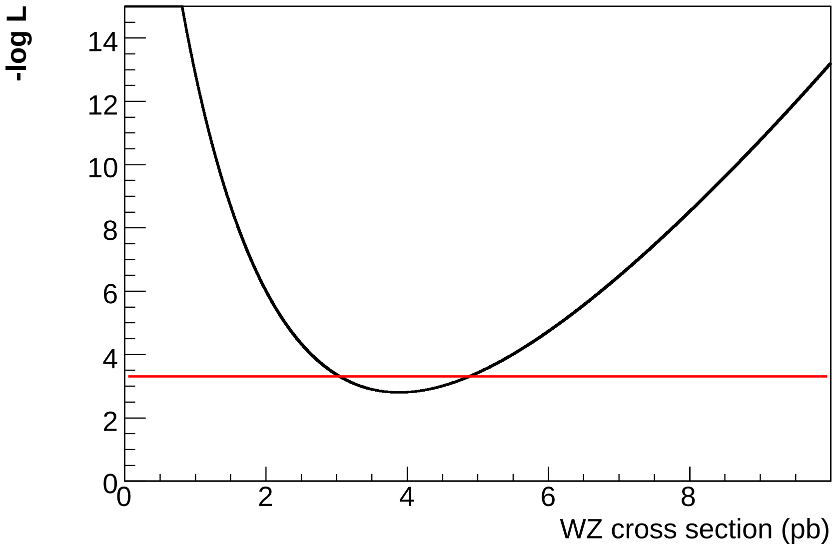

Figure 4-7: Negative log likelihood versus the value of the combined cross section. Intersections of the red line and the likelihood curve indicate a one sigma uncertainty interval.

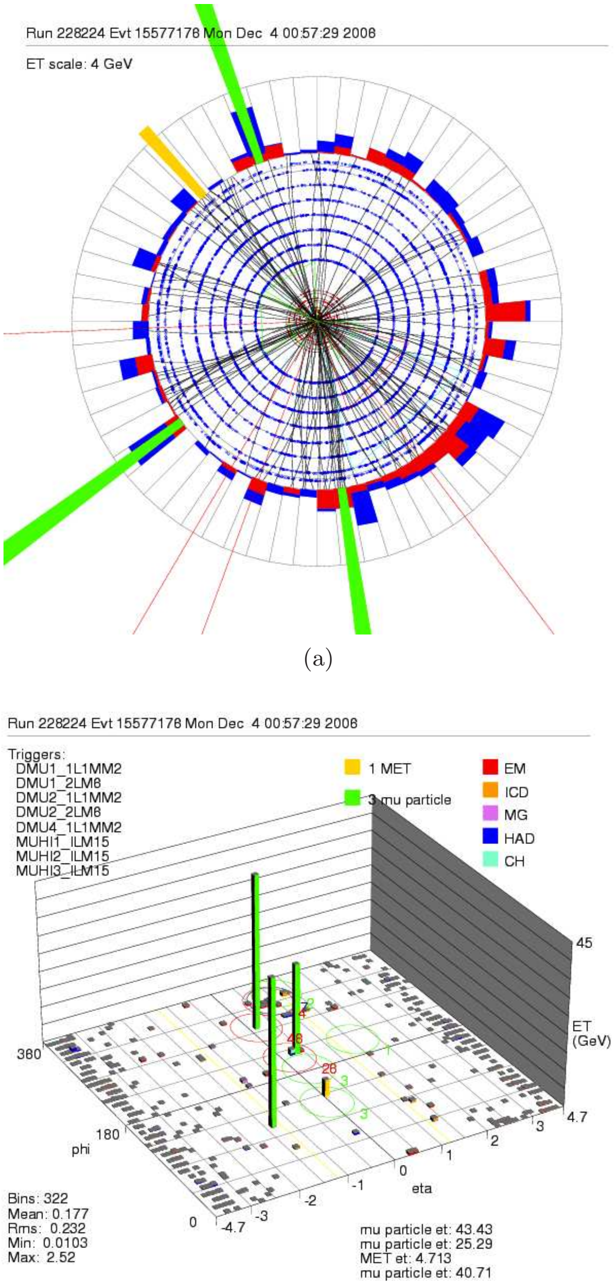

(a)

(b)

Figure 4-8: Event display for a $\mu\nu\mu\bar{\mu}$ candidate event with run number 228224 and event number 15577176 recorded December 4, 2008. (a) The XY view gives a good overview of tracking system and the energy deposited in the calorimetry, while the (b) lego view focuses on the energy deposited in the calorimeter. In both event displays, the muon (green) track p_Ts, from the central tracker, are overlaid. The missing energy is represented in yellow.

5 Search for Flavor Changing Neutral Current t $\rightarrow$ Zq Decays

With an estimated branching ratio of $\mathcal{O}(10^{-14})$ for $t \rightarrow Zc$ (and $\mathcal{O}(10^{-17})$ for $t \rightarrow Zu$), the flavor changing neutral current (FCNC) top quark decay is extremely difficult to measure since it is highly suppressed and only possible through radiative corrections in the SM [84, 85]. There are some BSM models, such as supersymmetric extensions of the SM with or without R-parity violation, or quark compositeness, that predict branching fractions as high as $\mathcal{O}(10^{-4})$ [85, 86, 87]. The observation of the FCNC decay $t \rightarrow Zq$ would therefore provide evidence of contributions from BSM physics.

As mentioned in the Introduction, we assume that the $t \rightarrow Zq$ decay (and its charge conjugate $\bar{t} \rightarrow Z\bar{q}$, hereafter implied, likewise for $t \rightarrow Wb$) is generated by adding an additional FCNC term to the SM Lagrangian. As we are only interested in Z boson coupling, we set the γ coupling parameters in Eq. 1-18 to zero and ignore the κ_Z and $\tilde{\kappa}_Z$ parameters, leaving

$$\mathcal{L}_{\mathrm{FCNC}} = \frac{g}{2\cos\theta_W}\, \bar{t}\,\gamma_\mu (v_{tqZ} - a_{tqZ}\gamma_5)\; q\, Z^\mu \;+ h.c., \tag{5-1}$$

where q and t are fields for the up or charmed quarks and top quarks, respectively, and Z is the Z boson field. Here we introduce the vector, v_{tqZ}, and axial-vector, a_{tqZ}, couplings as defined in Ref. [31]. We find in Refs. [88, 89] that the NLO effects due to perturbative QCD corrections are negligible when extracting the branching ratio limits to the LO on Eq. 5-1.

This is the first search for FCNC in $t\bar{t}$ decays to tri-lepton plus missing energy final states. Despite the low statistics, this channel provides an almost background-free signature. The CDF Collaboration has set an upper limit of $BR(t \rightarrow Zq) < 3.7\%$ (5.0%) observed (expected) at the 95% C.L. using 1.9 fb^{-1} of integrated luminosity, assuming a top quark mass of $m_t = 175$ GeV and a cross section of $\sigma_{t\bar{t}} = 8.8 \pm 1.1$ pb [90].

They require a final state of two isolated leptons plus four or more jets, where the Z boson decays leptonically while the W boson from $t \to Wb$ decays hadronically. While the di-lepton signature allows for more events, it does suffer from an increased background as compared to the tri-lepton final states. The most recent results coming out of the LHC are from the ATLAS Collaboration. Using a final state of three isolated leptons, missing transverse momentum, and two jets, they set a branching fraction of $BR(t \to Zq) < 1.1\%$ observed with a less than 1.3% expected limit at 95% C.L. using 0.7 fb^{-1} [91].

As with the WZ analysis, we look for final states where the W and Z bosons decay leptonically, as shown in Fig. 5-1. The u, c, and b quarks then hadronize, producing a final state with three charged highly energetic leptons, $\not\!\!E_T$, and jets.

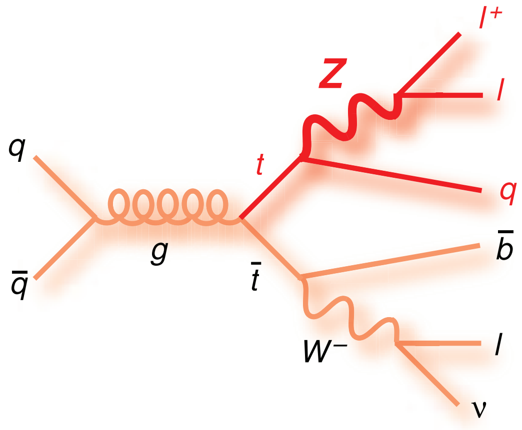

Figure 5-1: Leading-order diagram for flavor changing $t\bar{t} \to WbZq$ production, where we consider the q quark to be either a u or a c quark and the W and Z bosons to decay leptonically.

This analysis is an extension of the 4.1 fb^{-1} WZ cross section measurement, described in Chapter 4 and in detail in Ref. [68]. A couple of inconsistencies in the $X\nu e\bar{e}$ channels have been addressed in-between the two analyses, without the recalculation of the WZ cross section. In the WZ analysis, an incorrect run range was used, resulting in two extra data events that should not have passed the run number cut for the integrated luminosity used. Also, an event was missed when skimming jobs that had failed were not recovered. One of the largest changes comes from not correcting the z_{dca} of a charged track with the primary vertex. In MC simulation the PV is always set to the (x,y) coordinates of (0,0), but this is not true of data events since the beam is not centered perfectly in the detector. While this does not effect MC events (since the z_{dca} of a track and the PV are almost always close) it does effect data events, leading to two events that should have been collected. Lastly, a newer version of the MET recomputation is used which applied the correct electron energy scale factors in the MET calculations, while this did not in practice affect data, it did have minor changes to the MC sample yields. These corrections result in an extra event passing the kinematic criteria.

Section 5.1 describes the new FCNC signal MC samples used in this analysis, followed by the object identification criteria and event selection in Section 5.2. Section 5.3 describes the estimation of the data-driven backgrounds and how the methods have changed with the new signal, while the results are presented in Section 5.4.

5.1 Data and Monte Carlo Samples

We use the same datasets as described in Chapter 4.1, using a total integrated luminosity of 4.1 fb^{-1}.

The new signal becomes $p\bar{p} \to t\bar{t} \to WbZq$, while WZ production is now the major background source and is estimated using the same MC samples as in the WZ analysis. PYTHIA MC is used to simulate the new FCNC signal. Samples are generated for $p\bar{p} \to t\bar{t} \to WbZq$ and $p\bar{p} \to t\bar{t} \to ZqZq$ production and events are filtered at the parton level to derive the branching ratios for $BR(t \to Wb)$ and $BR(t \to Zq)$. The total selection efficiency, calculated as a function of $B = \Gamma(t \to Zq)/\Gamma_{total}$, where Γ_{total} contains $t \to Zq$ and $t \to Wb$ decays only, can be written as:

$$\epsilon_{t\bar{t}} = (1-B)^2 \cdot \epsilon_{t\bar{t}\to WbWb} + 2B(1-B) \cdot \epsilon_{t\bar{t}\to WbZq} + B^2 \cdot \epsilon_{t\bar{t}\to ZqZq}, \tag{5-2}$$

yielding the number of $t\bar{t}$ events as a function of B. The efficiency, $\epsilon_{t\bar{t}\to WbWb}$, is the efficiency for the SM $t\bar{t}$ background production and is found using MC, along with the efficiencies $\epsilon_{t\bar{t}\to WbZq}$ and $\epsilon_{t\bar{t}\to ZqZq}$ that include the FCNC top quark decays.

The naive assumption that simply replacing the $t \to Wb$ process by $t \to Zq$ in PYTHIA turns out to be incorrect, as it does not contain the proper helicity structure. Therefore we need to reweight the samples to include the correct helicity structure – FCNC vector couplings, v_{tqZ}, and axial-vector couplings, a_{tqZ}, as defined in Eq. 5-1 [31] and discussed in more detail in Appendix 1 of Ref. [92]. The reweighting is done using the COMPHEP generator [93], where we assume the couplings for the SM neutral currents, i.e. $v_{tqZ} = 0.5 - (4/3)\sin^2\theta_W$ and $a_{tqZ} = 0.5$. To be able to claim a result independent of the (v_{tqZ}, a_{tqZ}) parameters, we also consider the cases where ($v_{tqZ} = a_{tqZ} = 1/\sqrt{2}$), ($v_{tqZ} = 1$, $a_{tqZ} = 0$), and ($v_{tqZ} = 0$, $a_{tqZ} = 1$). The differences in results are taken as systematic uncertainties. This analysis does not separate the $q = u$ quarks from the $q = c$ quarks, but we do find that when we did separate the two quark final states, that the selection efficiencies and kinematic distributions were consistent and did not depend on the different helicity structure of the tuZ couplings versus the tcZ couplings [92]. The minor differences were taken as systematic uncertainties. Therefore, the results obtained are independent of the helicity structure of the FCNC signal and of the quark flavor, and any differences are assigned as systematic uncertainties.

The FCNC MC samples are generated using the CTEQ6L1 PDF set [69] at a top quark mass of $m_t = 172.5$ GeV. The MC samples used for RunIIa and RunIIb, along with the NLO cross section multiplied by branching fractions and the number of events before data quality cuts are applied, are listed in Table 5-1. To increase statistics for the ZZ background, we added additional MC samples over what was used in the WZ analysis.

Table 5-1: MC samples used in the analysis. The cross section times branching ratios (if known) and the number of events before data quality cuts are applied are listed. In the FCNC signal MC samples, X represents the jets in the event.

Process	$\sigma_{NLO} \times BR$	Events before DQ	
	(pb)	RunIIa	RunIIb
$t\bar{t} \to WbZu \to 3\ell 3\nu + X, \ell = e, \mu, \tau$	–	350811	534677
$t\bar{t} \to ZuZu \to 4\ell + X$	–	67980	82774
$t\bar{t} \to WbZc \to 3\ell 3\nu + X$	–	368637	647869
$t\bar{t} \to ZcZc \to 4\ell + X$	–	71506	100062
$t\bar{t} \to WbZu \to 3\ell 3\nu + X$, $m_t = 175$ GeV	–	–	252887
$t\bar{t} \to ZuZu \to 4\ell + X$, $m_t = 175$ GeV	–	–	48447
$t\bar{t} \to WbZc \to 3\ell 3\nu + X$, $m_t = 175$ GeV	–	–	207297
$t\bar{t} \to ZcZc \to 4\ell + X$, $m_t = 175$ GeV	–	–	40398
$WZ \to 3\ell 3\nu, \ell = e, \mu, \tau$	0.1064	188412	363320
$ZZ \to$ inclusive	1.334	590647	1440860
$t\bar{t}$ $+Xlp \to 2\ell 2\nu 2b + Xlp, X = 0, 1, 2$	0.782	3180331	1201819

5.2 Object and Event Selection

We use the same physics objects described in Section 4.2. These objects include electrons, electrons within the ICR, muons, and $\not{E}_T$. To select the q or b quarks, we now include jets in our final state selection. Candidate events are again categorized into six distinct final state channels, each further divided up into n_{jet} jet bins, with $n_{\text{jet}} = 0$, 1, ≥ 2; $\mu\nu\mu\bar{\mu} + n_{\text{jet}}$, $e\nu\mu\bar{\mu} + n_{\text{jet}}$, $\mu\nu e\bar{e} + n_{\text{jet}}$, $e\nu e\bar{e} + n_{\text{jet}}$, and $\mu\nu e\bar{e}_{ICR} + n_{\text{jet}}$ and $\mu\nu e\bar{e}_{ICR} + n_{\text{jet}}$, where one leg of the Z boson is reconstructed in the ICR.

We use the same selection criteria outlined in Chapter 4.2, without reoptimizing to $s/\sqrt{s+b}$. For the signal and backgrounds we now measure the yields in three exclusive jet bins. We require that the jets

- meet the “good” JCCB jet ID requirement for RunIIa, or
- meet the “vertex confirmed” JCCB jet ID requirement for RunIIb,
- transverse energy $E_T > 20$ GeV for each jet, and
- that the jets be reconstructed within a $|\eta_{det}| < 2.5$.

We further require that the $\Delta\mathcal{R}$ separation between the jets and electrons, including those reconstructed in the ICR, be greater than 0.5. While there is no explicit cut on the muon and jet separation, the muon isolation requirement used rejects most muons with $\Delta\mathcal{R} < 0.4$ of the jet.

5.2.1 Acceptance × Efficiency

We determine the Acceptance × efficiency ($\mathcal{A} \times \epsilon$) by starting with the FCNC signal MC before it passes through data quality selection and before it is reweighted to the correct helicity structure. It is here that we separate out the two signals we are interested in; $t\bar{t} \rightarrow WbZq$ and $t\bar{t} \rightarrow ZqZq$. We create two samples of MC, one with only the $t\bar{t} \rightarrow WbZq$ contribution by removing $t\bar{t} \rightarrow ZqZq$ and $t\bar{t} \rightarrow WbWb$ events and another with only $t\bar{t} \rightarrow ZqZq$ by removing the $t\bar{t} \rightarrow WbZq$ and $t\bar{t} \rightarrow WbWb$ events. We do not consider $t\bar{t} \rightarrow WbWb$ events that are generated in the FCNC MC sample. The $\mathcal{A} \times \epsilon$ is then determined by dividing the number of events that pass the kinematic criteria with all efficiencies applied (ID, trigger, etc.) by the total number of events generated before data quality is applied.

Tables 5-2 and 5-3 list the $\mathcal{A} \times \epsilon$ in each final state for each jet multiplicity for the FCNC $t\bar{t} \rightarrow WbZq$ and FCNC $t\bar{t} \rightarrow ZqZq$ signals, respectively.

5.3 Data-Driven Background Estimation

The approach to estimating the data-driven backgrounds changes slightly now that we include jets in the event selection. The new methods are described here.

5.3.1 Vector Boson + Jets Background

We follow the same basic method as described in Sec. 4.3.1 to determine the $V +$ jets background. We first determine the misidentification ratios of both electrons and muons in eahc of the three jet multiplicity bins, excluding the highest-p_T jet, as it is assumed to be the trigger object. We again use the CSG QCD skims, discussed in

Table 5-2: Acceptance × efficiencies for $t\bar{t} \to WbZq$ for each channel in the three jet multiplicity bins, also including the jet inclusive case, with statistical and systematic uncertainties.

Channel	Acceptance × efficiency for $t\bar{t} \to WbZq$ (in %)	
	Inclusive Jets	0 Jets
$e\nu e\bar{e}$	$1.36 \pm 0.01 \pm 0.22$	$(6.39 \pm 0.30 \pm 1.01) \times 10^{-2}$
$\mu\nu e\bar{e}$	$1.46 \pm 0.02 \pm 0.17$	$(5.72 \pm 0.28 \pm 0.68) \times 10^{-2}$
$e\nu\mu\bar{\mu}$	$1.23 \pm 0.01 \pm 0.13$	$(3.45 \pm 0.22 \pm 0.37) \times 10^{-2}$
$\mu\nu\mu\bar{\mu}$	$1.48 \pm 0.01 \pm 0.19$	$(3.28 \pm 0.23 \pm 0.43) \times 10^{-2}$
$e\nu e\bar{e}_{ICR}$	$0.30 \pm 0.01 \pm 0.04$	$(1.25 \pm 0.12 \pm 0.16) \times 10^{-2}$
$\mu\nu e\bar{e}_{ICR}$	$0.35 \pm 0.01 \pm 0.04$	$(1.06 \pm 0.12 \pm 0.11) \times 10^{-2}$
	1 Jet	$\geq$ 2 Jets
$e\nu e\bar{e}$	$(4.75 \pm 0.08 \pm 0.75) \times 10^{-1}$	$(8.17 \pm 0.01 \pm 0.13) \times 10^{-1}$
$\mu\nu e\bar{e}$	$(4.74 \pm 0.08 \pm 0.56) \times 10^{-1}$	$(9.30 \pm 0.01 \pm 0.11) \times 10^{-1}$
$e\nu\mu\bar{\mu}$	$(3.51 \pm 0.07 \pm 0.38) \times 10^{-1}$	$(8.41 \pm 0.01 \pm 0.09) \times 10^{-1}$
$\mu\nu\mu\bar{\mu}$	$(3.91 \pm 0.07 \pm 0.51) \times 10^{-1}$	$(10.6 \pm 0.01 \pm 0.14) \times 10^{-1}$
$e\nu e\bar{e}_{ICR}$	$(0.98 \pm 0.04 \pm 0.13) \times 10^{-1}$	$(1.86 \pm 0.01 \pm 0.02) \times 10^{-1}$
$\mu\nu e\bar{e}_{ICR}$	$(1.06 \pm 0.04 \pm 0.12) \times 10^{-1}$	$(2.35 \pm 0.01 \pm 0.02) \times 10^{-1}$

Table 5-3: Acceptance × efficiencies for $t\bar{t} \to ZqZq$ for each channel in the three jet multiplicity bins, also including the jet inclusive case, with statistical and systematic uncertainties.

Channel	Acceptance × efficiency for $t\bar{t} \to ZqZq$ (in %)	
	Inclusive Jets	0 Jets
$e\nu e\bar{e}$	$1.02 \pm 0.03 \pm 0.16$	$(4.26 \pm 0.56 \pm 0.67) \times 10^{-2}$
$\mu\nu e\bar{e}$	$2.96 \pm 0.05 \pm 0.35$	$(8.88 \pm 0.88 \pm 1.06) \times 10^{-2}$
$e\nu\mu\bar{\mu}$	$1.41 \pm 0.03 \pm 0.15$	$(3.71 \pm 0.55 \pm 0.40) \times 10^{-2}$
$\mu\nu\mu\bar{\mu}$	$2.75 \pm 0.05 \pm 0.36$	$(3.93 \pm 0.52 \pm 0.51) \times 10^{-2}$
$e\nu e\bar{e}_{ICR}$	$0.21 \pm 0.01 \pm 0.03$	$(0.44 \pm 0.15 \pm 0.06) \times 10^{-2}$
$\mu\nu e\bar{e}_{ICR}$	$0.75 \pm 0.02 \pm 0.08$	$(2.40 \pm 0.50 \pm 0.24) \times 10^{-2}$
	1 Jet	$\geq$ 2 Jets
$e\nu e\bar{e}$	$(3.51 \pm 0.18 \pm 0.56) \times 10^{-1}$	$(6.24 \pm 0.24 \pm 0.99) \times 10^{-1}$
$\mu\nu e\bar{e}$	$(8.83 \pm 0.29 \pm 1.05) \times 10^{-1}$	$(19.8 \pm 0.44 \pm 2.36) \times 10^{-1}$
$e\nu\mu\bar{\mu}$	$(3.79 \pm 0.18 \pm 0.41) \times 10^{-1}$	$(9.95 \pm 0.29 \pm 1.06) \times 10^{-1}$
$\mu\nu\mu\bar{\mu}$	$(6.49 \pm 0.25 \pm 0.84) \times 10^{-1}$	$(20.6 \pm 0.43 \pm 2.68) \times 10^{-1}$
$e\nu e\bar{e}_{ICR}$	$(0.62 \pm 0.08 \pm 0.08) \times 10^{-1}$	$(1.40 \pm 0.11 \pm 0.18) \times 10^{-1}$
$\mu\nu e\bar{e}_{ICR}$	$(2.04 \pm 0.13 \pm 0.21) \times 10^{-1}$	$(5.17 \pm 0.20 \pm 0.52) \times 10^{-1}$

App. B. Once the highest-p_T jet has been identified, we search in a cone of $\Delta\mathcal{R} > \pi/2$ for non-isolated leptons (*false* leptons) and leptons that pass the standard object ID criteria (*true* leptons). The definitions for *true* and *false* leptons can be found in Sec. 4.3.1. We search for any jets with $E_T > 20$ GeV at a $\Delta\mathcal{R} > \pi/2$, which determines which jet bin the ratio value falls into. We also require that the non-isolated leptons be separated from the jets by a $\Delta\mathcal{R} > 0.5$ to ensure that the *false* lepton did not come from the jet. Figures 5-2 and 5-3 shows the muon misidentification ratios for the inclusive jet bin, along with the three exclusive jet bins, as a function of η_{det} and p_T for RunIIa and RunIIb, respectively. Again, p_T distributions are used as a consistency check.

Similarly, the electron misidentification ratios can be found in Ref. [92].

We then create the normalization sample from the 2MUhighpt skim that consists of two *true* leptons and only one *false* lepton, where the two *true* leptons are used to reconstruct the Z boson candidate. We again require that the *false* lepton be isolated from the jets in the event by $\Delta\mathcal{R} > 0.5$, to avoid jet double counting. A *false* lepton is not rejected if it is found near a jet but the jet is not included in determining which jet bin the event falls into. As in the WZ analysis, the η_{det} distribution of the normalized samples' *false* leptons are then multiplied by the appropriate misidentification ratio for each bin in η_{det}. The $V+$jets background is estimated by the integral of this product distribution.

5.3.2 $Z\gamma$ Background

The $Z\gamma$ NLO Baur MC simulation used in the WZ analysis does not include jet hadronization. To fold that information in, we also include PYTHIA MC to estimate the $Z\gamma$ background jet multiplicities and $\not\!\!E_T$ distributions. Using the PYTHIA MC, we estimate the background contribution using the same selection criteria used in the signal and other MC sample backgrounds. We determine the number of events in each jet multiplicity bin in the PYTHIA MC and then normalize the overall event yield to the value determined using the Baur MC in the WZ analysis.

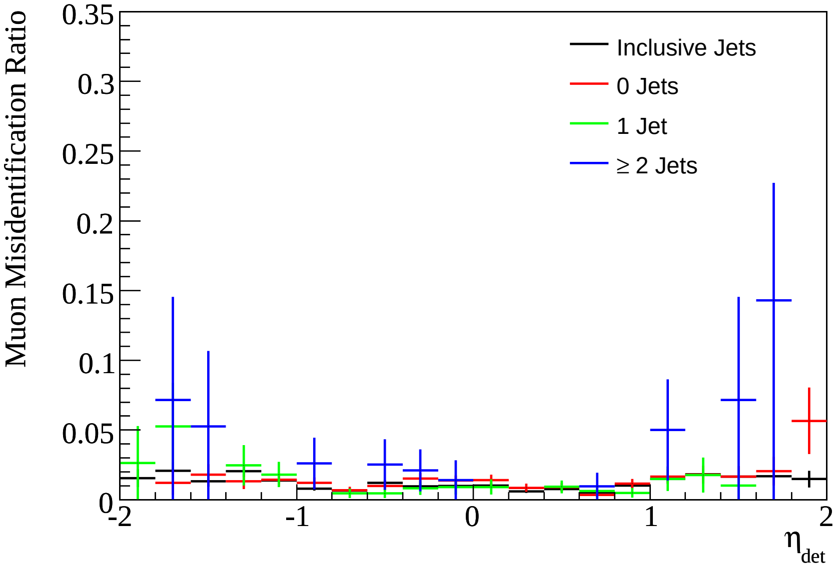

(a)

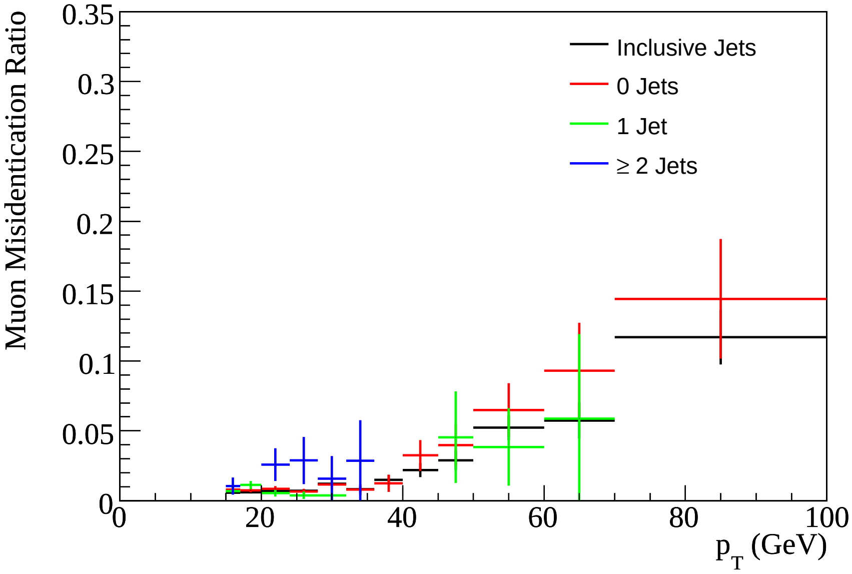

(b)

Figure 5-2: The "Medium, TrkLoose, NPTight" quality muon misidentification ratios versus (a) η_{det} and (b) p_T for the RunIIa dataset for the three jet multiplicities and the inclusive jet case.

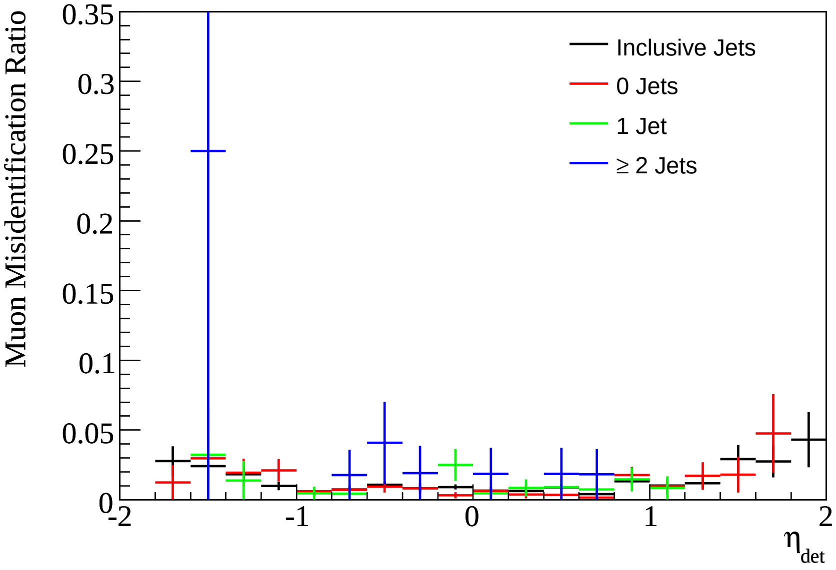

(a)

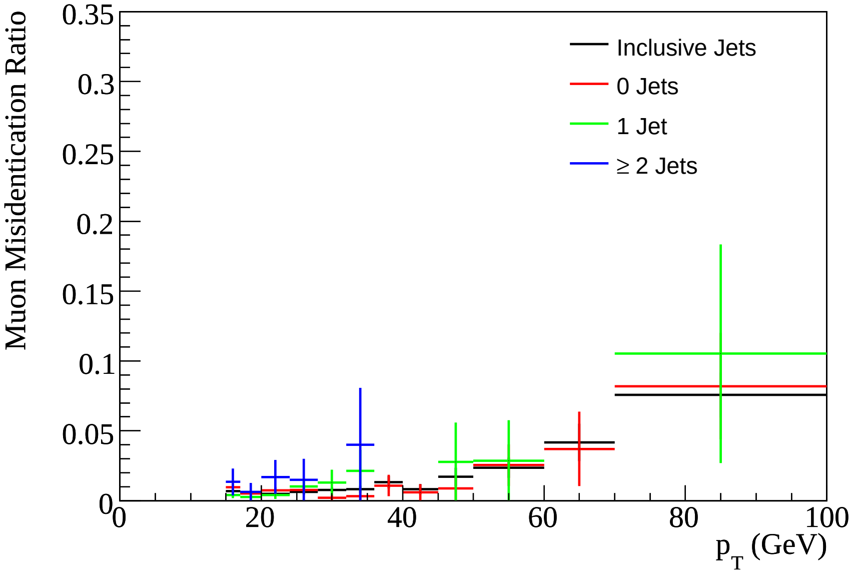

(b)

Figure 5-3: The "Medium, TrkLoose, NPTight" quality muon misidentification ratios versus (a) η_{det} and (b) p_T for the RunIIb dataset for the three jet multiplicities and the inclusive jet case.

5.4 Results

5.4.1 Event Yields

We observe a total of 35 candidate events, with an expected background from SM processes of 31.7 ± 0.3(*stat*) ± 3.9(*syst*). For events with zero jets, we observe 30 candidates and expect 25.7 ± 0.3 ± 3.3 background events; for events with one jet, we find four candidate events and estimate 5.1 ± 0.1 ± 0.6 background events; and, finally, for $n_{\text{jet}} \geq 2$ jet events we measure one candidate event and estimate 0.9 ± 0.1 ± 0.1 background events. Observed candidate and background events for each final state in each jet multiplicity bin, including the inclusive jet case, are summarized in Tables 5-4 – 5-7.

Figure 5-4 shows the n_{jet} distribution of data (black), with FCNC signal (red hatched histogram) and the WZ (cyan histogram) and other backgrounds (dark blue and purple histograms) overlaid. In this figure and all following figures in this Chapter, an arbitrary branching ratio of $B = 5\%$ was used.

Table 5-4: Number of observed data events and the expected number of background events for each final state with statistical and systematic uncertainties for the inclusive jet case.

Source	$e\nu e\bar{e}$	$\mu\nu e\bar{e}$	$e\nu\mu\bar{\mu}$
WZ	$5.17 \pm 0.07 \pm 0.97$	$5.72 \pm 0.07 \pm 0.89$	$4.75 \pm 0.06 \pm 0.70$
ZZ	$0.25 \pm 0.03 \pm 0.05$	$1.29 \pm 0.06 \pm 0.20$	$0.46 \pm 0.04 \pm 0.07$
$V + \text{jets}$	$0.42 \pm 0.11 \pm 0.08$	$0.14 \pm 0.04 \pm 0.06$	$0.48 \pm 0.10 \pm 0.01$
$Z\gamma$	$0.18 \pm 0.05 \pm 0.07$	< 0.001	$0.66 \pm 0.08 \pm 0.38$
$t\bar{t}$	$0.03 \pm 0.01 \pm 0.01$	$0.015 \pm 0.004 \pm 0.002$	$0.05 \pm 0.01 \pm 0.01$
Total bkg.	$6.05 \pm 0.14 \pm 0.98$	$7.17 \pm 0.10 \pm 0.91$	$6.40 \pm 0.15 \pm 0.80$
Observed	7	10	9

Source	$\mu\nu\mu\bar{\mu}$	$e\nu e\bar{e}_{ICR}$	$\mu\nu e\bar{e}_{ICR}$
WZ	$6.10 \pm 0.07 \pm 1.00$	$1.46 \pm 0.03 \pm 0.24$	$1.78 \pm 0.04 \pm 0.25$
ZZ	$1.30 \pm 0.06 \pm 0.21$	$0.09 \pm 0.02 \pm 0.01$	$0.47 \pm 0.04 \pm 0.07$
$V + \text{jets}$	$0.22 \pm 0.05 \pm 0.03$	$0.18 \pm 0.07 \pm 0.08$	$0.26 \pm 0.18 \pm 0.16$
$Z\gamma$	< 0.001	$0.10 \pm 0.01 \pm 0.03$	< 0.001
$t\bar{t}$	$0.04 \pm 0.01 \pm 0.01$	$0.011 \pm 0.004 \pm 0.002$	$0.024 \pm 0.005 \pm 0.004$
Total bkg.	$7.66 \pm 0.11 \pm 1.02$	$1.84 \pm 0.08 \pm 0.26$	$2.53 \pm 0.19 \pm 0.31$
Observed	5	1	3

Table 5-5: Number of observed data events and the expected number of background events for each final state with statistical and systematic uncertainties for $n_{\text{jet}} = 0$.

Source	$e\nu e\bar{e}$	$\mu\nu e\bar{e}$	$e\nu\mu\bar{\mu}$	$\mu\nu\mu\bar{\mu}$	$e\nu e\bar{e}_{ICR}$	$\mu\nu e\bar{e}_{ICR}$
WZ	$4.40 \pm 0.06 \pm 0.82$	$4.82 \pm 0.06 \pm 0.75$	$3.98 \pm 0.06 \pm 0.58$	$5.13 \pm 0.07 \pm 0.84$	$1.23 \pm 0.03 \pm 0.20$	$1.53 \pm 0.03 \pm 0.22$
ZZ	$0.17 \pm 0.02 \pm 0.03$	$1.02 \pm 0.05 \pm 0.16$	$0.32 \pm 0.03 \pm 0.05$	$1.04 \pm 0.05 \pm 0.17$	$0.05 \pm 0.01 \pm 0.01$	$0.38 \pm 0.03 \pm 0.05$
$V + \text{jets}$	$0.16 \pm 0.07 \pm 0.08$	$0.05 \pm 0.02 \pm 0.03$	$0.23 \pm 0.07 \pm 0.01$	$0.15 \pm 0.04 \pm 0.03$	$0.07 \pm 0.05 \pm 0.04$	$0.26 \pm 0.18 \pm 0.16$
$Z\gamma$	$0.11 \pm 0.04 \pm 0.04$	< 0.001	$0.47 \pm 0.07 \pm 0.28$	< 0.001	$0.09 \pm 0.01 \pm 0.03$	< 0.001
$t\bar{t}$	$0.002 \pm 0.001 < 0.001$	$0.001 \pm 0.001 < 0.001$	$0.001 \pm 0.001 < 0.001$	$0.004 \pm 0.003 \pm 0.001$	< 0.001	$0.004 \pm 0.002 \pm 0.001$
Total bkg.	$4.84 \pm 0.10 \pm 0.83$	$5.89 \pm 0.08 \pm 0.77$	$5.00 \pm 0.12 \pm 0.65$	$6.32 \pm 0.10 \pm 0.86$	$1.44 \pm 0.06 \pm 0.21$	$2.17 \pm 0.19 \pm 0.23$
Observed	6	8	8	4	1	3

Table 5-6: Number of observed data events and the expected number of background events for each final state with statistical and systematic uncertainties for $n_{\text{jet}} = 1$.

Source	$e\nu e\bar{e}$	$\mu\nu e\bar{e}$	$e\nu\mu\bar{\mu}$	$\mu\nu\mu\bar{\mu}$	$e\nu e\bar{e}_{ICR}$	$\mu\nu e\bar{e}_{ICR}$
WZ	$0.69 \pm 0.02 \pm 0.13$	$0.78 \pm 0.03 \pm 0.12$	$0.68 \pm 0.02 \pm 0.10$	$0.84 \pm 0.03 \pm 0.14$	$0.20 \pm 0.01 \pm 0.03$	$0.23 \pm 0.01 \pm 0.03$
ZZ	$0.07 \pm 0.02 \pm 0.01$	$0.25 \pm 0.03 \pm 0.04$	$0.12 \pm 0.02 \pm 0.02$	$0.23 \pm 0.03 \pm 0.04$	$0.02 \pm 0.01 \pm 0.01$	$0.09 \pm 0.02 \pm 0.01$
$V + \text{jets}$	$0.21 \pm 0.08 \pm 0.04$	$0.06 \pm 0.03 \pm 0.02$	$0.21 \pm 0.06 \pm 0.01$	$0.07 \pm 0.03 \pm 0.03$	$0.04 \pm 0.03 \pm 0.04$	< 0.001
$Z\gamma$	$0.04 \pm 0.03 \pm 0.02$	< 0.001	$0.15 \pm 0.04 \pm 0.09$	< 0.001	$0.016 \pm 0.004 \pm 0.005$	< 0.001
$t\bar{t}$	$0.014 \pm 0.004 \pm 0.003$	$0.007 \pm 0.003 \pm 0.001$	$0.012 \pm 0.003 \pm 0.002$	$0.019 \pm 0.005 \pm 0.003$	$0.008 \pm 0.003 \pm 0.001$	$0.009 \pm 0.002 \pm 0.001$
Total bkg.	$1.02 \pm 0.09 \pm 0.14$	$1.10 \pm 0.05 \pm 0.13$	$1.17 \pm 0.08 \pm 0.14$	$1.16 \pm 0.05 \pm 0.15$	$0.28 \pm 0.03 \pm 0.05$	$0.33 \pm 0.02 \pm 0.03$
Observed	1	1	1	1	0	0

5.4.2 Systematic Uncertainties

We start by using the same systematic uncertainties as discussed in Section 4.4.2, but now consider additional uncertainties since the signal has changed. We introduce a

Table 5-7: Number of observed data events and the expected number of background events for each final state with statistical and systematic uncertainties for $n_{\text{jet}} \geq 2$.

Source	$e\nu e\bar{e}$	$\mu\nu e\bar{e}$	$e\nu\mu\bar{\mu}$
WZ	$0.09 \pm 0.01 \pm 0.02$	$0.12 \pm 0.01 \pm 0.02$	$0.09 \pm 0.01 \pm 0.01$
ZZ	$0.008 \pm 0.005 \pm 0.002$	$0.026 \pm 0.009 \pm 0.004$	$0.018 \pm 0.006 \pm 0.003$
$V +$ jets	$0.06 \pm 0.05 \pm 0.08$	$0.04 \pm 0.03 \pm 0.01$	$0.03 \pm 0.03 \pm 0.01$
$Z\gamma$	$0.03 \pm 0.02 \pm 0.01$	< 0.001	$0.04 \pm 0.02 \pm 0.02$
$t\bar{t}$	$0.013 \pm 0.004 \pm 0.002$	$0.007 \pm 0.003 \pm 0.001$	$0.03 \pm 0.01 \pm 0.01$
Total bkg.	$0.20 \pm 0.06 \pm 0.08$	$0.19 \pm 0.03 \pm 0.02$	$0.21 \pm 0.04 \pm 0.02$
Observed	0	1	0

Source	$\mu\nu\mu\bar{\mu}$	$e\nu e\bar{e}_{ICR}$	$\mu\nu e\bar{e}_{ICR}$
WZ	$0.12 \pm 0.01 \pm 0.02$	$0.03 \pm 0.01 \pm 0.01$	$0.03 \pm 0.01 \pm 0.01$
ZZ	$0.026 \pm 0.007 \pm 0.004$	$0.004 \pm 0.003 < 0.001$	$0.008 \pm 0.004 \pm 0.001$
$V +$ jets	< 0.001	$0.07 \pm 0.04 \pm 0.04$	< 0.001
$Z\gamma$	< 0.001	$0.001 \pm 0.001 < 0.001$	< 0.001
$t\bar{t}$	$0.018 \pm 0.004 \pm 0.003$	$0.002 \pm 0.001 < 0.001$	$0.012 \pm 0.004 \pm 0.002$
Total bkg.	$0.16 \pm 0.01 \pm 0.02$	$0.11 \pm 0.04 \pm 0.04$	$0.05 \pm 0.01 \pm 0.01$
Observed	0	0	0

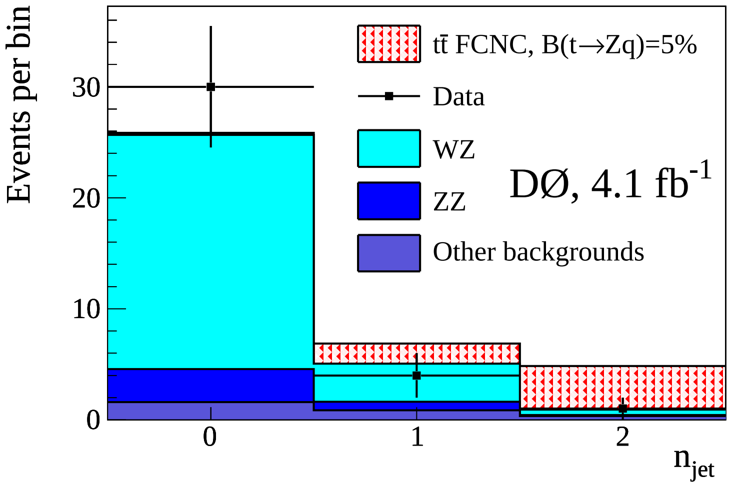

Figure 5-4: The n_{jet} distribution of data (black), with FCNC signal (red hatched histogram) and the WZ (cyan histogram) and other backgrounds (dark blue and purple histogram) overlaid.

5% uncertainty due to the signal PDF choice and assign a 10% uncertainty to the theoretical WZ background cross section. We also assign a 9% uncertainty on $\sigma_{t\bar{t}}$ [94], which includes a dependence on the uncertainty of the top quark mass [95].

We must now include uncertainties related to jet production. Systematic uncertainties in the jet energy scale (JES), jet energy resolution (JER), and jet reconstruction and ID efficiencies are applied by rerunning the analysis with the values of the energy scale, energy smearing, and jet removal probabilities shifted by $\pm 1\sigma$. The uncertainty is then the difference between each of these results and the nominal value. For $n_{\text{jet}} = 0$ the uncertainty is found to be 1%, for $n_{\text{jet}} = 1$ it is 5%, and for $n_{\text{jet}} \geq 2$ it is 20%.

To assess the systematic uncertainties due to the signal modeling, the generated top quark mass is changed from 172.5 GeV to 175 GeV with the difference assigned as an uncertainty. As discussed in Sec. 5.1, the coupling variables v_{tqZ} and a_{tqZ} are varied and found to have a negligible effect on the branching ratio limits. We also include the reweighting function used by CDF [90]. The resulting signal distributions are used as a shape uncertainty in the limit calculation [92].

5.4.3 Branching Ratio Limits on $t \to Zq$ Decays

To achieve better separation between signal and background, we look at three discriminating variables; n_{jet}, H_T (defined as the scalar sum of the transverse momenta of the three leptons, jets, and missing transverse energy, or $H_T = \Sigma p_T^{\ell} + \not{E}_T + \Sigma p_T^{\text{jets}}$), and m_t^{reco}, the reconstructed top quark mass using the Z boson leptons and any jets found in the event.

Figure 5-5 shows the distributions of H_T for the three jet multiplicity bins. As expected, as the number of jets increases, the H_T peak also increases.

In events where $n_{\text{jet}} = 0$, m_t^{reco} is undefined and therefore this variable is not used in the limit setting. For one jet events, m_t^{reco} is defined as the invariant mass calculated from the 4-vectors of the Z boson and the jet. While for $n_{\text{jet}} \geq 2$, we check the $Z+\text{jets}$ mass of each jet and choose the jet with the $Z+\text{jets}$ mass closest to $m_t = 172.5$ GeV. Since the $t \to Zq$ decay doesn't produce a neutrino, we expect to be able to fully reconstruct the top mass. The reconstructed top quark mass is shown in Fig. 5-6 for events with $n_{\text{jet}} \geq 1$, while Fig. 5-7 is a 2D scatter plot of the H_T distribution versus

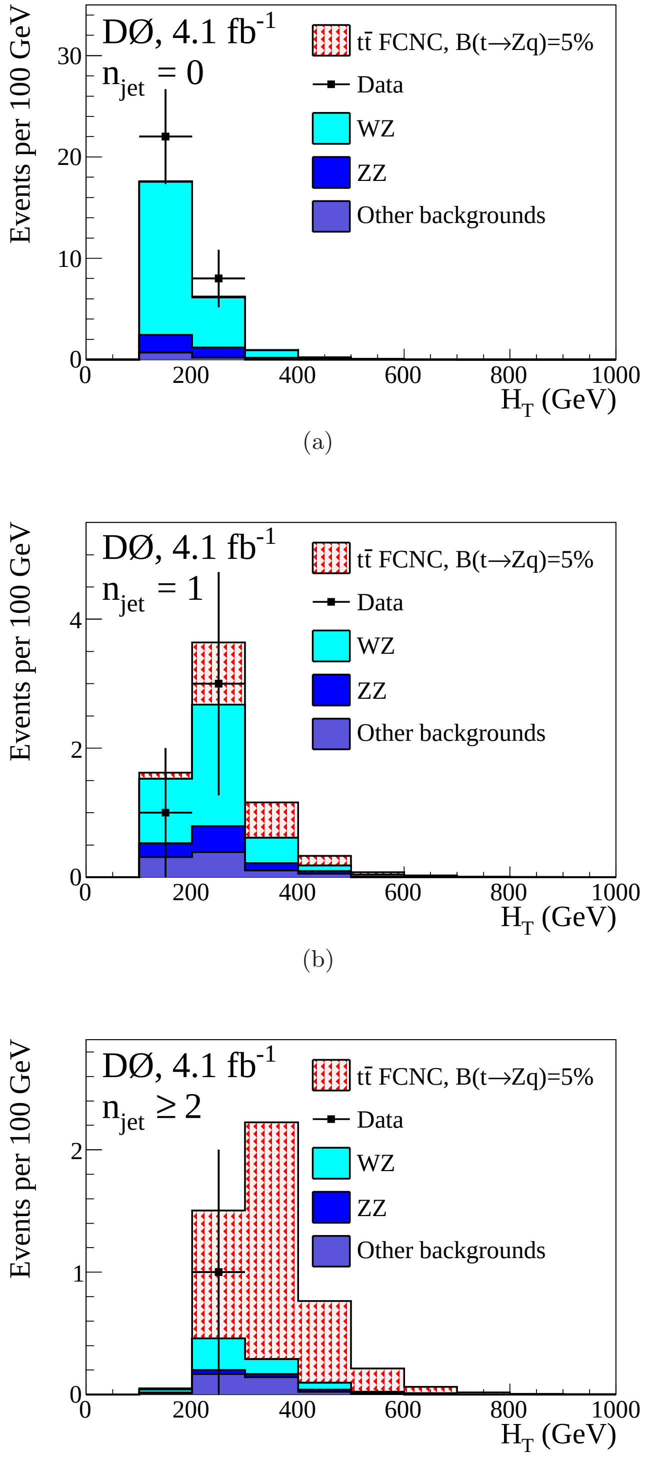

(a)

(b)

(c)

Figure 5-5: H_T distributions for (a) $n_{\text{jet}} = 0$, (b) $n_{\text{jet}} = 1$, and (c) $n_{\text{jet}} \geq 2$ jets with data (black), and FCNC signal (red hatched histogram) and the WZ (cyan histogram) and other backgrounds (dark blue and purple histogram) overlaid.

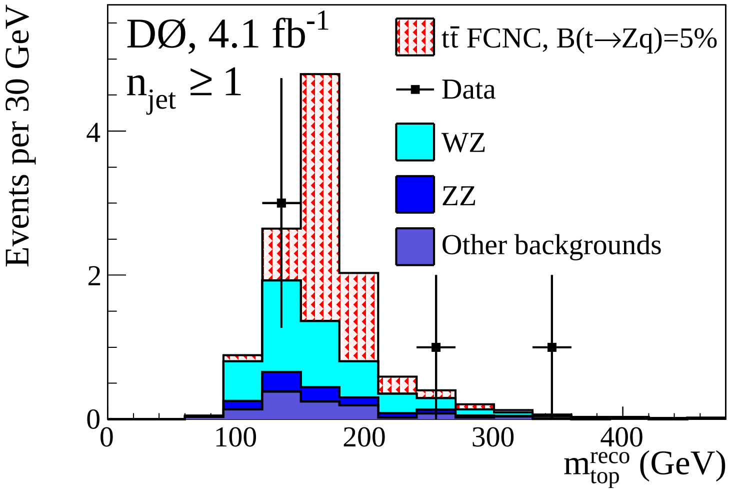

Figure 5-6: Reconstructed top quark mass using $Z + \geq 1$ jets in data (black), with FCNC signal (red hatched histogram) and the WZ (cyan histogram) and other backgrounds (dark blue and purple histogram) overlaid.

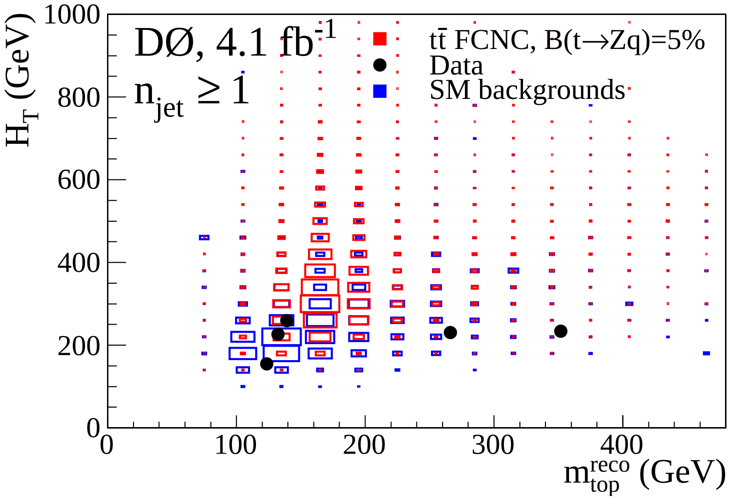

Figure 5-7: Two-dimensional scatter plot of H_T versus the reconstructed top quark mass for events with $n_{\text{jet}} \geq 1$, with data (black), the FCNC signal (red box), and the SM backgrounds (blue box) overlaid.

the reconstructed top quark mass.

From Fig. 5-7, we see decent separation between the FCNC signal and the SM backgrounds. To further increase the sensitivity, we divide the H_T distribution into ten bins when we set the branching ratio limits, and for events with $n_{\text{jet}} \geq 1$, we further

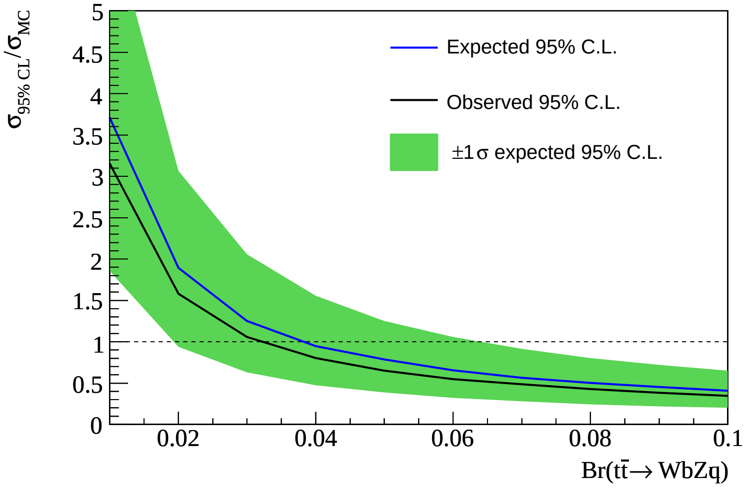

Figure 5-8: The ratio of the measured to theoretical $t\bar{t} \to WbZq$ cross section as a function of $BR(t \to Zq)$. The green shaded area represents the $\pm 1\sigma$ band around the expected limits (blue line). The observed limit is shown as a black line.

divide into four m_t^{reco} bins as follows; $m_t^{reco} < 120$ GeV, 120 GeV $< m_t^{reco} < 150$ GeV, 150 GeV $< m_t^{reco} < 200$ GeV, and $m_t^{reco} > 200$ GeV. These distributions are then fed into a limit extraction program called COLLIE [96] (discussed more in Section 6.3.4), and a simple Gaussian smearing technique is used to extract the limits at the 95% C.L. We see no evidence of FCNC production and therefore set an observed limit of $BR(t \to Zq) < 3.2\%$ at the 95% C.L.. The expected limit is less than 3.8%. Figure 5-8 shows the ratio of the measured to theoretical $t\bar{t} \to WbZq$ cross section as a function of $BR(t \to Zq)$, where the green shaded bands represent the $\pm 1\sigma$ band around the expected limits.

Figure 5-9 shows a good example of a clean tri-lepton $e\nu\mu\bar{\mu} + 1$ jet candidate event. The jet (in red and blue) at $\sim \eta \times \phi = 1.6 \times 225$ rad is clearly seen. The electron is shown in brown, the muons in green, and the missing transverse energy in yellow. The $Z+$jet mass is 266.4 GeV.

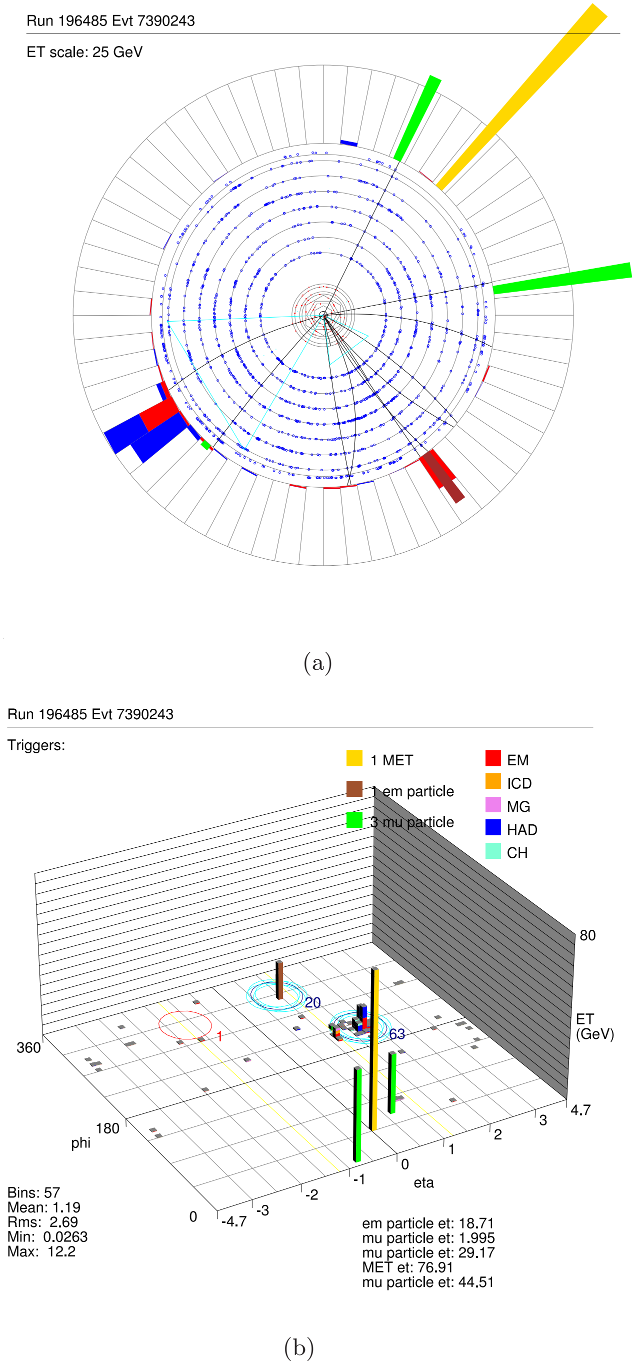

Figure 5-9: Event display for a $e\nu\mu\bar{\mu}$ + 1 jet candidate event with run number 196485 and event number 7390243 recorded August 18, 2004. (a) The XY view gives a good overview of tracking system and the energy deposited in the calorimetry, while the (b) lego view focuses on the energy deposited in the calorimeter. In both event displays, the muon (green) track p_Ts, from the central tracker, are overlaid. The electron is represented in brown, the jet cluster in red and blue, and the missing energy in yellow.

6 Search for Standard Model Higgs Boson in Associated Production of VH

At the Tevatron the associated production of $q\bar{q} \to WH$ and $q\bar{q} \to ZH$, Fig. 6-1, has the highest cross section after the leading gluon-gluon fusion $gg \to H$ production. With the dominant SM $H \to WW^*$ branching ratio, for Higgs boson masses above $m_H = 135$ GeV, and this $VH \to VWW^*$ production, where V is either the W or Z boson, we have a good process to use to search for the Higgs boson. A popular approach is to use the hadronic decays of the W bosons, due to the much higher branching fraction, but then this also produces a large hadronic background, which is difficult to separate from the signal. Similarly, the $H \to WW^* \to \ell\nu\ell\nu$ decay suffers from a large $Z/\gamma^* \to \ell\bar{\ell}$ background. By requiring a third lepton, this background becomes much more manageable. Contributions from $H \to ZZ$ decays are significant in the tri-lepton final states and are therefore included in the signal modeling, along with the less significant $H \to WW^*$ decay and vector boson fusion $q\bar{q} \to q\bar{q}H$ production.

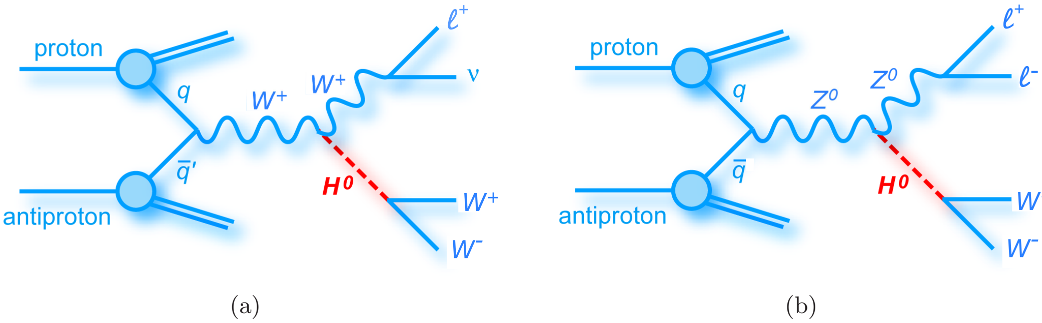

Figure 6-1: Leading-order (a) WH and (b) ZH associated production to tri-lepton final state diagrams.

CDF has preliminary 8.2 fb^{-1} results on a high mass Higgs boson search using the tri-lepton final states [97]. To increase the sensitivity to the WH and ZH signals individually, the data and MC samples are split into three categories; 1) same-flavor opposite-sign di-lepton pair (ie. $e\bar{e}$) reconstructed in the Z boson peak plus a reconstructed jet, 2) same-flavor opposite-sign di-lepton pair reconstructed in the Z boson peak plus two or more reconstructed jets, and 3) same-flavor opposite-sign di-lepton pair not found in the Z boson peak. Channels 1 and 2 are sensitive to ZH production, where the jet(s) are decay products of $H \to WW^*$ and one or both of the W bosons decays hadronically. Channel 3 is predominantly WH production. Between these three channels, CDF is able to set an upper limit on the cross section of $\sim 5.8\sigma_{SM}$ at the 95% C.L. at a Higgs boson mass of 160 GeV, where σ_{SM} is the SM cross section.

In this chapter, a search is presented for the Higgs boson with a final state containing at least three isolated leptons and missing transverse momentum. Due to the better sensitivity and lower backgrounds, we focus on the channels; $ee\mu$ and $\mu\mu e$. The $ee\mu$ channel is described here, while details involving the $\mu\mu e$ final state can be found in Ref. [98]. Due to time constraints, the two same three-flavor channels (eee and $\mu\mu\mu$) were not included in this iteration of the analysis. The analysis takes advantage of the full dataset recorded during RunII operations, corresponding to 9.7 fb^{-1} of integrated luminosity collected between April 2002 and September 2011.

Section 6.1 describes the data and MC samples used in this analysis, followed by the object identification and event selection criteria in Section 6.2. The results are given in Sec. 6.3. A description of the multivariate analysis (MVA) training technique is provided in Sec. 6.3.3, while the cross section limit results are given in Section 6.3.4.

6.1 Data and Monte Carlo Samples

We use the complete DØ RunII dataset for this analysis, corresponding to 9.7 fb^{-1} of integrated luminosity after the standard data quality [36] requirements have been applied. Candidate data events are selected using the EMinclusive data skims officially produced by the CSG, details of which are listed in Appendix B.

The signal and SM background processes have been generated using the CTEQ6L [69] PDF set in PYTHIA 6.323 and 6.409 [70]. The main background processes for the trilepton final states are diboson production (WZ, ZZ, and WW), $Z+$jets – where a jet is misidentified as a lepton, $t\bar{t}$ decays, and $W+$jets/γ^* production. ALPGEN [71] was used to generate the $Z/\gamma^* \to \ell\bar{\ell} +$ jet and $W \to \ell\nu +$jet backgrounds. The appropriate k-factors, with the heavy flavor factors applied on top of the light flavor k-factors, are applied, the details of which are listed in Appendix A and Table A-1. We also apply the appropriate heavy flavor (HF) skimming to the $W/Z +$ jets samples, so as to remove the phase space overlap between the $V \to$ light partons, $V \to cc$, and $V \to bb$ ALPGEN samples.

The standard MC reweighting is applied as recommended by the Common Analysis Format (CAFe) framework [99]. A more in-depth description of the reweighting of the Z–p_T, W–p_T, WW–p_T, instantaneous luminosity, and beam position can be found in Appendix A.

The Monte Carlo signal and background samples used are listed in Appendix D.

6.1.1 Trigger Efficiency

To maximize the signal acceptance, we do not apply any trigger requirements on the leptons beyond those used to get into the official CSG skims. To study the effect of the trigger efficiency, we start with the $\mu\mu e$ channel, as muons have a lower trigger efficiency than electrons. Using $\mu\mu e$ data, we compare the total number of events reconstructed to the number of events gathered by a logical OR of the single muon and single electron trigger. We also calculate the efficiency for the single muon and single electron triggers in MC using the efficiencies measured by the respective ID groups. We then parameterized the turn-on curves in data and MC with respect to the sum of the momenta of the three leptons and correct the turn-on curves in MC by the turn-on curves in the data. The result is an average efficiency in MC of 96.5% that varies little with the sum of p_T. We have not repeated the study for the $ee\mu$ final state, but as the single electron trigger is more efficient than the single muon, we expect the $ee\mu$ efficiency to be higher. While we do not apply this trigger efficiency to the MC samples, we do assign a flat 3.5% systematic uncertainty to both the signal and background MC samples to account for it.

6.2 Object and Event Selection

As with the two previous analyses, events are required to have at least three energetic leptons, at minimum two electrons and one muon, and significant imbalance of transverse momentum. Again, only events with at least one primary vertex within ±60 cm around the detector origin are considered.

We require at least two electrons that meet the "Point05" criteria in the CC and "Point1" in the EC. ICR-electrons are not considered in this analysis. We also require at least one muon to be of "Loose, NewMedium, TopScaledLoose" muon ID, track, and isolation quality, respectively. Loose lepton p_T cuts are applied to increase the signal acceptance and allow softer second and third leptons to be selected. The $\Delta\mathcal{R}$ cuts help to insure that the leptons are isolated, while the Δz_{dca} cuts force the leptons to come from the same primary vertex. The kinematic requirements to select $ee\mu$ events are as follows:

- p_T of the most energetic (leading) electron must be greater than 15 GeV,
- p_T of the two other leptons must be greater than 10 GeV,
- $M_{e_1e_2} > 15$ GeV,
- $\Delta\mathcal{R} > 0.3$ between any two leptons,
- $\Delta z_{dca}^{e_1e_2} < 3$ cm between the two electrons' tracks, and
- $min(\Delta z_{dca}^{e_1,\mu}, \Delta z_{dca}^{e_2,\mu}) < 1$ cm

6.3 Results

6.3.1 Event Yields and Kinematic Distributions

The number of observed data events, the expected signal yields for $m_H = 115$ GeV, 125 GeV, 135 GeV, 145 GeV, and 165 GeV, and the estimated number of background events are shown in Table 6-1 for RunII.

Table 6-1: Number of observed data events, the expected number of signal events for $m_H = 115$ GeV, 125 GeV, 135 GeV, 145 GeV, and 165 GeV, and the estimated number of background events. Errors reflect the statistical uncertainties on the number of generated background events.

Samples / m_H	115 GeV	125 GeV	135 GeV	145 GeV	165 GeV
Data	96				
Signal	0.716 ± 0.009	0.924 ± 0.010	1.233 ± 0.010	1.386 ± 0.011	0.964 ± 0.009
WH	0.329 ± 0.007	0.400 ± 0.007	0.512 ± 0.008	0.547 ± 0.008	0.431 ± 0.006
ZH	0.351 ± 0.006	0.418 ± 0.006	0.521 ± 0.006	0.574 ± 0.006	0.464 ± 0.005
HZZ	0.033 ± 0.000	0.099 ± 0.001	0.193 ± 0.002	0.258 ± 0.002	0.054 ± 0.000
HWW	0.002 ± 0.001	0.006 ± 0.003	0.005 ± 0.002	0.007 ± 0.003	0.013 ± 0.004
VBF	0.001 ± 0.000	0.001 ± 0.000	0.002 ± 0.001	0.001 ± 0.000	0.002 ± 0.001
Total Backgnd	89.41 ± 2.36				
$Z \to ee +$jets	48.26 ± 2.23				
$Z \to \tau\tau +$jets	4.33 ± 0.64				
WZ	23.45 ± 0.35				
ZZ	11.09 ± 0.16				
WW	0.69 ± 0.13				
$t\bar{t}$	1.38 ± 0.07				
$W +$jets	0.21 ± 0.12				

Figs. 6-2 – 6-32 show the kinematic distributions[c] using the full dataset available, along with the distributions of the training variables listed in Sec. 6.3.3, for an expected SM Higgs boson signal at $m_H = 145$ GeV, multiplied by a factor of 10. This mass point is used as it has the highest signal acceptance. The individual lepton distributions are shown first, followed by the multi-lepton distributions. The variables – those not shown as single or multi-lepton distributions – used to train the multivariate analysis (MVA) decision trees (DT) (discussed in Sec. 6.3.3) are shown last. The last bin in each distribution is the overflow bin, meaning that events past the x-axis maximum limit are put into this bin. Each distribution has a corresponding Kolmogorov-Smirnov test [100] (KS-test or KS probability) attached to the upper right corner. The higher the value, the more consistent the data and MC background distributions are to one another, with a maximum value of 1.

We study each of the following distributions in detail to determine which will be used in the MVA training to better separate out the tiny signal from the overwhelming background. We start by looking at how well the variables in data are modelled with

---

[c] Distributions are marked as "Preliminary" as they have been approved by the DØ Collaboration for public presentation but not yet for publication.

respect to MC background by looking at the KS probability. We also include variables that will help discriminant against the background. For example, we use the tri-lepton transverse momentum, the closest $\Delta\mathcal{R}$ between any two leptons, and the invariant mass of the di-electrons to help train against the WZ background. Variables that are less well modelled, such as the muon p_T, are not included in the MVA training. Once we have the initial set of variables, we train them at a mass of 145 GeV and study the DT output. If the KS probability for the overtraining of the training versus test samples is reasonable, we then train the rest of the mass points with those variables. It is possible to train different variables at different mass points to gain more sensitivity to the Higgs boson signal, but that is not done here. Once all the mass points have been trained, we look at the final discriminant distributions, Sec. 6.3.3, and providing that they look reasonable, we continue on to calcaluate the cross section limits.

While most variables are modelled well or are at least within the uncertainty given the statistics of the analysis, we do see disagreement in some of the kinematic distributions. The most obvious is the discrepancy at low muon p_T, which is then propagated into other variables that depend on muon p_T. We believe this comes from a mismodelling of the $Z+$jets background at low energy where the jet $\rightarrow \mu$ fake rate is poorly estimated. To account for this, we assign a 30% systematic uncertainty to the $Z+$jets MC background but find that it has little impact on the cross section limits.

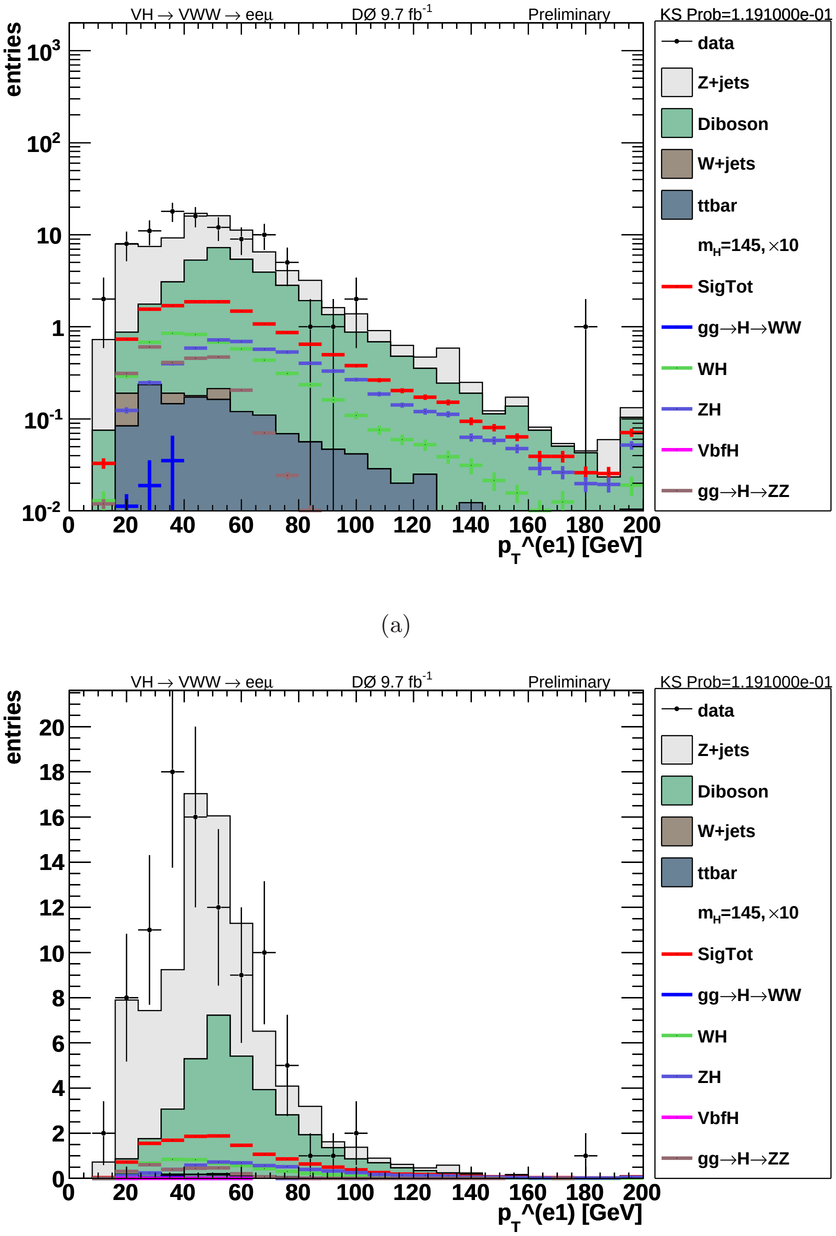

(a)

(b)

Figure 6-2: Distribution of the transverse momentum of the leading electron, $p_T^{e_1}$, in (a) logarithmic scale and (b) linear scale for data (points) and sum of all the backgrounds (histograms). The expected signal, multiplied by a factor of 10, for a 145 GeV SM Higgs boson is also shown in red.

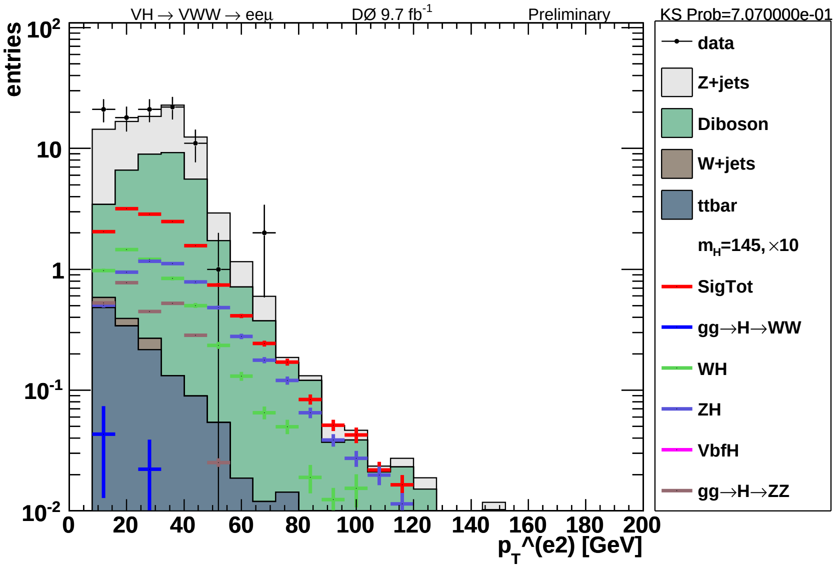

(a)

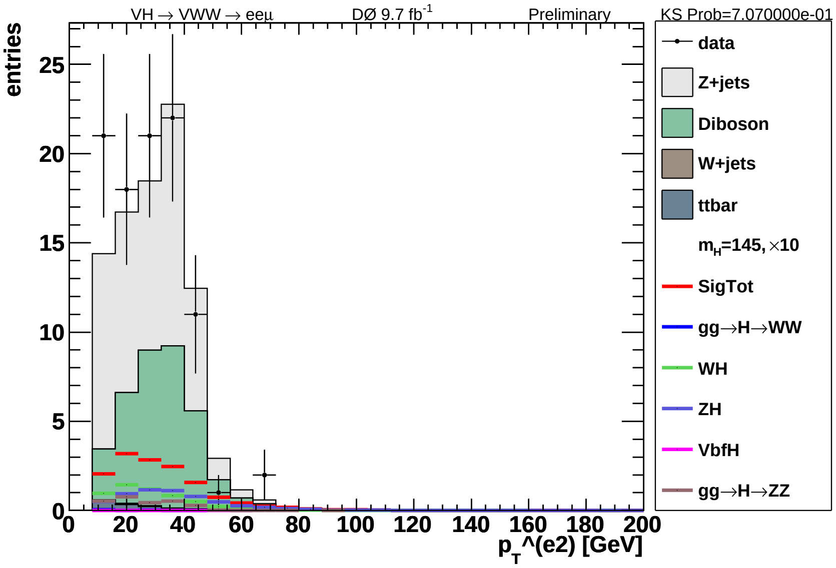

(b)

Figure 6-3: Distribution of the transverse momentum of the trailing electron, $p_T^{e_2}$, in (a) logarithmic scale and (b) linear scale for data (points) and sum of all the backgrounds (histograms). The expected signal, multiplied by a factor of 10, for a 145 GeV SM Higgs boson is also shown in red.

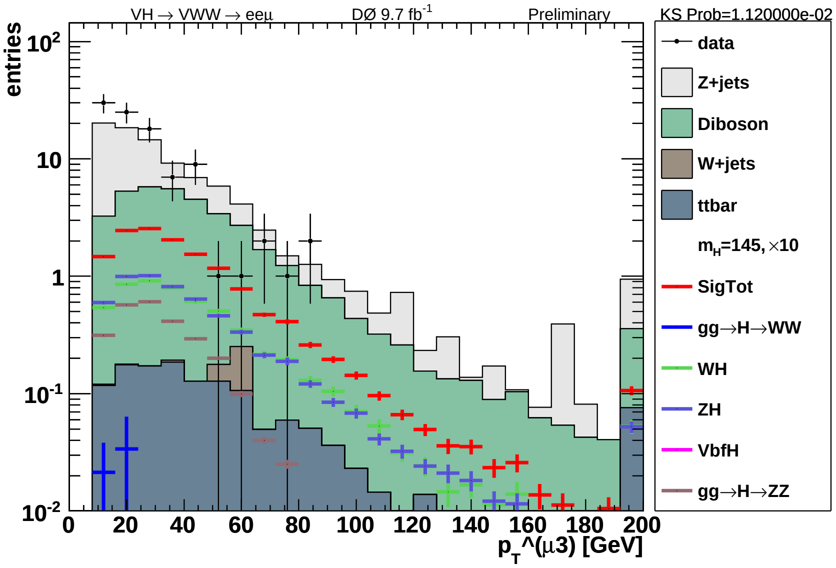

(a)

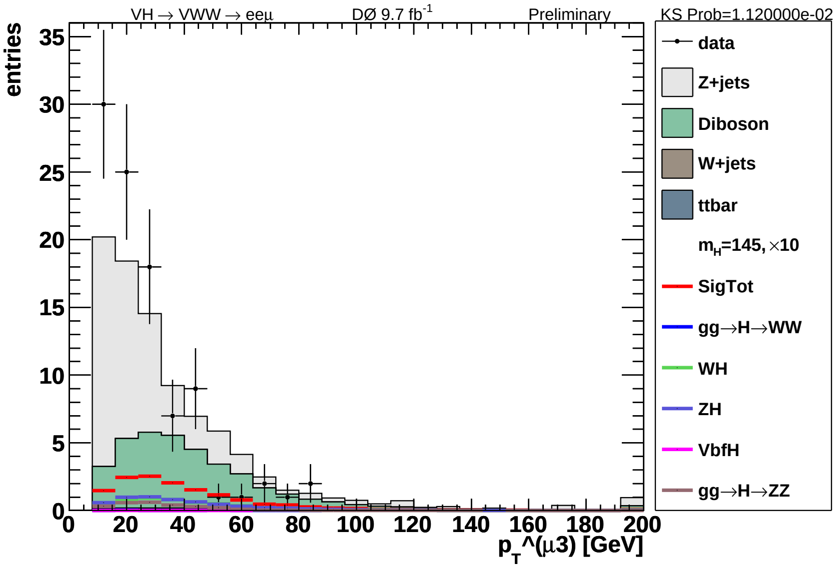

(b)

Figure 6-4: Distribution of the transverse momentum of the muon, p_T^μ, in (a) logarithmic scale and (b) linear scale for data (points) and sum of all the backgrounds (histograms). The expected signal, multiplied by a factor of 10, for a 145 GeV SM Higgs boson is also shown in red.

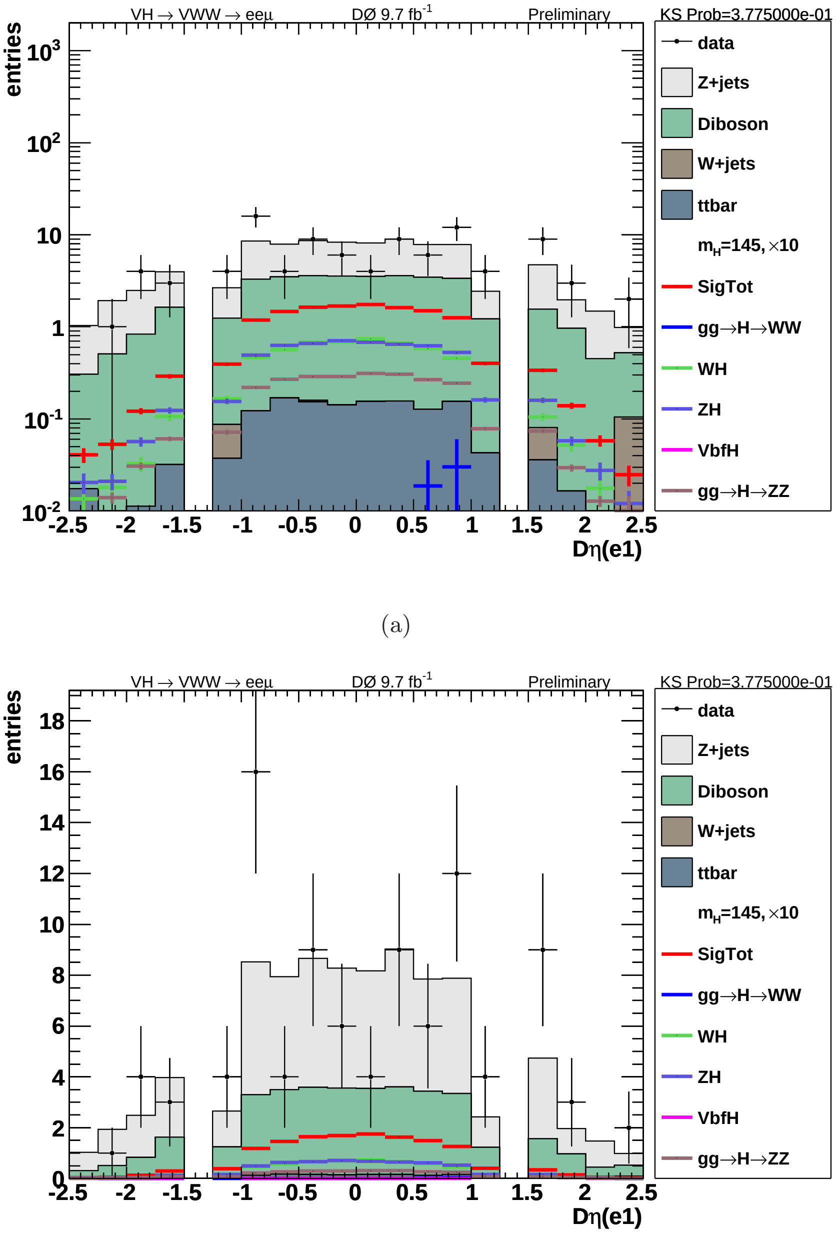

(a)

(b)

Figure 6-5: Distribution of the detector η for the leading electron, $\eta_{det}^{e_1}$, in (a) logarithmic scale and (b) linear scale for data (points) and sum of all the backgrounds (histograms). The expected signal, multiplied by a factor of 10, for a 145 GeV SM Higgs boson is also shown in red.

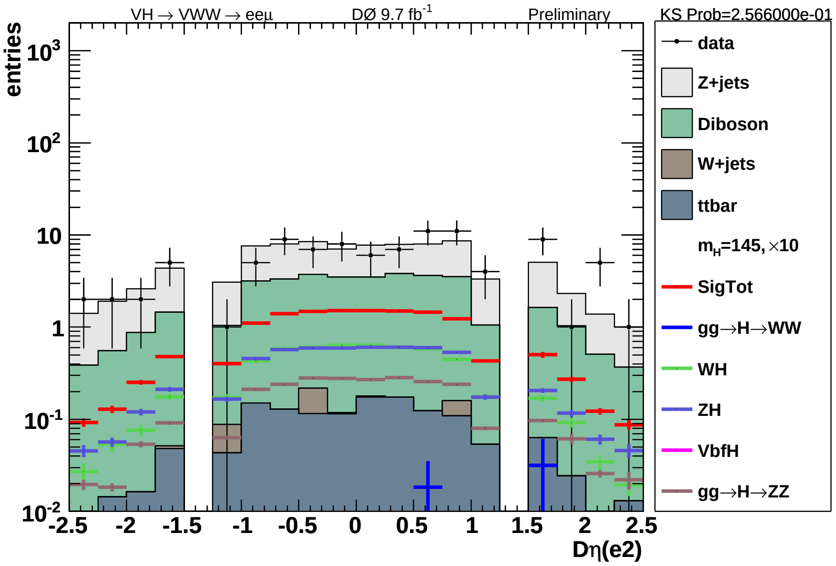

(a)

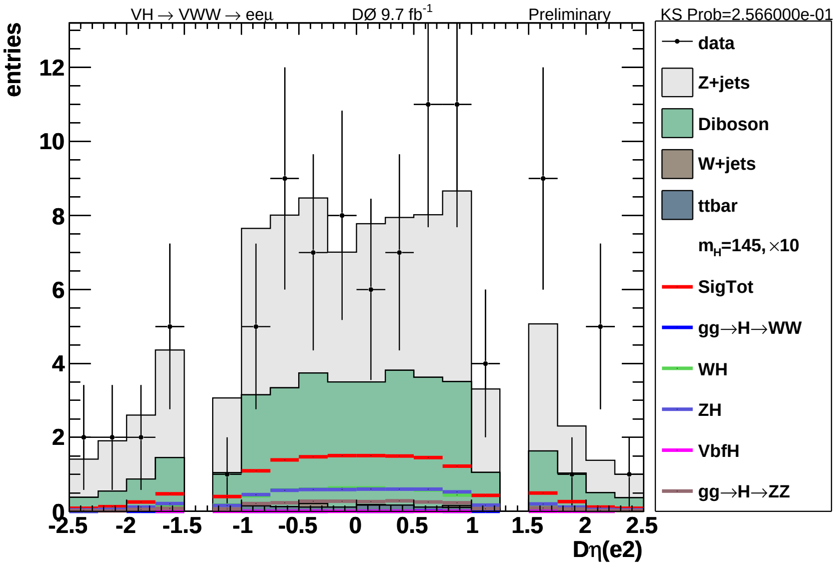

(b)

Figure 6-6: Distribution of the detector η for the trailing electron, η_{det}^{e2}, in (a) logarithmic scale and (b) linear scale for data (points) and sum of all the backgrounds (histograms). The expected signal, multiplied by a factor of 10, for a 145 GeV SM Higgs boson is also shown in red.

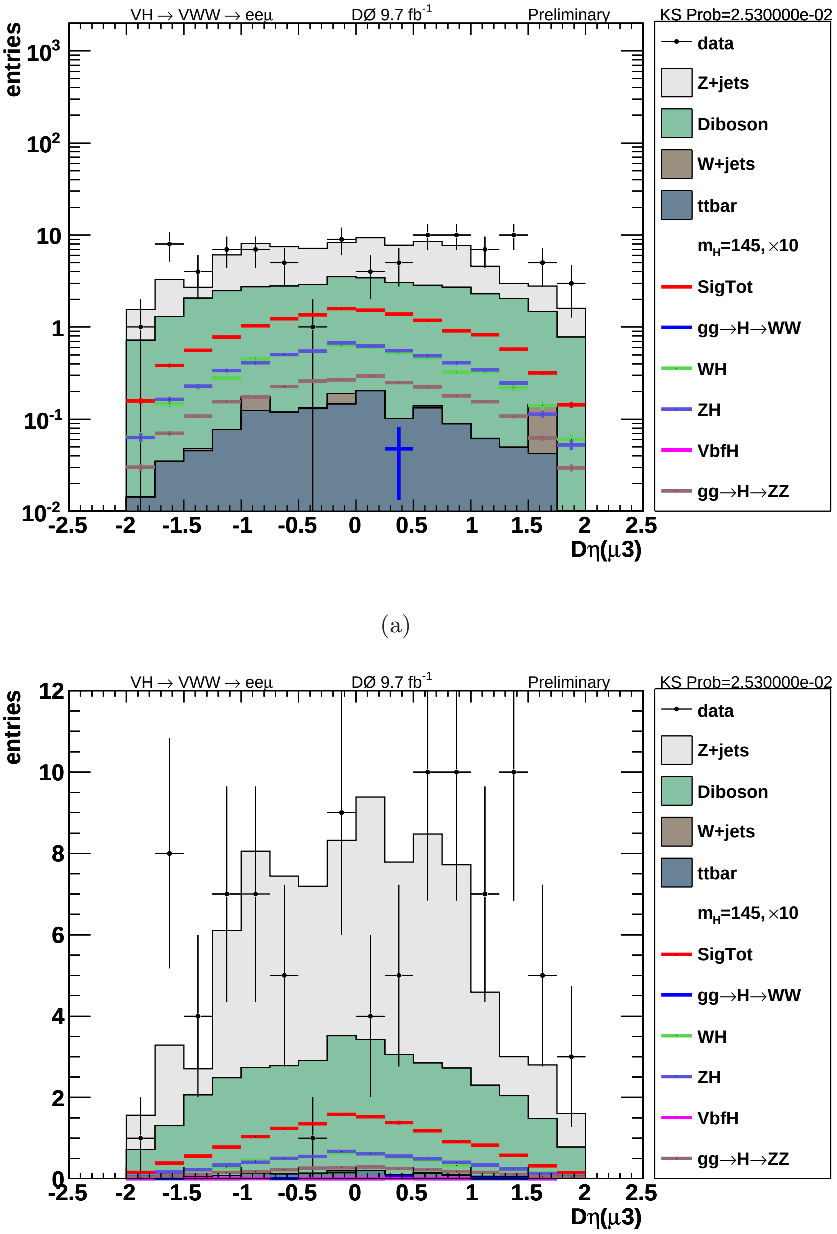

(a)

(b)

Figure 6-7: Distribution of the detector η for the muon, η^{μ}_{det}, in (a) logarithmic scale and (b) linear scale for data (points) and sum of all the backgrounds (histograms). The expected signal, multiplied by a factor of 10, for a 145 GeV SM Higgs boson is also shown in red.

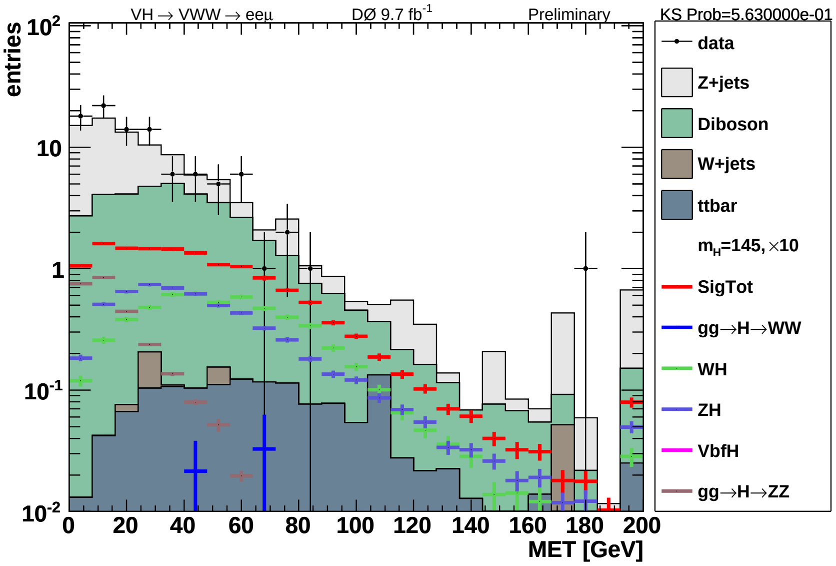

(a)

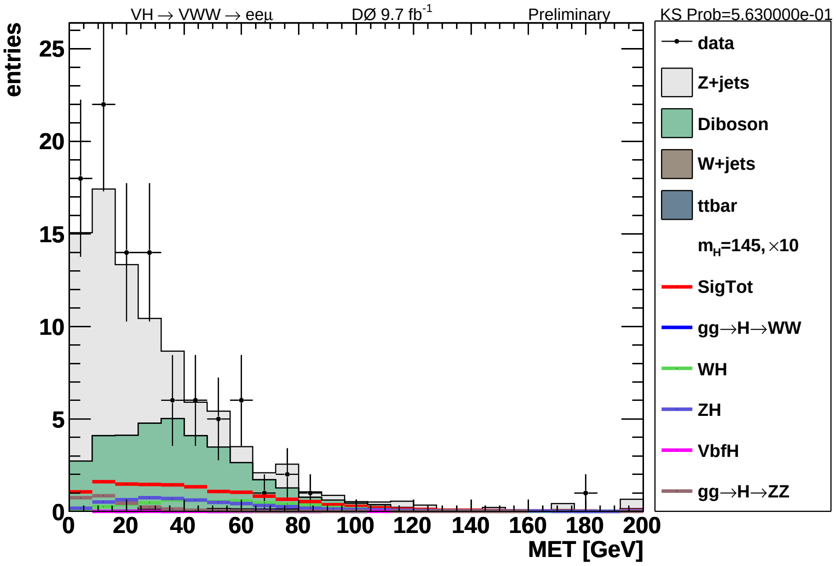

(b)

Figure 6-8: Distribution of the missing transverse momentum, $\not\!\!E_T$, in (a) logarithmic scale and (b) linear scale for data (points) and sum of all the backgrounds (histograms). The expected signal, multiplied by a factor of 10, for a 145 GeV SM Higgs boson is also shown in red.

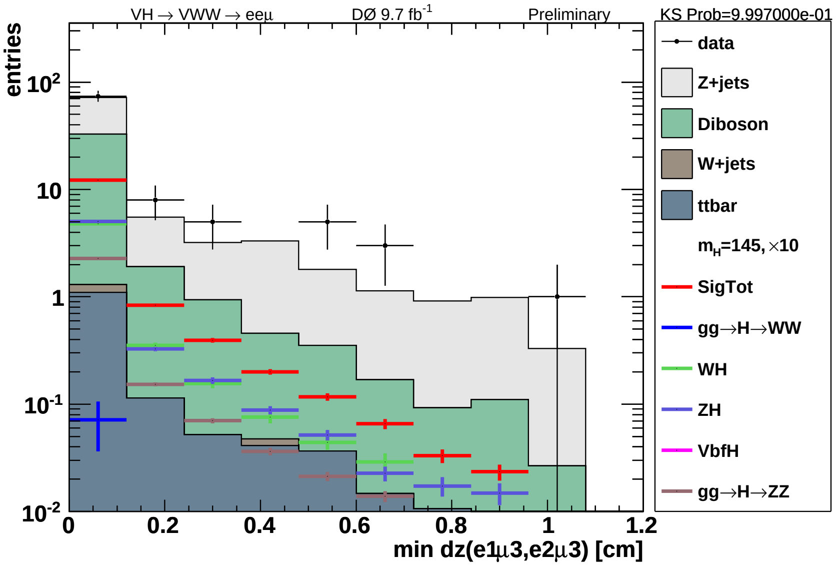

(a)

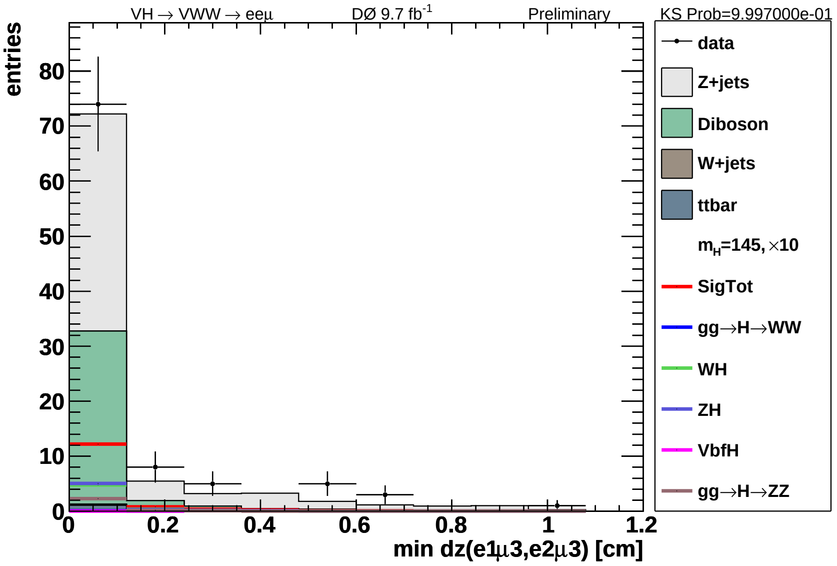

(b)

Figure 6-9: Distribution of the minimum distance of Δz between either the leading or trailing electron and the muon, $|min(\Delta z_{(e_1,\mu)}, \Delta z_{(e_2,\mu)})|$, in (a) logarithmic scale and (b) linear scale for data (points) and sum of all the backgrounds (histograms). The expected signal, multiplied by a factor of 10, for a 145 GeV SM Higgs boson is also shown in red.

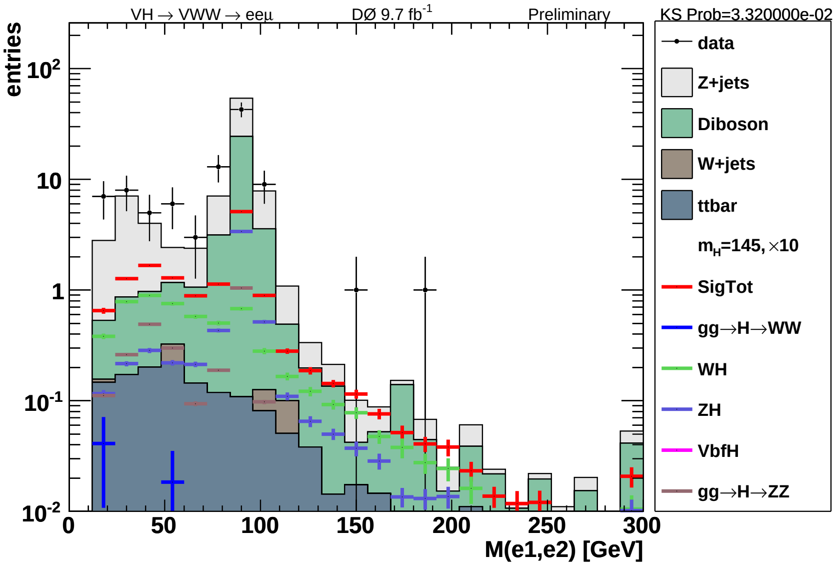

(a)

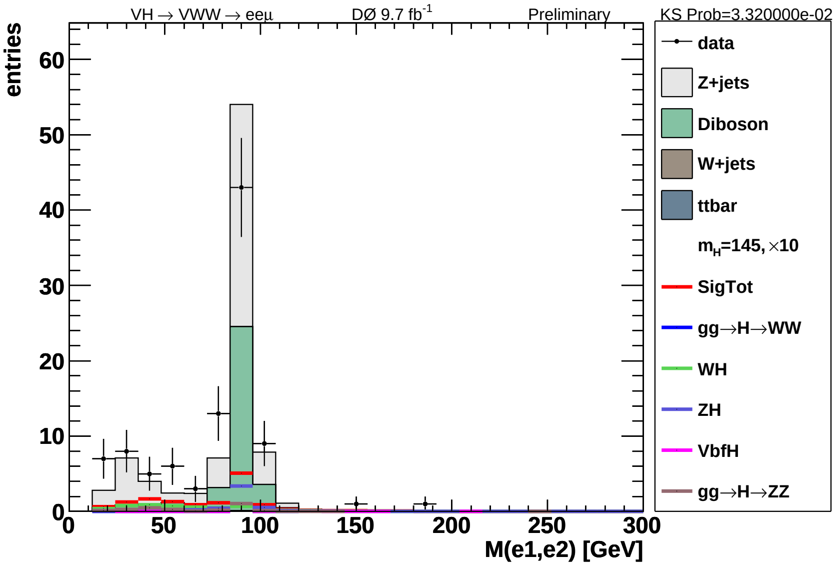

(b)

Figure 6-10: Distribution of the invariant mass of the di-electron pair, $M_{(e_1 e_2)}$, in (a) logarithmic scale and (b) linear scale for data (points) and sum of all the backgrounds (histograms). The expected signal, multiplied by a factor of 10, for a 145 GeV SM Higgs boson is also shown in red.

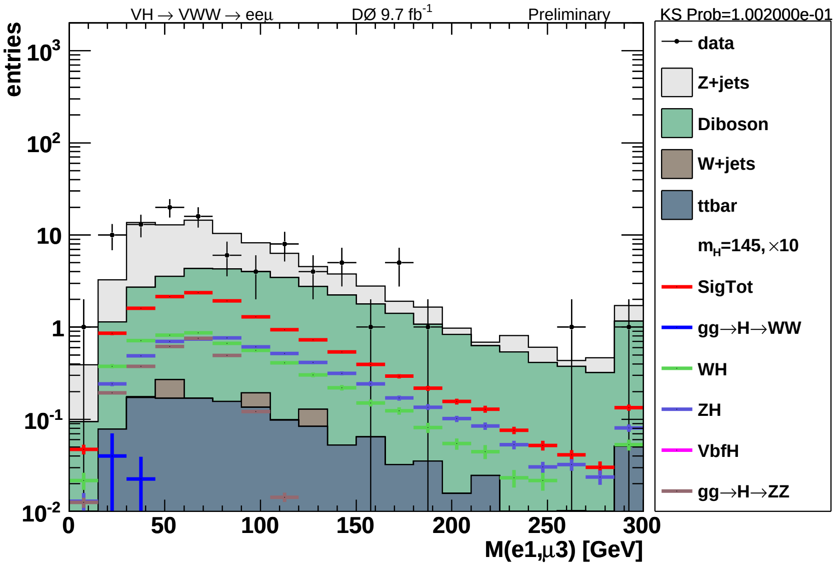

(a)

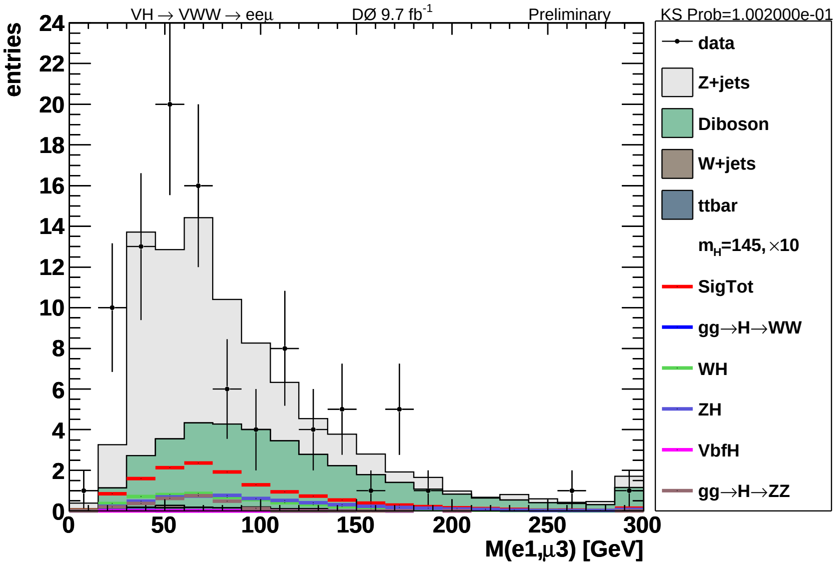

(b)

Figure 6-11: Distribution of the invariant mass of the leading electron with the muon, $M_{(e_1\mu)}$, in (a) logarithmic scale and (b) linear scale for data (points) and sum of all the backgrounds (histograms). The expected signal, multiplied by a factor of 10, for a 145 GeV SM Higgs boson is also shown in red.

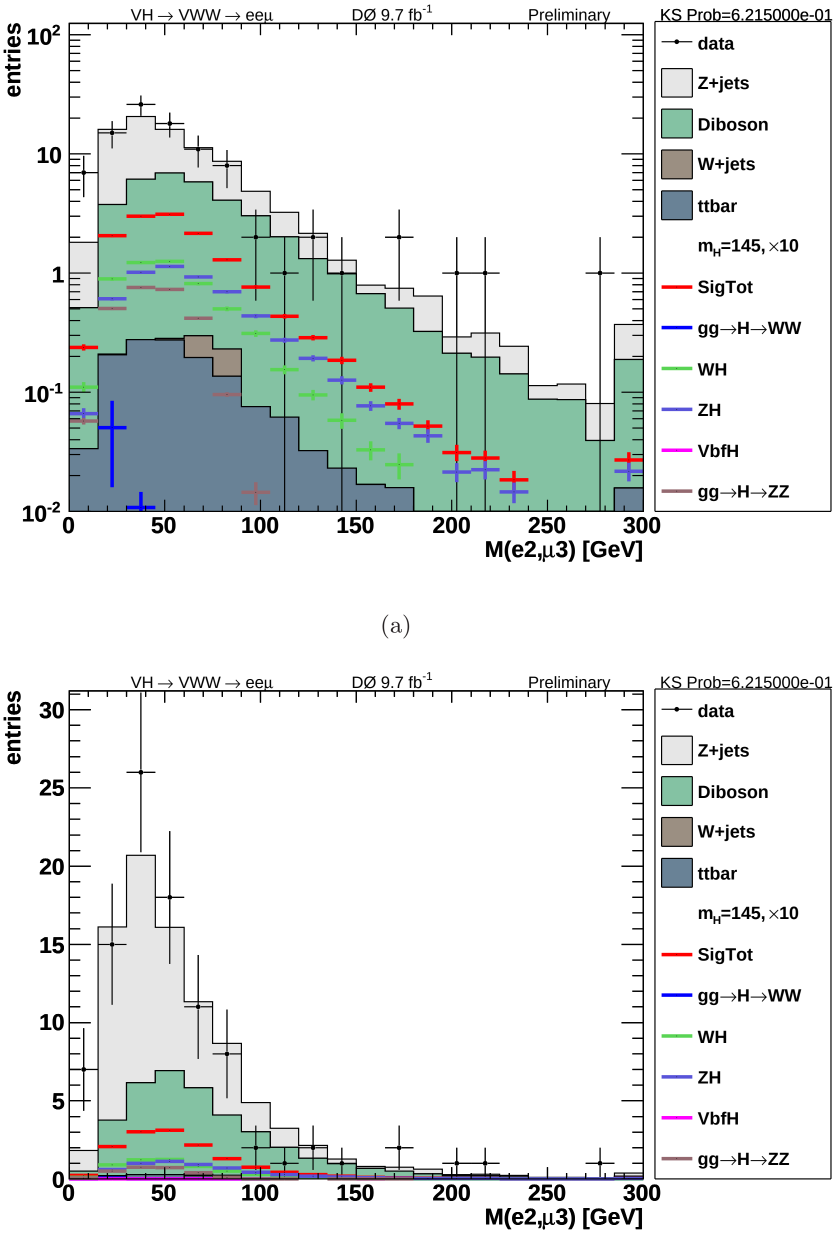

(a)

(b)

Figure 6-12: Distribution of the invariant mass of the trailing electron with the muon, $M_{(e_2\mu)}$, in (a) logarithmic scale and (b) linear scale for data (points) and sum of all the backgrounds (histograms). The expected signal, multiplied by a factor of 10, for a 145 GeV SM Higgs boson is also shown in red.

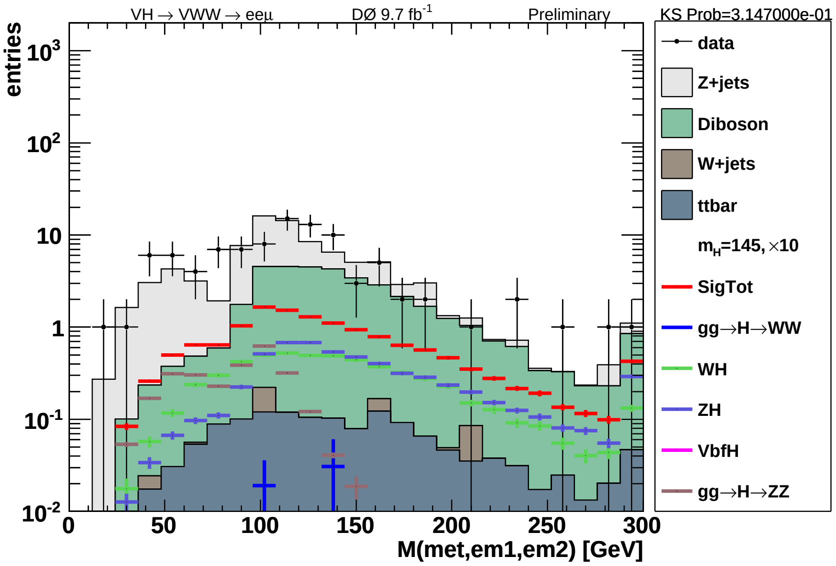

(a)

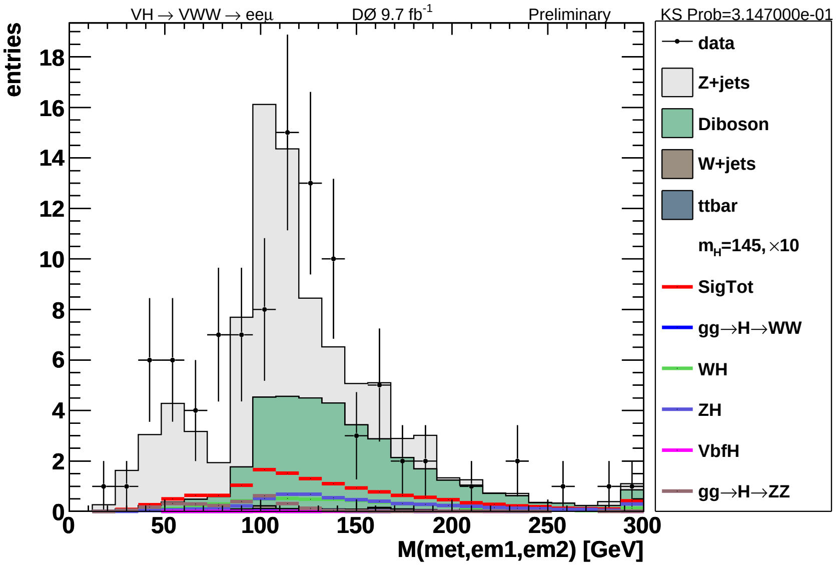

(b)

Figure 6-13: Distribution of the invariant mass of the di-electron pair with missing transverse energy $\not{E}_T$, $M_{(e_1e_2MET)}$, in (a) logarithmic scale and (b) linear scale for data (points) and sum of all the backgrounds (histograms). The expected signal, multiplied by a factor of 10, for a 145 GeV SM Higgs boson is also shown in red.

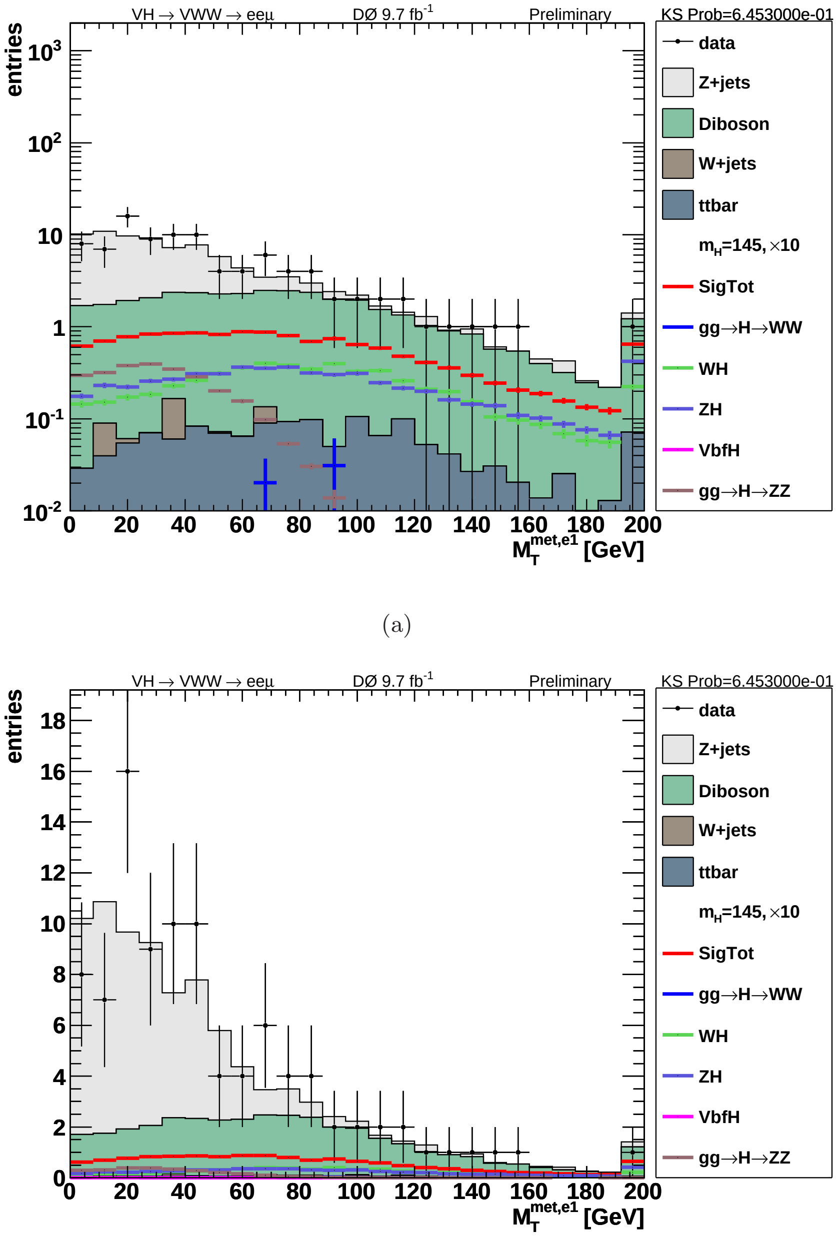

(a)

(b)

Figure 6-14: Distribution of the transverse mass between the leading electron and $\not\!\!E_T$, $M_T^{(e_1,MET)}$, in (a) logarithmic scale and (b) linear scale for data (points) and sum of all the backgrounds (histograms). The expected signal, multiplied by a factor of 10, for a 145 GeV SM Higgs boson is also shown in red.

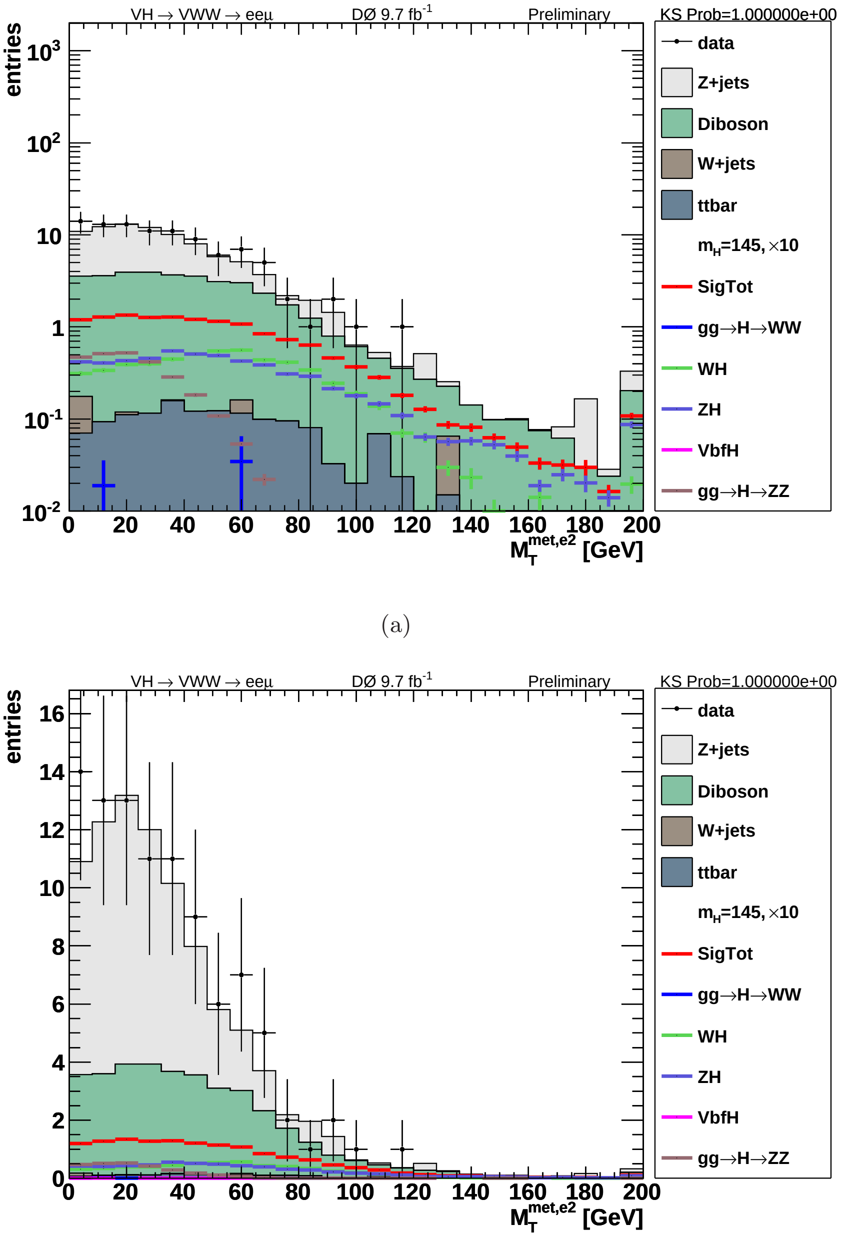

(a)

(b)

Figure 6-15: Distribution of the transverse mass between the trailing electron and $\not\!\!E_T$, $M_T^{(e_2,MET)}$, in (a) logarithmic scale and (b) linear scale for data (points) and sum of all the backgrounds (histograms). The expected signal, multiplied by a factor of 10, for a 145 GeV SM Higgs boson is also shown in red.

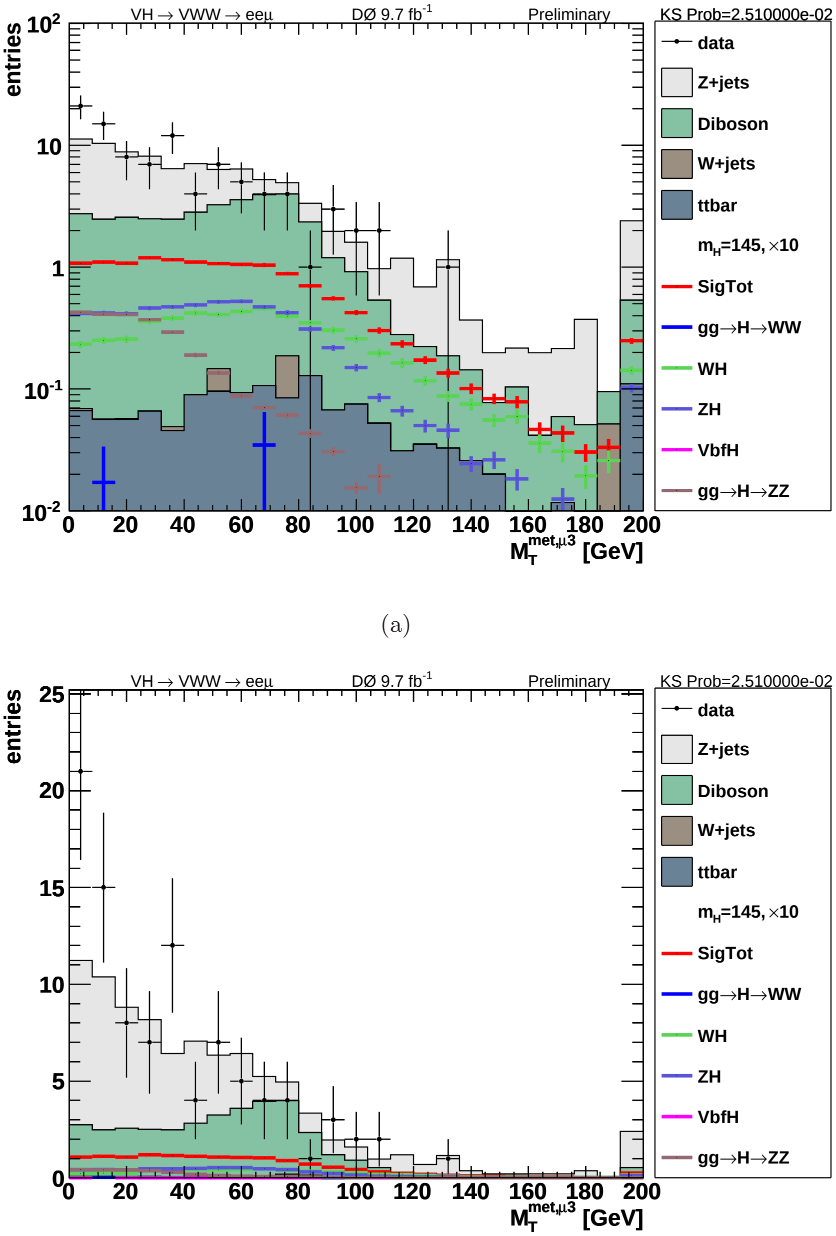

(a)

(b)

Figure 6-16: Distribution of the transverse mass between the muon and $\not{E}_T$, $M_T^{(\mu,MET)}$, in (a) logarithmic scale and (b) linear scale for data (points) and sum of all the backgrounds (histograms). The expected signal, multiplied by a factor of 10, for a 145 GeV SM Higgs boson is also shown in red.

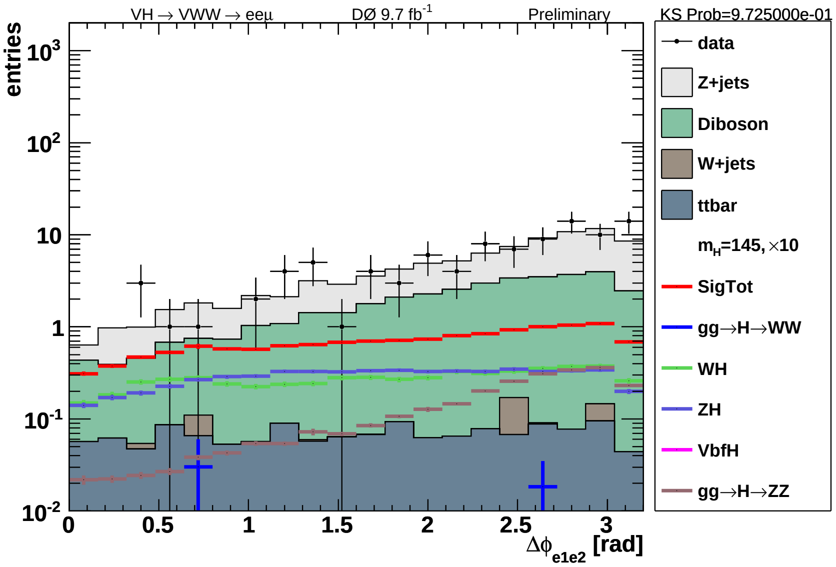

(a)

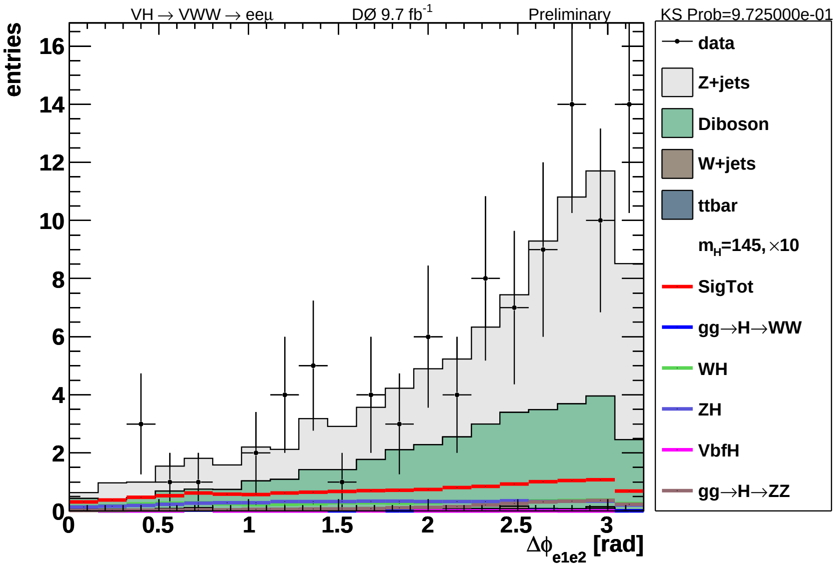

(b)

Figure 6-17: Distribution of the opening angle between the di-election pair, $\Delta\phi_{(e_1,e_2)}$, in (a) logarithmic scale and (b) linear scale for data (points) and sum of all the backgrounds (histograms). The expected signal, multiplied by a factor of 10, for a 145 GeV SM Higgs boson is also shown in red.

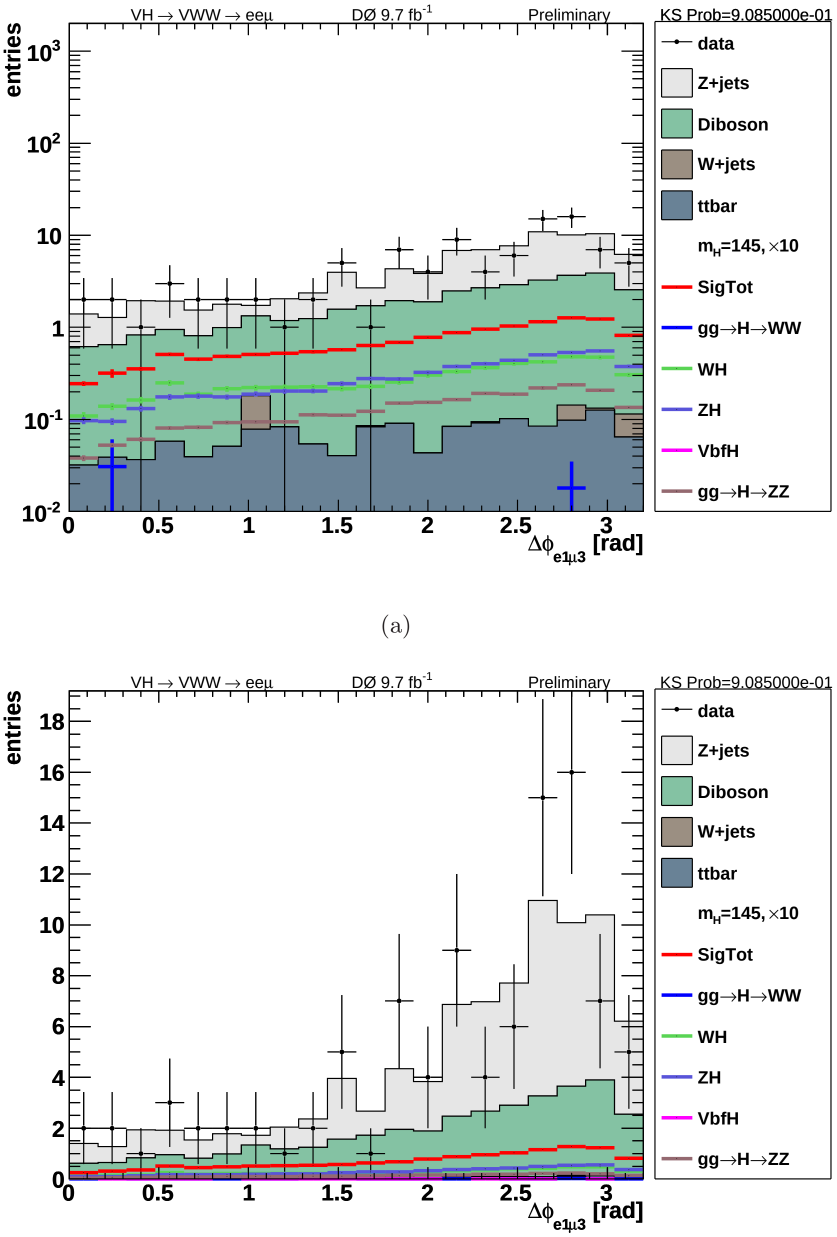

(a)

(b)

Figure 6-18: Distribution of the opening angle between the leading electron and the muon, $\Delta\phi_{(e_1,\mu)}$, in (a) logarithmic scale and (b) linear scale for data (points) and sum of all the backgrounds (histograms). The expected signal, multiplied by a factor of 10, for a 145 GeV SM Higgs boson is also shown in red.

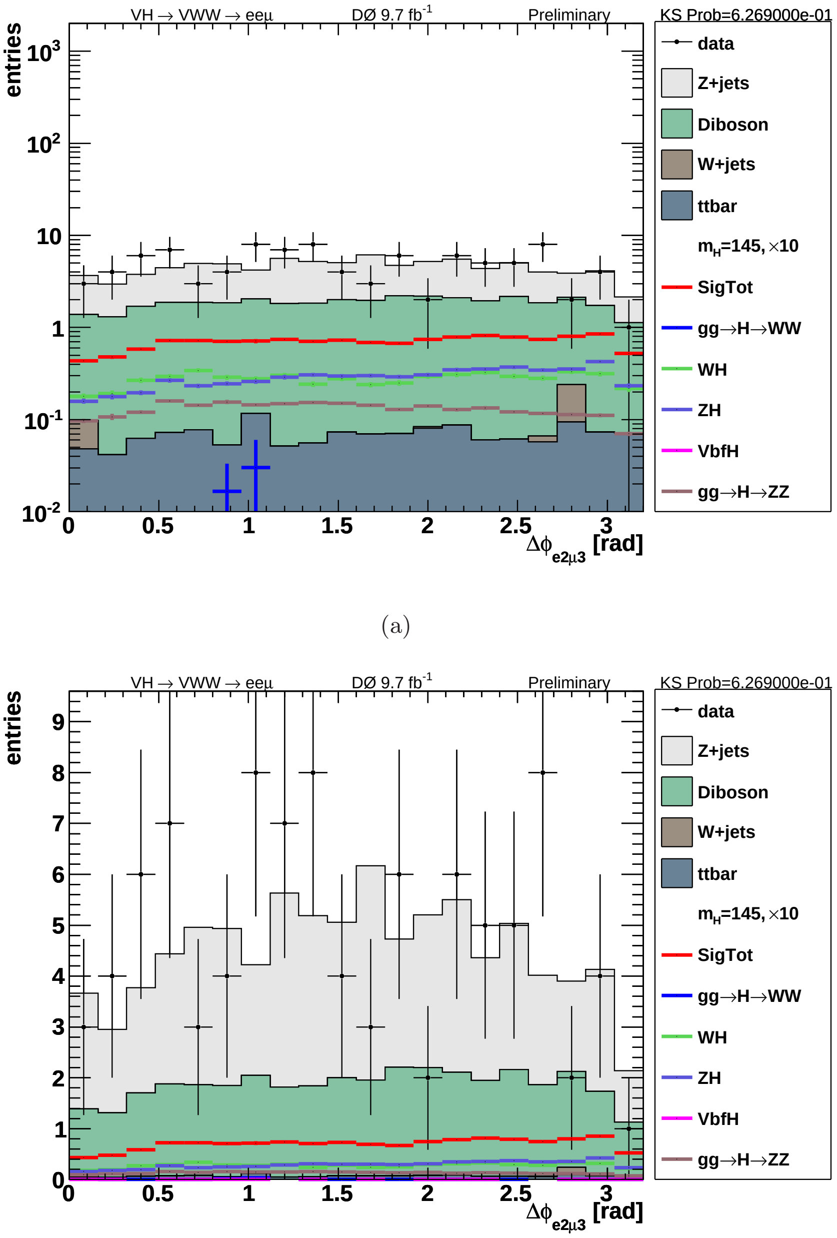

(a)

(b)

Figure 6-19: Distribution of the opening angle between the trailing electron and the muon, $\Delta\phi_{(e_2,\mu)}$, in (a) logarithmic scale and (b) linear scale for data (points) and sum of all the backgrounds (histograms). The expected signal, multiplied by a factor of 10, for a 145 GeV SM Higgs boson is also shown in red.

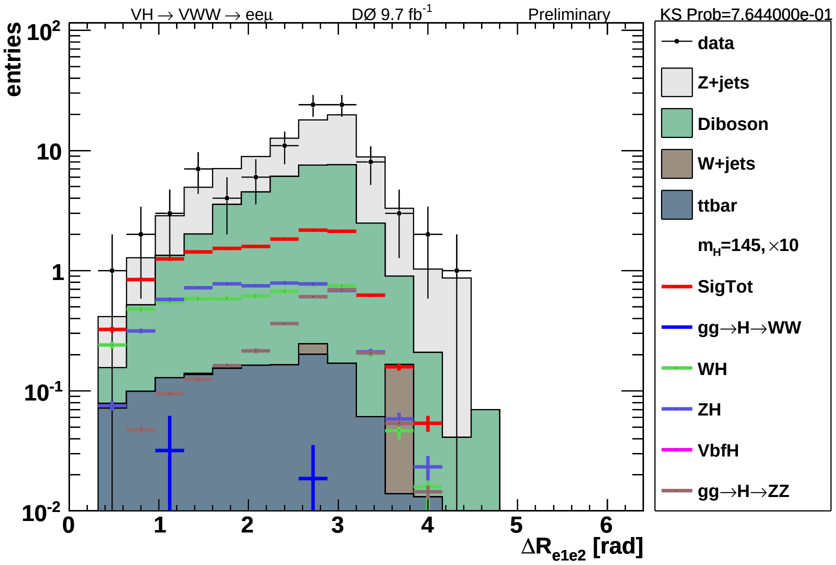

(a)

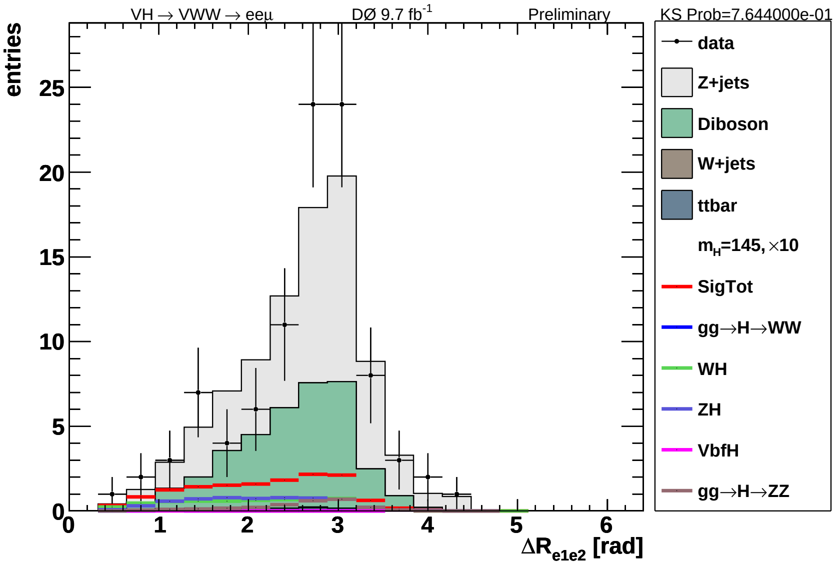

(b)

Figure 6-20: Distribution of the $\Delta\mathcal{R}$ between the di-electron pair, $\Delta\mathcal{R}_{(e_1,e_2)}$, in (a) logarithmic scale and (b) linear scale for data (points) and sum of all the backgrounds (histograms). The expected signal, multiplied by a factor of 10, for a 145 GeV SM Higgs boson is also shown in red.

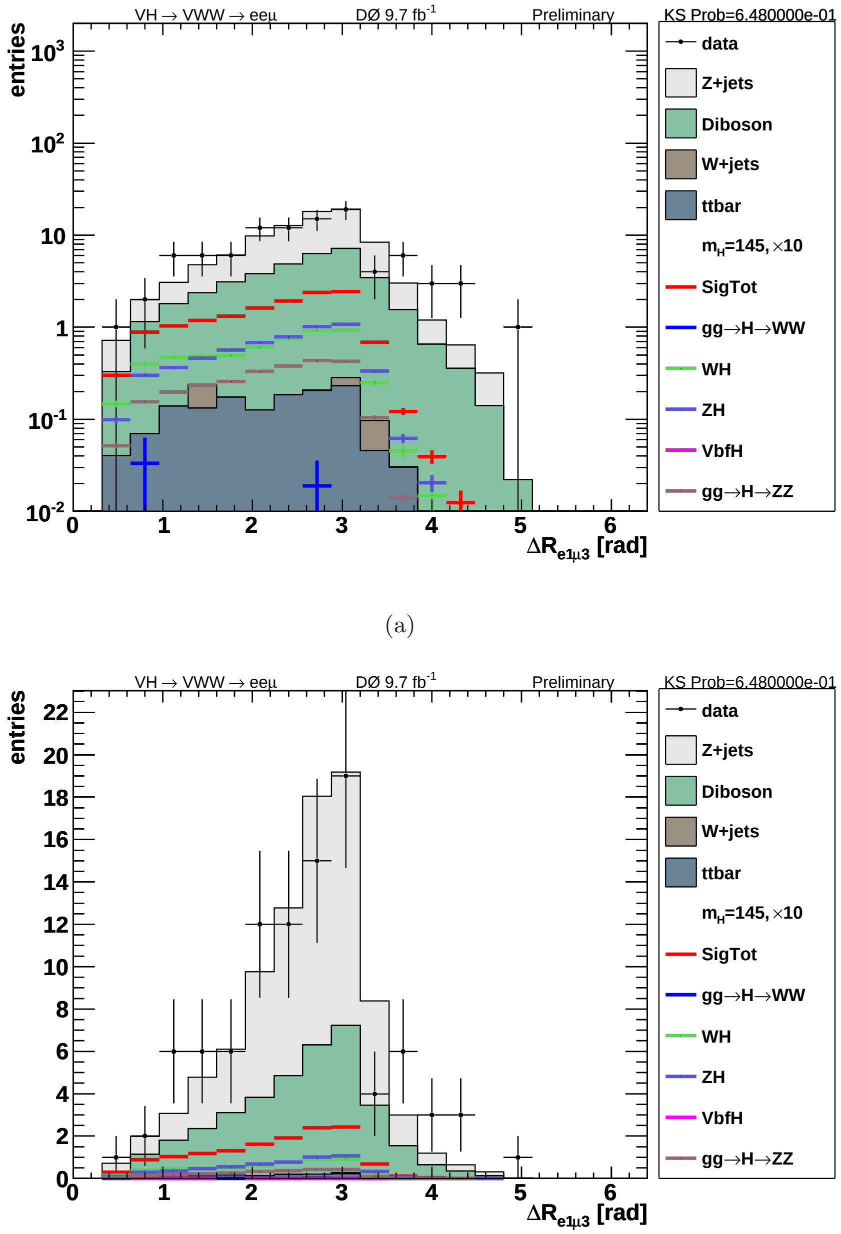

(a)

(b)

Figure 6-21: Distribution of the $\Delta\mathcal{R}$ between the leading electron and the muon, $\Delta\mathcal{R}_{(e_1,\mu)}$, in (a) logarithmic scale and (b) linear scale for data (points) and sum of all the backgrounds (histograms). The expected signal, multiplied by a factor of 10, for a 145 GeV SM Higgs boson is also shown in red.

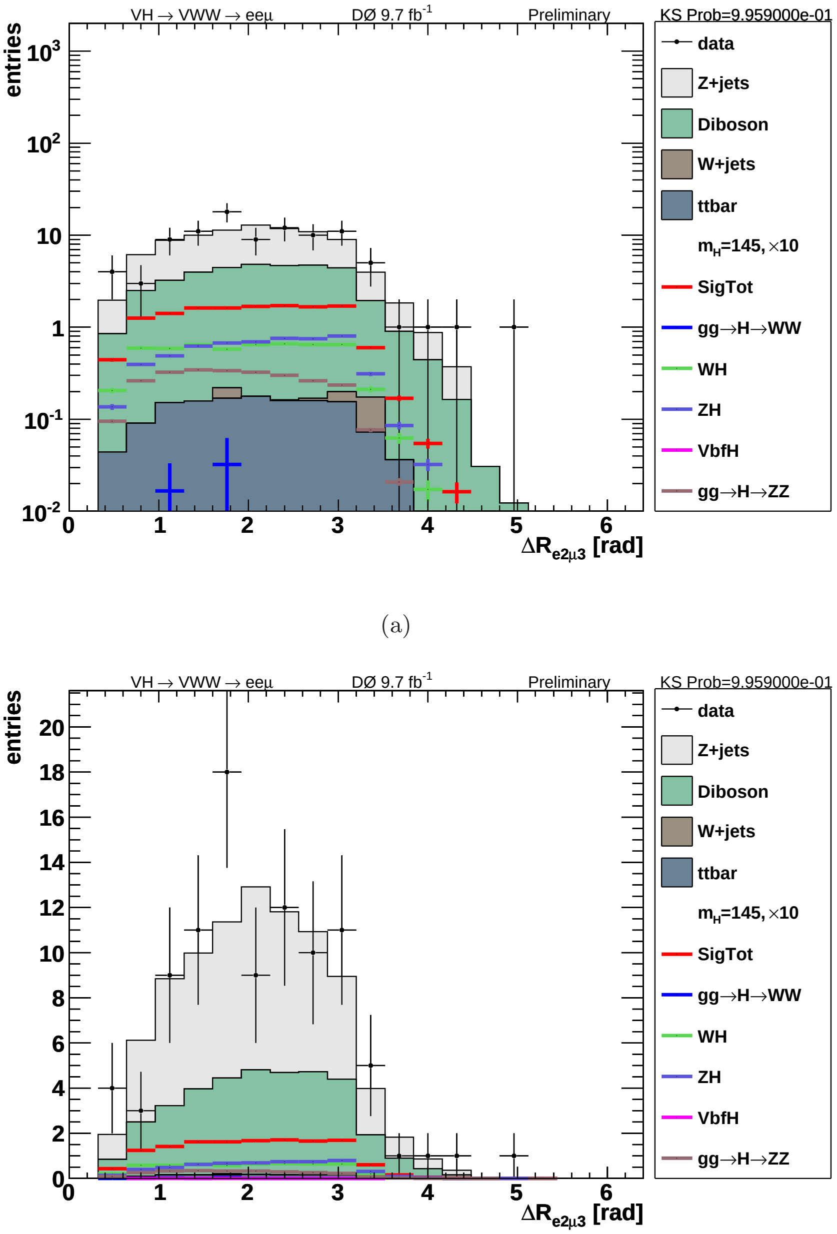

(a)

(b)

Figure 6-22: Distribution of the $\Delta\mathcal{R}$ between the trailing electron and the muon, $\Delta\mathcal{R}_{(e_2,\mu)}$, in (a) logarithmic scale and (b) linear scale for data (points) and sum of all the backgrounds (histograms). The expected signal, multiplied by a factor of 10, for a 145 GeV SM Higgs boson is also shown in red.

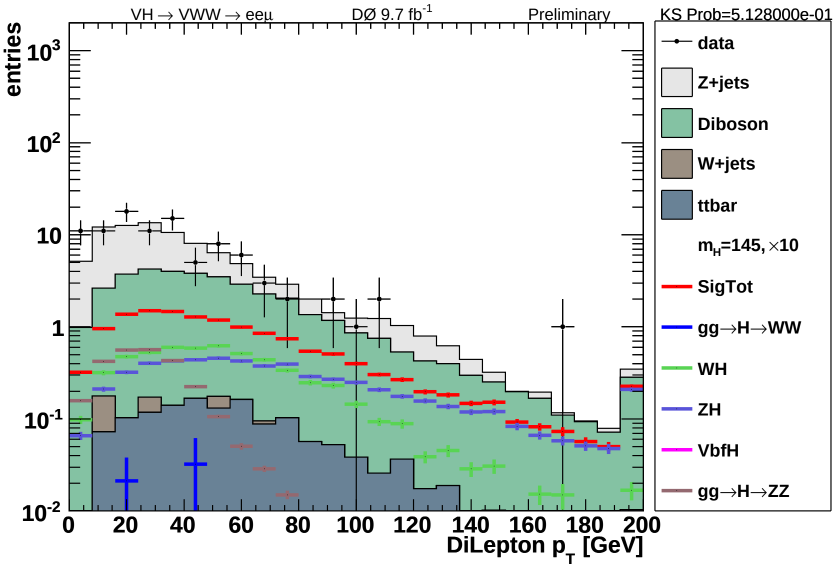

(a)

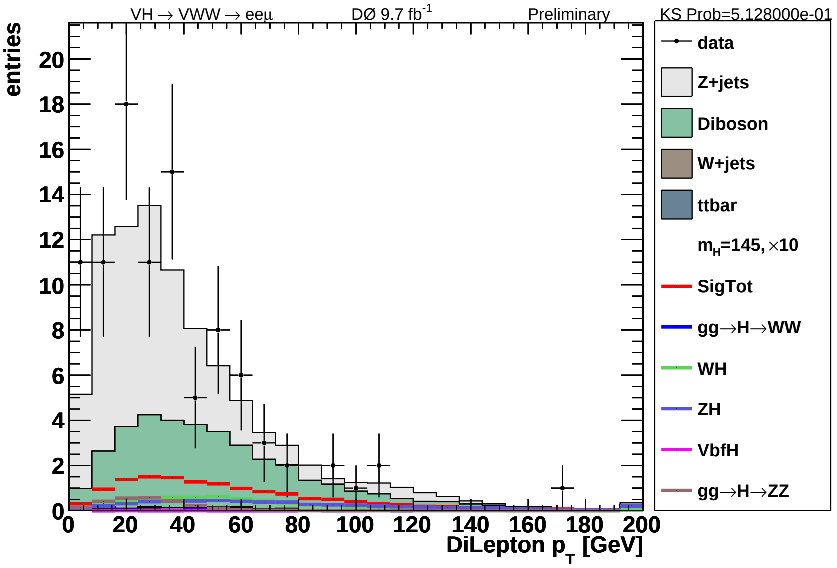

(b)

Figure 6-23: Distribution of the transverse momentum of the di-electron system, $p_T^{e_1e_2}$, in (a) logarithmic scale and (b) linear scale for data (points) and sum of all the backgrounds (histograms). The expected signal, multiplied by a factor of 10, for a 145 GeV SM Higgs boson is also shown in red.

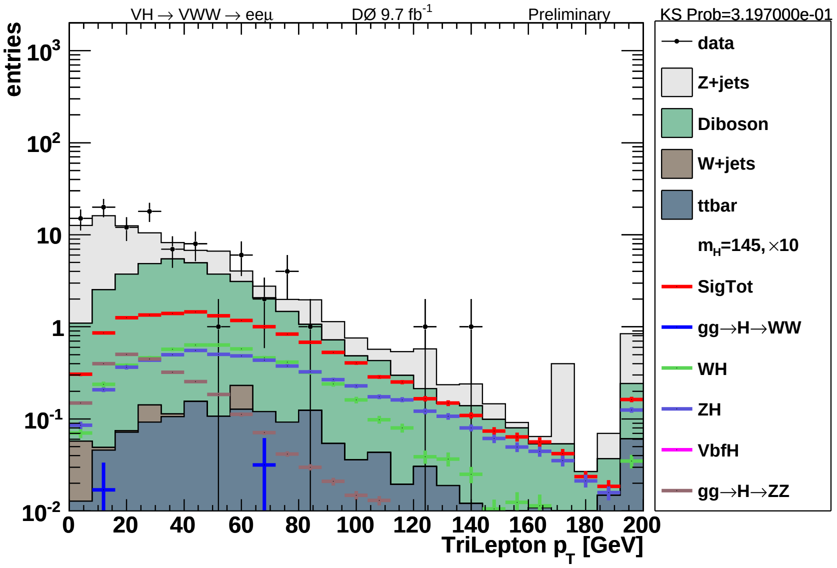

(a)

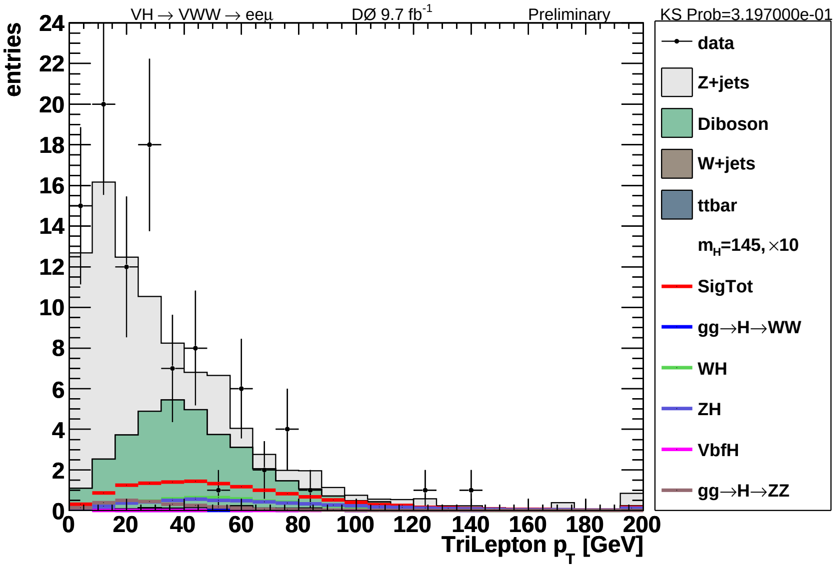

(b)

Figure 6-24: Distribution of the transverse momentum of the di-electron system with the muon, $p_T^{e_1 e_2 \mu}$, in (a) logarithmic scale and (b) linear scale for data (points) and sum of all the backgrounds (histograms). The expected signal, multiplied by a factor of 10, for a 145 GeV SM Higgs boson is also shown in red.

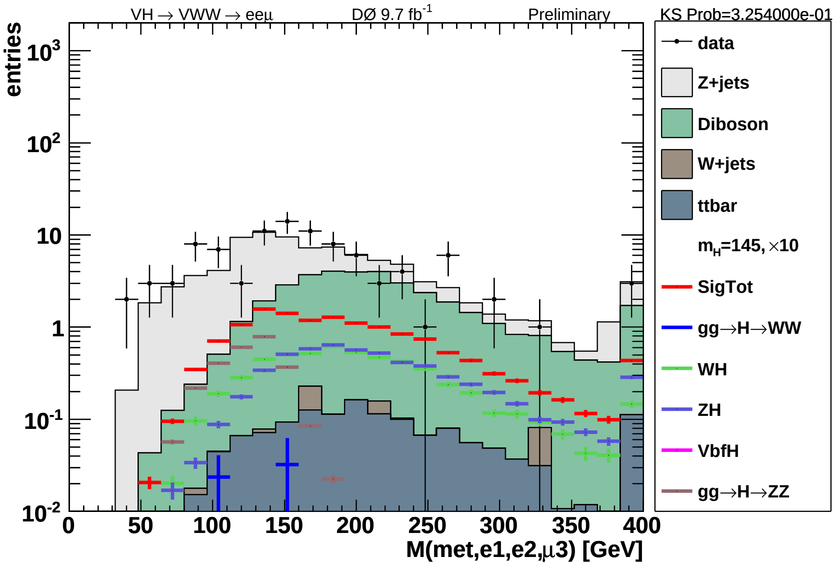

(a)

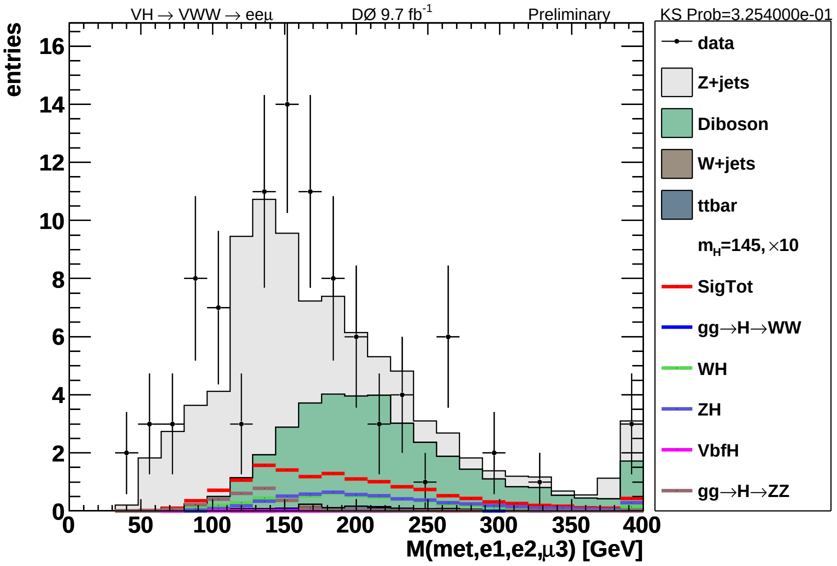

(b)

Figure 6-25: Distribution of the invariant mass of the di-electron pair with the muon and $\not\!\!E_T$, $M_{(e_1 e_2 \mu MET)}$, in (a) logarithmic scale and (b) linear scale for data (points) and sum of all the backgrounds (histograms). The expected signal, multiplied by a factor of 10, for a 145 GeV SM Higgs boson is also shown in red.

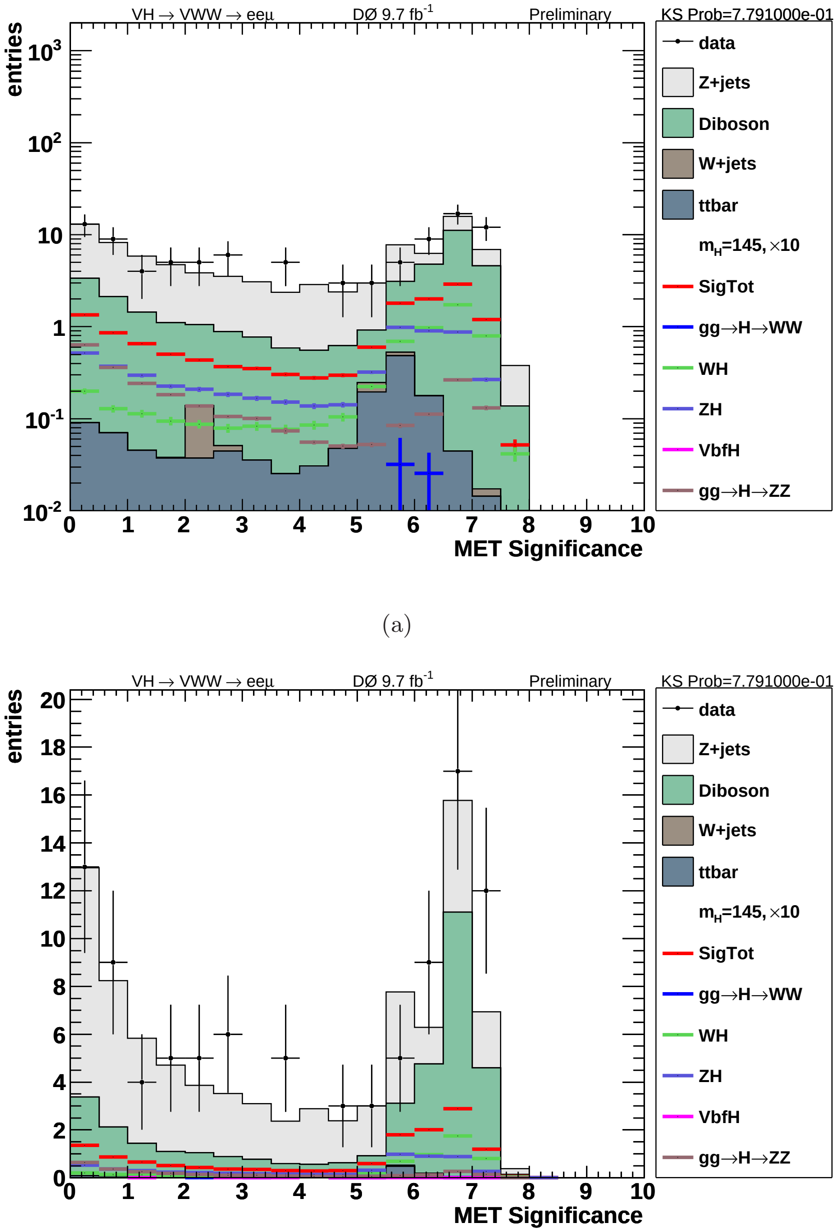

(a)

(b)

Figure 6-26: Distribution of the missing transverse momentum significance, ${\not\!\!E_T}^{signif}$ – defined in Section 3.5, in (a) logarithmic scale and (b) linear scale for data (points) and sum of all the backgrounds (histograms). The expected signal, multiplied by a factor of 10, for a 145 GeV SM Higgs boson is also shown in red.

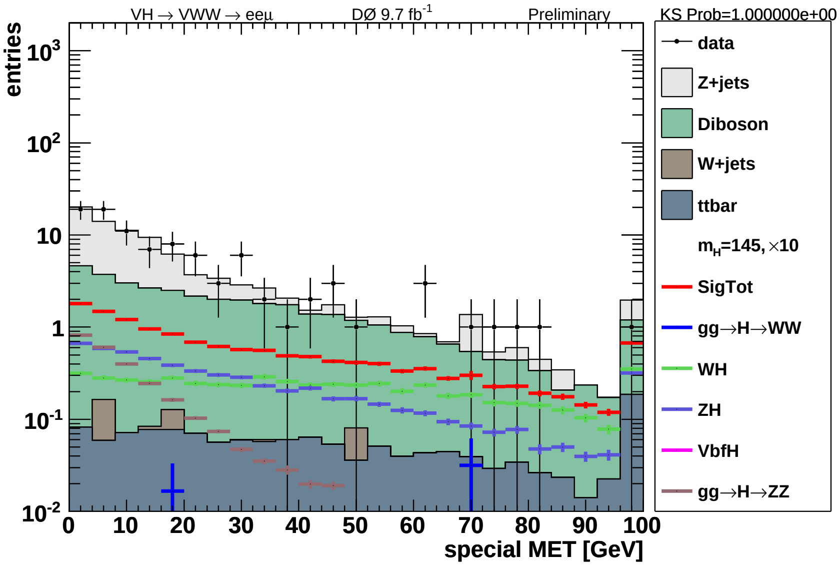

(a)

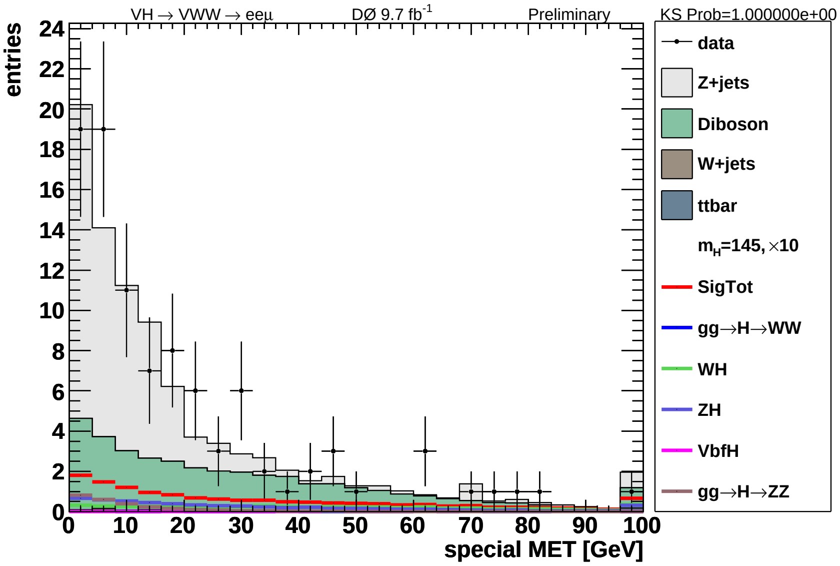

(b)

Figure 6-27: Distribution of the special missing transverse momentum, $\not\!\!E_T{}^{special}$ – defined in Section 3.5, in (a) logarithmic scale and (b) linear scale for data (points) and sum of all the backgrounds (histograms). The expected signal, multiplied by a factor of 10, for a 145 GeV SM Higgs boson is also shown in red.

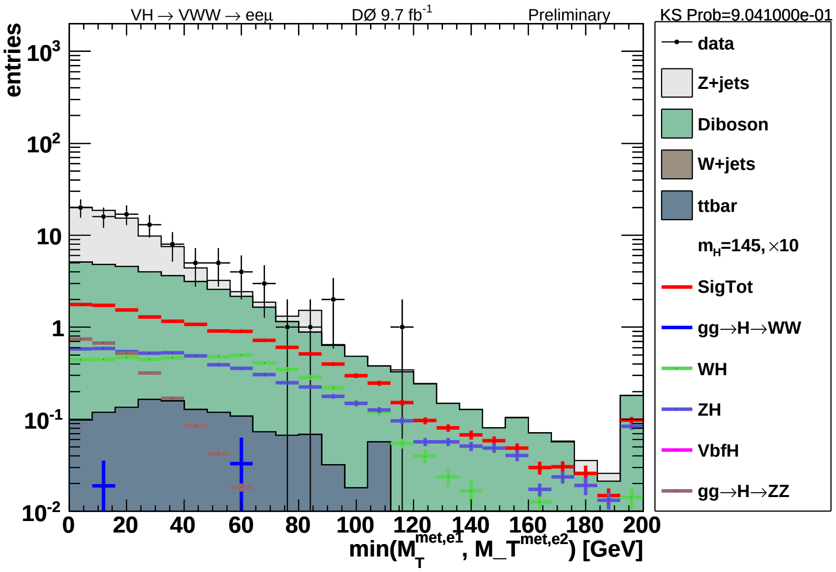

(a)

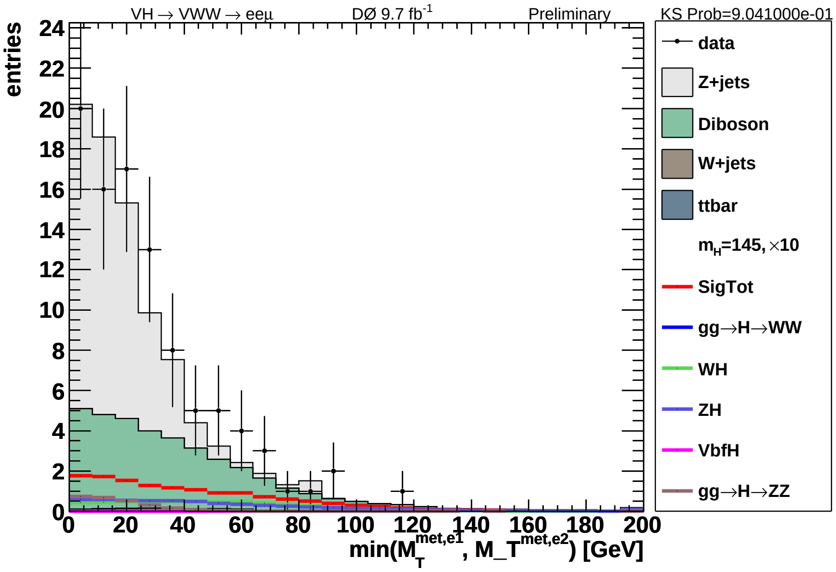

(b)

Figure 6-28: Distribution of the minimum transverse mass between either leading or trailing electron and $\not\!\!E_T$, $min\left(M_T^{(e_1,MET)}, M_T^{(e_2,MET)}\right)$, in (a) logarithmic scale and (b) linear scale for data (points) and sum of all the backgrounds (histograms). The expected signal, multiplied by a factor of 10, for a 145 GeV SM Higgs boson is also shown in red.

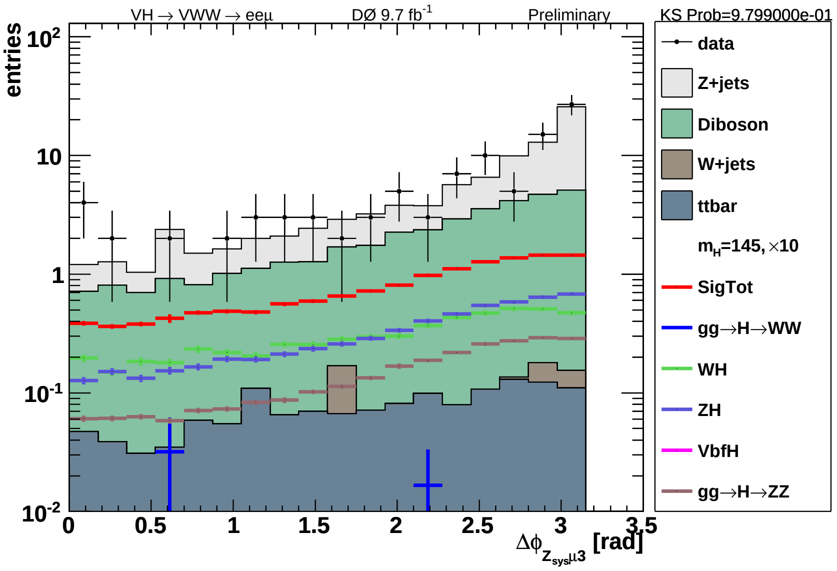

(a)

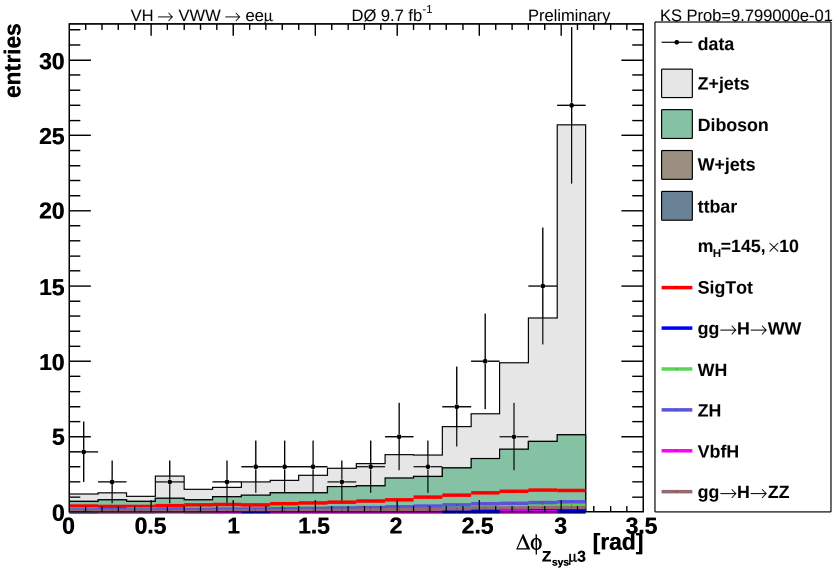

(b)

Figure 6-29: Distribution of the opening angle between the di-electron system and the muon, $\Delta\phi_{(e_1e_2,\mu)}$, in (a) logarithmic scale and (b) linear scale for data (points) and sum of all the backgrounds (histograms). The expected signal, multiplied by a factor of 10, for a 145 GeV SM Higgs boson is also shown in red.

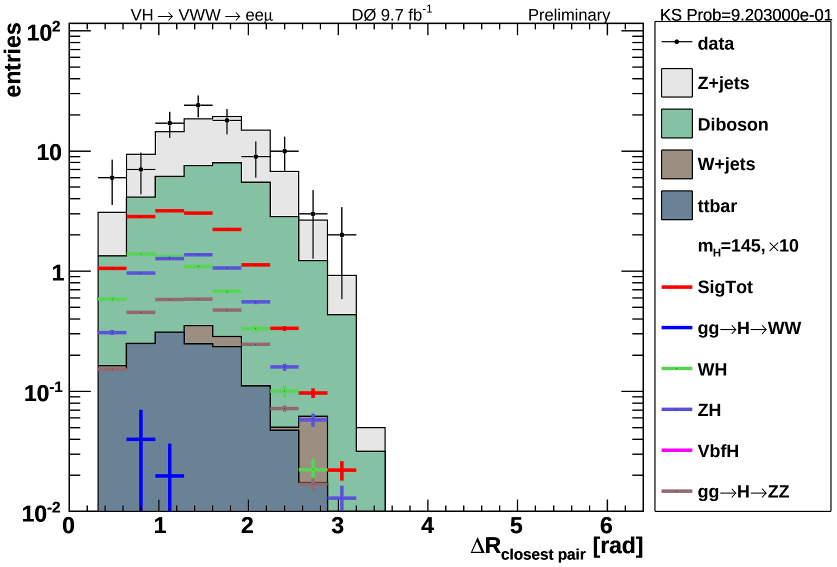

(a)

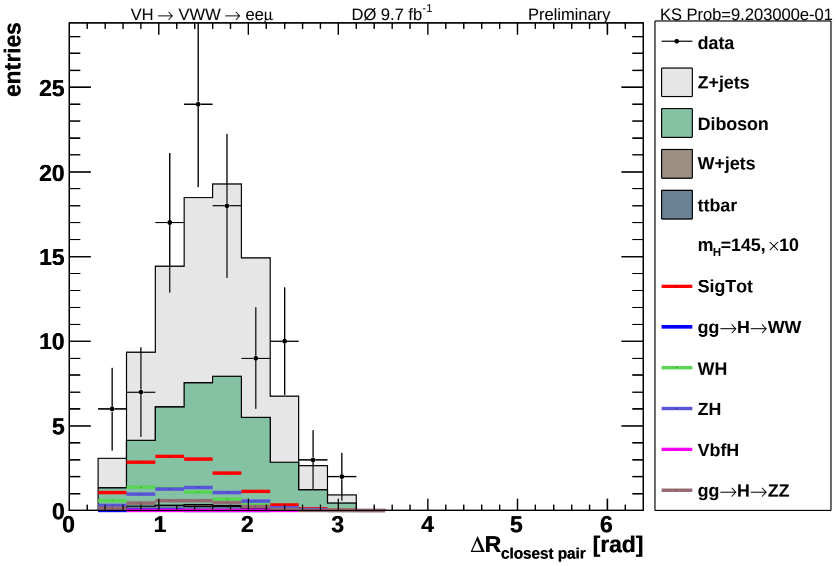

(b)

Figure 6-30: Distribution of the minimum or closest $\Delta\mathcal{R}$ between all three possible lepton pairs, $min(\Delta\mathcal{R}_{(e_1,e_2)}, \Delta\mathcal{R}_{(e_1,\mu)}, \Delta\mathcal{R}_{(e_2,\mu)})$, in (a) logarithmic scale and (b) linear scale for data (points) and sum of all the backgrounds (histograms). The expected signal, multiplied by a factor of 10, for a 145 GeV SM Higgs boson is also shown in red.

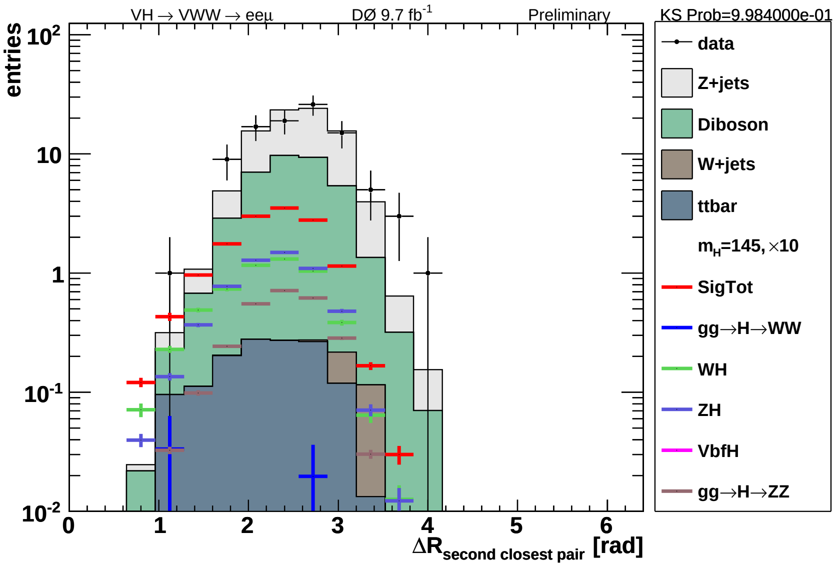

(a)

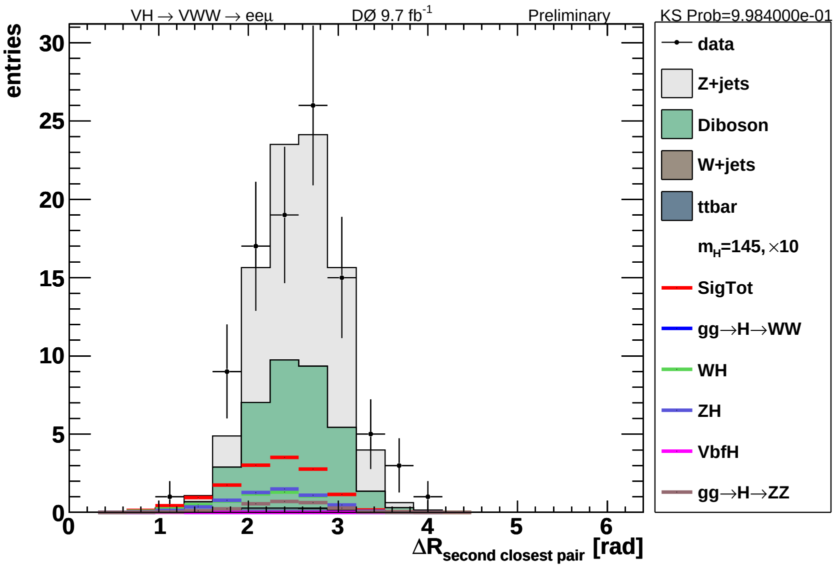

(b)

Figure 6-31: Distribution of the second closest $\Delta\mathcal{R}$ between all three possible lepton pairs, $med(\Delta\mathcal{R}_{(e_1,e_2)}, \Delta\mathcal{R}_{(e_1,\mu)}, \Delta\mathcal{R}_{(e_2,\mu)})$, in (a) logarithmic scale and (b) linear scale for data (points) and sum of all the backgrounds (histograms). The expected signal, multiplied by a factor of 10, for a 145 GeV SM Higgs boson is also shown in red.

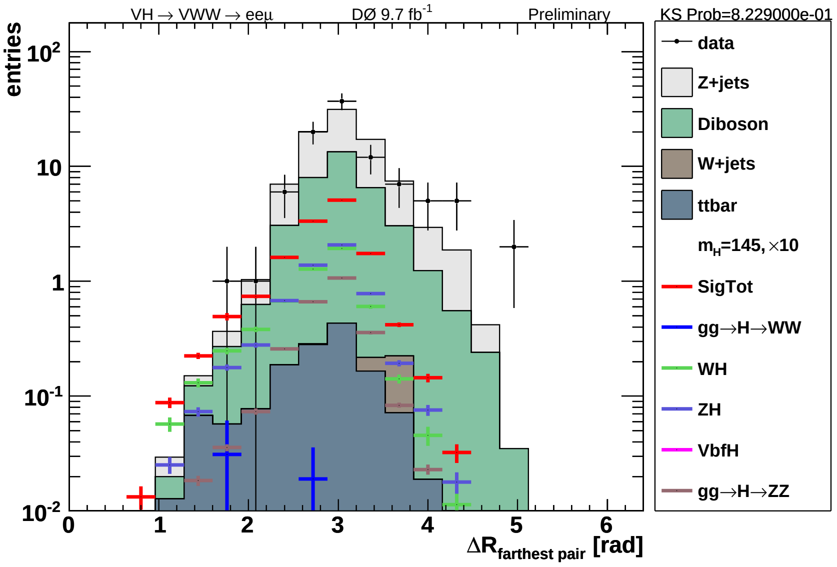

(a)

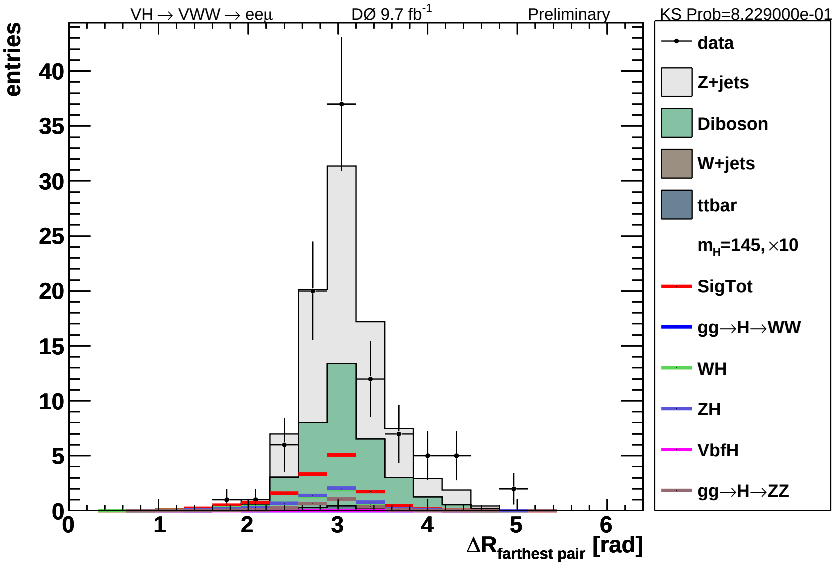

(b)

Figure 6-32: Distribution of the farthest distance in $\Delta\mathcal{R}$ between all three possible lepton pairs, $max(\Delta\mathcal{R}_{(e_1,e_2)}, \Delta\mathcal{R}_{(e_1,\mu)}, \Delta\mathcal{R}_{(e_2,\mu)})$, in (a) logarithmic scale and (b) linear scale for data (points) and sum of all the backgrounds (histograms). The expected signal, multiplied by a factor of 10, for a 145 GeV SM Higgs boson is also shown in red.

6.3.2 Systematic Uncertaintes

We apply both flat (constant value for all mass points) and shape (the central value is shifted by $\pm 1\sigma$ and then run through the entire analysis chain. The difference in the cross section limits is then taken as the uncertainty) systematic uncertainties to the limit calculation. They are as follows.

To account for the lepton ID efficiencies, a 2.5% (4%) systematic uncertainty is applied for each electron (muon) in the final state. A PDF uncertainty of 2.5% and a trigger efficiency uncertainty of 3.5% is applied to both the signal and background MC samples. We assign a 6.2% theoretical cross section uncertainty to the associated production (VH) signals, a 5% cross section uncertainty to the gluon-gluon fusion ($ggH, H \to VV$) signals, and a 4.9% uncertainty on the vector boson fusion ($q\bar{q} \to q\bar{q}H$) signal. A 6% theoretical cross section uncertainty is applied to the diboson background MC, while a 7% uncertainty is added to the $t\bar{t}$ sample. The theoretical cross section uncertainty for the $Z + \text{jets}$ and $W + \text{jets}$ backgrounds are estimated to be $\pm 6\%$ each with an additional 30% uncertainty on these samples due to the uncertainty on the jet-to-lepton fake rate. The luminosity uncertainty is assigned to be 6.1%.

An uncertainty in the shape of the Z–p_T reweighting distributions is calculated by shifting the reweighting function by $\pm 1\sigma$. The uncertainty due to electron (muon) p_T resolution is estimated by applying a $\pm 1\sigma$ variation in the electron (muon) smearing function.

Table 6-2 summarizes the systematic uncertainties applied to the $ee\mu$ final state.

6.3.3 Multivariate Analysis Training

To get as much separation between signal and background as possible, we use decision trees (DTs) within the multivariate analysis (MVA) framework TMVA [101], discussed in more detail in Appendix C. DTs are trained for each of the Higgs boson mass points from $m_H = 100 - 200$ GeV in intervals of 5 GeV.

In order to ensure that the final discriminant DT is performed on an independent

Table 6-2: Systematic uncertainties applied.

	Systematic Uncertainties in percent					
	Signal	$\sum$ Bkgnd	Diboson	$t\bar{t}$	$Z+$jets	$W+$jets
			Flat Systematics			
EM ID	2.5	2.5	–	–	–	–
MU ID	4	4	–	–	–	–
Luminosity	6.1	6.1	–	–	–	–
PDF	2.5	2.5	–	–	–	–
σ_{VH}	6.2	–	–	–	–	–
σ_{ggH}	7.0	–	–	–	–	–
σ_{VFB}	4.9	–	–	–	–	–
σ_{Bkgnd}	–	–	6	7	6	6
jet $\rightarrow \mu$ fake rate	–	–	–	–	30	30
Trigger	3.5	3.5	–	–	–	–
			Shape Systematics			
Z-p_T rew.	–	–	–	–	$\pm 1\sigma$	–
Electron smearing	$\pm 1\sigma$	$\pm 1\sigma$	–	–	–	–
Muon smearing	$\pm 1\sigma$	$\pm 1\sigma$	–	–	–	–

sample of events, both the signal and background are split into two equal parts, depending on the run and event numbers (one for training and testing and the other for limit setting). The WH and ZH MC samples are used to train the signal, while all backgrounds are included to train against the background. To increase the statistics available for training, neighboring mass points are added together.

The following list of 12 input variables are used for the $ee\mu$ channel training and testing:

- transverse momentum of the trailing electron (Fig. 6-3),
- invariant mass of the di-electron pair (Fig. 6-10),
- invariant mass of the di-electron pair with the muon and $\not{E}_T$ (Fig. 6-25),
- transverse momentum of the di-electron pair with the muon (Fig. 6-24),
- transverse momentum of the di-electron pair (Fig. 6-23),
- opening angle in ϕ between the di-electron system and the muon (Fig. 6-29),

- opening angle in η and ϕ space between the closest two leptons (Fig. 6-30),
- opening angle in η and ϕ space between the second closest two leptons (Fig. 6-31),
- opening angle in ϕ between the di-electron pair (Fig. 6-17),
- ${\not\!\!E_T}^{signif}$ (Fig. 6-26),
- ${\not\!\!E_T}^{special}$ (Fig. 6-27), and
- minimum transverse mass between either electron and $\not\!\!E_T$ or MET (Fig. 6-28).

Figure 6-33 shows the signal versus background separation for the variables used to train the DTs, while Fig. 6-34 shows the overtraining distribution, both for a Higgs boson mass of $m_H = 145$ GeV. Overtraining is due to training on statistical fluctuations rather than on real events and can lead to grossly under/over-estimated limits. We optimize the training variables at $m_H = 145$ GeV only (since it has the highest signal acceptance) and use the KS probability between the independent training and testing samples, given in Fig. 6-34, to determine if the training results are acceptable. We look to see if both the training and test signal and background samples are statistically consistent, indicating that the test sample demonstrates that the DT is not overtrained.

Figures 6-35 – 6-40 show the final discriminant (FD) DT distributions for the Higgs boson masses of 105 GeV, 115 GeV, 125 GeV, 135 GeV, 145 GeV, and 165 GeV, with the expected signal multiplied by a factor of 10. As the mass increases, the separation between the signal and background distributions becomes more significant. This is due to the increase in $H \to WW^*$ production sensitivity at higher masses. We can also see that for increasing mass, the $H \to ZZ$ signal becomes very background-like, as we are training with a number of missing energy variables that discriminate against the lack of $\not\!\!E_T$ in the four lepton final state. The rest of the final discriminant DT distributions can be found in Appendix E.

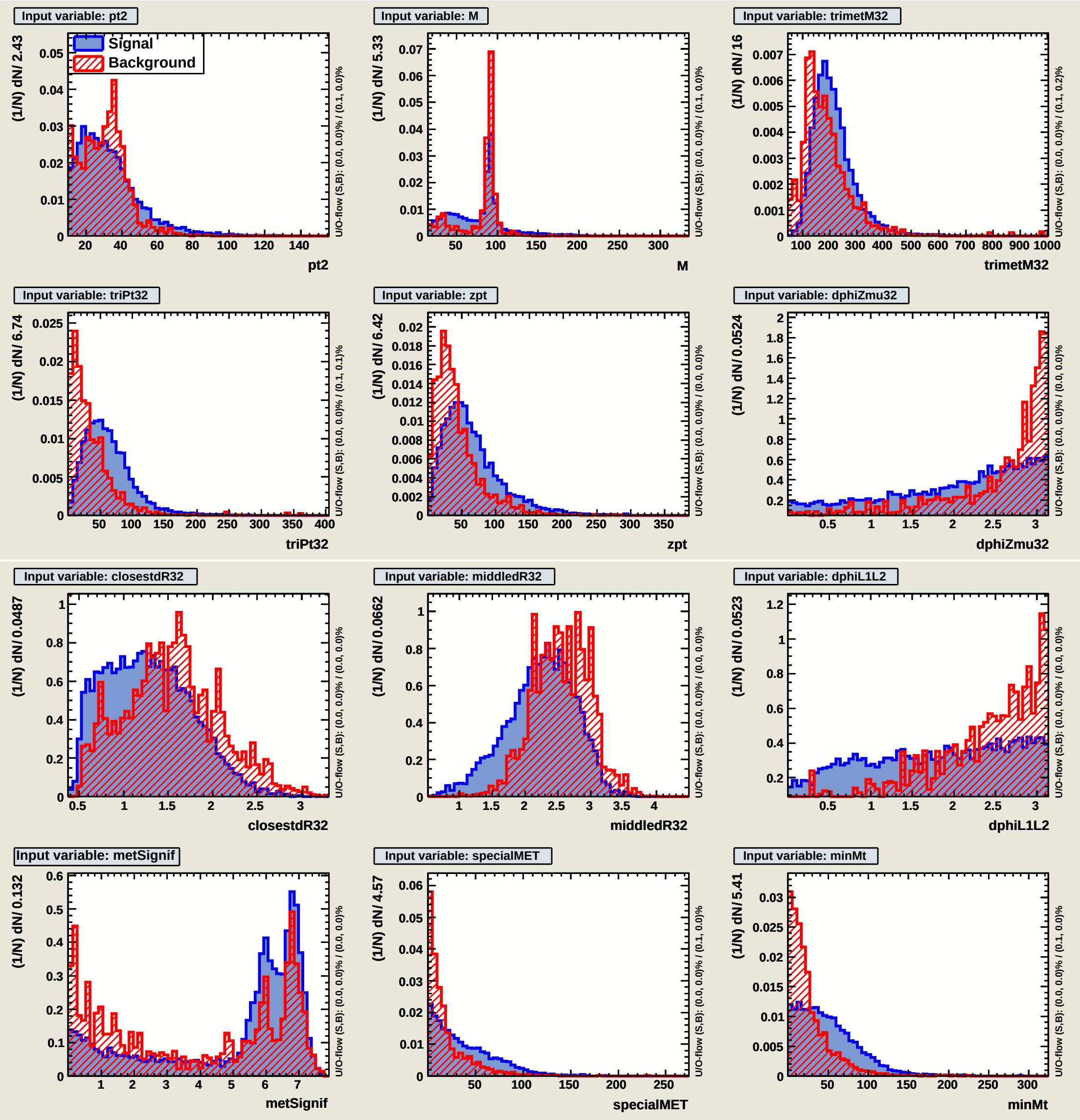

Figure 6-33: The signal versus background separation distributions for the 12 variables used to train the DTs for a Higgs boson mass of $m_H = 145$ GeV.

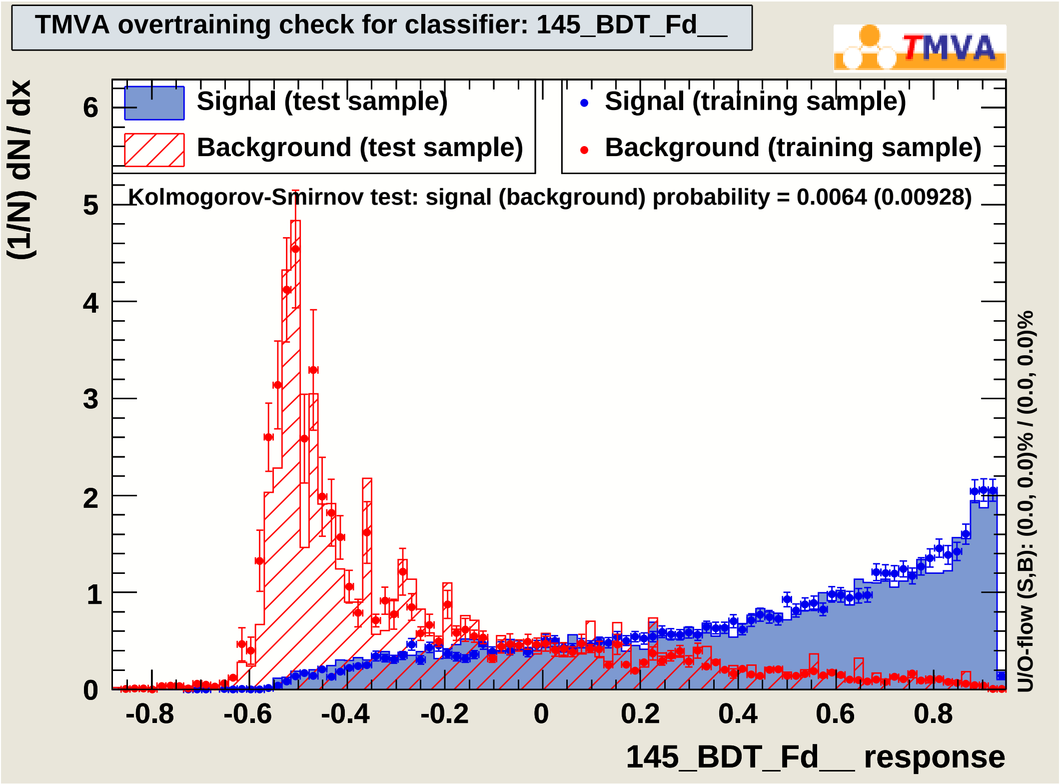

Figure 6-34: The training and testing samples signal versus background overtraining distributions for a Higgs boson mass of $m_H = 145$ GeV.

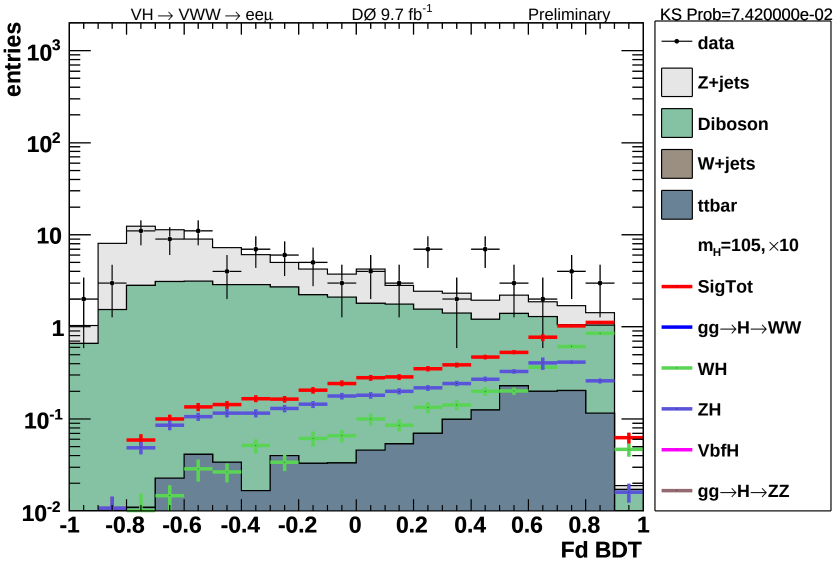

(a)

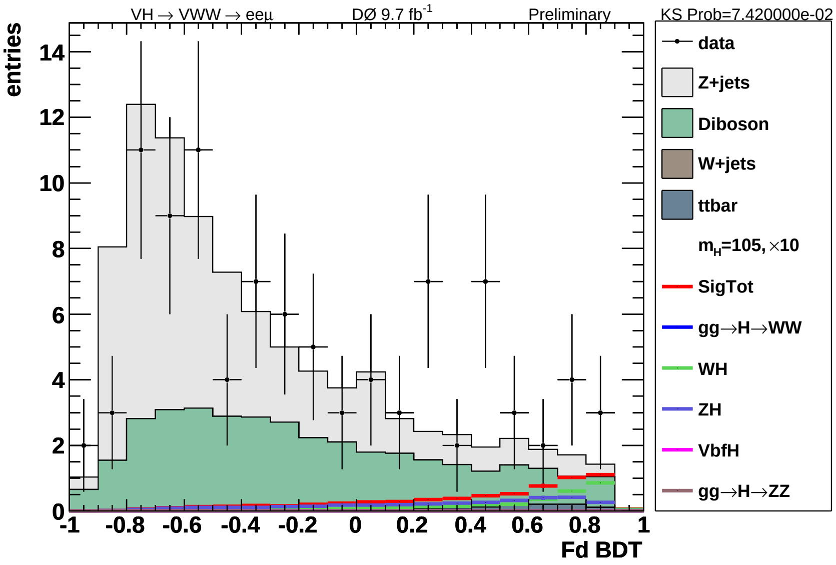

(b)

Figure 6-35: The final discriminant DT distribution in (a) logarithmic scale and (b) linear scale for data (points) and sum of all the backgrounds (histograms). The expected signal, multiplied by a factor of 10, for a 105 GeV SM Higgs boson is also shown in red. MC signal samples for $H \to WW^*$, $H \to ZZ$, and VBF are not available for this mass.

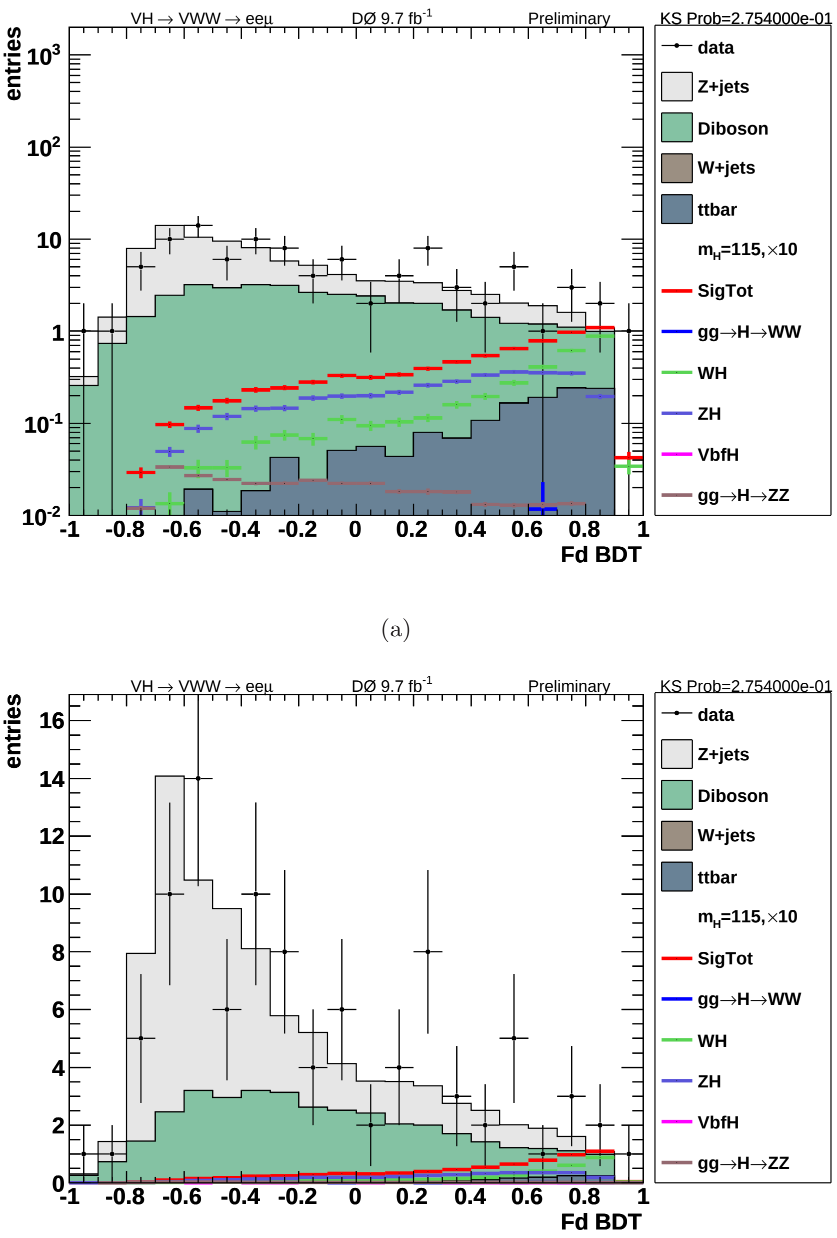

(a)

(b)

Figure 6-36: The final discriminant DT distribution in (a) logarithmic scale and (b) linear scale for data (points) and sum of all the backgrounds (histograms). The expected signal, multiplied by a factor of 10, for a 115 GeV SM Higgs boson is also shown in red.

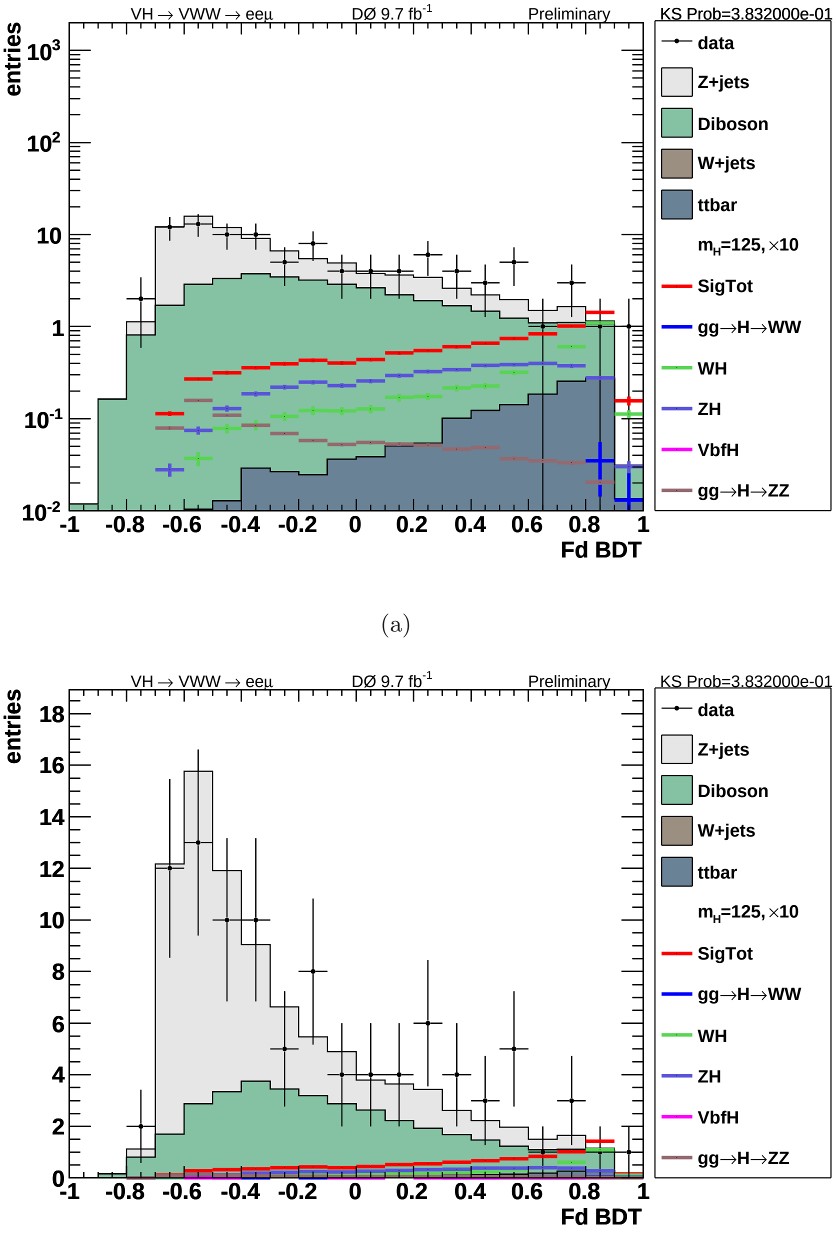

(a)

(b)

Figure 6-37: The final discriminant DT distribution in (a) logarithmic scale and (b) linear scale for data (points) and sum of all the backgrounds (histograms). The expected signal, multiplied by a factor of 10, for a 125 GeV SM Higgs boson is also shown in red.

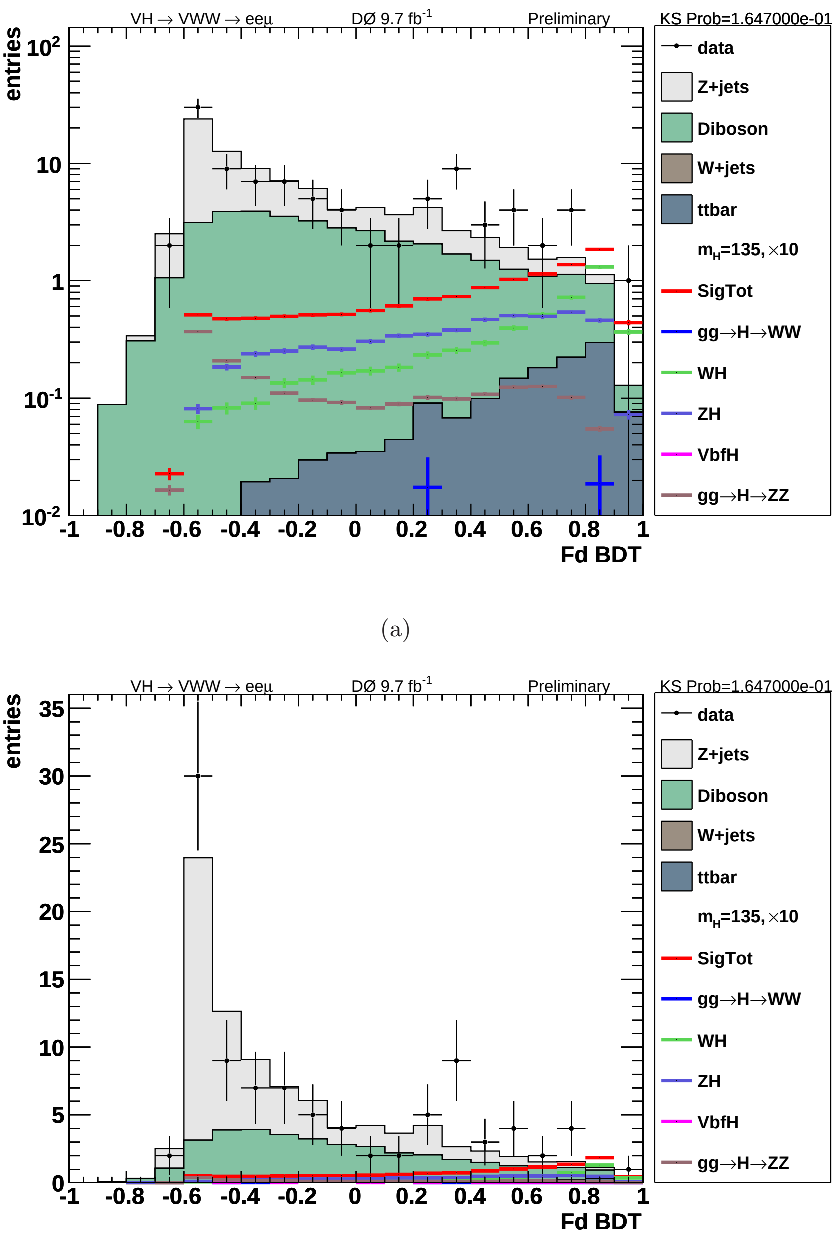

(a)

(b)

Figure 6-38: The final discriminant DT distribution in (a) logarithmic scale and (b) linear scale for data (points) and sum of all the backgrounds (histograms). The expected signal, multiplied by a factor of 10, for a 135 GeV SM Higgs boson is also shown in red.

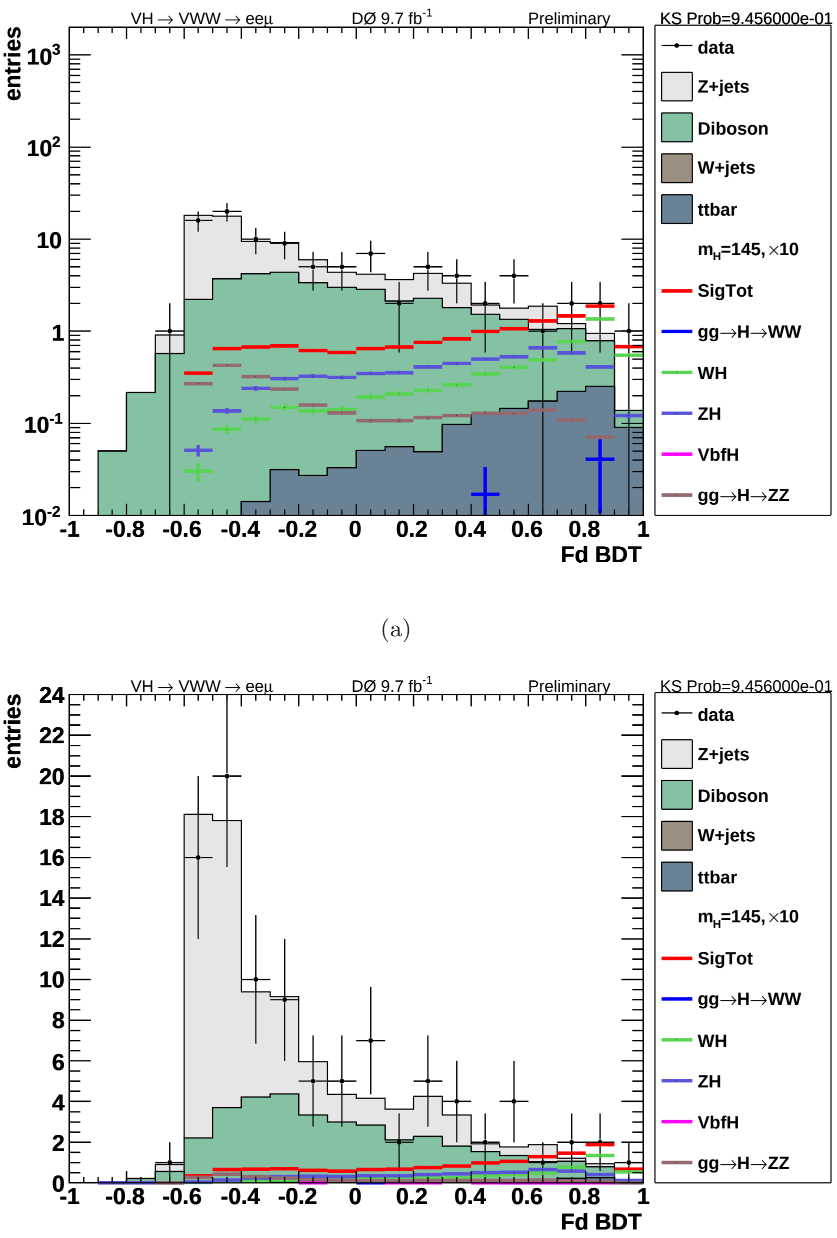

(a)

(b)

Figure 6-39: The final discriminant DT distribution in (a) logarithmic scale and (b) linear scale for data (points) and sum of all the backgrounds (histograms). The expected signal, multiplied by a factor of 10, for a 145 GeV SM Higgs boson is also shown in red.

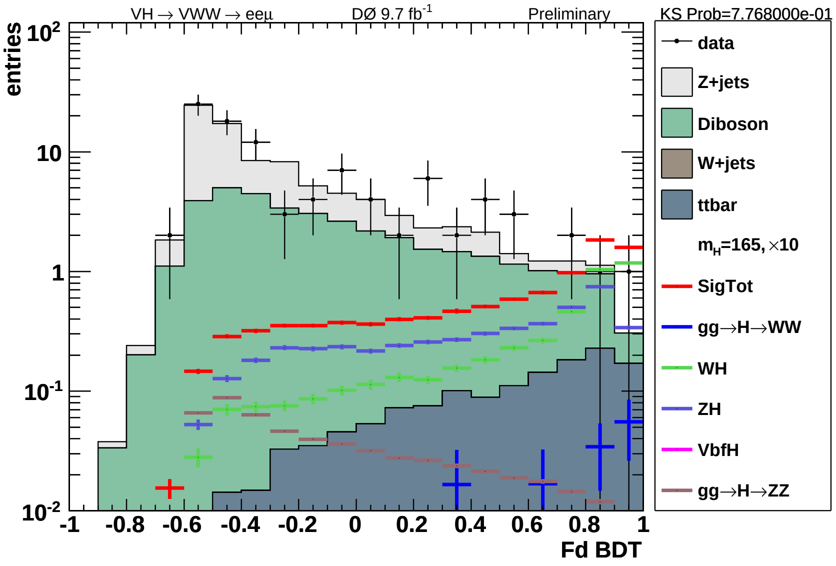

(a)

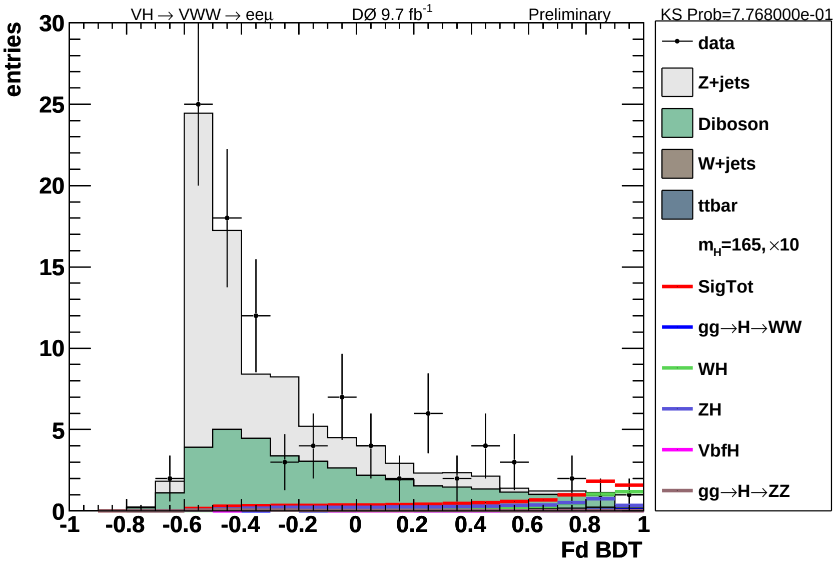

(b)

Figure 6-40: The final discriminant DT distribution in (a) logarithmic scale and (b) linear scale for data (points) and sum of all the backgrounds (histograms). The expected signal, multiplied by a factor of 10, for a 165 GeV SM Higgs boson is also shown in red.

6.3.4 Cross Section Limits

Limits are calculated using a modified frequentist approach [102], where the signal confidence level CL_s, defined as the ratio of the confidence level for the signal+background (test) hypothesis to the background-only (null) hypothesis ($CL_s = CL_{s+b}/CL_b$), is calculated by integrating the distributions of a test statistic over the outcomes of pseudo-experiments generated according to Poisson statistics for the signal+background and background-only hypotheses. The test statistic is calculated as a joint log-likelihood ratio (LLR) [28] given by

$$LLR = -2\ ln\left(\frac{p(data|H_1)}{p(data|H_0)}\right), \tag{6-1}$$

where H_1 denotes the test hypothesis, while H_0 represents the null hypothesis, and *data* is either an ensemble of pseudo-experiment data or actual observed data. The best-fit value of the nuisance parameters is used to calculate the probabilities p for each pseudo-experiment separately for each hypothesis. Nuisance parameters are hypothesis parameters that are unspecified but not of immediate interest to the test [103], such as luminosity. The parameters can be a systematic uncertainties or theoretical parameters. Priors, or prior probabilities, describe a parameter likelihood in the absence of a definitive measurement of the true value of the parameter [103]. Systematic uncertainties are incorporated via Gaussian smearing of Poisson probabilities for signal and backgrounds in the pseudo-experiments.

Two p-values, where a p-value is the probability that a purely random sampling would produce a result more extreme than the observed result, are defined as

$$\begin{aligned} CL_{s+b} &= p(LLR \geq LLR_{obs}|H_1), & (6\text{-}2)\\ 1 - CL_b &= p(LLR \leq LLR_{obs}|H_0), & (6\text{-}3) \end{aligned}$$

where LLR_{obs} is the observed/data value of the test statistic. $1 - CL_b$ is the probability that an upward fluctuation in the background will result in a signal+background data observation, while CL_{s+b} is the probability of a downward fluctuation of the sum of the signal+background in data [28]. Small values of CL_{s+b} indicate inconsistencies with the test hypothesis. Similarly, a particular test hypothesis can be excluded at the 95% C.L. if $CL_s < 0.05$.

To reduce the impact of systematic uncertainties on the sensitivity of the analysis, the individual signal and background contributions are fitted to the data, by allowing a variation of the background (or signal+background) prediction, within its systematic uncertainties [96]. The likelihood is constructed via a joint Poisson probability over the number of bins in the calculation, and is a function of scaling factors for the systematic uncertainties, which are given as Gaussian constraints associated with their priors.

Figures 6-41 – 6-42 show the "CLFast" and "CLFastApprox" cross section limits and log-likelihood ratios, respectively, while Fig. 6-43 shows the "CLFit2" cross section limits and log-likelihood ratio. Table 6-3 shows the individual mass points expected and observed limits for all three limit setting methods. The CLFast method is used as a quick and dirty diagnostic tool that ignores systematic uncertainties when calculating the limit values, while CLFastApprox is similar but takes systematics into account. CLFit2 performs a double binned likelihood fit that is maximized over the systematic uncertainties and hence is more accurate.

The cross section limit plots, Figs. 6-41(a), 6-42(a), and 6-43(a), show the measured cross section as a ratio to the SM cross section at 95% C.L.. The dashed black line is the expected limit, while the solid black line represents the observed limit. The green (yellow) shaded area is the $\pm 1\sigma$ ($\pm 2\sigma$) uncertainty bands on the expected limits. A mass range may be excluded when both the expected and observed limits drop below $\sigma/\sigma_{SM} = 1$ without the two distributions deviating more than one standand deviation from one another, as seen in the high mass region in Fig. 1-8. An excess is visible when the observed limit is significantly higher than the expected value. The slight broad excess from 100 – 150 GeV in the following limit distributions is due to statistical fluctuation rather than an actual Higgs boson signal.

The LLR plots, Figs. 6-41(b), 6-42(b), and 6-43(b), show the log-likelihood ratio distribution as a function of the Higgs boson mass. Here the dashed black line represents the background-only hypothesis, while the dashed red line is the signal+background hypothesis. The separation between the two distributions is an indication of the sensitivity of the experiment to distinguish in-between the two hypotheses, the greater the difference the more sensitive that channel is to measuring the signal. If the Higgs boson is truely (not) there in the observed limit, then the solid black line will follow the dashed red (black) line.

Table 6-3: Table summarising the CLFast, CLFastApprox, and CLFit2 limits for the $ee\mu$ final state. Limits are given at the 95% C.L. on the Higgs boson production cross section times the SM branching fraction as a ratio of the SM prediction.

m_H(GeV)	100	105	110	115	120	125	130	135	140	145	150
					CLFast						
Expected	16.70	17.62	17.85	16.18	14.57	13.02	10.82	9.25	8.89	8.37	7.96
Observed	31.80	34.78	27.63	25.90	22.92	19.89	17.39	14.64	12.71	12.94	11.05
					CLFastApprox						
Expected	18.43	19.18	19.58	17.78	15.67	14.32	11.09	10.15	9.79	9.05	8.69
Observed	34.62	45.91	30.13	29.94	29.47	22.47	19.11	15.58	14.69	14.53	13.26
					CLFit2						
Expected	19.09	19.84	20.29	18.30	16.03	15.28	12.29	10.81	10.27	9.54	9.16
Observed	36.22	40.97	30.83	29.11	24.94	22.24	19.23	16.06	13.82	14.17	11.97
m_H(GeV)	155	160	165	170	175	180	185	190	195	200	
					CLFast						
Expected	8.00	8.77	8.97	9.74	10.92	11.73	12.23	12.75	14.04	15.13	
Observed	11.28	11.26	11.47	10.94	11.84	13.14	14.65	12.36	12.91	15.43	
					CLFastApprox						
Expected	8.52	8.91	9.22	10.17	10.97	12.66	13.15	14.22	15.55	16.83	
Observed	13.51	13.85	14.56	15.15	14.86	18.01	17.60	15.60	17.16	18.86	
					CLFit2						
Expected	9.13	9.70	9.73	10.35	11.98	13.31	13.83	15.45	16.35	17.80	
Observed	11.79	11.73	11.75	11.46	12.36	13.59	15.29	13.64	13.79	16.69	

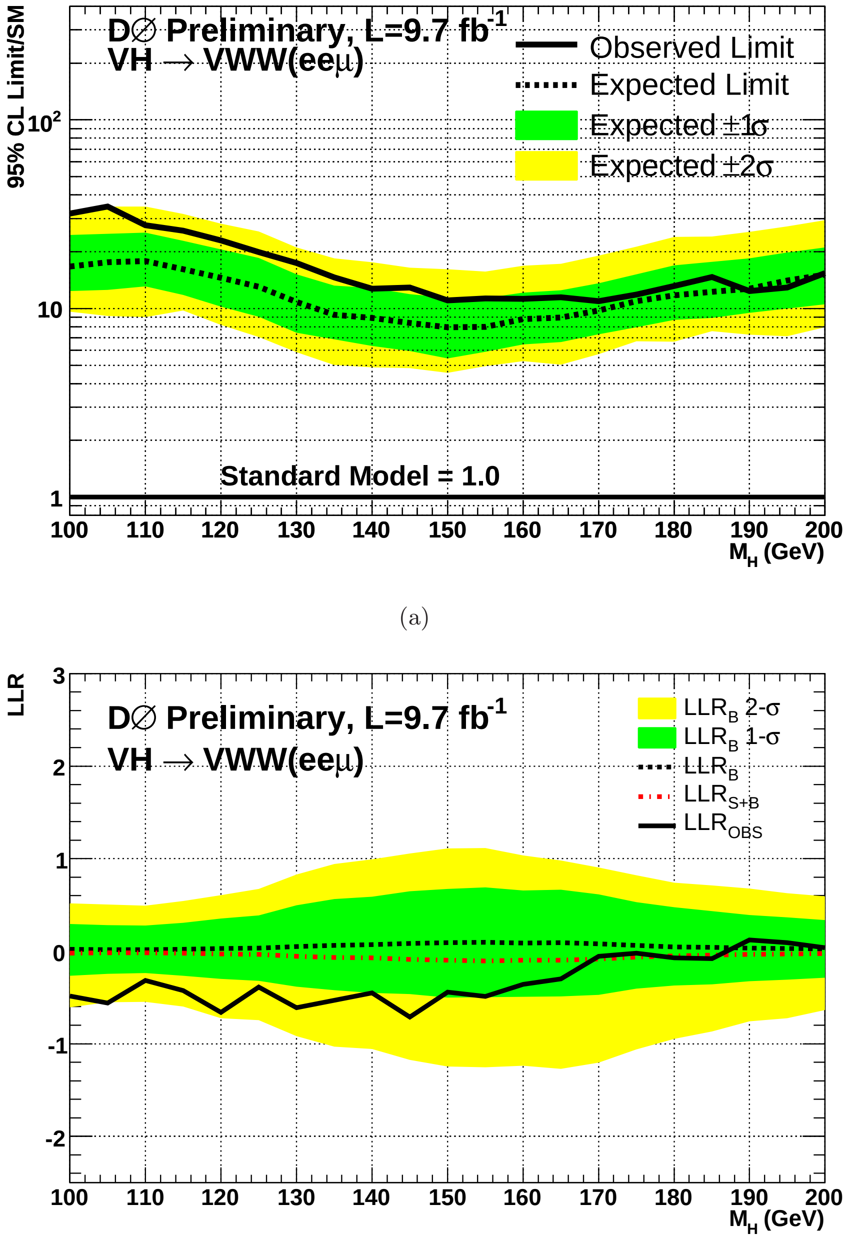

(a)

(b)

Figure 6-41: CLFast (a) limits and (b) log-likelihood ratio.

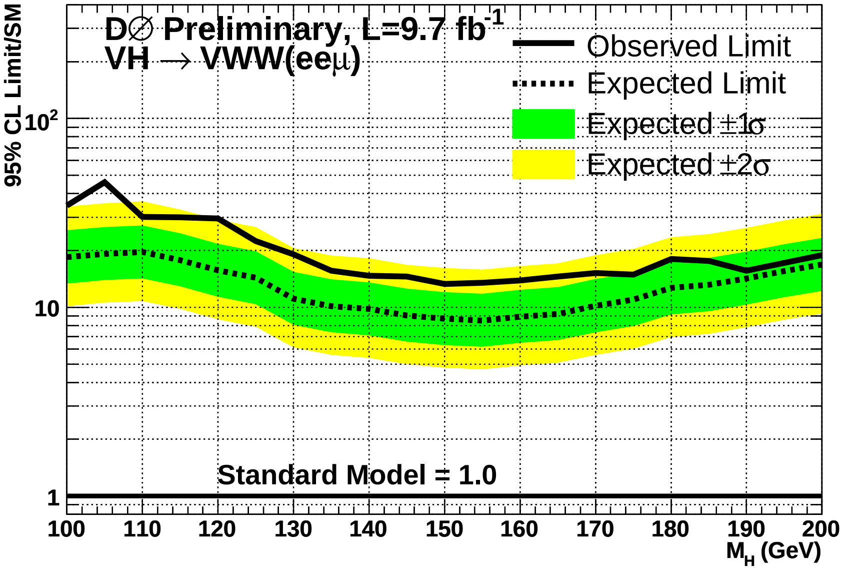

(a)

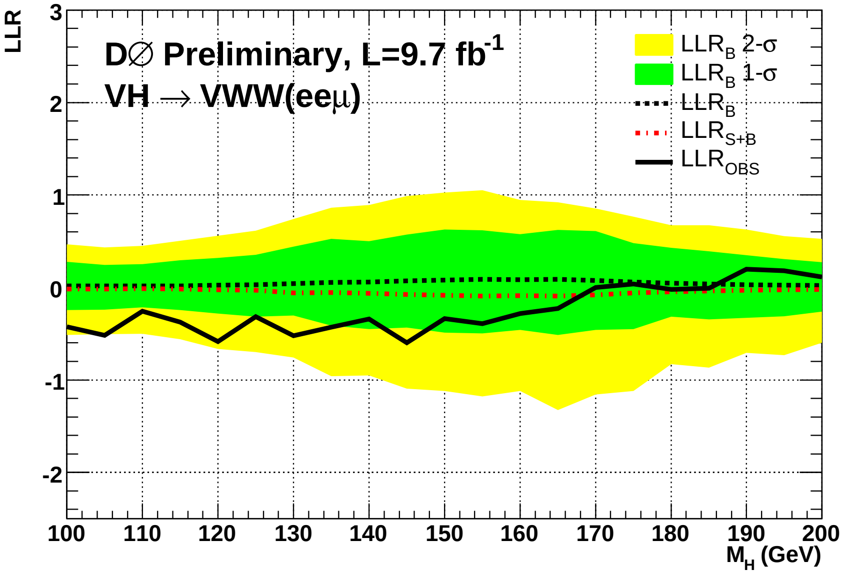

(b)

Figure 6-42: CLFastApprox (a) limits and (b) log-likelihood ratio.

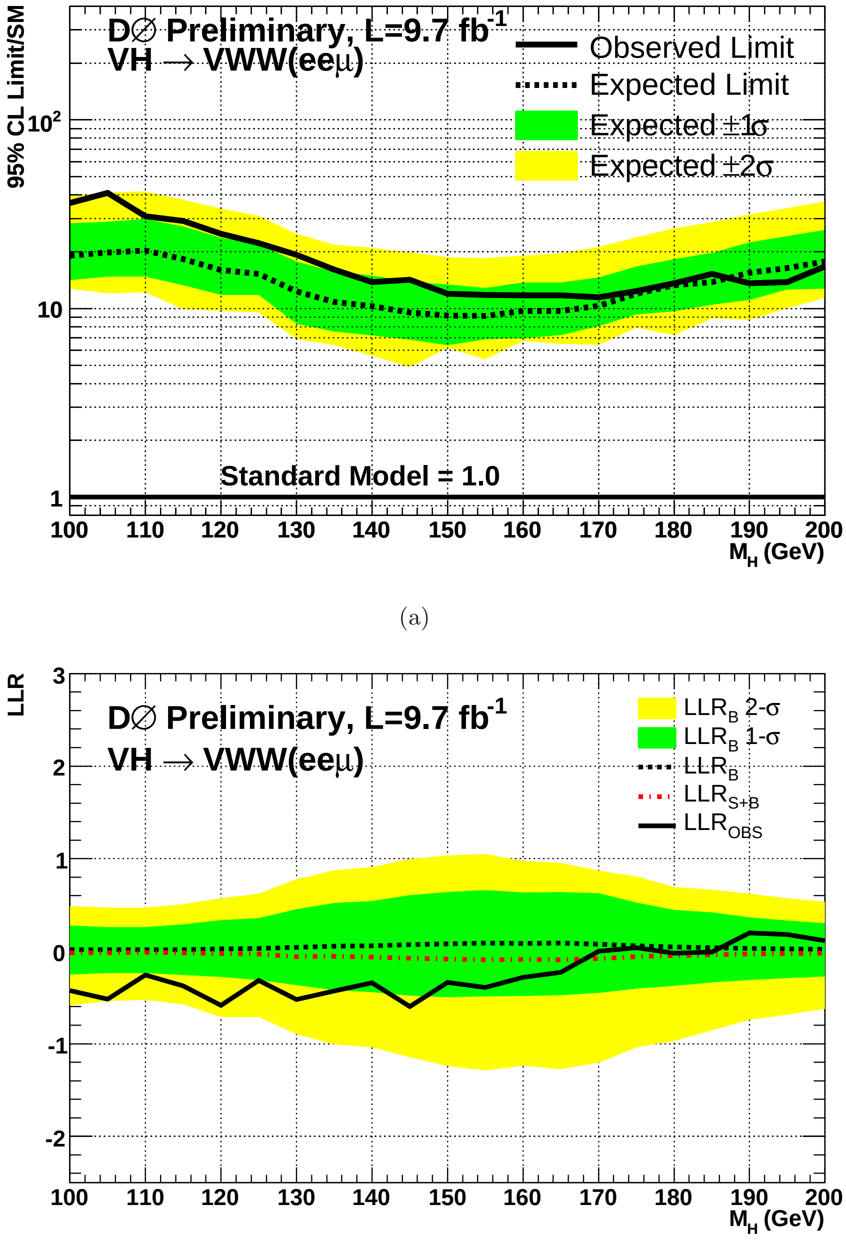

(a)

(b)

Figure 6-43: CLFit2 (a) limits and (b) log-likelihood ratio.

7 Conclusion

Presented here are three searches for final states with three or more leptons, either electrons or muons, plus an imbalance of transverse energy using Tevatron $p\bar{p}$ collisions at a center–of–mass energy of $\sqrt{s} = 1.96$ TeV with the DØ detector at Fermilab.

The first analysis reports a measurement of the $WZ \rightarrow \ell'\nu\ell\bar{\ell}$ cross section. Using 4.1 fb^{-1} of integrated luminosity, the cross section of $3.90^{+1.01}_{-0.85}(stat + syst) \pm 0.31(lumi)$ pb is found to be in good agreement with the SM NLO prediction of 3.68 pb.

We then look for the flavor changing neutral current decay of $t \rightarrow Zq$ in $t\bar{t} \rightarrow WbZq \rightarrow \ell'\nu\ell\bar{\ell} +$ jets, where q is considered to be either a u or c quark, and both the q and b quarks decay hadronically and are reconstructed as jets. We find no evidence of FCNC production and set upper limits on the branching ratio of $BR(t \rightarrow Zq) < 3.2\%$ observed, with an expected limit of $< 3.8\%$, at the 95% C.L..

Finally, a search for the SM Higgs boson is presented, using associated production of WH and ZH, in the $ee\mu$ final state plus an imbalance of transverse momentum. With the full DØ RunII data available, we observe no excess above the SM background prediction and extract limits on the Higgs boson production cross section times branching ratio for a Higgs boson mass range of $m_H = 100 - 200$ GeV, in intervals of 5 GeV. We find that we are most sensitive to the Higgs boson at the 155 GeV mass point, where we expect to set a cross section limit of $9.1\sigma_{SM}$ at 95% C.L., with an observed limit of $11.8\sigma_{SM}$.

A Monte Carlo Reweighting

We find in most instances that the Monte Carlo used does not completely replicate the data, since some processes are only known to leading-order. In those cases, it is customary to apply scale factors to the MC so it better describes what is seen in data. The analyses presented apply the following standard MC reweightings, as recommended by the official Object ID groups.

A.1 Lepton Smearing and Efficiency

The MC simulations predict better lepton momentum resolution than is seen in data. This could possibly arise from mismodellings in the simulation of hit efficiencies, the simulation of hit resolution, the magnetic field mapping, the alignments of the detector elements, or some matter effects [104]. The di-lepton invariant mass distributions of $p\bar{p} \rightarrow J/\psi \rightarrow \mu\bar{\mu}$ [104] and $p\bar{p} \rightarrow Z/\gamma^* \rightarrow \mu\bar{\mu}, e\bar{e}$ [104, 105] are used to "smear" the MC to match the data.

Lepton reconstruction and identification is more efficient in MC simulation than in data. Lepton ID efficiencies, used to determine the scale factor, are calculated from data using a tag and probe method [63] for different 2 – 3D parameterizations such as p_T, η_{det}, or luminosity. The tag and probe method consists of tight selection criteria on one lepton (the tag object; in data, this is usually the lepton that triggered the event) and looser criteria on a second lepton (the probe), while forcing the di-leptons to reconstruct the Z boson peak. The probe lepton is then used to determine the efficiency of identification criteria. A scale factor, as a ratio of the efficiency in data to the efficiency in MC, is then applied per lepton, given a minimum ID quality requirement, per event to the global event weight in MC to account for the lower efficiency in data.

A.2 Weak Gauge Boson p_T Reweighting

The Z–p_T distribution is not properly modelled at low values of boson p_T in the ALPGEN+PYTHIA MC samples. To correct for this, a weight is applied to the $Z+$ jets samples per event according to Ref. [106]. The $Z+$jets samples are adjusted based on the differential Z boson production cross section, measured as a function of p_T, in $Z \to \ell\bar{\ell}$ events in RunIIa and RunIIb data. The ratio of the adjusted to the default MC rate is then fitted using a modified Fermi function.

Similarly, $W+$ jets events are reweighted according to a correction based on the ratio of the next-to-next-to-leading order (NNLO) W–p_T to the NNLO Z–p_T [107] distributions, where the Z–p_T reweighting, described above, is used in this ratio.

A.3 Light and Heavy Flavor Parton Reweighting

k-factors are used to scale the leading-logarithmic (LL) ALPGEN+PYTHIA $Z/W+$jets cross section to the NNLO cross sections. These scale factors are applied to $Z+$ jets and $W+$jets ALPGEN+PYTHIA MC samples. The k-factors for heavy flavor partons, b and c quarks, are applied in addition to the light flavor k-factors, summarized in Table A-1.

Table A-1: The default k-factors used to scale the LL ALPGEN+PYTHIA $V+$jets cross section to the NNLO $V+$jets cross section, where $V = W$ or Z boson.

MC Sample	k-factor
$Z + lp$ jets	1.30
$Z + b\bar{b} + lp$ jets	1.30 × 1.52
$Z + c\bar{c} + lp$ jets	1.30 × 1.67
$W + lp$ jets	1.30
$W + b\bar{b}/c\bar{c} + lp$ jets	1.30 × 1.47

A.4 Instantaneous Luminosity and Beam Vertex Reweighting

An instantaneous luminosity reweighting is done since the luminosity profile of the zero-bias overlay applied to the MC production does not correspond to the luminosity profile measured in data.

The beam z-vertex position in the MC is assumed to be Gaussian, while the data shows it to be slightly non-Gaussian. The MC is then reweighted to match the vertex distribution found in data.

B Common Sample Group Skims

To make the data more manageable for the physics groups, the Common Sample Group (CSG) [108] produces official skims of the data, collecting events of a particular nature. Detailed definitions can be found at Ref. [109]. The skims used in the analyses are detailed below:

- EMinclusive : subskim consisting of at least one high-p_T electron.

Skim Name	Cut Thresholds
1EM2JET	One electron with $p_T > 12$ GeV and HMx8 < 75 AND a JCCB jet with $p_T > 8$ GeV AND a JCCB jet with $p_T > 8$ GeV
1EMloose	One electron with $p_T > 20$ GeV
2EM	One electron with $p_T > 7$ GeV AND One electron with $p_T > 7$ GeV
EM1TRK	One electron with $p_T > 8$ GeV
JES_B	One electron with $p_T > 4$ GeV, coming in on any one of the following electron triggers [110]: E1_ISH30, E1_ISHT22, E1_L70, E1_SH35, E1_SHT25, E2_ISH30, E2_ISHT22, E2_L70, E2_SH35, E2_SHT25, EM13, EM17, EM5, EM9

- 2MUhighpt : subskim consisting of two or more high-p_T muons.

Skim Name	Cut Thresholds
2MUhighpt	One Loose quality muon with central track $p_T > 15$ GeV AND one Loose quality muon
2MU1TRK	One Medium quality muon with central track $p_T > 15$ GeV AND CHP with $p_T > 15$ GeV AND CHP with $p_T > 15$ GeV where CHP is a set of hits in the muon chambers, but not necessarily matched to a track
MU2TRKhighpt	One Loose quality muon with central track $p_T > 10$ GeV AND one Loose quality muon with central track $p_T > 10$ GeV

- QCD : subskim consisting of jet triggers.

Skim Name	Cut Thresholds
QCD	Coming in on any one of the following jet triggers [111]: DIJTA_L3M430, DIJTB_L3M100, DIJTB_L3M200, DIJTB_L3M280, DIJTB_L3M430, JT125_L3J125, JT25, JT45, JT65, JT8, JT9, JT95

C Multivariate Analysis - Boosted Decision Tree Approach

To get the most sensitivity out of the Higgs boson selection criteria, a multivariate analysis (MVA) approach is used instead of a cut-based analysis (as was used in the WZ and FCNC analyses). A brief description follows.

Decision trees (DTs) [101] are a learning algorithm technique that, given a desired output, uses training samples to classify an event as either signal or background. Trees are grown through a number of cuts that are either pass or fail, until a predetermined event size is reached (known as the “minimum events per final leaf”). The optimal splitting for each node in the tree is determined using the Gini index. It is defined as $p(1-p)$, where p is the purity and is given by $s/\sqrt{s+b}$, where s (b) is the weighted sum of the signal (background) events. Figure C-1 [101] shows this structure. Starting from a root node, a cut is applied in which the event either passes or fails. Each split uses a variable which maximizes the difference between signal events and background events. The algorithm is then applied recursively until the stop criterion is fulfilled. The terminal node is called a “leaf” and is labeled as signal (background) if the purity is larger (smaller) than 0.5.

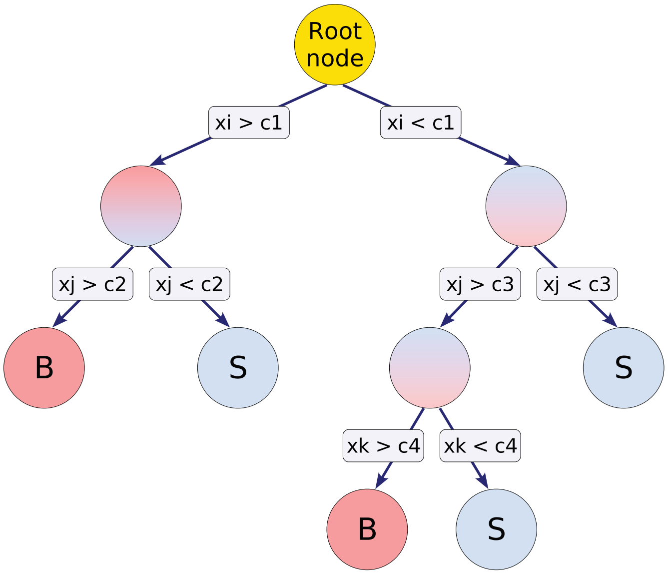

Figure C-1: Diagram of a DT tree structure [101].

Complications arise when a training sample has been overtrained, occurring when there are too few data points to properly set the model parameters. Overtraining leads to an increase in the performance of the training sample but decreases the performance when measured with an independent testing sample. Comparisons between the training samples and independent test samples are used to determine if a sample has been overtrained and additional statistics helps to fight against overtraining.

Boosting a decision tree (BDT) is a way to enhance the performance of the typically weak DT method by sequentially applying reweight (boosted) versions of the training data and then taking a weighted average to produce the final DT. In extending this to multiple trees, known as a forest, the boosting stabilizes the response of the DTs with respect to the fluctuations in the training sample and is able to increase the performance with respect to a single tree.

The Higgs analysis presented uses a form of boosting called "gradient". Gradient boosting uses the following binomial log-likelihood loss-function for classification:

$$L(F, y) = \ln(1 + e^{-2F(\mathbf{x})y}), \tag{C-1}$$

where $F(\mathbf{x})$ is the weighted sum of parameterised base functions or "weak learners", $f(x; \alpha_m)$, such that

$$F(\mathbf{x}; P) = \sum_{m=0}^{M} \beta_m f(x; \alpha_m); \qquad P \in \{\beta_m; \alpha_m\}_0^M. \tag{C-2}$$

The parameter P is adjusted such that the deviation (measured by $L(F, y)$) between the model response, $F(\mathbf{x})$, and the true value obtained from the training sample, y, is minimized. By using a log-likelihood form of the loss-function, the classifier is more robust in handling mislabelled data points or outliers. The loss-function's minimization is evaluated using a steepest-decent approach, which is done by calculating the current gradient of the loss-function and then adjusting the leaf values of a grown regression tree to match the gradient's mean value. The desired set of DTs are produced when the procedure is iterated enough times to minimize the loss-function.

Gradient boosting is usually less susceptable to overtraining. The “Shrinkage” parameter is used to reduce the algorithm’s rate of learning by controlling the weight on the individual trees. A small Shrinkage value, such as 0.1 – 0.3, needs more trees but can significantly improve the accuracy of the prediction when presented with difficult settings. By setting the “UseBaggedGrad” flag to true, a bagging-like resampling is introduced. Bagging is a resampling technique where the DT is repeatedly trained using resampled training events such that it essentially smears over the statistical fluctuations of the training sample. The “GradBaggingFraction” parameter is used to control the fraction of the sample used in each iteration, and is typically between 0.5 and 0.8. The gradient boost configuration was chosen for the VH analysis, the details of which are as follows:

- 150 trees,
- UseBaggedGrad flag set to true,
- GradBaggingFraction = 0.6,
- Shrinkage = 0.2,
- maximal-depth of the tree = 5,
- minimum events per final leaf = 50,
- UseYesNoLeaf flag is set to false,
- SeparationType is set to GiniIndex, and
- NoPruning.

Pruning is the process by which a tree is cut back from the bottom up after it has reached its maximum size, removing the statistically insignificant nodes and reducing overtraining.

A typical BDT output, usually ranging from -1 to 1, is shown in Fig. C-2 [101]. The signal is designed to peak towards 1, while the background tends to peak towards -1. Depending on the background contribution, numerous BDT's may be employed to separate out the signal.

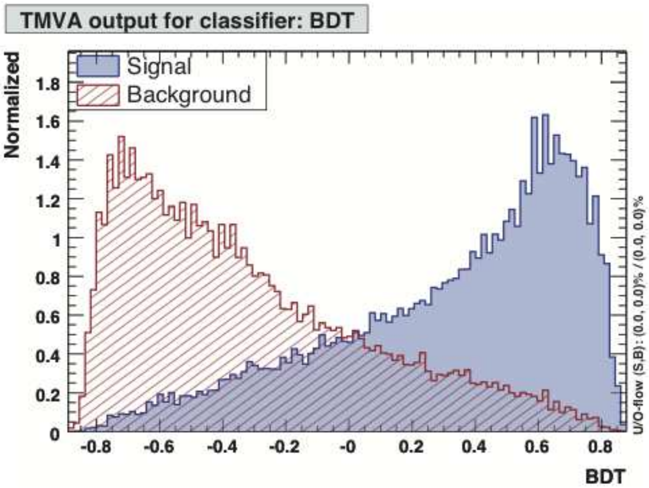

Figure C-2: Example of the final discriminant output in signal versus background separation for a boosted decision tree [101].

D VH $\rightarrow$ VWW* $\rightarrow$ Tri-leptons Monte Carlo Samples

D.1 Monte Carlo Signal Samples

Tables D-1 – D-7 list the cross section (in pb) multiplied by the appropriate branching fraction and the number of events before data quality cuts have been applied for the MC samples at each signal mass point for the WH, ZH, $H \rightarrow ZZ \rightarrow \ell\bar{\ell}\ell'\bar{\ell}'$, $H \rightarrow ZZ \rightarrow \ell\bar{\ell}jj$, $H \rightarrow ZZ \rightarrow \ell\bar{\ell}\nu\bar{\nu}$, $gg \rightarrow H \rightarrow WW^*$, and vector boson fusion (VBF) signals, respectively, for RunIIa, RunIIb1, and RunIIb2 data periods.

Table D-1: WH signal MC samples used in the analysis. The cross section times branching ratios and the number of events before data quality cuts are applied are listed.

$WH, H \rightarrow WW^*, ZZ, \gamma\gamma, ee, \mu\mu, \tau\tau, \gamma Z$ $(W, Z\ incl)$

Mass (m_H)	$\sigma \times BR$ (pb)	Events before data quality		
		RunIIa	RunIIb1	RunIIb2
100	0.0296	97684	1097752	1111425
105	0.0259	98509	1091735	1101561
110	0.0231	97631	1134725	1108029
115	0.0209	99494	1454989	1102941
120	0.0191	97516	1442567	1103440
125	0.0182	98823	1457879	1088920
130	0.0179	100831	1450712	1108882
135	0.0174	100185	1465159	1104716
140	0.0164	96292	1463866	1100574
145	0.0159	99295	1455563	1097401
150	0.0149	100198	1460418	1105918
155	0.0140	95632	1453455	1100703
160	0.0127	100763	1467030	1101580
165	0.0121	101145	1453460	1105933
170	0.0106	98393	1447315	1105181
175	0.0092	81548	1469040	1104756
180	0.0081	100923	1453653	1093269
185	0.0075	97404	1481774	1106886
190	0.0066	97248	1457897	1106376
195	0.0056	101661	1459030	1102487
200	0.0052	99680	1479698	1099180

Table D-2: ZH signal MC samples used in the analysis. The cross section times branching ratios and the number of events before data quality cuts are applied are listed.

$ZH, H \to WW^*, ZZ, \gamma\gamma, ee, \mu\mu, \tau\tau, \gamma Z$ (W, Z *incl*)				
Mass	$\sigma \times BR$	Events before date quality		
(m_H)	(pb)	RunIIa	RunIIb1	RunIIb2
100	0.0172	99854	1094019	1095475
105	0.0152	86683	1097982	1100942
110	0.0137	101269	1101159	1102372
115	0.0120	98633	1278785	1097288
120	0.0110	100397	1284541	1106757
125	0.0107	96955	1279452	1102359
130	0.0108	96657	1283024	1105819
135	0.0102	100133	1266791	1101742
140	0.0098	100840	1281876	1110725
145	0.0096	102044	1280939	1109595
150	0.0091	100145	1283047	1100903
155	0.0085	100987	1279872	1100568
160	0.0077	100733	1264588	1107189
165	0.0069	101373	1278474	1104386
170	0.0061	100074	1281889	1104272
175	0.0056	98952	1294395	1111705
180	0.0051	101752	1266624	1103005
185	0.0046	81001	1280691	1107344
190	0.0042	100392	1263568	1105986
195	0.0039	100317	1283357	1098232
200	0.0035	101020	1276434	1099330

Table D-3: $H \to ZZ \to \ell\bar{\ell}\ell'\bar{\ell}'$ signal MC samples used in the analysis. The cross section times branching ratios and the number of events before data quality cuts are applied are listed.

$H \to ZZ \to \ell\bar{\ell}\ell'\bar{\ell}'$				
Mass	$\sigma \times BR$	Events before data quality		
(m_H)	(pb)	RunIIa	RunIIb1	RunIIb2
115	0.0001082	95321	95799	185515
120	0.0001749	96351	90462	183621
125	0.0002584	96508	93387	187137
130	0.0003555	94751	89818	188241
135	0.0004218	96278	90247	184499
140	0.0004731	95869	91606	185832
145	0.0004874	96275	91355	184659
150	0.0004551	96961	88733	182249
155	0.0003632	96458	89484	187495
160	0.0001834	96218	89454	188396
165	0.0000869	95574	90800	184168
170	0.0000828	100193	90123	183833
175	0.0001020	96861	88340	189581
180	0.0001714	97355	88472	183934
185	0.0003856	101331	99095	184604
190	0.0004859	96491	90085	182576
195	0.0005049	100788	88814	186311
200	0.0004936	97250	94388	187630

Table D-4: $H \to ZZ \to \ell\bar{\ell}jj$ signal MC samples used in the analysis. The cross section times branching ratios and the number of events before data quality cuts are applied are listed.

$H \to ZZ \to \ell\ell jj$				
Mass	$\sigma \times BR$	Events before data quality		
(m_H)	(pb)	RunIIa	RunIIb1	RunIIb2
115	0.001499	194459	178748	186535
120	0.002422	192569	180818	184396
125	0.003578	200935	177803	184897
130	0.004784	195032	182138	186708
135	0.005841	195767	180807	183504
140	0.006552	195058	181569	188047
145	0.006750	195114	180540	183409
150	0.006302	195715	181127	182567
155	0.005029	195540	179224	185764
160	0.002539	194787	187273	182315
165	0.001203	195040	179290	182651
170	0.001146	194796	179434	183387
175	0.001412	196415	179955	182527
180	0.002373	195669	180649	181678
185	0.005339	193870	180423	182822
190	0.006728	193724	186184	185447
195	0.006991	193140	179064	186089
200	0.006835	194792	180877	189470

Table D-5: $H \to ZZ \to \ell\bar{\ell}\nu\bar{\nu}$ signal MC samples used in this analysis. The cross section times branching ratios and the number of events before data quality cuts are applied are listed.

$H \to ZZ \to \ell\ell\nu\bar{\nu}$				
Mass	$\sigma \times BR$	Events before data quality		
(m_H)	(pb)	RunIIa	RunIIb1	RunIIb2
115	0.000429	100306	94839	92897
120	0.000693	96522	93621	92378
125	0.001024	100933	93827	93950
130	0.001369	100205	93210	91851
135	0.001671	100286	95717	89601
140	0.001874	80464	91576	94092
145	0.001931	102225	91248	92486
150	0.001803	99716	91199	93738
155	0.001439	99881	89876	91404
160	0.000726	97255	90049	90637
165	0.000344	101052	90082	94007
170	0.000328	100913	89785	92652
175	0.000404	101598	89854	91647
180	0.000679	100561	90795	92198
185	0.001527	101859	92065	93359
190	0.001925	99984	90931	89947
195	0.002000	93800	88495	91519
200	0.001955	100844	90848	92246

Table D-6: $H \to WW^*$ signal MC samples used in the analysis. The cross section times branching ratios and the number of events before data quality cuts are applied are listed.

$gg \to H \to WW^* \to \ell\nu\ell'\nu'$				
Mass	$\sigma \times BR$	Events before data quality		
(m_H)	(pb)	RunIIa	RunIIb1	RunIIb2
115	0.0111	393095	629107	176243
120	0.0161	403430	739440	166455
125	0.0215	399325	838458	171939
130	0.0270	558057	639726	162299
135	0.0318	477318	644697	175290
140	0.0355	397688	835658	162786
145	0.0380	402574	640931	164846
150	0.0396	489921	646052	165327
155	0.0405	499425	629676	183909
160	0.0413	393904	742357	358311
165	0.0387	491159	649330	185115
170	0.0349	506397	647834	183280
175	0.0311	199022	623631	182000
180	0.0273	394496	751606	186561
185	0.0223	400840	648465	185368
190	0.0188	401967	639840	178074
195	0.0165	492096	653706	164614
200	0.0147	249100	832321	164050

Table D-7: VBF signal MC samples used in the analysis. The cross section times branching ratios and the number of events before data quality cuts are applied are listed.

$q\bar{q} \to q\bar{q}H \to q\bar{q}WW^* \to q\bar{q}\ell\nu\ell'\nu'$				
Mass	$\sigma \times BR$	Events before data quality		
(m_H)	(pb)	RunIIa	RunIIb1	RunIIb2
115	0.000716	147465	187032	172727
120	0.001092	150314	187106	173686
125	0.001522	148453	191269	166338
130	0.001989	147626	184364	175275
135	0.002433	153560	193855	167061
140	0.002815	148789	188441	174348
145	0.003128	152235	188994	181182
150	0.003362	153367	183945	183885
155	0.003544	151953	201717	164679
160	0.003761	146883	91172	163562
165	0.003689	147403	181489	158029
170	0.003445	147586	185932	172946
175	0.003179	148087	92407	173656
180	0.002877	150220	182737	174471
185	0.002419	147887	184470	173077
190	0.002096	150977	91565	165530
195	0.001884	147563	187685	175489
200	0.001712	148169	186118	176239

D.2 Monte Carlo Background Samples

Tables D-8 – D-11 list the cross section (in pb) multiplied by the appropriate branching fraction (unless otherwise noted), and the number of events before data quality cuts have been applied for the MC background samples of diboson and $t\bar{t}$, W/γ^*+ jets, $Z/\gamma^* \rightarrow e\bar{e}$, and $Z/\gamma^* \rightarrow \tau\bar{\tau}$, respectively, for RunIIa, RunIIb1, and RunIIb2 data periods.

Table D-8: Diboson and $t\bar{t}$ MC samples used in the analysis. The cross section and the number of events before data quality cuts are applied are listed.

Process	σ	Events before data quality		
	(pb)	RunIIa	RunIIb1	RunIIb2
WW inclusive	11.34	1162309	5386321	4571843
WZ inclusive	3.45	1160285	5399075	4558103
ZZ inclusive	1.50	1166493	3649345	4566854
$t\bar{t}$+$Xlp \rightarrow 2\ell 2\nu 2b + Xlp, X = 0,1,2$	0.834	52972	1844313	3860599

Table D-9: W+jets MC samples used in the analysis. The cross section and the number of events before data quality cuts are applied are listed.

Process	σ	Events before data quality		
	(pb)	RunIIa	RunIIb1	RunIIb2
W(inclusive) + $0lp$	4597.68	12757416	111892275	176133306
W(inclusive) + $1lp$	1234.91	19639769	57000840	85568590
W(inclusive) + $2lp$	301.89	14478273	32931691	31398763
W(inclusive) + $3lp$	72.62	4030756	14322111	7998923
W(inclusive) + $4lp$	16.57	2962409	5813460	1954046
W(inclusive) + $5lp$	5.01	982524	2550973	774450
W(inclusive) + $2b0lp$	9.49	1404726	9614027	4496018
W(inclusive) + $2b1lp$	4.16	667504	7499729	2244441
W(inclusive) + $2b2lp$	1.61	251539	5185990	1094989
W(inclusive) + $2b3lp$	0.75	281005	3407056	583169
W(inclusive) + $2c0lp$	23.37	720891	9770245	8986441
W(inclusive) + $2c1lp$	13.49	741998	7527601	4671764
W(inclusive) + $2c2lp$	5.53	343667	5593570	2309287
W(inclusive) + $2c3lp$	2.41	447680	3873973	1165874

Table D-10: $Z/\gamma^* \to e\bar{e}$ MC samples used in the analysis. The cross section times branching ratios and the number of events before data quality cuts are applied are listed.

Process	Mass Range	$\sigma \times BR$	Events before data quality		
	(GeV)	(pb)	RunIIa	RunIIb1	RunIIb2
$Z/\gamma^* \to ee + 0lp$	$15 < M < 75$	338.18	541647	1947741	8514612
$Z/\gamma^* \to ee + 1lp$	$15 < M < 75$	40.02	434495	971687	3807118
$Z/\gamma^* \to ee + 2lp$	$15 < M < 75$	10.04	164654	558398	1786834
$Z/\gamma^* \to ee + 3lp$	$15 < M < 75$	2.76	79836	540609	820815
$Z/\gamma^* \to ee + 0lp$	$75 < M < 130$	133.34	2885796	1184432	9521588
$Z/\gamma^* \to ee + 1lp$	$75 < M < 130$	40.29	1803874	567964	4496603
$Z/\gamma^* \to ee + 2lp$	$75 < M < 130$	9.99	883878	268050	1998843
$Z/\gamma^* \to ee + 3lp$	$75 < M < 130$	3.09	838336	127397	756433
$Z/\gamma^* \to ee + 0lp$	$130 < M < 250$	0.86	289871	353562	1225431
$Z/\gamma^* \to ee + 1lp$	$130 < M < 250$	0.37	182052	179663	743795
$Z/\gamma^* \to ee + 2lp$	$130 < M < 250$	0.095	87902	161061	329870
$Z/\gamma^* \to ee + 3lp$	$130 < M < 250$	0.032	82319	301536	141695
$Z/\gamma^* \to ee + 0lp$	$250 < M < 1960$	0.069	200051	727511	794470
$Z/\gamma^* \to ee + 1lp$	$250 < M < 1960$	0.034	94812	522780	365658
$Z/\gamma^* \to ee + 2lp$	$250 < M < 1960$	0.012	44612	482825	159115
$Z/\gamma^* \to ee + 3lp$	$250 < M < 1960$	0.0039	39775	302967	62507
$Z/\gamma^* \to ee + 2b0lp$	$15 < M < 75$	0.51	196429	175794	1556485
$Z/\gamma^* \to ee + 2b1lp$	$15 < M < 75$	0.20	92788	85274	742617
$Z/\gamma^* \to ee + 2b2lp$	$75 < M < 130$	0.42	197276	196234	1578942
$Z/\gamma^* \to ee + 2b1lp$	$75 < M < 130$	0.20	95851	92749	750449
$Z/\gamma^* \to ee + 2b2lp$	$75 < M < 130$	0.099	45121	43735	336722
$Z/\gamma^* \to ee + 2b0lp$	$130 < M < 250$	0.0034	104542	89607	397262
$Z/\gamma^* \to ee + 2b1lp$	$130 < M < 250$	0.0018	11136	45485	183204
$Z/\gamma^* \to ee + 2b2lp$	$130 < M < 250$	0.00088	43876	44116	162329
$Z/\gamma^* \to ee + 2b0lp$	$250 < M < 1960$	0.00034	189972	187426	201816
$Z/\gamma^* \to ee + 2b1lp$	$250 < M < 1960$	0.00011	173053	162968	73639
$Z/\gamma^* \to ee + 2c0lp$	$15 < M < 75$	4.14	195217	183226	1669836
$Z/\gamma^* \to ee + 2c1lp$	$15 < M < 75$	0.95	97283	181186	824348
$Z/\gamma^* \to ee + 2c2lp$	$15 < M < 75$	0.34	101456	173590	418538
$Z/\gamma^* \to ee + 2c0lp$	$75 < M < 130$	0.93	202586	183416	1693444
$Z/\gamma^* \to ee + 2c1lp$	$75 < M < 130$	0.55	105298	89474	919700
$Z/\gamma^* \to ee + 2c2lp$	$75 < M < 130$	0.28	48680	47555	412598
$Z/\gamma^* \to ee + 2c0lp$	$130 < M < 250$	0.0076	95713	182250	417011
$Z/\gamma^* \to ee + 2c1lp$	$130 < M < 250$	0.0044	47990	92496	198697
$Z/\gamma^* \to ee + 2c2lp$	$130 < M < 250$	0.0028	48864	93503	202989
$Z/\gamma^* \to ee + 2c0lp$	$250 < M < 1960$	0.00062	192829	231640	202114
$Z/\gamma^* \to ee + 2c1lp$	$250 < M < 1960$	0.00044	194512	229822	91935
$Z/\gamma^* \to ee + 2c2lp$	$250 < M < 1960$	0.00026	194353	232880	93262

Table D-11: $Z/\gamma^* \rightarrow \tau\bar{\tau}$ MC samples used in the analysis. The cross section times branching ratios and the number of events before data quality cuts are applied are listed.

Process	Mass Range (GeV)	$\sigma \times BR$ (pb)	Events before data quality		
			RunIIa	RunIIb1	RunIIb2
$Z/\gamma^* \rightarrow \tau\tau + 0lp$	$15 < M < 75$	336.57	562840	1586361	7505429
$Z/\gamma^* \rightarrow \tau\tau + 1lp$	$15 < M < 75$	39.90	444702	541471	3629834
$Z/\gamma^* \rightarrow \tau\tau + 2lp$	$15 < M < 75$	9.94	165650	292363	1583448
$Z/\gamma^* \rightarrow \tau\tau + 3lp$	$15 < M < 75$	2.78	78685	284646	733987
$Z/\gamma^* \rightarrow \tau\tau + 0lp$	$75 < M < 130$	133.17	2848207	1523002	8718476
$Z/\gamma^* \rightarrow \tau\tau + 1lp$	$75 < M < 130$	40.70	1883348	565253	3630904
$Z/\gamma^* \rightarrow \tau\tau + 2lp$	$75 < M < 130$	10.01	862808	274866	1927464
$Z/\gamma^* \rightarrow \tau\tau + 3lp$	$75 < M < 130$	3.29	832161	174114	784879
$Z/\gamma^* \rightarrow \tau\tau + 0lp$	$130 < M < 250$	0.88	282414	359959	891820
$Z/\gamma^* \rightarrow \tau\tau + 1lp$	$130 < M < 250$	0.34	182711	171386	660315
$Z/\gamma^* \rightarrow \tau\tau + 2lp$	$130 < M < 250$	0.099	86420	163102	292835
$Z/\gamma^* \rightarrow \tau\tau + 3lp$	$130 < M < 250$	0.032	84516	158390	259020
$Z/\gamma^* \rightarrow \tau\tau + 0lp$	$250 < M < 1960$	0.034	193465	537185	707118
$Z/\gamma^* \rightarrow \tau\tau + 1lp$	$250 < M < 1960$	0.035	91471	463755	329720
$Z/\gamma^* \rightarrow \tau\tau + 2lp$	$250 < M < 1960$	0.011	44152	330563	143985
$Z/\gamma^* \rightarrow \tau\tau + 3lp$	$250 < M < 1960$	0.0039	41417	145686	56650
$Z/\gamma^* \rightarrow \tau\tau + 2b0lp$	$15 < M < 75$	0.51	197621	185687	1359761
$Z/\gamma^* \rightarrow \tau\tau + 2b1lp$	$15 < M < 75$	0.20	90550	89711	647222
$Z/\gamma^* \rightarrow \tau\tau + 2b2lp$	$15 < M < 75$	0.078	94714	82677	289337
$Z/\gamma^* \rightarrow \tau\tau + 2b0lp$	$75 < M < 130$	0.42	198561	193456	1399352
$Z/\gamma^* \rightarrow \tau\tau + 2b1lp$	$75 < M < 130$	0.20	96586	97887	493698
$Z/\gamma^* \rightarrow \tau\tau + 2b2lp$	$75 < M < 130$	0.099	45232	43988	295780
$Z/\gamma^* \rightarrow \tau\tau + 2b0lp$	$130 < M < 250$	0.0034	102956	88308	350658
$Z/\gamma^* \rightarrow \tau\tau + 2b1lp$	$130 < M < 250$	0.0018	46731	44554	165306
$Z/\gamma^* \rightarrow \tau\tau + 2b2lp$	$130 < M < 250$	0.00088	43221	41299	145048
$Z/\gamma^* \rightarrow \tau\tau + 2b0lp$	$250 < M < 1960$	0.00034	191925	177774	175445
$Z/\gamma^* \rightarrow \tau\tau + 2b1lp$	$250 < M < 1960$	0.00017	185678	174520	74127
$Z/\gamma^* \rightarrow \tau\tau + 2b2lp$	$250 < M < 1960$	0.00011	331713	161733	64784
$Z/\gamma^* \rightarrow \tau\tau + 2c0lp$	$15 < M < 75$	4.14	202444	180704	1464669
$Z/\gamma^* \rightarrow \tau\tau + 2c1lp$	$15 < M < 75$	0.95	95762	182060	734397
$Z/\gamma^* \rightarrow \tau\tau + 2c2lp$	$15 < M < 75$	0.34	99201	179776	359299
$Z/\gamma^* \rightarrow \tau\tau + 2c0lp$	$75 < M < 130$	0.93	196586	260691	1564469
$Z/\gamma^* \rightarrow \tau\tau + 2c1lp$	$75 < M < 130$	0.55	97555	101099	546371
$Z/\gamma^* \rightarrow \tau\tau + 2c2lp$	$75 < M < 130$	0.28	48194	50843	371917
$Z/\gamma^* \rightarrow \tau\tau + 2c0lp$	$130 < M < 250$	0.0076	96791	92369	367012
$Z/\gamma^* \rightarrow \tau\tau + 2c1lp$	$130 < M < 250$	0.0044	48398	48962	182397
$Z/\gamma^* \rightarrow \tau\tau + 2c2lp$	$130 < M < 250$	0.0028	47987	46871	184947
$Z/\gamma^* \rightarrow \tau\tau + 2c0lp$	$250 < M < 1960$	0.00062	194299	179531	183791
$Z/\gamma^* \rightarrow \tau\tau + 2c1lp$	$250 < M < 1960$	0.00044	195289	182470	83502
$Z/\gamma^* \rightarrow \tau\tau + 2c2lp$	$250 < M < 1960$	0.00026	200315	189460	83160

E $\mathbf{VH \rightarrow VWW^* \rightarrow}$ Tri-leptons Final Discriminant DT Distributions

The complete set of final discriminant distributions for all mass points not shown in Chapter 6.3.3 are presented here.

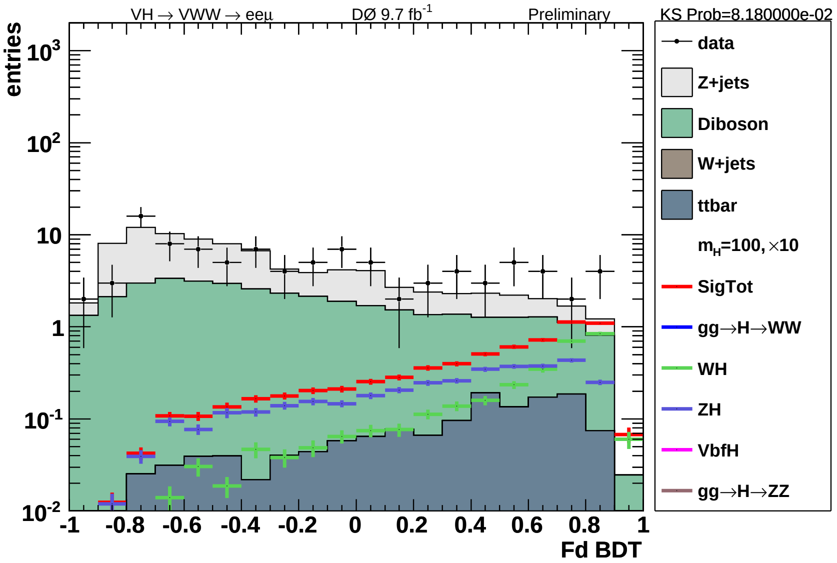

(a)

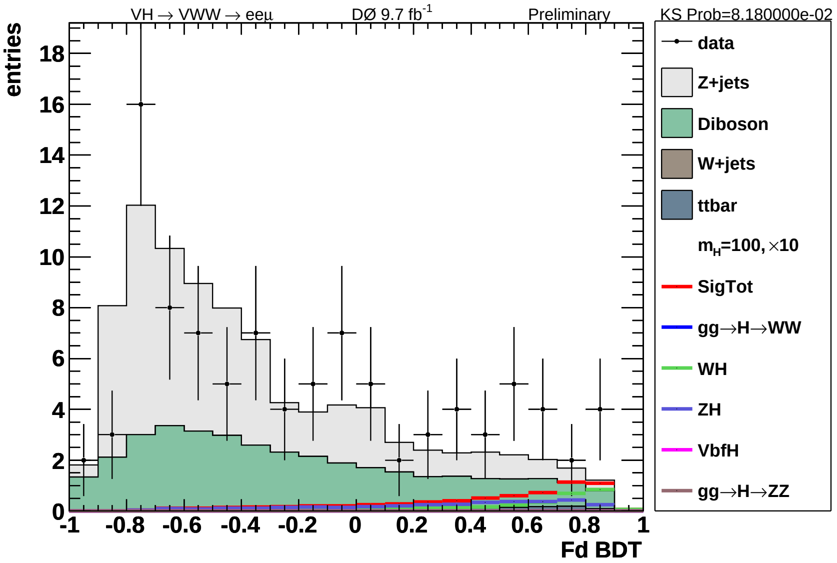

(b)

Figure E-1: The final discriminant DT distribution in (a) logarithmic scale and (b) linear scale for data (points) and sum of all the backgrounds (histograms). The expected signal, multiplied by a factor of 10, for a 100 GeV SM Higgs boson is also shown in red. MC signal samples for $H \to WW^*$, $H \to ZZ$, and VBF are not available for this mass.

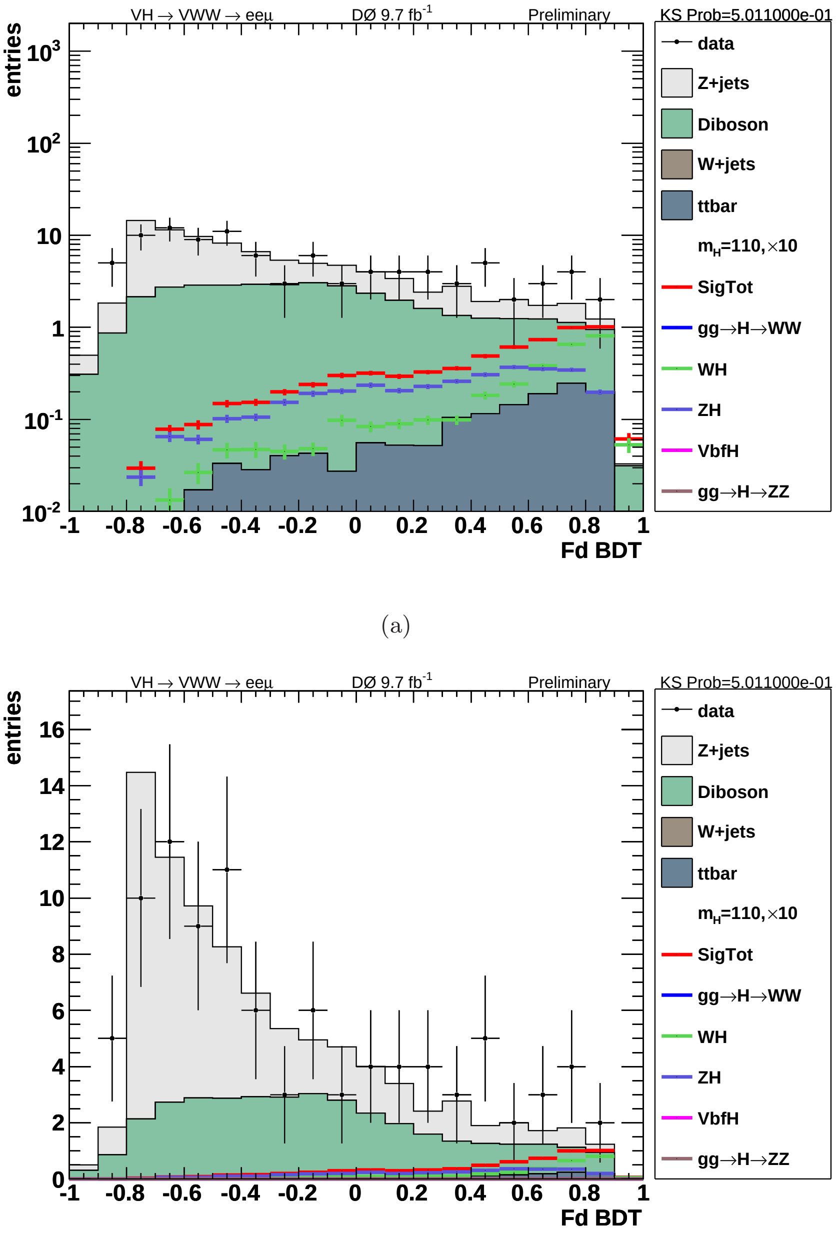

(a)

(b)

Figure E-2: The final discriminant DT distribution in (a) logarithmic scale and (b) linear scale for data (points) and sum of all the backgrounds (histograms). The expected signal, multiplied by a factor of 10, for a 110 GeV SM Higgs boson is also shown in red. MC signal samples for $H \rightarrow WW^*$, $H \rightarrow ZZ$, and VBF are not available for this mass.

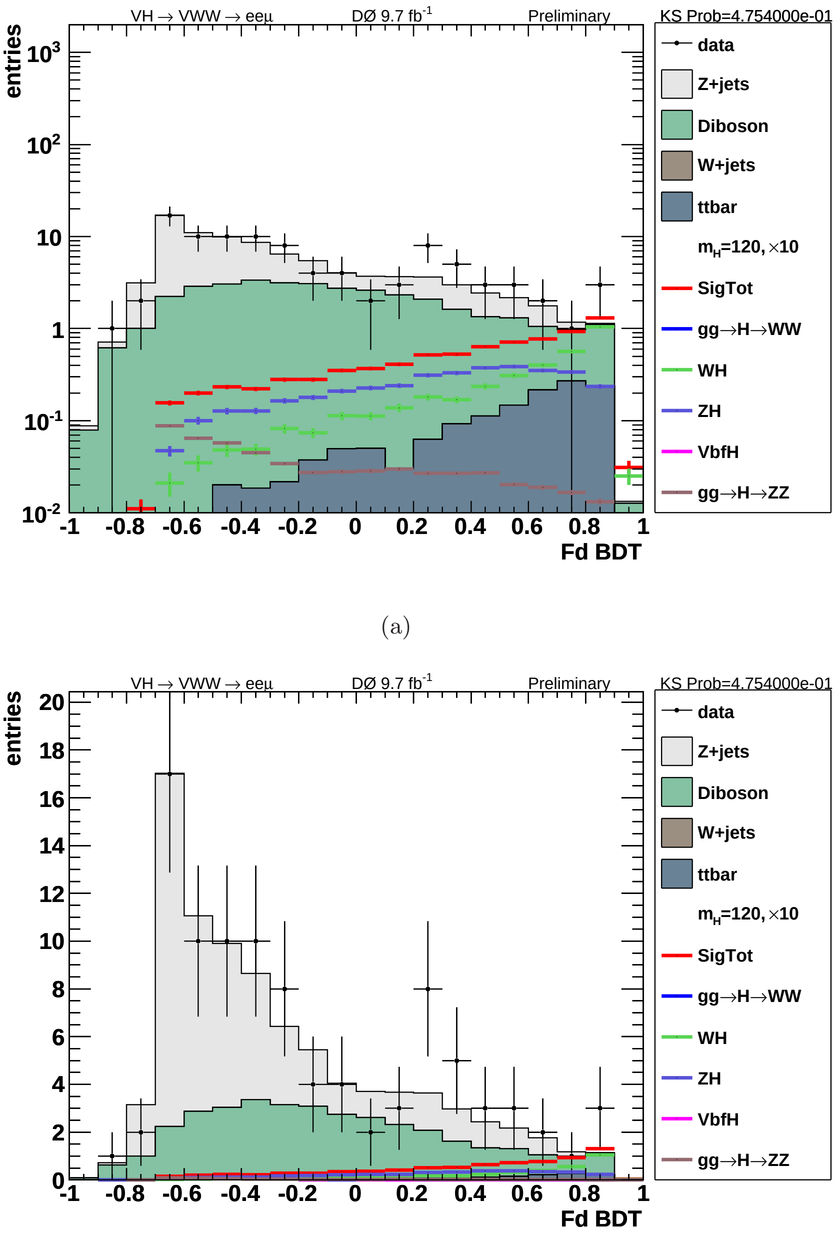

(a)

(b)

Figure E-3: The final discriminant DT distribution in (a) logarithmic scale and (b) linear scale for data (points) and sum of all the backgrounds (histograms). The expected signal, multiplied by a factor of 10, for a 120 GeV SM Higgs boson is also shown in red.

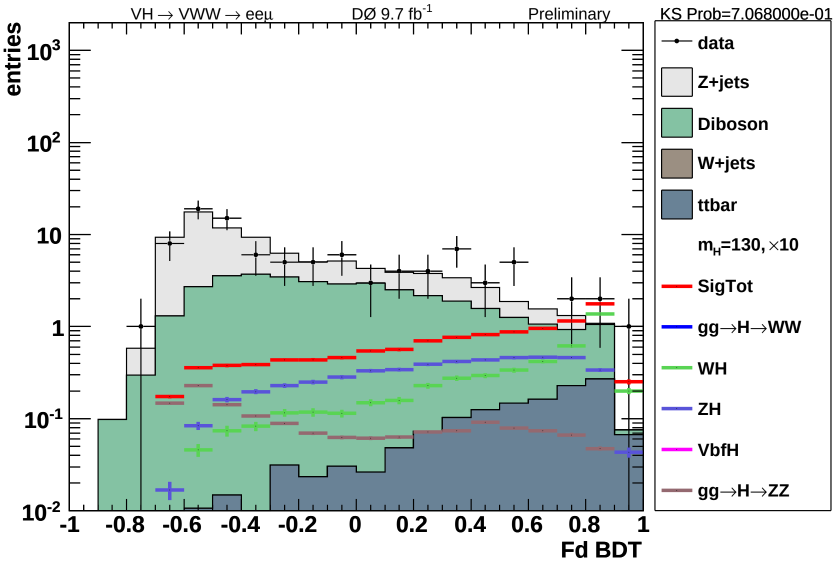

(a)

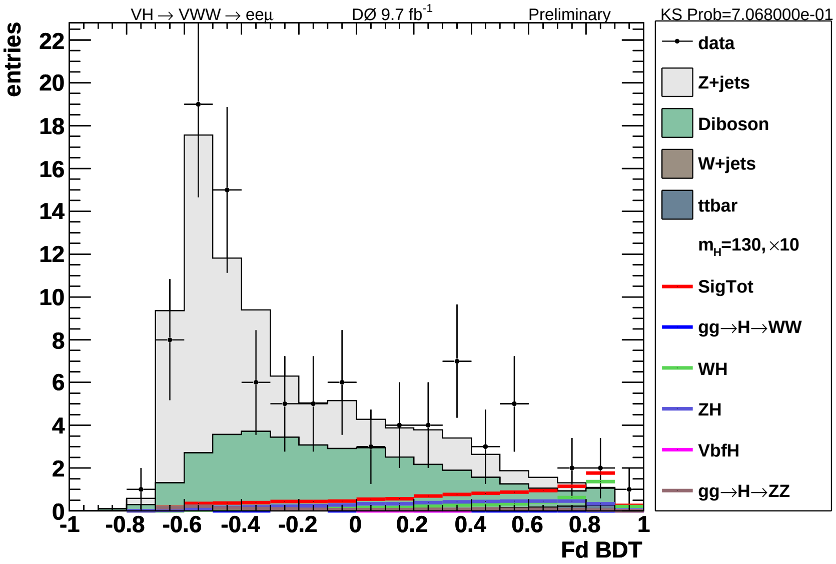

(b)

Figure E-4: The final discriminant DT distribution in (a) logarithmic scale and (b) linear scale for data (points) and sum of all the backgrounds (histograms). The expected signal, multiplied by a factor of 10, for a 130 GeV SM Higgs boson is also shown in red.

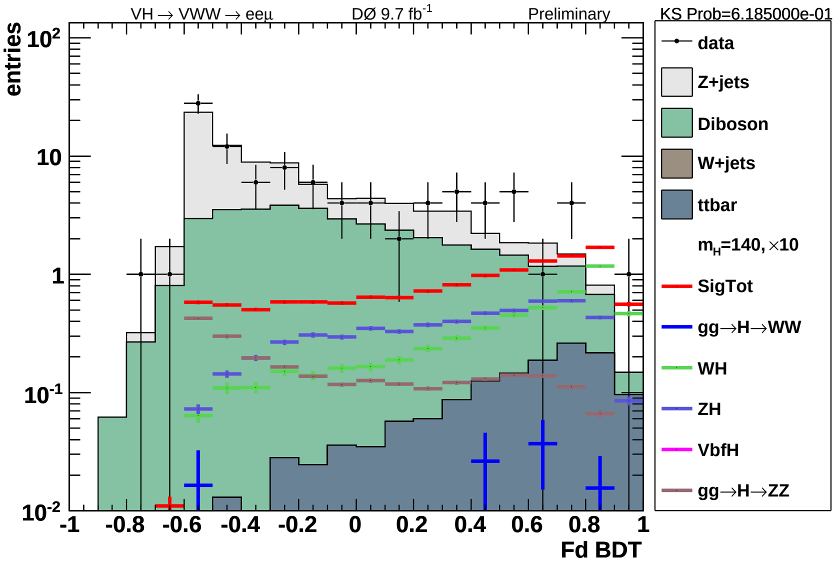

(a)

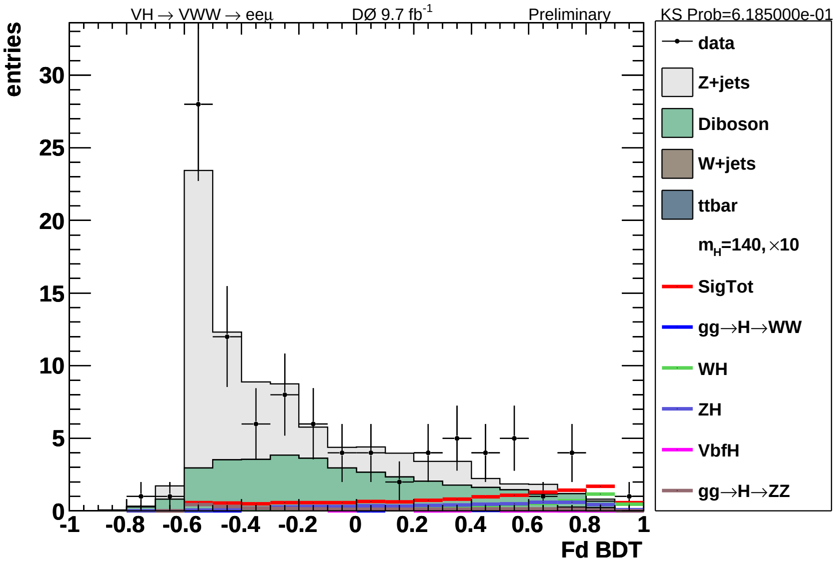

(b)

Figure E-5: The final discriminant DT distribution in (a) logarithmic scale and (b) linear scale for data (points) and sum of all the backgrounds (histograms). The expected signal, multiplied by a factor of 10, for a 140 GeV SM Higgs boson is also shown in red.

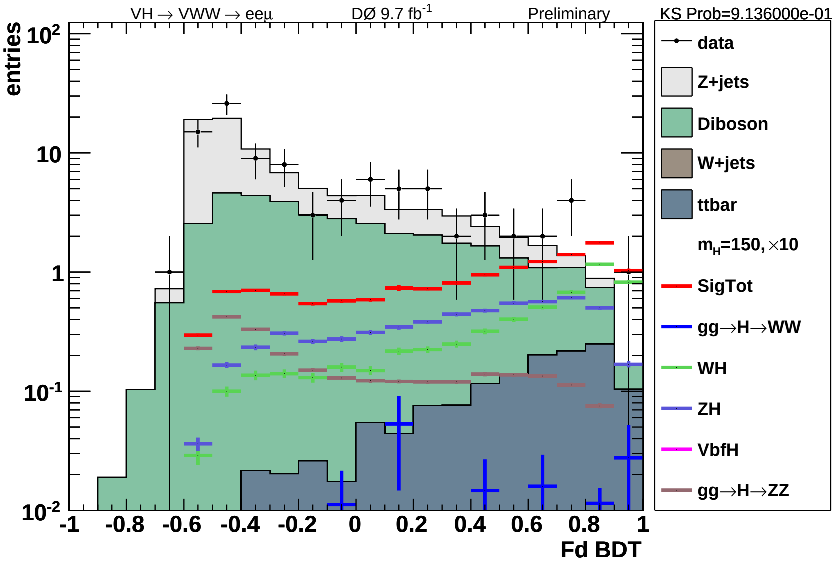

(a)

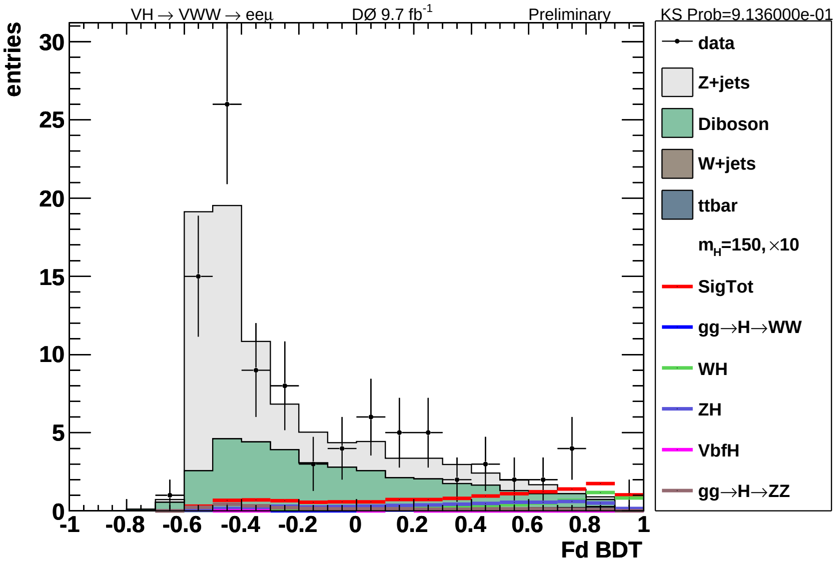

(b)

Figure E-6: The final discriminant DT distribution in (a) logarithmic scale and (b) linear scale for data (points) and sum of all the backgrounds (histograms). The expected signal, multiplied by a factor of 10, for a 150 GeV SM Higgs boson is also shown in red.

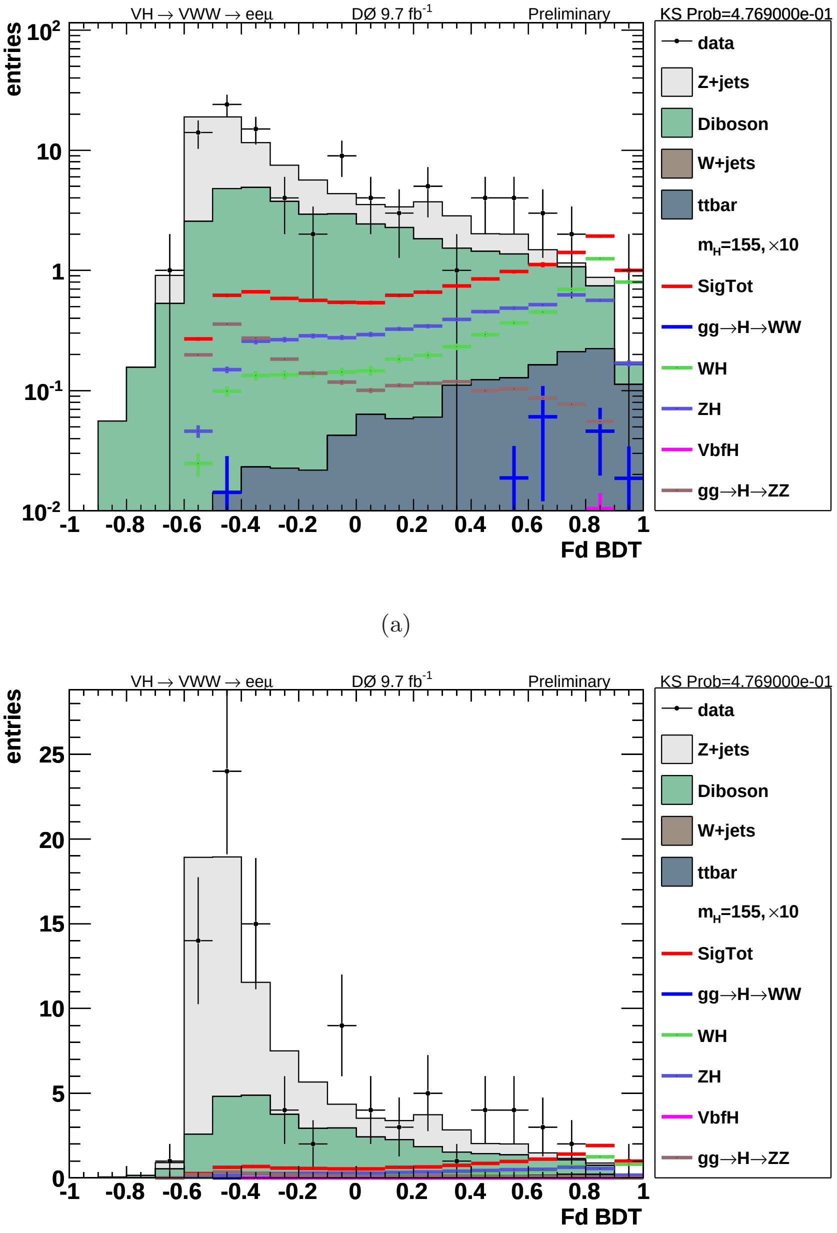

(a)

(b)

Figure E-7: The final discriminant DT distribution in (a) logarithmic scale and (b) linear scale for data (points) and sum of all the backgrounds (histograms). The expected signal, multiplied by a factor of 10, for a 155 GeV SM Higgs boson is also shown in red.

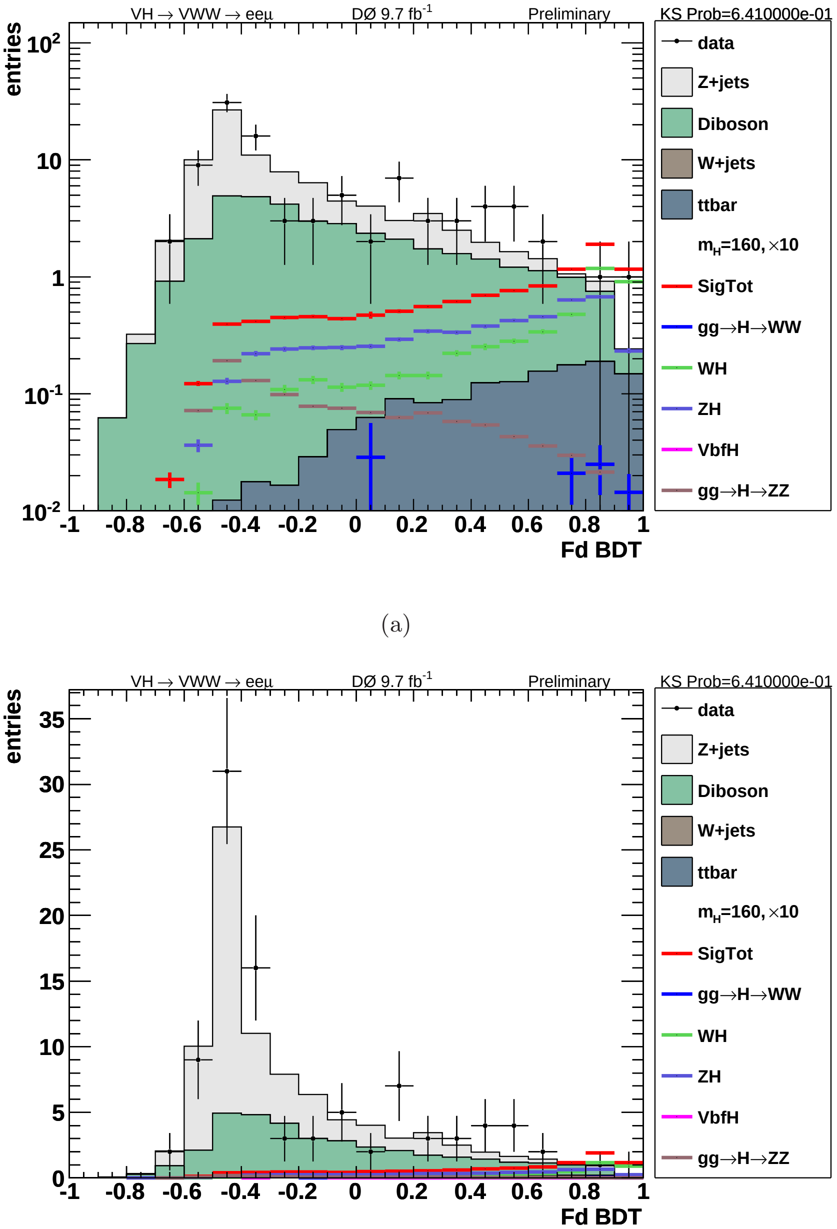

(a)

(b)

Figure E-8: The final discriminant DT distribution in (a) logarithmic scale and (b) linear scale for data (points) and sum of all the backgrounds (histograms). The expected signal, multiplied by a factor of 10, for a 160 GeV SM Higgs boson is also shown in red.

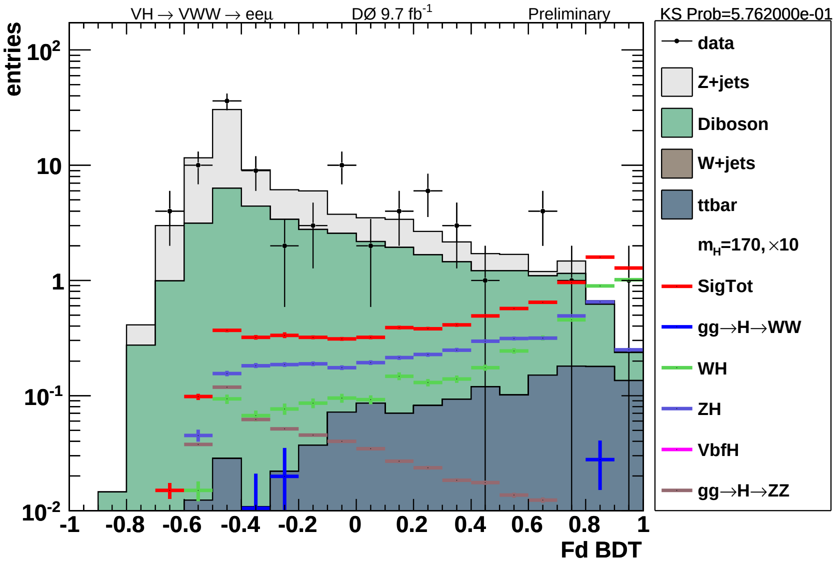

(a)

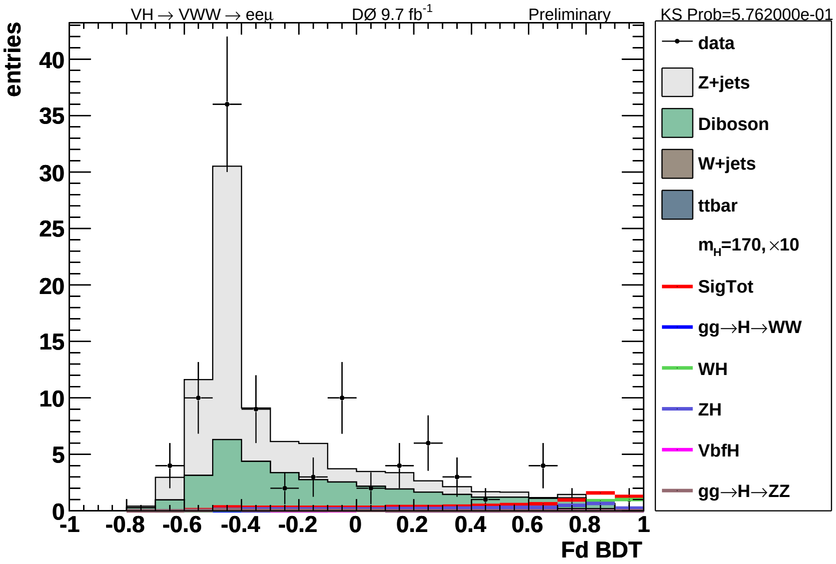

(b)

Figure E-9: The final discriminant DT distribution in (a) logarithmic scale and (b) linear scale for data (points) and sum of all the backgrounds (histograms). The expected signal, multiplied by a factor of 10, for a 170 GeV SM Higgs boson is also shown in red.

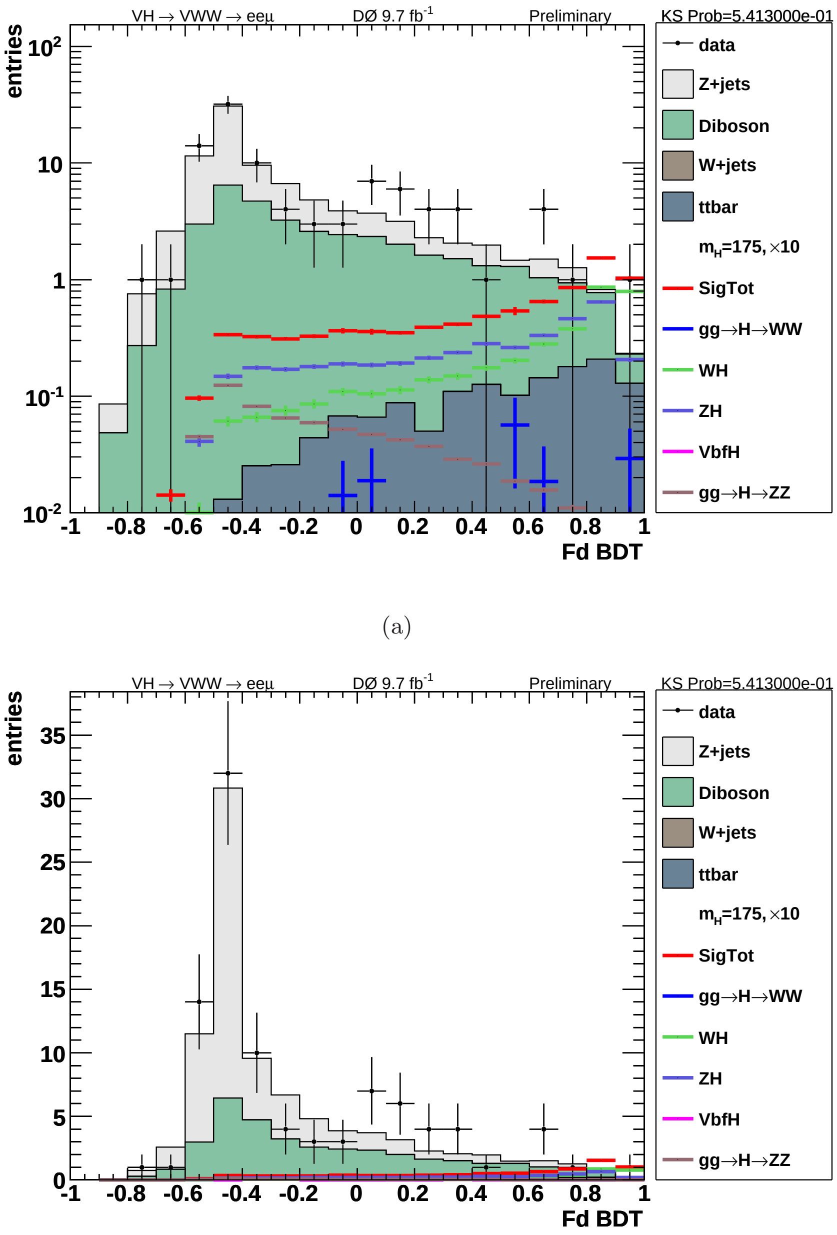

(a)

(b)

Figure E-10: The final discriminant DT distribution in (a) logarithmic scale and (b) linear scale for data (points) and sum of all the backgrounds (histograms). The expected signal, multiplied by a factor of 10, for a 175 GeV SM Higgs boson is also shown in red.

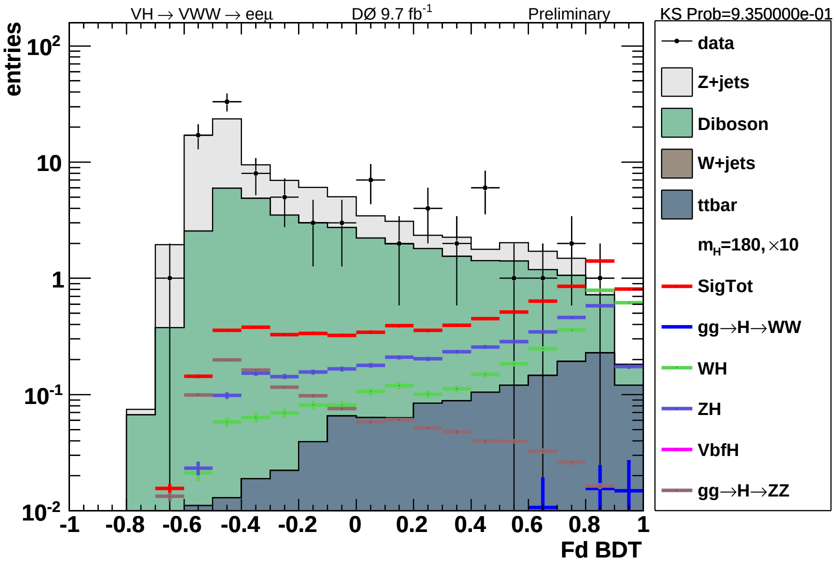

(a)

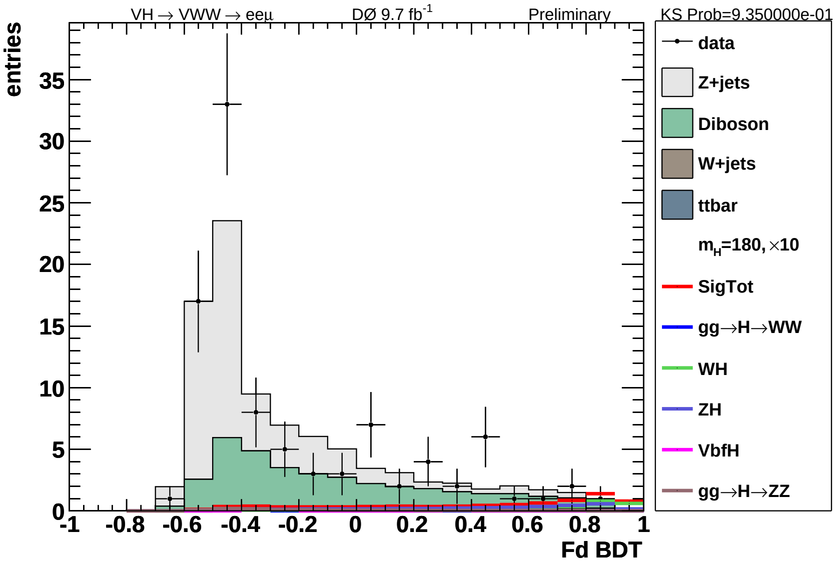

(b)

Figure E-11: The final discriminant DT distribution in (a) logarithmic scale and (b) linear scale for data (points) and sum of all the backgrounds (histograms). The expected signal, multiplied by a factor of 10, for a 180 GeV SM Higgs boson is also shown in red.

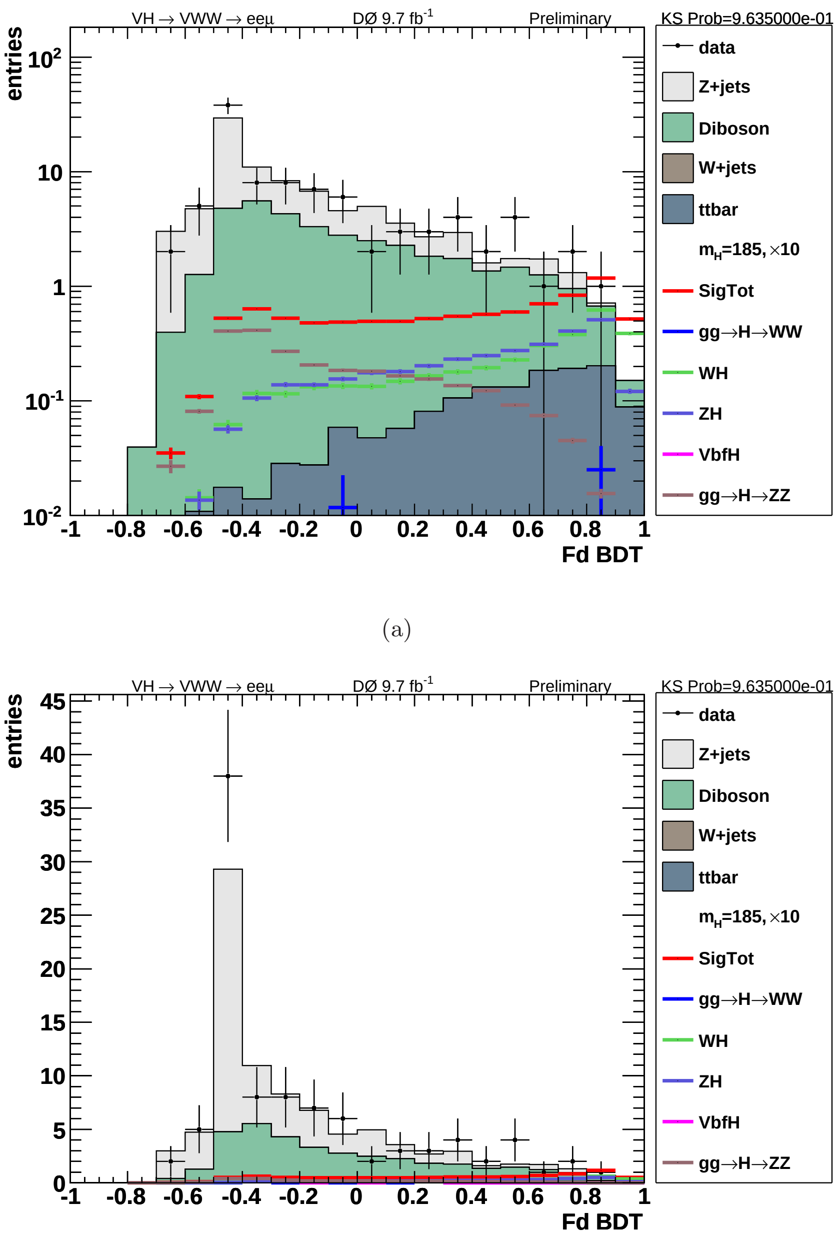

(a)

(b)

Figure E-12: The final discriminant DT distribution in (a) logarithmic scale and (b) linear scale for data (points) and sum of all the backgrounds (histograms). The expected signal, multiplied by a factor of 10, for a 185 GeV SM Higgs boson is also shown in red.

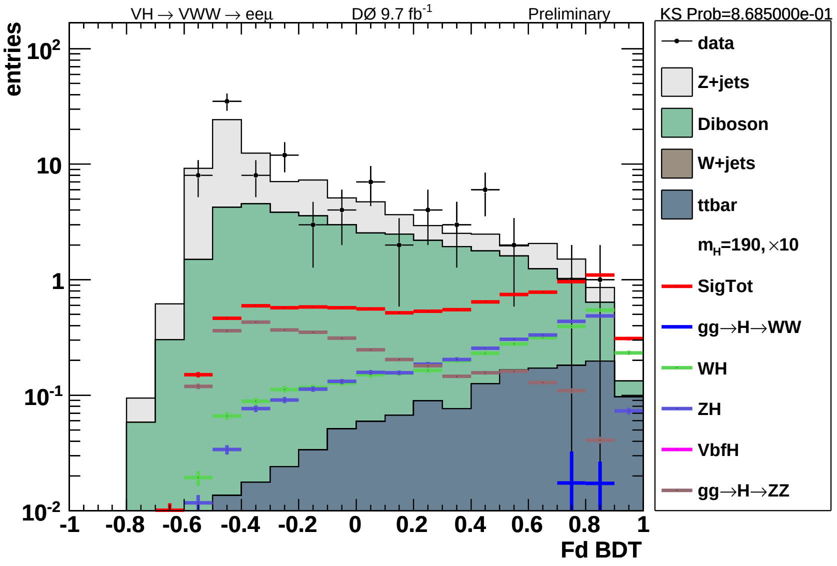

(a)

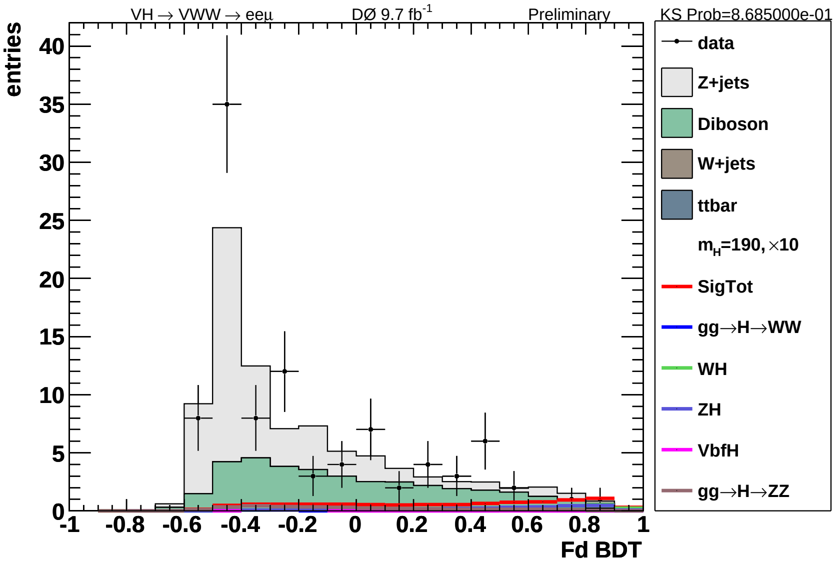

(b)

Figure E-13: The final discriminant DT distribution in (a) logarithmic scale and (b) linear scale for data (points) and sum of all the backgrounds (histograms). The expected signal, multiplied by a factor of 10, for a 190 GeV SM Higgs boson is also shown in red.

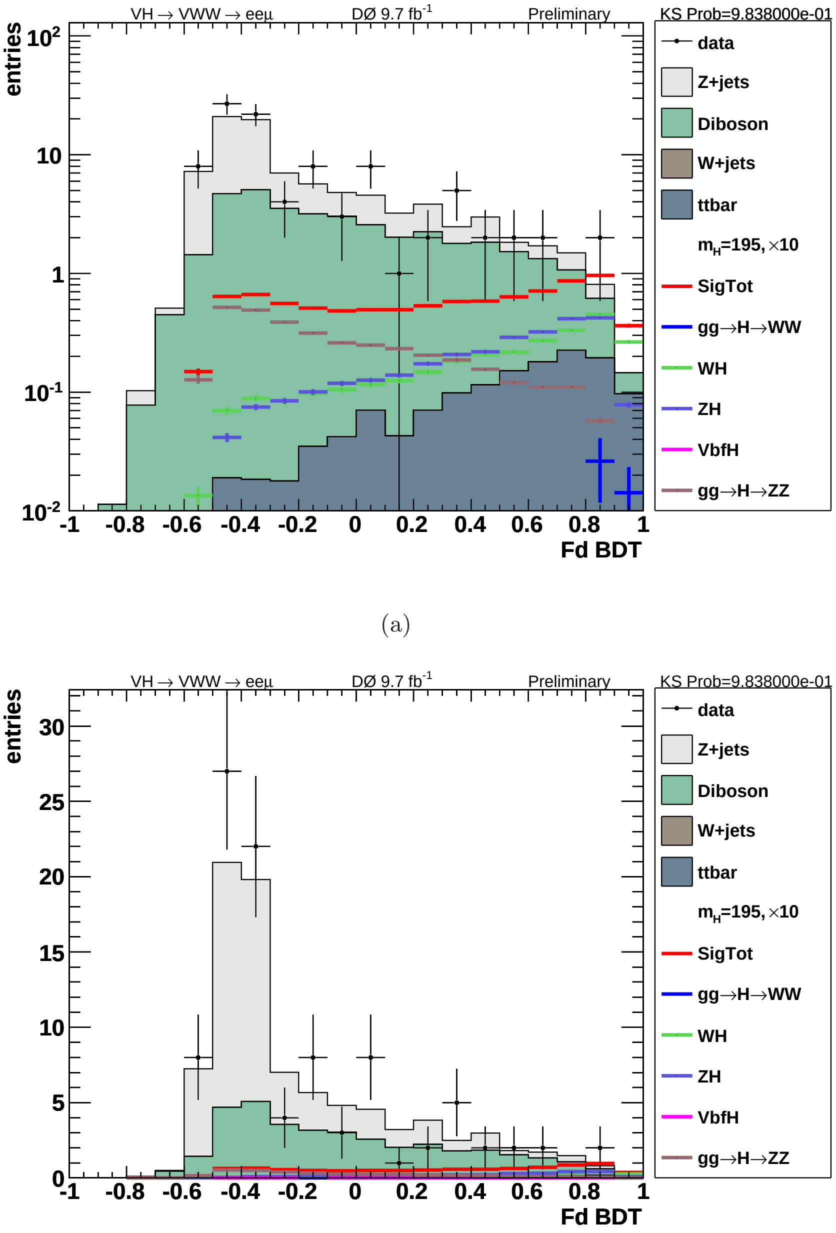

(a)

(b)

Figure E-14: The final discriminant DT distribution in (a) logarithmic scale and (b) linear scale for data (points) and sum of all the backgrounds (histograms). The expected signal, multiplied by a factor of 10, for a 195 GeV SM Higgs boson is also shown in red.

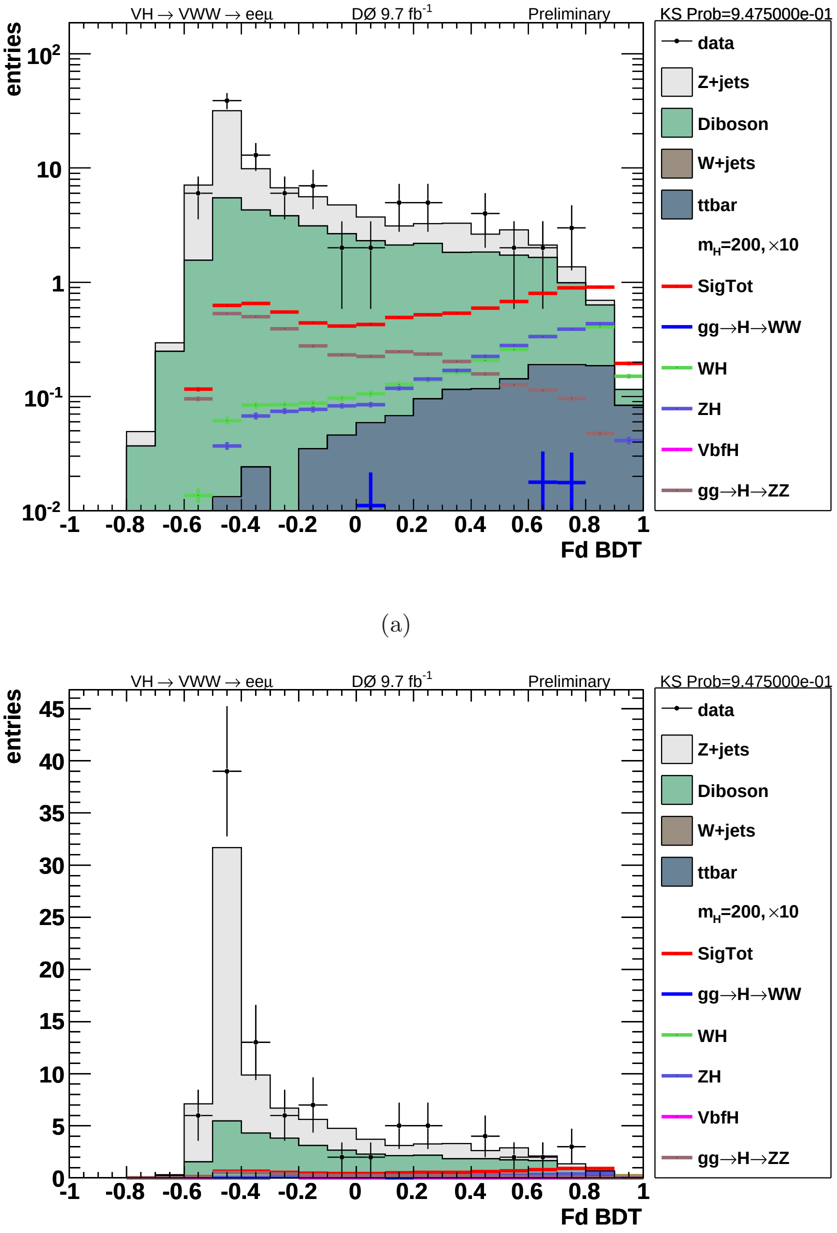

(a)

(b)

Figure E-15: The final discriminant DT distribution in (a) logarithmic scale and (b) linear scale for data (points) and sum of all the backgrounds (histograms). The expected signal, multiplied by a factor of 10, for a 200 GeV SM Higgs boson is also shown in red.

References

[1] Tevatron New Phenomena, Higgs Working Group [The TEVNPH Working Group], FERMILAB-CONF-11-372-E , arXiv:1108.3331v2 [hep-ex], 2011.

[2] http://en.wikipedia.org/wiki/Standard_Model

[3] F. J. Hasert *et al.* [Gargamelle Collaboration], Phys. Lett. B **46**, 121 (1973);
Phys. Lett. B **46**, 138 (1973);
F. J. Hasert *et al.* [Gargamelle Collaboration], Nucl. Phys. B **73**, 1 (1974).

[4] G. Amison *et al.* [UA1 Collaboration], Phys. Lett. B **122**, 103 (1983);
Phys. Lett. B **126**, 398 (1983); Phys. Lett. B **129**, 273 (1983);
M. Banner *et al.* [UA2 Collaboration], Phys. Lett. B **122**, 476 (1983);
P. Bagnaia *et al.* [UA2 Collaboration], Phys. Lett. B **129**, 130 (1983).

[5] J.E. Augustin *et al.*, Phys. Rev. Lett. **33**, 1406 (1974);
J.J. Aubert *et al.*, Phys. Rev. Lett. **33**, 1404 (1974).

[6] H. Fritzsch and M. Gell-Mann, Proc. 16th Int. Conf. on High Energy Physics (Chicago-Batavia, 1972), Vol. 2, p. 135;
H. Fritzsch, M. Gell-Mann, and H. Leutwyler, Phys. Lett. B **47**, 365 (1973);
H.D. Politzer, Phys. Rev. Lett. **30**, 1346 (1973);
D.J. Gross and F. Wilczek, Phys. Rev. Lett. **30**, 1343 (1973).

[7] F. Abe *et al.* [CDF Collaboration], Phys. Rev. Lett. **74**, 2626 (1995);
S. Abachi *et al.* [DØ Collaboration], Phys. Rev. Lett. **74**, 2632 (1995).

[8] Y. Fukuda *et al.* [Super-Kamiokande Collaboration], Phys. Rev. Lett. **81**, 1158 (1998).

[9] S. Weinberg, Phys. Rev. D **13**, 974 (1976); Phys. Rev. D **19**, 1277 (1979);
E. Gildener, Phys. Rev. D **14**, 1667 (1976);

L. Susskind, Phys. Rev. D **20**, 2619 (1979);

G. t Hooft, Proc. of the NATO Advanced Summer Institute, Cargese 1979, (Plenum, 1980).

[10] H. Miyazawa, Prog. Theor. Phys. **36**, 1266 (1966); Phys. Rev. **170**, 1586 (1968); Yu Golfand and E. Likhtman, ZhETF Pis. Red. **13**, 452 (1971); (JETP Lett. **13**, 323 (1971)).

J.L. Gervais and B. Sakita, Nucl. Phys. B **34**, 632 (1971);

A. Neveu and J.H. Schwarz, Nucl. Phys. B **31**, 86 (1971);

P. Ramond, Phys. Rev. D **3**, 2415 (1971);

D.V. Volkov and V.P. Akulov, Phys. Lett. B **46**, 109 (1973);

J. Wess and B. Zumino, Nucl. Phys. B **70**, 39 (1974); Phys. Letters B **49**, 52 (1974); Nucl. Phys. B **78**, 1 (1974).

[11] V. M. Abazov *et al.* [DØ Collaboration], Phys. Rev. Lett. **94**, 151801 (2005).

[12] A. Abulencia *et al.* [CDF Collaboration], Phys. Rev. Lett. **98**, 161801 (2007).

[13] V. M. Abazov *et al.* [DØ Collaboration], Phys. Rev. Lett. **101**, 171803 (2008).

[14] http://www.fnal.gov/pub/presspass/press_releases/Higgs-mass-constraints-20100726-images.html

[15] F. Abe *et al.* [CDF Collaboration], Phys. Rev. Lett. **78**, 4536 (1997).

[16] B. Abbott *et al.* [DØ Collaboration], Phys. Rev. D **60**, 072002 (1999).

[17] K. Hagiwara, J. Woodside, and D. Zeppenfeld, Phys. Rev. D **41**, 2113 (1990).

[18] H. Baer and J. Wells, Phys. Rev. D **57**, 4446 (1998).

[19] U. Egede, "The search for a standard model Higgs at the LHC and electron identification using transition radiation in the ATLAS tracker" . Ph.D. Thesis, Lund University, 1997.

[20] http://maltoni.home.cern.ch/maltoni/TeV4LHC/SM.html

[21] http://www.physics.ucdavis.edu/∼conway/research/higgs/smhiggs-tev.html

[22] Precision Electroweak Measurements and Constraints on the Standard Model. arXiv:1012.2367, January 2011.

[23] G. Abbiendi *et al.* [ALEPH Collaboration, DELPHI Collaboration, L3 Collaboration, and OPAL Collaboration, The LEP Working Group for Higgs Boson Searches], Phys. Lett. B **565**, 61 (2003).

[24] The CDF and DØ Collaborations, the Tevatron New Phenomena, Higgs Working Group, "Combined CDF and DØ upper limits on Standard Model Higgs Boson production". arXiv:hep-ex/1107.5518v2, July 2011.
CDF Note 10606 and DØ Note 6226.

[25] http://indico.cern.ch/conferenceDisplay.py?confId=164890

[26] The ATLAS Collaboration, "Combined search for the Standard Model Higgs boson using up to 4.9 fb^{-1} of pp collision data at $\sqrt{s} = 7$ TeV with the ATLAS detector at the LHC". arXiv:hep-ex/1202.1408v2, 2012.

[27] The CMS Collaboration, "Combination of SM Higgs Searches". CMS Physics Analysis Summary, HIG-11-032, 2011.

[28] The CDF and DØ Collaborations, the Tevatron New Phenomena, Higgs Working Group, "Combined CDF and DØ Search for Standard Model Higgs Boson Production with up to 10 fb^{-1} of Data". FERMILAB-CONF-12-065-E, 2012.
CDF Note 10806 and DØ Note 6303

[29] C. Amsler *et al.* [Particle Data Group], Phys. Lett. B **667**, 1 (2008).

[30] F. Halzen and A.D. Martin, *Quarks and Leptons*, (New York: Wiley, 1984)

[31] T. Han and J.L. Hewett, Phys. Rev. D **60**, 074015 (1999).

[32] I. Zaw, "Search for the Flavor Changing Neutral Current Decay $t \rightarrow qZ$ in $p\bar{p}$ Collisions at $\sqrt{s} = 1.96$ TeV". Ph.D. Thesis, Harvard University, 2007.

[33] http://www.fnal.gov/pub/science/accelerator/

[34] Accelerator Concepts Rookie Book, http://www-bdnew.fnal.gov/operations, 2009.

[35] V.M. Abazov *et al.* [DØ Collaboration], Nucl. Instr. and Methods A **565**, 463 (2006).

[36] Data Quality Group webpage:
http://www-d0.fnal.gov/computing/data quality/d0_private/forusers.html

[37] J. Haley, "First Evidence for WW and WZ Diboson Production with Semi-Leptonic Decays at a Hadron Collider". Ph.D. Thesis, Princeton University, 2009.

[38] R. Jesik, "Triggering at DØ". University of DØ Presentation, December 9, 2010.

[39] M. Prewitt, "Operation of the Run IIb DØ Luminosity System and Determination of the Run IIb Luminosity Constant". Masters Thesis, Rice University, 2010.

[40] S. Klimenko, J. Konigsberg, and T.M. Liss, "Averaging of the Inelastic Cross Sections Measured by the CDF and the E811 Experiments". Fermilab-FN-0741, 2003.

[41] T. Andeen *et al.*, "The DØ Experiment's Integrated Luminosity for Tevatron Run IIa". FERMILAB-TM-2365, 2007.

[42] J. Olsen, "CFT/CPS Axial Daughterboard DFEA, Technical Design Report". Internal Note 4163, DØ Collaboration, 2005.

[43] CTT AND/OR Terms
http://www-d0online.fnal.gov/www/groups/cft/CTT/online/AOterms/ctt.html

[44] A. Khanov, "HTF: histogramming method for finding tracks. The algorithm description". Internal Note 3778, DØ Collaboration, 2000.

[45] G. Borissov, "Ordering a Chaos or... Technical Details of AA Tracking". http://www-d0.fnal.gov/global_tracking/talks/20030228/talk-adm-030228.ps

[46] H. Greenlee, "The DØ Kalman Track Fit". Internal Note 4304, DØ Collaboration, 2004.

[47] J. Kozminski *et al.*, "Electron Likelihood in p14". Internal Note 4449, DØ Collaboration, 2004.

[48] F. Fleuret, "The DØ Electron/Photon Analysis Package EMAnalyze". Internal Note 3888, DØ Collaboration, 2001.

[49] D. Whiteson and L. Phaf, "Electron Likelihood". Internal Note 4184, DØ Collaboration, 2003.

[50] J. Zhu, "Determination of Electron Energy Scale and Energy Resolution using p14 $Z^0 \to e^+e^-$ data". Internal Note 4323, DØ Collaboration, 2003.

[51] K. Kaadze, "Study of WZ Production with the DØ Detector". Ph.D. Thesis, Kansas State University, 2010.

[52] O. Atramentov and Y. Maravin, "Utilizing CFT and SMT hits count for photon and electron reconstruction". Internal Note 4444, DØ Collaboration, 2004.

[53] X. Bu and Y. Liu, "Artificial neural network for Run IIb electron and photon identification". Internal Note 5545, DØ Collaboration, 2007.

[54] O. Atramentov *et al.*, "Electron and Photon Identification with p20 data". Internal Note 5761, DØ Collaboration, 2008.

[55] M. Aoki, "Electron Likelihood in p20". Internal Note 5675, DØ Collaboration, 2009.

[56] B. Calpas, J. Kraus, and T. Yasuda, "ICR Electron Efficiencies for Run IIa". Internal Note 5939, DØ Collaboration, 2009.

[57] https://plone4.fnal.gov/P1/D0Wiki/object-id/emid/emdev/optEleID-2009/description_eleID

[58] G. Blazey *et al.*, “RunII Jet Physics”. Internal Note 3750, DØ Collaboration, 2000. arXiv:hep-ex/0005012

[59] E. Busato and B. Andrieu, “Jet Algorithms in the DØ RunII Software: Description and User’s Guide”. Internal Note 4457, DØ Collaboration, 2004.

[60] K. Herner, “Well MET: Understanding Missing E_T at DØ”. University of DØ Presentation, November 3, 2011.

[61] A. Schwartzman,“$\not\!\!E_T$ Significance Algorithm in RunII Data”. Internal Note 4254, DØ Collaboration, 2003.

[62] http://www-d0.fnal.gov/nikhef/muon_reco/segmentreco/MuonSegmentReconstruction.pdf

[63] O. Brandt *et al.*, “Muon Identification Certification for the Summer 2009 Extended Dataset (Run IIb-1 and -2)”. Internal Note 6025, DØ Collaboration, 2010.

[64] B. Abbott *et al.* [DØ Collaboration], Phys. Rev. D **60**, 072002 (1999).

[65] D. Acosta *et al.* [CDF Collaboration], Phys. Rev. D **71**, 091105 (2005).

[66] V.M. Abazov *et al.* [DØ Collaboration], Phys. Rev. Lett. **95**, 141802 (2005).

[67] V.M. Abazov *et al.* [DØ Collaboration], Phys. Rev. D **76**, 111104 (2007).

[68] A. Askew *et al.*, “Measurement of the $WZ \to \ell'\nu\ell\bar{\ell}$ cross section and limits on anomalous triple gauge couplings”. Internal Note 6021, DØ Collaboration, 2010; V.M. Abazov *et al.* [DØ Collaboration], Phys. Lett. B **695**, 67 (2011).

[69] J. Pumplin *et al.*, JHEP 0207, 012 (2002).

[70] T. Sjöstrand *et al.*, Computer Phys. Commun. **135**, 238 (2001), arXiv:hep-ph/0010017.

[71] M.L. Mangano *et al.*, JHEP 0307, 001 (2003), arXiv:hep-ph/0206293.

[72] See https://plone4.fnal.gov/P1/D0Wiki/tdaq/tsg/caftriggers/singleetriggers and https://plone4.fnal.gov/P1/D0Wiki/tdaq/tsg/triggerrun2b/singleeletriggers for lists

[73] See https://plone4.fnal.gov/P1/D0Wiki/tdaq/tsg/caftriggers/singlemutriggers and https://plone4.fnal.gov/P1/D0Wiki/tdaq/tsg/triggerrun2b/singlemuontriggers for lists

[74] J. Kraus, T. Gadfort, and O. Atramentov, "p20 ICR Electron Identification". Internal Note 5691, DØ Collaboration, 2008.

[75] J. Campbell and K. Ellis, "Monte Carlo for FeMtobarn processes". http://mcfm.fnal.gov/

[76] U. Baur and E. Berger, Phys. Rev. D **47**, 4889 (1993).

[77] For more information see http://www-d0.fnal.gov/computing/MonteCarlo/pmcs/pmcs_doc/pmcs.html

[78] Uncertainties assumed to be similar to Tight operating point. Systematic uncertainties for several operating points listed on EM-ID Wiki page; https://plone4.fnal.gov/P1/D0Wiki/object-id/emid/emcert/Moriond2009/uncertainty_moriond09

[79] S. Cho *et al.*, "Muon ID Certification for p20 data". Internal Note 5824, DØ Collaboration, 2008.

[80] P.M. Nadolsky *et al.*, Phys. Rev. D **78**, 013004 (2008).

[81] W. Beenakker *et al.*, Phys. Rev. D **40**, 54 (1989).

[82] J.M. Campbell and R.K. Ellis, Phys. Rev. D **60**, 113006 (1999).

[83] http://www-clued0.fnal.gov/∼nunne/cross-sections/mcfm_cross-sections.html

[84] H. Fritzsch, Phys. Lett. B **224**, 423 (1989).

[85] J. A. Aguilar-Saavedra, Acta Phys. Polon. B **35**, 2695 (2004).

[86] F. Larios, R. Martinez, and M.A. Perez, Phys. Rev. D **72**, 057504 (2005).

[87] P.M. Ferreira, R.B. Guedes, and R. Santos, Phys. Rev. D **77**, 114008 (2008).

[88] J.J. Zhang *et al.*, Phys. Rev. Lett. **102**, 072001 (2009); Phys. Rev. D **82**, 073005 (2010).

[89] J. Drobnak *et al.*, Phys. Rev. Lett. **104**, 252001 (2010); Phys. Rev. D **82**, 073016 (2010).

[90] T. Aaltonen *et al.* [CDF Collaboration], Phys. Rev. Lett. **101**, 192002 (2008).

[91] ATLAS Collaboration, "Search for FCNC Top Quark Processes at 7 TeV with the ATLAS Detector". ATLAS-CONF-2011-154 (2011).

[92] A. Askew *et al.*, "Branching ratio limits on flavor changing top quark decay $t \to Zq$ using $\ell'\nu\ell\bar{\ell}$ + jets final states". Internal Note 6102, DØ Collaboration, 2011;
V.M. Abazov *et al.* [DØ Collaboration], Phys. Lett. B **701**, 313 (2011).

[93] E. Boos *et al.* [CompHEP Collaboration], Nucl. Instr. and Methods A **534**, 250 (2004).

[94] S. Moch and P. Uwer, Phys. Rev. D **78**, 034003 (2008).

[95] CDF and DØ Collaborations, "Combination of CDF and D0 Results on the Mass of the Top Quark". arXiv:1007.3178 [hep-ex], July 2010.

[96] W. Fisher, “Systematics and Limit Calculations”. FERMILAB-TM-2386-E, 2006.

[97] T. Aaltonen *et al.*, “Search for $H \rightarrow WW^*$ Production at CDF Using 8.2 fb^{-1} of Data”. Public Note 10599, CDF Collaboration, 2011.

[98] J. Kraus and C.L. McGivern,“Search for Standard Model Higgs Boson with Trileptons and Missing Transverse Energy with 9.7 fb^{-1} at $p\bar{p}$ collisions at $\sqrt{s} =$ 1.96 eV”, DØ Conference Note 6276-CONF, 2012.

[99] http://www-d0.fnal.gov/Run2Physics/cs/caf/

[100] Chakravarti, Laha, and Roy, (1967). *Handbook of Methods of Applied Statistics, Volume I*, John Wiley and Sons, pp. 392-394.

[101] Toolkit for Multivariate Data Analysis with ROOT, http://tmva.sourceforge.net/

[102] T. Junk, Nucl. Instrum. Methods in Phys. Res. A **434**, 435 (1999);
A. Read, in *”1st Workshop on Confidence Limits,”* CERN Report No. CERN-2000-005, 2000.

[103] W. Fisher, “Collie: A Confidence Level Limit Evaluator”. Internal Note 5595, DØ Collaboration, 2009.

[104] M. Cooke *et al.*, “Muon Momentum Oversmearing Update for p20 Data”. Internal Note 6031, DØ Collaboration, 2010.

[105] P. Gris, “Electron Smearing Studies with RunIIa Data”. Internal Note 5400, DØ Collaboration, 2007.

[106] M. Shamim and T. Bolton, “Generator Level Reweighting of Z boson p_T”. Internal Note 5565, DØ Collaboration, 2008.

[107] G. Hesketh, “Generator Level Re-weighting of the Inclusive W-p_T Distribution”. Internal Note 5786, DØ Collaboration, 2008.

[108] http://www-d0.fnal.gov/Run2Physics/cs/index.html

[109] http://www-d0.fnal.gov/Run2Physics/cs/skimming/p20_pass2_skims.html

[110] See https://plone4.fnal.gov/P1/D0Wiki/tdaq/tsg/caftrigger/singleetriggers and https://plone4.fnal.gov/P1/D0Wiki/tdaq/tsg/triggerrun2b/singleeletriggers for lists

[111] https://plone4.fnal.gov/P1/D0Wiki/tdaq/tsg/triggerrun2b/jets